

# Grain Boundaries in Ultrathin Organic Semiconductors

Toward Controlling Their Emergence, Electrical Properties,  
and Impact on Device Performance

Lisa Sophie Walter



Munich 2022



# Grain Boundaries in Ultrathin Organic Semiconductors

Toward Controlling Their Emergence, Electrical Properties,  
and Impact on Device Performance

Lisa Sophie Walter

A dissertation submitted  
to the Faculty of Physics at the  
Ludwig-Maximilians-Universität München  
for the degree of  
DOCTOR RERUM NATURALIUM



Munich, October 21, 2022

First referee: Prof. Dr. Thomas Weitz

Second referee: PD Dr. Bert Nickel

Day of submission: October 21, 2022

Day of the oral examination: December 14, 2022

# Zusammenfassung

(Summary in German)

Organische Halbleiter bieten gegenüber anorganischen Halbleitern deutliche Vorteile, da sie sich in dünneren Filmen und bei geringeren Energien prozessieren lassen, auf nahezu jede Oberfläche aufgebracht werden können und zudem in ihren optischen und elektrischen Eigenschaften auf bestimmte Zwecke abgestimmt werden können. Diese einzigartigen Eigenschaften organischer Halbleiter ermöglichen die Einsparung von Materialien, Energie, Platz und Kosten und prädestinieren sie für Anwendungen in kundenspezifischen Endprodukten.

Obwohl organische Halbleiter seit Jahren in Halbleiterbauelemente wie z.B. organische Solarzellen, organische Leuchtdioden, organische Feldeffekttransistoren oder Sensoren implementiert werden, weisen diese im Vergleich zu anorganischen Bauelementen immer noch schlechtere Leistungen auf, insbesondere in Bezug auf reduzierte Mobilität, Effizienz, Reproduzierbarkeit und Stabilität. Als eine der Hauptursachen für diese Nachteile werden allgemein Korngrenzen in organischen Halbleitern betrachtet, da sie Orte mit erhöhten Ladungsträgerfallen, Rekombinations- und Degradationsraten darstellen. Warum und wie Korngrenzen entstehen (strukturell und energetisch) und welche ihrer Eigenschaften die Leistung von Halbleiterbauelementen hauptsächlich beeinflussen, wird dagegen noch untersucht.

Da die Beantwortung dieser Fragen dazu beitragen kann, den Ladungstransport in organischen Halbleitern zu kontrollieren und die Leistung und Effizienz von organischen Halbleiterbauelementen zu verbessern, werden in dieser Arbeit die grundlegenden Eigenschaften von Korngrenzen in Monolagen eines organischen kleinen Moleküls untersucht. Diese Filme zeichnen sich durch hohe Kristallinität und atomare Ebenheit auch über Korngrenzen hinweg aus. Diese strukturellen Eigenschaften sowie die Tatsache, dass Filme in Monolagen aufgebracht werden können, erlauben es, einzelne Körner und Korngrenzen genau dort zu charakterisieren, wo Ladungstransport in organischen Feldeffekttransistoren stattfindet, und zwar an der Grenzfläche zwischen Halbleiter und Isolator.

Mithilfe von Kelvin-Sondenkraftmikroskopie (KPFM für englisch *Kelvin probe force microscopy*) können als erstes Ergebnis Korngrenzen als Energiebarrieren oder -täler charakterisiert werden. Darüber hinaus werden verschiedene Präparationstechniken präsentiert, die in organischen Filmen resultieren, in denen entweder ein spezifischer Korngrenztyp vorherrscht, oder Barrieren und Täler koexistieren. Während es insbesondere für zukünftige Experimente von Vorteil ist, die Existenz verschiedener Korngrenztypen in organischen Materialien kontrollieren zu können, lassen die Filme mit beiden Typen den Schluss zu, dass es sich tatsächlich um unterschiedliche Strukturen mit grundlegend verschiedenen Eigenschaften handelt.

Die in dieser Arbeit präsentierten KPFM-Messungen erlauben neben der qualitativen Unterscheidung von Barrieren und Tälern auch eine quantitative Beschreibung durch die (energetische) „Höhe“ einer Korngrenze. Die Höhe einer Barriere, genauso wie die Tiefe eines Tals, kann durch Erhöhen der Ladungsträgerdichte im organischen Halbleiterfilm verringert werden. Beide Größen werden aber erst bei Ladungsträgerdichten verschwindend klein, die oberhalb des typischen Betriebsregimes organischer Solarzellen und organischer Leuchtdioden liegen, was wiederum die Relevanz für Ladungstransportmessungen an Korngrenzen unterstreicht. Daher wird anschließend mithilfe von zeitaufgelösten KPFM-Messungen untersucht, inwiefern Ladungsträger an Korngrenzen und anderen Fehlstellen eingefangen und freigelassen werden, und ob und wie diese Mechanismen die globalen Parameter eines Feldeffekttransistors beein-

flussen. Während Täler wie tiefe Fallen fungieren und damit Ladungsträger einfangen, werden diese an Barrieren reflektiert und/oder gestreut. Darüber hinaus scheinen Barrieren aber auch zu erhöhten Fallendichten an der Grenzfläche zwischen Halbleiter und Isolator zu führen, und damit zu einer stärkeren Reduktion des Ladungstransports als Täler. Täler hingegen definieren hauptsächlich die globalen Eigenschaften des Feldeffekttransistors, wie zum Beispiel die Einschalt- und Schwellspannung oder das qualitative Verhalten der Hysterese. Diese Erkenntnis macht klar, warum nicht nur die Korngrenzendichte in organischen Halbleitern, sondern auch deren Typ und Höhe kontrolliert werden können müssen.

Da es jedoch schwierig ist, die Existenz und die Eigenschaften von Korngrenzen in organischen Halbleitern mit experimentellen Methoden zu kontrollieren, präsentiert diese Arbeit ein alternatives Experiment mit dem Ziel, Ladungstransport über Korngrenzen hinweg zu manipulieren, und zwar durch Beleuchtung mit Licht aus dem ferninfraroten Bereich. Es wird angenommen, dass Photonen dieser Strahlungsquelle absorbiert werden, was zur Anregung von Ladungsträgern aus Tälern heraus oder über Barrieren hinweg führt und damit zu einem messbaren Fotostrom. Dieser Fotostrom kann mithilfe eines modifizierten Fourier-Transformations-Infrarotspektrometers energieaufgelöst gemessen werden und damit Korngrenzen auch in voluminösen Materialien detektier- und charakterisierbar machen. Der Auf- und Umbau des Spektrometers zu einem Fotostrom-Messplatz wird in dieser Arbeit zusammen mit vorläufigen Fotostrommessungen präsentiert.

Letztendlich wird der Ladungstransport in einem neuartigen Material aus der Klasse von metallorganischen Gerüstverbindungen untersucht, um die Rolle von Korngrenzen in organischen Halbleitern in einen Kontext zu stellen. Der Ladungstransport in diesem Material, welcher richtungsabhängig, sowie global und lokal gemessen wurde, wird weniger durch Korngrenzen, als durch die Schichtungsrichtung des Materials beeinflusst.

Zusammenfassend lässt sich sagen, dass die Ergebnisse dieser Arbeit es ermöglichen, die Eigenschaften von Korngrenzen in organischen Halbleitern sowie ihre Rolle in Halbleiterbauelementen wie z.B. organischen Feldeffekttransistoren, organischen Solarzellen oder organischen Leuchtdioden zu kontrollieren.

# Summary

(Summary in English)

Organic semiconductors stand out over their inorganic counterparts, since they can be processed in thinner films and at lower energies, onto nearly any surface, and with tunable optical and electrical properties for specific purposes. These unique properties of organic semiconductors allow to save material, energy, space and cost and make them ideal for applications in customer-specific end-products.

Although organic semiconductors have been implemented in semiconductor devices such as organic solar-cells, organic light-emitting diodes, organic field-effect transistors or sensors for years, these devices still show inferior performances compared to inorganic devices, especially in terms of reduced mobility, efficiency, reproducibility and stability. It is widely accepted that grain boundaries in organic semiconductors are one of the main responsables for these drawbacks, since they act as trapping, recombination and/or degradation sites. However, why and how grain boundaries emerge (structurally and energetically), and which properties of grain boundaries mainly influence the device performance is still under investigation.

Since addressing these questions will help to control charge transport in organic semiconductors and improve device performance, this work presents a fundamental investigation of grain boundaries in monolayer-thin films of an organic small molecule. These films stand out due to high crystallinity and atomically smoothness across grain boundaries. This, as well as their thinness, allows to characterize single grains and grain boundaries at the location where charge transport takes place in organic field-effect transistors, namely at the semiconductor-insulator interface.

By Kelvin probe force microscopy (KPFM) grain boundaries are found as a first result to act as energy barriers or valleys, and different thin-film application techniques are presented resulting in films in which either a specific type of grain boundary predominates, or in films where barriers and valleys coexist. While it is particularly advantageous for future experiments to be able to control the existence of different types of grain boundaries in organic materials, the films with both types prove the fundamental difference between energy barriers and valleys.

KPFM measurements not only allow a qualitative differentiation of barriers and valleys, but also a quantitative description of „grain boundary heights“. Valley depths and barrier heights can both be decreased by increasing the charge-carrier density in the organic semiconductor-film. However, they only vanish at charge-carrier densities above the typical operating regime of organic solar-cells and organic light-emitting diodes, which underlines the relevance of investigating charge transport at grain boundaries.

Consequently, time-resolved KPFM measurements are conducted to investigate the trapping and detrapping mechanisms at grain boundaries and other local impurities, as well as their influence on global device parameters. While valleys trap charge carriers in deep traps, barriers backscatter electrons, but also indicate an increased trap-state density at the organic-semiconductor interface, thereby leading to a stronger reduction of charge transport than valleys. Valleys, on the contrary, are found to mainly define the global device parameters such as the turn-on and threshold voltage or the qualitative behavior of hysteresis. This finding underlines the need to be able to control not only the grain-boundary density in organic semiconductors, but also their type and absolute height.

However, since it is challenging to control the emergence and electric properties of grain

boundaries in organic semiconductors by experimental methods, an alternative experiment is presented with the aim to manipulate charge transport across grain boundaries by illumination with far-infrared light.

It is assumed that photons from this light source are absorbed, leading to the excitation of charge carriers out of valleys or across barriers and thus to a measurable photocurrent. This photocurrent can be measured energy-resolved by using a modified Fourier transform infrared spectrometer, which allows to detect and characterize grain boundaries even in bulk-like materials.

Finally, charge transport in a novel metal-organic framework is investigated directionally, globally and locally, to put the role of grain boundaries in organic semiconductors into a context. It is found that in this special material grain boundaries do not play an as important role as the stacking direction of single planes of the metal-organic framework.

To summarize, the findings of this work lead toward controlling the properties of grain boundaries in organic semiconductors and their role in organic semiconductor devices such as field-effect transistors, organic solar-cells or organic light-emitting diodes.

## Publications

This dissertation is based on the following journal articles, listed in chronological order:

- P1** *Interfacial Synthesis of Layer-Oriented 2D Conjugated Metal-Organic Framework Films toward Directional Charge Transport.*  
 Z. Wang\*, **L.S. Walter\***, M. Wang\*, P.S. Petkov, B. Liang, H. Qi, N.N. Nguyen, M. Hambsch, H. Zhong, M. Wang, S.W. Park, L. Renn, K. Watanabe, T. Taniguchi, S.C.B. Mannsfeld, T. Heine, U. Kaiser, S. Zhou, R.T. Weitz, X. Feng, and R. Dong.  
 Journal of the American Chemical Society 2021, 143(34), pp. 13624–13632.  
 DOI: [10.1021/jacs.1c05051](https://doi.org/10.1021/jacs.1c05051).

\* These authors contributed equally.

Reprinted in Chapter 7.

- P2** *Revealing and Controlling Energy Barriers and Valleys at Grain Boundaries in Ultrathin Organic Films.*  
**L.S. Walter**, A. Axt, J.W. Borchert, T. Kammerbauer, F. Winterer, J. Lenz, S.A.L. Weber, and R.T. Weitz.  
 Small 2022, 18(34), 2200605.  
 DOI: [10.1002/sml.202200605](https://doi.org/10.1002/sml.202200605).

Reprinted in Chapter 4.

Other peer-reviewed publications:

- P3** *Flexible and Ultrasoft Inorganic 1D Semiconductor and Heterostructure Systems Based on SnIP.*  
 C. Ott, F. Reiter, M. Baumgartner, M. Pielmeier, A. Vogel, P. Walke, S. Burger, M. Ehrenreich, G. Kieslich, D. Daisenberger, J. Armstrong, U.K. Thakur, P. Kumar, S. Chen, D. Donadio, **L.S. Walter**, R.T. Weitz, K. Shankar, and T. Nilges.  
 Advanced Functional Materials 2019, 29(18), p. 1900233.  
 DOI: [10.1002/adfm.201900233](https://doi.org/10.1002/adfm.201900233).
- P4** *Charge Traps in All-Inorganic CsPbBr<sub>3</sub> Perovskite Nanowire Field-Effect Phototransistors.*  
 F. Winterer, **L.S. Walter**, J. Lenz, S. Seebauer, Y. Tong, L. Polavarapu, and R.T. Weitz.  
 Advanced Electronic Materials 2021, 7(6), p. 2100105.  
 DOI: [10.1002/aelm.202100105](https://doi.org/10.1002/aelm.202100105).
- P5** *All About the Interface: Do Residual Contaminants at A High-Quality h-BN Monolayer Perylene Diimide Interface Cause Charge Trapping?*  
 L. Renn, **L.S. Walter**, K. Watanabe, T. Taniguchi, and R.T. Weitz.  
 Advanced Materials Interfaces 2022, 9(10), p. 2101701.  
 DOI: [10.1002/admi.202101701](https://doi.org/10.1002/admi.202101701).



## Abbreviations

2D c-MOF	two-dimensional conductive MOF
AC	alternating current
AFM	Atomic Force Microscopy
Ag	silver
AM	amplitude modulated
ATR	attenuated total reflection
Au	gold
BGBC	bottom-gate bottom-contact
BGTC	bottom-gate top-contact
BSC	back-sweep current
c-AFM	conductive AFM
CdTe	cadmium telluride
CPD	contact potential difference
CVD	chemical vapor deposition
DC	direct current
DLATGS	deuterated L-alanine doped triglycine sulfate
DMP	dimethylphthalate
DOS	density of states
e-beam PVD	electron-beam physical vapor deposition
EA	electron affinity
ELR	extrapolation in the linear regime
EPPA	4-ethoxyphenylphosphonic acid
FET	field-effect transistor
FFT	fast Fourier transform
FIR	far infrared
FM	frequency modulated
FTIR	Fourier transform infrared
FTPC	Fourier transform photoelectric current
hBN	hexagonal boron nitride
HD-PE	high-density polyethylene
HgTe	mercury telluride
HOMO	highest occupied molecular orbital
IP	ionization potential
IR	infrared

KPFM	Kelvin probe force microscopy
LCAO	linear combination of atomic orbitals
LUMO	lowest unoccupied molecular orbital
MCT	mercury cadmium telluride
MIR	mid infrared
MOF	metal-organic framework
NIR	near infrared
ODTS	octadecyltrichlorosilane
OFET	organic field-effect transistor
OLED	organic light-emitting diode
OPV	organic photo-voltaic
PDI	perylene diimide
PDI1EPCN2	N,N'-di((S)-1-ethylpentyl)-1,7(6)-dicyano-perylene-3,4:9,10-bis(dicarboximide)
PDI1MPCN2	N,N'-di((S)-1-methylpentyl)-1,7(6)-dicyano-perylene-3,4:9,10-bis(dicarboximide)
PDMS	poly(dimethylsiloxane)
PET	poly(ethylene terephthalate)
POM	polarized optical microscopy
PtIr	platinum iridium
PVD	physical vapor deposition
SAM	self-assembled monolayer
Si	silicon
SiC	silicon carbide
SNR	signal-to-noise ratio
TDPA	tetradecylphosphonic acid
TFT	thin-film transistor
TGBC	top-gate bottom-contact
TGTC	top-gate top-contact
TLM	transfer-length measurement
Tol	toluene
TPX	polymethylpentene

# Contents

<b>Zusammenfassung (Summary in German)</b>	<b>i</b>
<b>Summary (Summary in English)</b>	<b>iii</b>
<b>Publications</b>	<b>v</b>
<b>Abbreviations</b>	<b>vii</b>
<b>1 Introduction</b>	<b>1</b>
<b>2 Theoretical Foundations</b>	<b>5</b>
2.1 Fundamentals of Organic Molecules . . . . .	5
2.1.1 Electronic States of a Single Molecule . . . . .	5
2.1.2 Optical Excitations . . . . .	6
2.1.3 Molecular Vibrations . . . . .	8
2.1.4 Properties of PDI1MPCN2 . . . . .	10
2.2 Organic Thin-films . . . . .	11
2.2.1 Formation of Organic Thin-films . . . . .	11
2.2.2 Energy Levels of Crystalline Films . . . . .	15
2.3 Charge Transport in Organic Semiconductors . . . . .	17
2.3.1 Electronic Properties of Charged Molecules and Films . . . . .	17
2.3.2 Photoexcitation of Electric Currents . . . . .	18
2.3.3 Transport Models in Single Grains . . . . .	18
2.3.4 Charge-transport Models at Grain Boundaries . . . . .	20
2.4 Organic Field-effect Transistors . . . . .	21
2.4.1 Structure of Organic Field-effect Transistors . . . . .	21
2.4.2 Working Principle of Organic Field-effect Transistors . . . . .	21
2.4.3 Device Parameters . . . . .	23
2.4.4 Deviations from the Ideal Behavior . . . . .	25
2.5 Introduction to Metal-organic Frameworks . . . . .	27
2.5.1 Binding Mechanisms in Metal-organic Frameworks . . . . .	27
2.5.2 Structure of Metal-organic Frameworks . . . . .	28
2.5.3 Charge Transport Models in Metal-organic Frameworks . . . . .	30
2.5.4 Synthesis and Device Integration . . . . .	31
<b>3 Experimental Methods</b>	<b>35</b>
3.1 Device Fabrication . . . . .	35
3.1.1 Substrate Preparation . . . . .	35
3.1.2 Thin-Film Application . . . . .	36
3.1.3 Contacting . . . . .	37
3.1.4 Preparation of field-effect transistors (FETs) with metal-organic frameworks (MOFs) . . . . .	37
3.2 Structural Characterization . . . . .	38
3.2.1 Polarized Optical Microscopy . . . . .	38
3.2.2 Atomic Force Microscopy . . . . .	39
3.3 Electric Characterization . . . . .	42
3.3.1 Conductive Atomic Force Microscopy . . . . .	42
3.3.2 Kelvin Probe Force Microscopy . . . . .	43

3.3.3	Probe Station . . . . .	45
3.4	Spectroscopic Methods . . . . .	46
3.4.1	Fourier Transform Infrared Spectroscopy . . . . .	46
3.4.2	Fourier-Transform Photocurrent Spectroscopy in the Far Infrared . . . . .	50
<b>4</b>	<b>Revealing and Controlling Energy Barriers and Valleys at Grain Boundaries in Ultrathin Organic Films</b>	<b>55</b>
<b>5</b>	<b>Grain Boundaries Influence Global Device Parameters of Organic Thin-film Transistors</b>	<b>65</b>
5.1	Motivation . . . . .	65
5.2	Experimental Details . . . . .	66
5.3	Results and Discussion . . . . .	67
5.3.1	Time Dependence of the Surface Potential as a Function of Gate Voltage	67
5.3.2	Extraction of Screening Times and Local Threshold Voltages . . . . .	68
5.3.3	Charge-carrier Detrapping at Zero Gate Voltage . . . . .	70
5.3.4	Investigation of Hysteresis Effects . . . . .	71
5.4	Conclusion and Outlook . . . . .	72
<b>6</b>	<b>Can Charge Transport Across Grain Boundaries be Manipulated with Light?</b>	<b>73</b>
6.1	Motivation . . . . .	73
6.2	Experimental Details . . . . .	74
6.3	Toward Photocurrent Spectroscopy of Grain Boundaries in Organic Thin-films	75
6.3.1	Preliminary Measurements . . . . .	76
6.3.2	Restrictions for Device and Experiment Design . . . . .	77
6.3.3	Absolute Photocurrent in Polycrystalline Films . . . . .	79
6.4	Conclusion and Outlook . . . . .	80
<b>7</b>	<b>Interfacial Synthesis of Layer-Oriented 2D Conjugated Metal-Organic Framework Films toward Directional Charge Transport</b>	<b>83</b>
<b>8</b>	<b>Conclusion and Outlook</b>	<b>93</b>
	<b>Appendix</b>	<b>97</b>
A	Influence of Grain Boundaries on the Activation Energy . . . . .	97
A.1	Motivation . . . . .	97
A.2	Technical Details . . . . .	98
A.3	Results . . . . .	100
A.4	Discussion and Outlook . . . . .	100
B	Technical Details on Shadow Masks . . . . .	101
C	Technical Details on Atomic Force Microscopy . . . . .	102
D	Technical Details on Fourier Transform Infrared Spectroscopy . . . . .	103
E	Supporting Information to Chapter 4 . . . . .	104
F	Supporting Information to Chapter 5 . . . . .	125
F.1	Supplementary Data . . . . .	125
F.2	Extraction of the Screening Factor $\beta$ . . . . .	125
F.3	Suggestions for an Improved Device Design . . . . .	127
G	Supporting Information to Chapter 7 . . . . .	129
H	Related Theses . . . . .	171
	<b>References</b>	<b>173</b>
	<b>Danksagung (Acknowledgments)</b>	<b>189</b>

# 1 Introduction

Imagine an eight-month old baby. When it is sitting in front of a box filled with toys, its unwavering joy about dropping them shows that it doesn't think about possible limits of its resources or energy. This picture is unfortunately very similar to the prevalent way of thinking throughout the history of our society. The announcement of the physics Nobel prize in 2021, awarded „for the physical modeling of Earth's climate, quantifying variability and reliably predicting global warming“, [1] resembled a mother telling her child to stop dropping toys. More meaningful and concrete recommendations for action include e.g. to

- „increase the use of renewable energy,
- eliminate waste, prevent pollution, and increase recycling,
- (...) foster markets for sustainable technologies and environmentally preferable materials, products, and services,
- design, construct, maintain, and operate high-performance sustainable buildings“ [2].

Researchers all over the world have worked to find a way toward fulfilling these recommendations. One way is to use organic semiconductors in semiconductor devices. Organic semiconductors are primarily made of carbon and hydrogen, and these two materials define the unique properties and advantages of this materials class, like their abundant occurrence in nature, versatility, tunability, biocompatibility, or the possibility to apply ultra-thin films onto nearly every surface and at low temperatures. This allows to implement organic semiconductors into devices that are lighter, need less space, can be customized in a more versatile way, and overall, can be produced at smaller energies than inorganic semiconductor devices [3, 4]. As a consequence, organic semiconductors have been implemented in a variety of semiconductor devices, such as organic field-effect transistors (OFETs) [5, 6], organic photo-voltaic (OPV) devices [7, 8], sensors [9], or displays [10], especially since 1987 (1990) when organic films were first implemented into organic light-emitting diodes (OLEDs) [11, 12]. Recent advancements include rollable displays [13], transparent solar cells in windows [14] or clothes [15, 16], and sensors directly on the skin for medical application [17]. However, while the device efficiency of e.g. organic solar-cells has increased within the last years, inorganic solar-cells show still superior performance and account for 92% of the market share [18, 19].

Besides smaller device efficiencies, the inferior performance of organic semiconductors is represented by

- decreased mobilities compared to inorganic materials [20, 21], and good electron conductors are rare compared to good hole conductors [22–24]. Specifically for application in organic solar-cells and OLEDs, this poses a problem, since these devices require good charge-carrier extraction or injection, respectively, of both types of charge carriers.
- large contact resistances, which mainly influence the device performance rather than the semiconductor itself [25, 26]
- large device-to-device variability and low reproducibility [27–29]
- instability in air, under illumination, and/or under bias stress [30, 31]

While some of these drawbacks are intrinsically given by the nature of organic semiconductors, such as their bad compatibility with inorganic metal electrodes [32], and strong electron-electron interactions that define their optical and electrical properties [3], nearly all of them can also occur due to grain boundaries in the material. Organic films often consist of a high density of grain boundaries, especially when grown by vapor-based techniques. While these techniques are easier to control [32], researchers have put significant effort into developing solution-based application techniques that can result in highly-crystalline films [33,34]. Grain boundaries have been observed to influence the contact resistance [35], act as recombination sites [36–38], scattering and/or trapping sites [39], and to enhance device-performance degradation [40,41]. Despite these known maleficent effects on the device performance, there is no consensus on the following questions yet:

- Under which conditions do grain boundaries emerge? [42–44]
- How do grain boundaries influence the local energy distribution? [45–48]
- How does this energy distribution impact the charge transport across grain boundaries? [49–52]
- Can the answers to the previous questions explain the observed impact on devices?
- Can grain boundary-properties be manipulated and/or even be used, e.g. to tune device properties?

This work aims to provide insight into these questions using a perylene-diimide derivative, abbreviated PDI1MPCN2 (introduced in Section 2.1.4). This molecule stands out due to its high electron conductivity up to  $4 \text{ cm}^2/\text{Vs}$ , good air stability and solution processability, which allows to grow mono- to bilayer-thin films with comparably large grains. [53] These films are implemented in OFETs, where the charge transport in single grains or across a predefined number of grain boundaries can be investigated. Besides electrical transport measurements, optical microscopy, Atomic Force Microscopy (AFM), Kelvin probe force microscopy (KPFM), and photocurrent measurements are performed under varying temperatures, film thicknesses, and/or crystallinity. The theory, methods and results of these investigations are presented within this work in the following order:

**Chapter 2** presents the theory necessary to understand the charge-transport properties in organic semiconductors. This starts from a single molecule presenting its electrical, optical and vibrational properties, and proceeds in the following section to organic thin-films, including how they can be fabricated, how different techniques influence the grain growth, and to what extent the energetic properties change by intermolecular interactions. The interaction with charged molecules will be presented afterwards, making the transition to transport models in organic semiconductors and the presentation of the working principle of OFETs. The theory chapter closes with an introduction to MOFs, a novel class of materials related to organic materials which have been investigated within this work as a comparison model.

**Chapter 3** introduces the basics of device preparation and the relevant measurement techniques with a focus on KPFM and the arrangement of a setup for photocurrent-spectroscopy measurements.

**Chapter 4** presents the results of KPFM measurements at grain boundaries in thin films of PDI1MPCN2 at varying charge-carrier densities, providing details on the electrostatic energy distribution at grain boundaries. Grain boundaries are found to either act as energy barriers

or valleys, whereby both types can coexist in the same film. Furthermore, a method to force one of both grain-boundary types to emerge in the film is shown. The results presented in this chapter have recently been published under the title „Revealing and Controlling Energy Barriers and Valleys at Grain Boundaries in Ultrathin Organic Films“ (cf. Publication **P2**).

**Chapter 5** focuses on the time-dependence of electric charging using time-resolved KPFM. By detecting the local properties at different sites, i.e., grains, barriers, and valleys, the question is addressed how local impurities influence the charging of the semiconductor and the device-to-device variability. The experiments lead to evidence that especially valleys determine global device parameters, such as hysteresis effects, or the turn-on and threshold voltage of an OFET. This finding is summarized in the title „Grain Boundaries Influence Global Device Parameters of Organic Thin-film Transistors“.

**Chapter 6** uses the results of the two previous chapters and presents a method to manipulate the role of grain boundaries in OFETs or other semiconductor devices. It is based on the idea that electrons can be excited over grain boundaries, whereby the required activation energy is provided by photons. Since this energy corresponds to light from the far infrared, a commercial Fourier transform infrared spectrometer is modified into a setup to measure Fourier transform photocurrent spectra. The title of this chapter is „Can Charge Transport Across Grain Boundaries Be Manipulated with Light?“.

**Chapter 7** presents local and global transport measurements in a MOF. This chapter has been published in cooperation with chemists of the Technical University Dresden under the title „Interfacial Synthesis of Layer-Oriented 2D Conjugated Metal-Organic Framework Films“ (Publication **P1**). As the title suggests, the main part of this work presents the synthesis of a novel two-dimensional MOF with a predefined stacking direction. This achievement allows to detect directional charge-transport globally and locally, and therefore across several (polycrystalline) and few (crystalline) domains. The transport measurements reveal that neither contact resistance, nor grain boundaries or other local impurities are the main limitations to charge transport, but the distribution of delocalized electrons. These results deepen the understanding on transport mechanisms in two-dimensional MOFs, but also help to put the role of grain boundaries in organic films into context.

**Chapter 8** includes a conclusion and outlook for organic semiconductors and devices. Finally, a short technical section on activation energies is presented in **Appendix A** which skips detailed theory and research context due to time reasons.



## 2 Theoretical Foundations

*In this thesis, the transport mechanisms within organic semiconductor thin-films are investigated. The relevant theory will be presented in four steps: We will start this chapter with the fundamental properties of organic molecules in Section 2.1, followed by the presentation of how these change upon film formation in Section 2.2. While we will focus on neutral molecules in these first two sections, Section 2.3 will introduce the properties of charged molecules and films, and lead to charge transport models in single grains and across grain boundaries. To characterize the semiconductor thin-films, they were implemented in field-effect transistors, whose structure and working principle will be described in Section 2.4.*

*Finally, Section 2.5 gives a short introduction to metal-organic frameworks, their structure, properties and typical transport mechanisms.*

### 2.1 Fundamentals of Organic Molecules

Organic molecules are compounds mainly made of hydrocarbons and can be categorized depending on their size into long polymers and small molecules [3, 54]. The following description, based on the textbook by Köhler and Bässler [3], will first present the energetic, optical and vibrational properties of organic small molecules in general, before introducing the small molecule investigated in this work.

#### 2.1.1 Electronic States of a Single Molecule

Almost all properties of organic semiconductor molecules can be drawn back to the ability of carbon (the basic element of organic molecules) to hybridize. In its neutral state, the carbon atom has completely filled 1s and 2s orbitals and half-filled  $2p_x$  and  $2p_y$  orbitals. However, the  $2p_x$  and  $2p_y$  orbitals can mix with the 2s orbital, resulting in three half-filled  $sp^2$  orbitals. These three  $sp^2$  orbitals lie within one plane and enclose an angle of  $120^\circ$ , while the remaining  $p_z$  orbital stands perpendicular to this plane, as sketched in **Figure 2.1a**. This so-called  $sp^2$  hybridization is energetically favorable if the carbon atom binds to another.

If two carbon atoms bind to each other, their orbitals overlap, whereby the molecular orbitals  $\pi$  (out of overlapping  $p_z$  orbitals) and  $\sigma$  (out of overlapping  $sp^2$  orbitals) are formed. To describe the molecular orbitals energetically, one can construct them as linear combination of atomic orbitals (LCAO). The resulting molecular orbitals can be either a symmetric linear combination, forming a bonding orbital, (named  $\sigma$  or  $\pi$ ), or an antisymmetric linear combination, forming an anti-bonding orbital ( $\sigma^*$  or  $\pi^*$ ). Filling in all electrons of the contributing atoms (in the so-called molecular orbital model sketched in **Figure 2.1b**) finds that the highest occupied molecular orbital (HOMO) is a  $\pi$  orbital and the lowest unoccupied molecular orbital (LUMO) is a  $\pi^*$  orbital. Since the electrons in the  $\pi$  and  $\pi^*$  orbitals are highly delocalized, the HOMO and LUMO (the frontier orbitals) are the main contributors to charge transport or absorption. In so-called „conjugated aromatic systems“ (e.g. benzene, displayed in **Figure 2.1c**) the overlap of  $\pi$  ( $\pi^*$ ) orbitals above and below the molecular plane enables charge transport in the direction perpendicular to it („out of plane“). This direction shows improved transport with respect to the direction within the molecular plane („in plane“). In-plane bonds are defined by the overlap of localized  $\sigma$  orbitals, leading to

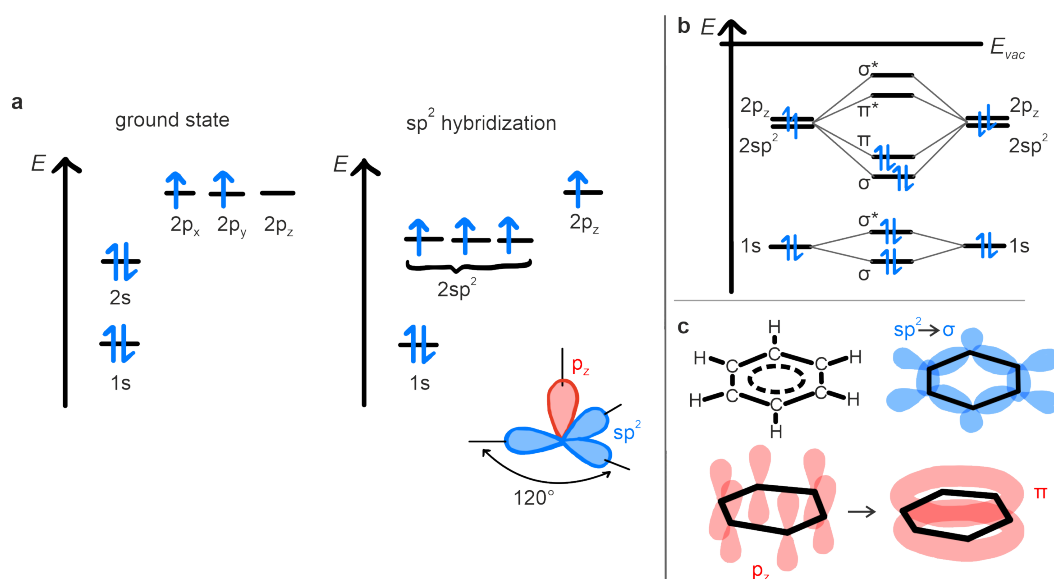


**Figure 2.1 Electronic structure of carbon atoms and organic molecules.** **a**, Electronic configuration of a carbon atom in its ground state and after  $sp^2$  hybridization, including the spatial distribution of the resulting orbitals. **b**, Filling of the molecular orbitals with all electrons of the contributing atoms according to the molecular orbital model, resulting in the highest occupied molecular orbital (HOMO)  $\pi$  and the lowest unoccupied molecular orbital (LUMO)  $\pi^*$ . **c**, Electronic structure and molecular orbitals of benzene as example for conjugated aromatic systems. Blue: localized  $\sigma$  orbitals formed out of overlapping  $sp^2$  orbitals. Red: delocalized  $\pi$  orbitals formed by the overlap of  $p_z$  orbitals. Figures adapted from References [3, 26, 55].

strong, covalent bonds that hold the molecule together (cf. **Figure 2.1c**). The intermolecular forces are consequently much smaller than the intramolecular forces, which is why processing of organic materials requires much smaller energies than of inorganic materials, and the properties of one molecule mostly define the properties of the whole material.

## 2.1.2 Optical Excitations

### Excited States

In the molecule's ground state, the HOMO is completely filled and the LUMO is completely empty, and the total spin adds up to  $S = 0$ , according to Hund's rules. The total spin of the system can change, if an electron is excited from the HOMO to the LUMO, resulting in a configuration with two unpaired electrons (one in the HOMO and one in the LUMO). Depending on the orientation of the unpaired electrons, the molecular spin sums up to either  $S = 0$  (antiparallel) or  $S = 1$  (parallel). Since only one configuration of  $S = 0$  is allowed quantum-mechanically, it is referred to as singlet excited state  $S_1$ , and higher excited states are denoted  $S_2, S_3, \dots$ . In contrast, a total spin of  $S = 1$  can come in with three different eigenvalues of the spin angular momentum and is therefore called triplet excited state  $T_1, T_2, T_3, \dots$ . Singlet and triplet excited states can be distinguished by different energies, as shown in **Figure 2.2a**.

### Interband Absorption

The excitation of an electron into the LUMO can be achieved by the absorption of a photon, which is specifically interesting for photo-excited currents (or „photocurrents“) described in Section 2.3. The number of absorbed (emitted) photons per time defines the absorption

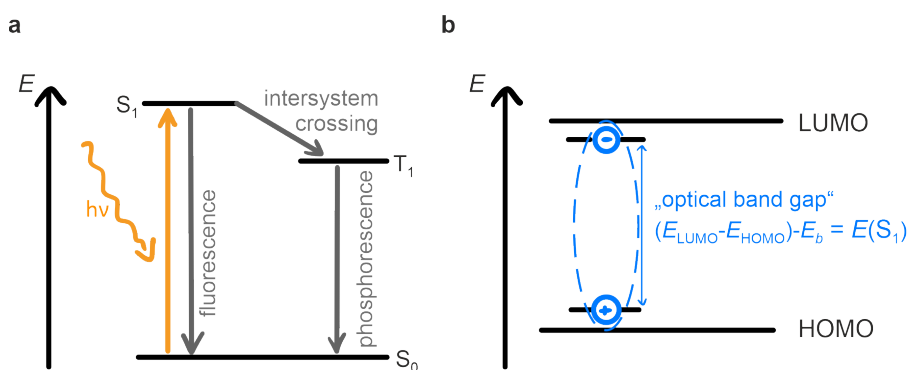


**Figure 2.2 Excited states of an organic molecule.** **a**, Energy diagram of the ground state  $S_0$  and the excited states  $S_1$  and  $T_1$ , including optical transitions. **b**, Sketch of the concept of an exciton bound by the binding energy  $E_b$ . Figures adapted from Reference [3].

(emission) intensity  $\mathcal{I}$  and corresponds to the transfer rate from the initial to the final state  $p_{i \rightarrow f}$ . This transition rate is given by the product of the density of final states  $\rho_f$  and the transition probability as

$$\mathcal{I} \propto p_{i \rightarrow f} = \frac{2\pi}{\hbar} \rho_f \cdot \left| \langle \Psi_f | \hat{H}' | \Psi_i \rangle \right|^2 \quad (\text{Fermi's Golden Rule}). \quad (2.1)$$

$\hat{H}'$  is the perturbation operator that causes the transition from the initial (i) to the final (f) state expressed by the molecule's wavefunction  $\Psi$ . The wavefunction can be divided into a part describing its charge, and a part describing its total angular momentum, i.e.,

$$|\Psi\rangle = |\Psi_{\text{ch}}\rangle |\Psi_{\text{mom}}\rangle, \quad (2.2)$$

assuming that the atomic nuclei move much slower than the electronic cloud (Born-Oppenheimer approximation). (The consequences of non-negligible molecular vibrations are presented in Section 2.1.3.)

Classically, the incoming light can be interpreted as electromagnetic wave, which accelerates the molecular electron cloud to follow its oscillation. This interpretation visualizes that photons do not interact with the angular momentum of electrons (expressed by  $\Psi_{\text{mom}}$ ), but only with their charge ( $\Psi_{\text{ch}}$ ). This interaction can be expressed by rewriting the perturbation operator with the electric dipole operator

$$\hat{H}' = e\hat{D} \quad (2.3)$$

( $e$  is the electric charge). Equation (2.1) results in

$$p_{i \rightarrow f} = \frac{2\pi}{\hbar} \rho_f \cdot \left| \langle \Psi_{\text{ch},f} | e\hat{D} | \Psi_{\text{ch},i} \rangle \right|^2 \cdot \left| \langle \Psi_{\text{mom},f} | \Psi_{\text{mom},i} \rangle \right|^2. \quad (2.4)$$

Since all three factors in Equation (2.4) have to be non-zero to result in finite absorption or emission intensity, the following conditions for optical excitation arise:

1.  $\rho_f \neq 0$ :

The density of final states can be written as

$$\rho_f = \begin{cases} 1 & : E_f - E_i = h\nu, \\ 0 & : \text{else.} \end{cases} \quad (2.5)$$

This equation represents **Planck's law**, stating that the transition can only take place if the energy of the incoming photon with frequency  $\nu$  equals the energy difference between the final and the initial state. This „optical energy gap“ is often expressed by the energy difference between HOMO and LUMO.

However, this approximation only holds when electron-electron interactions can be neglected, which is the case for inorganic materials. In organic materials, the optical gap is correctly described by the energy of the singlet excited state  $S_1$  as denoted in **Figure 2.2b**.

2.  $|\langle \Psi_{\text{ch},f} | e\hat{D} | \Psi_{\text{ch},i} \rangle|^2 \neq 0$ :

The transition probability is non-zero if the initial and the final-state wavefunctions have different parities. This condition corresponds to **charge conservation**. Furthermore, the transition probability increases with increasing overlap of the initial and final wavefunction, which is the case if the HOMO and LUMO are well extended and share the same positions on the molecule.

3.  $|\langle \Psi_{\text{mom},f} | \Psi_{\text{mom},i} \rangle|^2 \neq 0$ :

This condition represents **conservation of the total angular momentum**, i.e., the sum of the spin momentum and the orbital momentum. Transitions with a changing spin (especially  $T_1 \rightarrow S_0$ , known as phosphorescence) can therefore be observed if spin-orbit coupling is provided. On the contrary, the transition  $S_1 \rightarrow S_0$  (fluorescence) shows finite emission rates even without spin-orbit coupling, since the spin momentum is conserved. Both transitions are sketched in **Figure 2.2a**.

## Excitons

From Planck's law, and given that the energy of photons is quantized, it is straightforward that also the energy of excited states is quantized. The quantum-mechanical quasi-particle is the so-called exciton. It represents the excited electron-hole pair bound by Coulomb interactions with a binding energy  $E_b$  as sketched in **Figure 2.2b**. Separation of the exciton into a free electron in the LUMO and a hole in the HOMO requires this binding energy. Therefore, excitons are referred to as absorption below the band edge, the energy of which corresponds to the energy of visible light in organic semiconductors [3, 54].

### 2.1.3 Molecular Vibrations

So far, we have assumed that the atomic nuclei do not move. However, an organic molecule is not a rigid object, but the atomic nuclei vibrate at temperatures above 0 K, and especially if excited by infrared light, as presented in Section 3.4.1. Therefore, the basics of molecular vibrations will be presented in this section, according to References [55–57].

#### Normal Vibrational Modes

Classically, each intramolecular bond between two atoms can be described as a spring. It starts to oscillate if it is excited at its resonance frequency, determined by the nucleus masses and their interaction strength. If integer multiples of the resonance frequency are hit, overtones are excited.

If the molecule consists of more than two atoms, however, it becomes much more complicated to describe the whole set of molecular vibrations, because vibrations of different bonds can influence each other, and several vibrational modes with the same energy may exist. To

overcome this problem, for a molecule with  $N$  atoms and  $3N$  degrees of freedom,  $3N$  so-called normal coordinates

$$Q_i, \quad i = 1, 2, 3, \dots, 3N \quad (2.6)$$

are introduced. Each normal coordinate represents a group of atoms which reach maximal displacement and equilibrium at the same time. The normal coordinate then describes the effective mass  $m_i^*$  of this group and its maximum displacement from its equilibrium position  $\vec{d}_i$ .

The introduction of normal coordinates allows to diagonalize the Hamiltonian which describes the whole molecule  $\hat{H}$  and to split the Schrödinger equation  $\hat{H}|\Psi\rangle = E|\Psi\rangle$  into  $3N$  distinct equations. Since three of these equations describe rotational modes, and three describe translational modes,  $3N - 6$  equations remain to describe the vibrational modes. (For linear molecules only 2 rotation axes can be defined and therefore  $3N - 5$  vibrational modes can be differed.) The total vibrational energy of the molecule can consequently be written as the sum of all eigenenergies

$$E_{\text{vib}} = E_{\text{vib},1} + E_{\text{vib},2} + \dots + E_{\text{vib},3N-6}. \quad (2.7)$$

Practically, this means that each fundamental mode described by normal coordinates—the **fundamental normal mode**—brings in its own typical energy and does not influence other vibrational modes.

The energies of fundamental vibrational modes in organic molecules are in the range of 50 to 500 meV and can be excited by absorption of photons from the mid infrared (MIR). Overtones have higher energies in the near infrared (NIR) regime. Consequently, vibrational modes are typically detected by infrared (IR) spectroscopy, which will be introduced in more detail in Section 3.4.1.

### Absorption

Similar to the excitation of excitons, vibrational modes can be excited if a photon with a corresponding energy is absorbed. The intensity can be determined by Fermi's golden rule (compare Equation (2.1)), where we now have to introduce a third factor  $\Psi_{\text{vib}}$  to the molecular wavefunction in Equation (2.2). This factor considers the atomic nuclei, whose interaction with the electric dipole operator was neglected before, because it is much smaller than the contribution of the electronic clouds. Therefore, it is reasonable to expand the contribution of the atomic nuclei by a Taylor series. We will skip this lengthy mathematical description, which is described in more detail e.g. in the textbook by Califano [56] and directly come to the practical interpretation:

1. Planck's law, expressed in the density of final states (cf. Equation (2.5)), states that a vibrational mode can only be excited if the energy of the incoming light equals the energy of the vibrational mode. In reverse, each peak in an absorption spectrum can be assigned to a characteristic fundamental vibration.
2. A vibration can only be excited if it changes the molecular dipole moment, that is, if it has a non-zero **transition dipole moment**. This is in contrast to Raman spectroscopy, which detects a change of the molecule's polarizability. Therefore, the intensities of Raman and IR spectra are usually complementary [3].
3. The intensity of an excitation becomes maximal if the electric field of the incoming light is parallel to the molecule's transition dipole moment, and zero if they are perpendicular to each other.

## Vibrons and Phonons

As we have seen, the molecular vibrations are quantized in their energy and therefore also called vibrons. Vibrons describe intramolecular vibrations, in contrast to phonons, which represent lattice vibrations and may dampen charge transport at increased temperatures (cf. Section 2.3). In organic crystals, the phonon energy corresponds to the energy of light in the far infrared [54].

## Electronic Coupling to Excited States

The distance between two neighboring atoms determines the distribution of electrons and therefore the wavefunction of the molecule. Consequently, the vibration of atomic nuclei influences not only the absorption spectrum in the IR, but also the energy distributions of the ground and excited states, which get dependent on the normal coordinates. This so-called „vibronic coupling“ is displayed in **Figure 2.3**. For small displacements around the equilibrium position, the potential curve shown in **Figure 2.3** can be approximated by a quadratic potential, thereby describing a typical quantum-mechanical harmonic oscillator with quantized energies.

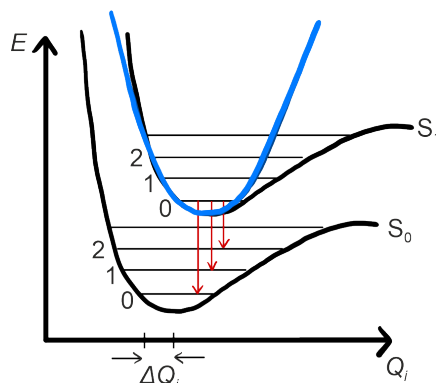


**Figure 2.3 Electronic coupling of vibrational modes.** The ground and excited states (here  $S_1$  is exemplary shown) depend on the normal coordinate. The relation can be approximated to a quadratic dependence at small displacements  $\Delta Q_i$  as exemplary shown for  $S_1$  (blue curve). Vibrational ground states and overtones are indicated by horizontal lines and some possible transitions between  $S_1$  and  $S_0$  by red arrows. Adapted from Reference [3].

For optical excitations, this means that an electron can be excited from each vibrational mode in the ground state  $S_0$  into each vibrational mode in the singlet or triplet excited state and lose its energy radiationless from the  $n$ -th to the 0th vibrational state (**internal conversion**). The resulting absorption spectrum in the visible range is a superposition of all possible transitions, leading to a broadening of the absorption or emission peaks.

### 2.1.4 Properties of PDI1MPCN2

In this work, the electrical and optical properties of the small molecule N,N'-di((S)-1-methylpentyl)-1,7(6)-dicyano-perylene-3,4:9,10-bis(dicarboximide) (PDI1MPCN2) are investigated. PDI1MPCN2 can be processed from solution to atomically flat, mono- to bilayer-thin films with comparably large grains, in which mobilities up to  $4 \frac{\text{cm}^2}{\text{Vs}}$  could be detected [53]. Its role in field-effect transistors has been investigated in References [48, 58, 59] and Publication **P5**, thereby using it as a model material for perylene diimides (PDIs) in general. The structure of PDI1MPCN2 with a total length of  $23.5 \text{ \AA}$  is shown in **Figure 2.4**. The PDI core has a length of  $11.5 \text{ \AA}$  and is twisted, resulting in a dipole moment of 1.70 Debye

normal to the molecular plane (calculated using density functional theory [48]). The twisting is originated in the strongly electron-withdrawing cyanide groups at the bay-positions, which are also responsible for the low LUMO level of 4.15 eV and good air stability [60]. The molecular packing and the good solubility of the material can be drawn back to the twisted alkyl chains at the imide positions.

After thin-film formation of PDI1MPCN2 from solution (also compare Section 2.2.1 for the theory on thin-film formation and Section 3.1 for experimental details), the molecules stand in an upright position tilted by  $38^\circ$  with respect to the surface normal; one monolayer then measures around 1.8 nm, as displayed in **Figure 2.4** [48, 53, 61].

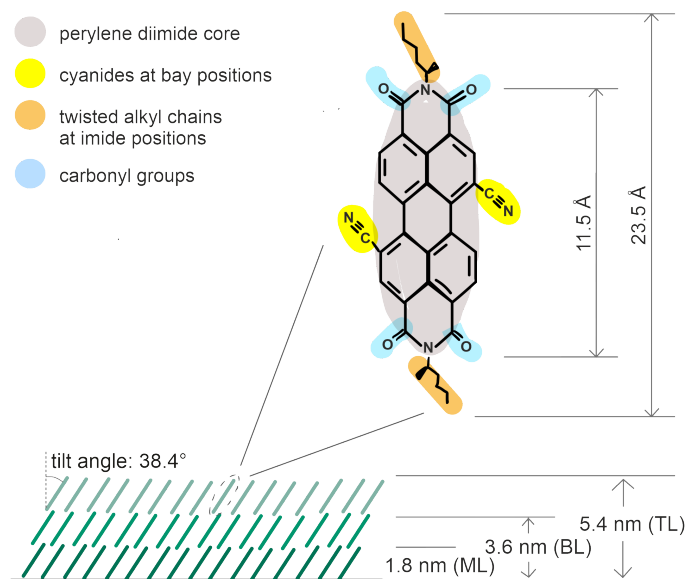


**Figure 2.4** Electronic structure of the small molecule PDI1MPCN2 consisting of C = carbon, O = oxygen, N = nitrogen.

## 2.2 Organic Thin-films

If organic molecules condense to a solid, they can either arrange randomly and form isotropic bulk-like structures, or in a periodic lattice, forming an organic crystal [54]. Crystal-like areas with different orientations or stacking arrangements—so-called grains—are separated by grain boundaries.

If speaking of organic semiconductors, we have to understand how the energetic properties change if single molecules condense to form a solid and how different structural arrangements impact the energy levels. While organic films often consist of a high density of grain boundaries and are considered as polycrystalline, this work focuses on highly-crystalline organic thin-films. This section therefore starts with the presentation of two different thin-film application-techniques and the emergence of grain boundaries in Section 2.2.1. Afterwards, we will present how intermolecular interactions impact the energy levels of a neutral molecule in Section 2.2.2.

### 2.2.1 Formation of Organic Thin-films

There are mainly two different possibilities to process organic molecules into films: from the vapor phase and from solution. While evaporation techniques allow to apply films of a certain thickness and at well-defined conditions, the resulting films consist of much smaller grains

than solution-based applied films.

Grain growth during film application can be explained by nucleation theory which will be shortly introduced with a focus on film growth from the vapor phase, but also holds for crystallization out of a solution. Films with larger grains (crystalline films) of PDI1MPCN2 are applied by a specific solution-based technique, whose theoretical principles will be presented afterwards. This section concludes discussing structural differences of grain boundaries and their emergence.

### Vapor-based Thin-film Application and Nucleation Theory

A common way to apply organic films is to evaporate the organic material in a vacuum chamber, where the molecules condensate on a substrate. The process of film formation can be divided into the three steps diffusion, adsorption, and nucleation. An evaporated molecule diffuses across the surface of a perfectly smooth substrate and adsorbs with a certain probability. If, during diffusion, a molecule meets another diffusing or already adsorbed molecule (or molecular group), the adsorption probability increases, which is why existing grains tend to grow before new grains are formed (the grain growth is sketched in **Figure 2.5a**). Since the diffusion energy and therefore the probability to meet other molecules or crystals during diffusion increases for increasing substrate temperatures  $T$ , the mean grain size can be increased by heating the substrate. However, larger temperatures also increase the probability for diffusing molecules to reevaporate. In sum, the crystallinity of the resulting film depends on the deposition flux, the substrate temperature, the surface properties of the substrate, intermolecular interactions, and interactions between the molecules and the surface [62, 63]. When an evaporated molecule crystallizes on a substrate, the first thermodynamic step is called nucleation. Nucleation is a thermodynamic process, describing the energy change upon condensation by the Gibbs free energy  $G$ . It represents the competition between

- the energy gained by nucleation due to beneficial intermolecular interactions, given by the chemical potentials in the crystalline and the vapor phase

$$\Delta\mu_c = \mu_c^{\text{crystal}} - \mu_c^{\text{vapor}},$$

and

- the energy penalty due to the creation of new interfaces between the crystal and the surrounding gas ( $A_{CG}$ ) and the crystal and the substrate ( $A_{CS}$ ). This energy penalty has to be smaller than the energy gained by reducing the interface between the gas and the substrate ( $A_{GS}$ ). The total energy penalty is therefore

$$\gamma A = \gamma_{CG}A_{CG} + \gamma_{CS}A_{CS} - \gamma_{GS}A_{GS} \quad (2.8)$$

with  $\gamma_i$  the surface tensions of the contributing interfaces, which fulfill

$$\sum_i \gamma_i = 0 \quad (2.9)$$

in the thermal equilibrium.

The change in the Gibbs free energy for a system with  $N$  molecules is consequently

$$\Delta G = -N\Delta\mu_c + \gamma A.$$

$\Delta G$  becomes maximal at a critical nucleus size  $N^*$  and at larger  $N^*$ , grain growth is energetically favored. To reach the critical grain size at reasonable temperatures and time

scales, it is usually reduced by oversaturating the surrounding gas with the molecule. This can e.g. be achieved by reducing the gas pressure in a vacuum chamber. [62–64]

### Surface Mediated Crystallization

If the organic molecule under investigation is solvable, it can also be applied by solution-based techniques, such as spin coating [42, 65], various blading techniques [66, 67], solution casting [68], and other, more specified techniques [33, 69–71]. Recently, a special drop casting method was developed for PDI1MPCN2, with which highly-crystalline monolayer- to bilayer-thin films can be applied [53]. (In Thesis **T2** it was modified for a similar perylene-diimide derivative.) In this method a droplet with the solvated molecule is placed onto a substrate and allowed to dry. In contrast to other solvent-based methods its underneath lying physics ensures the growth of molecular monolayers, which we will shortly summarize in the following according to Reference [53].

The crystallization of the molecule can be described by a nucleation process of the solid molecule on top of a liquid surface. Hence, it is driven by the interplay of the surface free energies  $\gamma$  at the liquid-gas (LG), crystal-liquid (CL), and the crystal-gas (CG) interface. If

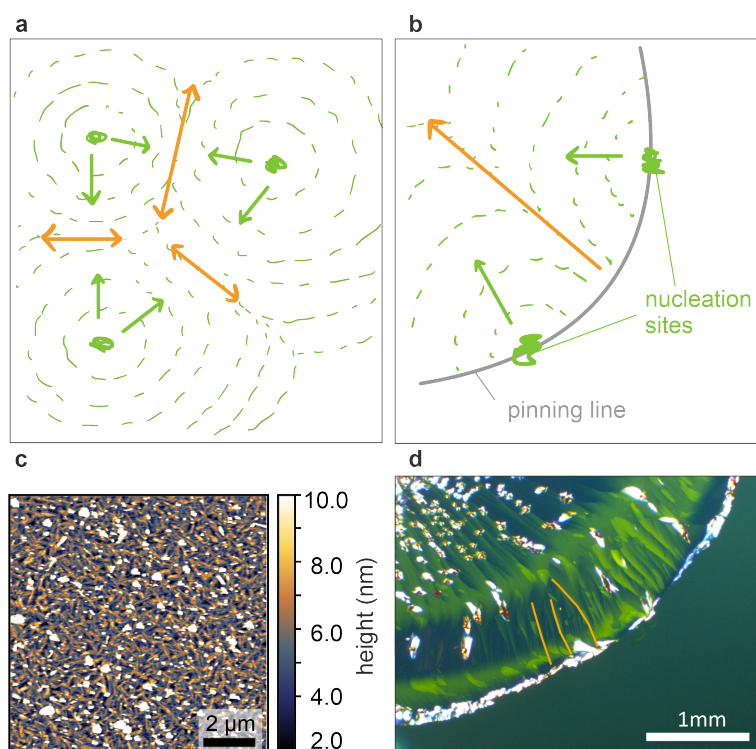


**Figure 2.5 Grain growth for different preparation methods and emergence of grain boundaries.** **a**, If the organic film is evaporated, grains adsorb on random sites on the substrate and grow radially from the nucleation sites. **b**, If the film grows via surface-mediated crystallization, the nucleation starts at the droplet border and grains grow from the pinning line of the droplet toward its center. The arrows in **a**, **b** indicate in green the vector normals of propagating fronts of neighboring grains, and in orange the emergence direction of the grain boundary. The sketches are inspired by Reference [42]. **c**, AFM image of a polycrystalline film of PDI1MPCN2 prepared from the vapor phase. **d**, Polarized optical microscopy image of a monolayer-thin film of PDI1MPCN2 prepared from solution. The orange lines mark some exemplary grain boundaries.

the surface free energies fulfill

$$\gamma_{LG} \geq \gamma_{CL} + \gamma_{CG},$$

the area of the liquid-gas interface is energetically less favored and becomes minimized by the crystallization of a monolayer of the solved molecule on the droplet's surface [53].

The nucleation starts at the border of the droplet, where the solvent evaporates faster than in its center, and the solution gets oversaturated. The grains grow consequently from the droplet border radially to its center (compare **Figure 2.5b** and the supplementary movie of Reference [53]). The evaporation rate of the solvent, determined by its viscosity and surface free energy, therefore determines whether the crystallization can take place at all, but also the shape and crystallinity of the resulting films. The film shape is influenced by the shape of the droplet, determined by its contact angle to

$$\cos(\theta_{\text{eq}}) = \frac{\gamma_{SG} - \gamma_{SL}}{\gamma_{LG}}$$

(this is a direct consequence of Equation (2.9)).  $\theta_{\text{eq}}$  remains constant during evaporation if the substrate is perfectly smooth and the droplet is completely homogeneous. However, a constant angle comes in with a decreasing droplet circumference, which leads to thick molecular clusters with random orientation. On the contrary, smooth crystalline films covering the whole contact area grow if the contact line is pinned by e.g. a rough surface, and if the droplet is sufficiently small, flat, and viscous [72–74].

### Grain Growth and Emergence of Grain Boundaries

**Figure 2.5c** and **d** display images of PDI1MPCN2 thin-films applied by thermal evaporation and from solution. The grains in the evaporated film are visibly much smaller than in the thin films applied from solution, which can be explained by the differences in grain growth for the different processing methods. This difference and the resulting impact on charge transport across grain boundaries is e.g. investigated by Lee et al. using conductive AFM (c-AFM) [42]. They find that grain boundaries in films from the vapor phase are much wider and have higher resistivities than grain boundaries in films deposited from solution and explain the different extent of structural disorder by fundamental differences in the film formation.

In evaporated films, grains grow simultaneously with molecular condensation and empty spaces are progressively filled when neighboring grains grow together. Grain boundaries may then contain voids on the sub- $\mu\text{m}$  length scale and reach down to the substrate, forming crevices (compare **Figure 2.6**). In contrast, if films are applied from a solution, the organic material is applied all at once on top of the whole area where film formation is supposed to take place. Hence, the molecule only gets in touch with the substrate when it is already crystallized. This results in smooth films, in which even high-resolution AFM in tapping mode is not capable of detecting grain boundaries [42]. Hence, measurement methods that probe the relative orientation of the molecules like transverse shear microscopy [75], polarized optical microscopy [67, 76], or photoluminescence spectroscopy [59] have to be used to visualize them. This finding is consistent with the measurements presented in Publication **P2** (Chapter 4). The growth conditions consequently determine the structure or morphology of grain boundaries and the following different grain-boundary types have been suggested before (also compare **Figure 2.6**):

- crevices (three dimensional), accompanied by a change in film thickness, are assumed to originate from vapor-based film-application [42]

- voids (two dimensional), can be formed upon growth from the vapor phase [42], but are also expected in films made from solution if the distance between two molecules of different grains is larger than the normal lattice constant and too small to fill in another molecule [48]
- voids (two dimensional) that are filled either with impurities [51] or a molecule of the same kind that is squeezed in [42, 48]
- the interface of neighboring grains with different molecular orientation (one dimensional) [51], assumed in monolayer-thin films made from solution

While this differentiation is of structural kind, grain boundaries can also be differed by their energetic distribution. They can either act as energy barriers or valleys on electron transport, as proposed by simulations [48]. These energy differences and their impact on charge transport are discussed in Section 2.3.

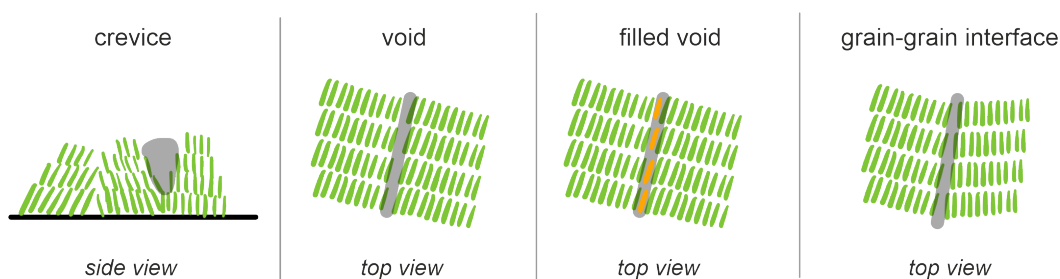


Figure 2.6 Structurally different grain boundary types as presented in the main text.

### 2.2.2 Energy Levels of Crystalline Films

In organic solids and films, the organic molecule is no more isolated, but interacts with its neighbors. While the intermolecular interactions influence the energy levels, the changes are only small, since the intramolecular forces are much stronger. Hence, the main properties described for the single molecule in Section 2.1 will also account for the organic thin-films. To get a feeling for the impact of intermolecular interactions, a system formed by two molecules, a so-called dimer, will be presented before advancing to a solid made of many molecules. The following description is according to the textbooks by Köhler and Bässler [3] or Schwoerer and Wolf [54].

#### Dimer Interaction

A dimer (subscript  $D$  in the following) is a system of two interacting molecules. It is described by the Schrödinger equation  $\hat{H}_D|\Psi_D\rangle = E_D|\Psi_D\rangle$  with the wavefunction of the dimer in the ground state. The dimer wavefunction can be composed of the wavefunctions of the two non-interacting molecules 1 and 2,

$$|\Psi_D\rangle = |\Psi_1\rangle|\Psi_2\rangle, \quad (2.10)$$

and the Hamiltonian  $\hat{H}$  can be written as

$$\hat{H}_D = \hat{H}_1 + \hat{H}_2 + \hat{V}_{12}. \quad (2.11)$$

$\hat{H}_{1,2}$  are the operators of the isolated molecules and  $\hat{V}_{12}$  their interaction potential. If the electronic overlap between the molecules is small, the interaction is weak, i.e. the interaction

potential is sufficiently small to solve the problem by perturbation theory. The energy of the system in the ground state is then described by

$$E_D = E_1 + E_2 + E_{\text{pol}} \quad (2.12)$$

$$\text{with } E_{\text{pol}} = \langle \Psi_1 \Psi_2 | \hat{V}_{12} | \Psi_1 \Psi_2 \rangle < 0. \quad (2.13)$$

Equation (2.12) shows that the dimer's energy is lowered compared to the total energy of the two single, non-interacting molecules by the interaction energy  $E_{\text{pol}}$ . It is also called polarization or Coulomb interaction energy, since it is caused by zero-point oscillations of the molecules that induce dipoles in the environment and polarize the adjacent molecule.

If one of the molecules is excited (indicated by an asterisk \*), the wavefunction of the dimer rewrites to the linear combination

$$|\Psi_{D\pm}^*\rangle = \frac{1}{\sqrt{2}} (|\Psi_1^* \Psi_2\rangle \pm |\Psi_1 \Psi_2^*\rangle). \quad (2.14)$$

Without interaction, the energies of the symmetric (+) and antisymmetric (-) dimer excited state are the same, and can be expressed by  $E_0$ , the energy of molecule 1 or 2 in the ground state, and the energy of one of the molecules in the excited states  $E^*$  to

$$E_+^* = E_-^* = E_0 + E^*. \quad (2.15)$$

Hence, the excited state of the dimer is two-fold degenerate. However, if the interaction is turned on, the energy of the excited dimer changes to

$$E_{\pm}^* = E_0 + E^* + E'_{\text{pol}} \pm \epsilon. \quad (2.16)$$

$E'_{\text{pol}}$  again describes the polarization energy between the excited molecule 1 and molecule 2 in the ground state, or vice versa. Compared to the ground state, we find an additional term  $\epsilon$  that lowers the energy of the excited state and splits the energies of the symmetric and antisymmetric wavefunction by  $2\epsilon$ .  $\epsilon$  is called resonance interaction energy, because it describes the resonant coupling of the two possible excited configurations  $|\Psi_1^* \Psi_2\rangle$  and  $|\Psi_1 \Psi_2^*\rangle$ . To summarize, the interaction of the dipole moments of adjacent molecules has two effects on the energetic states of a dimer: an overall shift to smaller energies as well as a splitting of the excited state.

### Intermolecular Interactions in Organic Crystalline Films

We now advance to an organic solid with many molecules. The intermolecular interaction qualitatively has the same effects as observed for the dimer. The properties of organic films with respect to the organic molecule are characterized by [54]:

- a shift of absorption/emission peaks to smaller energies: Each molecule can be considered to be surrounded by a solvent medium, composed of molecules of the same kind. This surrounding polarizes the molecule and shifts its energy levels. The observed shift of absorption and emission peaks to smaller energies is therefore also called „solvent shift“.
- a broadening of discrete energy levels and formation of bands: A system with  $N$  non-interacting molecules is  $N$ -fold degenerate, according to Equation (2.15). If interactions are turned on, the energy levels of the excited states split and form a band with a width of  $4\epsilon$ . These states are called Frenkel-exciton states.
- violation of quantum-mechanic selection-rules of the single molecule: The formation of a crystal leads to new symmetries and new selection rules.

- splitting of absorption/emission peaks into maximal  $M$  sub peaks if  $M$  molecules are in the unit cell of the crystal. This splitting is called „Davydov splitting“.

### Density of States in Disordered Crystals

As we have seen, intermolecular interactions can lead to the formation of broad energy bands with well-defined band edges, but only if each molecule in the solid is exposed to the same interactions. This is the case in a perfect crystal, or crystalline grain, where all molecules have the same orientation and distance to its neighbors. In contrast, in a solid with randomly oriented molecules, impurities or thermal fluctuations, each molecule interacts with a slightly different surrounding. As a consequence, localized states form within the band gap and the band edges smear out.

If the variations are only small and the film can still be considered crystalline, like in grains, the density of states (DOS) can be described by a Gaussian distribution

$$g(E) = \frac{1}{\sqrt{2\pi}\sigma} \exp\left(-\frac{(E - E_0)^2}{2\sigma^2}\right) \quad (2.17)$$

with the standard deviation  $\sigma$  and the band edge energy  $E_0$  [48, 77, 78]. In contrast, at grain boundaries the DOS is better modeled by an exponential function as [3, 48, 79]

$$g(E) = \frac{1}{\sigma} \exp\left(-\frac{(E - E_0)}{\sigma}\right). \quad (2.18)$$

## 2.3 Charge Transport in Organic Semiconductors

This work examines the impact of grain boundaries on charge transport in thin films of PDI1MPCN2. Therefore, the basics of charge transport in organic semiconductors are introduced in this section, according to the textbook by Köhler and Bäessler [3].

To enable charge transport, free charge carriers are injected into the semiconductor, which can move from one molecule to another. Section 2.3.1 introduces how additional charges change the electrical and optical properties of an organic molecule. In Section 2.3.2, one method to induce free charges into the semiconductor, will be presented, namely by optical excitation. The movement of free charge carriers through the crystalline areas of the semiconductor is presented by different transport models in Section 2.3.3. Existing models for charge transport across grain boundaries will finally be discussed in Section 2.3.4.

### 2.3.1 Electronic Properties of Charged Molecules and Films

The energy levels of a charged molecule can be described by the electron affinity (EA), which is the energy gained by the uptake of a single electron, and the ionization potential (IP), the energy needed to remove an electron from the molecule. When electron-electron interactions are neglected, the ionization energy corresponds to the HOMO and the electron affinity to the LUMO level of a molecule, which are therefore considered as the transport levels.

Advancing to organic films, the interaction of a charged molecule with its neighboring molecules has to be considered. Similar to the excited molecule described in Section 2.2.2, the charged molecule induces a dipole moment in an adjacent molecule. While the interaction range of the charged molecule is larger than that of the excited molecule, it also leads to a lowering of the energy levels, as well as to a broadening into transport bands. These can be compared to the valence band (HOMO) and the conduction band (LUMO) in inorganic materials.

Since transport bands with a finite width, as well as localized states within the gap between HOMO and LUMO are created by disorder in the film, it is reasonable to define a Fermi energy  $E_F$ . It describes the energy level from which charge carriers (specifically electrons) can be thermally excited into a transport level (into the LUMO) [52]. If an organic semiconductor likely conducts electrons, the Fermi level is assumed slightly below the LUMO level. Injecting a small amount of electrons into the semiconductor corresponds to shifting the Fermi level into the LUMO.

The difference between the Fermi level and the vacuum energy of an organic molecule is described by its work function

$$W = E_{\text{vac}} - E_F.$$

It is widely understood as the energy needed to remove an electron from the bulk material [80]. While it is originally defined for metals, it can be attributed to semiconducting materials as well [81].

### 2.3.2 Photoexcitation of Electric Currents

By photon absorption free charge carriers can be generated in a material, that lead to a photoexcited current (or photocurrent). Depending on the energy of the absorbed photons and the band gap of the material, photoexcitation can be described by three different effects: The **outer photoelectric effect** (or Hallwachs effect) is observed in metal surfaces if they are illuminated by ultraviolet light. Electrons are released out of the material, but only if the photon energy is larger than the material's work function [82]. A similar case to the outer photoelectric effect occurs if electrons are emitted from semiconducting surfaces, molecules or atoms. Since these materials are ionized upon electron emission, this process is called **photoionization**. It requires photon energies larger than the ionization potential and is the basis for photoemission spectroscopy [3, 83].

On the contrary, the **inner photoelectric effect** is observed in semiconductors by an increase in conductivity when photons with energies larger than the optical band gap are absorbed. Absorption creates an exciton, which can be separated by e.g. exothermic transfer to electron-accepting sites such as impurities, dopants, internal interfaces or electrodes. Exciton separation can also be achieved by processes that supply high enough energies, or high enough electric fields to break the binding energy of the electron-hole pair. Subsequent spatial separation of the free electron and hole, which builds up a voltage, is the basis of the photo-voltaic process used in organic solar cells [3].

Besides optical injection, free charge carriers can also be injected into a semiconductor electrostatically, which is the case for e.g. OLEDs and OFETs. The working principle of the latter will be presented in Section 2.4.

### 2.3.3 Transport Models in Single Grains

If a sufficient amount of free electrons is injected into a semiconductor, it gets conductive and the charges move from molecule to molecule. The transport of charges in crystal-like, well-ordered semiconductors is commonly quantified by the mobility  $\mu$ . It depends on the relative energetic distance of states, spatial arrangement of molecules, temperature, and the trap-state density. The most common models to describe their relation are band transport, hopping transport and the multiple-trapping-and-release model, which will be presented in the following in accordance with **Figure 2.7**.

- **Band transport** takes place if electrons (holes) move in the LUMO (HOMO) and the bands are spatially extended over many molecules (cf. **Figure 2.7a**). As presented in

Section 2.2, the HOMO and LUMO are well distributed, if the semiconductor is well ordered. However, the ordering is difficult to quantify. Therefore one typically considers band transport to be the main transport mechanism if  $\mu > 5 \frac{\text{cm}^2}{\text{Vs}}$ , and if the mobility decreases with increasing temperature as

$$\mu \propto T^{-n}, \quad 0 < n < 3.$$

The mobility reduction stems from enhanced scattering by acoustic phonons, impurities, and/or electron-electron interactions. Especially the latter is specific for organic semiconductors.

- **Hopping transport:** If the dynamic or static disorder in the organic semiconductor is high and homogeneously distributed, the HOMO and LUMO are localized on a single or few molecule(s). In this case, free charge carriers hop from one localized state to another, as sketched in **Figure 2.7b**, whereby energetically higher or further distant states can be reached at higher temperatures. Consequently, the mobility increases as

$$\mu \propto T.$$

- **Multiple trapping and release:** When the defect density is significantly smaller than the total density of states, a mixture of the above introduced models is considered. In fact, in typical organic semiconductors it is observed that the mobility increases upon cooling (at high temperatures) and decreases if the temperature is further decreased to low temperatures. To describe this temperature dependence, the multiple-trapping-and-release model was developed as an empirical model. It assumes that a charge carrier can be excited into a delocalized band, from which it can be trapped into a localized state, then hop to another localized state or be released into the band by thermal activation (cf. **Figure 2.7c**). The required energy is called activation energy  $E_A$  defined by the relationship [51]

$$\mu = \mu_0 \cdot n_t \cdot \exp\left(\frac{-E_A}{k_B T}\right), \quad (2.19)$$

with the trap-free mobility  $\mu_0$  and the trap-state density  $n_t$  [85].

The activation energy  $E_A$  can be extracted by an Arrhenius approach, that is, rewriting

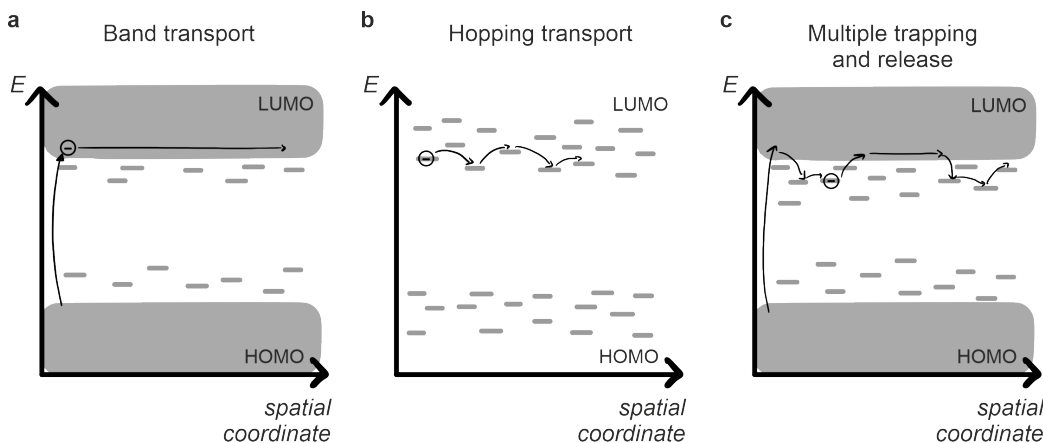


**Figure 2.7** Different transport models for charge transport in organic semiconductors. a, Band transport, b, Hopping transport, c, Multiple trapping and release. Figure according to [84].

Equation (2.19) to

$$\underbrace{\log(\mu)}_{y\text{-axis}} = \underbrace{\log(\mu_0)}_{y\text{-intersept}} + \underbrace{\frac{1}{T}}_{x\text{-axis}} \cdot \underbrace{\left(\frac{-E_A/k_B T}{\ln 10}\right)}_{\text{slope}}, \quad (2.20)$$

plotting  $\log(\mu)$  over  $1/T$ , and extracting the activation energy from the slope of a linear fit [3]. Recently, Meier et al. suggested by Monte-Carlo simulations, that the activation energy is affected by the type and height of grain boundaries (cf. Section 2.3.4). A short investigation on the relationship between the grain-boundary density and the activation energy in OFETs of PDI1MPCN2 is therefore presented in Appendix A.

Most organic materials only conduct either holes or electrons and are referred to as p- or n-conductive, respectively. Which type of charge carriers is the main contributor to charge transport, is mainly determined by two effects. Either charge transport within the organic semiconductor is limited due to a non-sufficient overlap of  $\pi$  or  $\pi^*$  orbitals and a confined HOMO (bad hole conductor) or LUMO (bad electron conductor), or charge-carrier injection into the HOMO (LUMO) is hindered by a large offset to the work function of the electrode material (contact resistance, cf. Section 2.4.4).

### 2.3.4 Charge-transport Models at Grain Boundaries

The multiple-trapping-and-release model describes well experimentally observed charge transport in crystalline or polycrystalline films on relatively large length scales. In contrast, the local transport processes at grain boundaries are not completely understood yet. It is widely accepted that grain boundaries limit charge transport in the sense that mobilities are reduced by one to two orders of magnitude if grain boundaries are introduced into otherwise crystalline films with a low defect density (compare e.g. Reference [52] or, for PDI1MPCN2, Thesis **T1** in Appendix H). Grain boundaries are therefore often considered as sites where trap states are highly concentrated [45, 70], or as electrically isolating walls [86]. Vladimirov et al. suggest according to theoretical simulations that both types can even coexist in the same organic semiconductor and describe them as energetic valleys (traps) or barriers (walls) [48]. Meier et al. use these findings and simulate the transport paths and mobilities for different grain boundary heights and widths by kinetic Monte Carlo calculations. They find that the energetic distribution at a grain boundary determines the transport mechanism in organic films and distinguish four cases:

1. Deep valleys form a transport path for electrons. Charge transport within the semiconductor is therefore confined to the grain boundaries.
2. Shallow valleys trap electrons. The trapped electrons have to be thermally excited back into the grains to contribute to charge transport. Meier et al. conclude that shallow valleys are therefore less beneficial for charge transport than deep valleys.
3. Energetic barriers backscatter electrons independent of their height. The barrier height only impacts the activation energy needed to overcome those barriers.
4. At narrow grain boundaries tunneling can be observed.

While describing grain boundaries as energetic barriers or valleys helps to understand the transport processes across grain boundaries, their structural origin is not considered. In Section 2.2 a summary of structurally different grain boundaries was introduced, whose impact on charge transport is investigated by Verlaak and Heremans [51] by calculating

the polarization energy of the different sites. They find that especially voids act as scatter centers and therefore can be understood as energetic barriers. Voids are therefore described as „intrinsic“ barriers, in contrast to grain boundaries that trap electrons, get charged, and consequently withdraw following electrons. Electron trapping is observed at sites where grains with different orientations meet [51]. For these grain boundaries, it is widely assumed that increasing orientational mismatch also increases the grain boundary resistance, or the valley depth, respectively [42, 48, 65, 87].

## 2.4 Organic Field-effect Transistors

The mobility of a semiconducting thin-film can be determined by electrical transport measurements in a FET. The structure and working principle of organic FETs will be explained within this section (Sections 2.4.1 and 2.4.2), before introducing the parameters extracted from transport measurements in Section 2.4.3 and deviations from the ideal behavior in Section 2.4.4. The introduced basics follow the textbooks by Köhler and Bässler [3] and Stallinga [88]; for a more detailed theoretical derivation the interested reader is referred to the textbook (for inorganic FETs) by Sze and Ng [80].

### 2.4.1 Structure of Organic Field-effect Transistors

The structure of an OFET is sketched in **Figure 2.8a**. Its centerpiece is the organic semiconductor under investigation. It is contacted by the two electrodes source (S) and drain (D) with distance  $L$ , defining the length of the conductive channel, and width  $W$ , defining the channel width. A third electrode, the gate (G), is separated from the semiconductor by an insulator with thickness  $d_{\text{ox}}$ .

The structure of the displayed OFET is called bottom-gate top-contact (BGTC) structure. The position of the gate and the source and drain contacts with respect to the semiconductor can also be switched, or all three are located on the same side of the semiconductor. The resulting structures are correspondingly called top-gate bottom-contact (TGBC), bottom-gate bottom-contact (BGBC) or top-gate top-contact (TGTC).

BGTC and BGBC devices are the used geometries within this work, where the sample substrate acts as gate (highly doped silicon (Si)) and insulator ( $\text{SiO}_2$  or  $\text{Al}_2\text{O}_3$ ), respectively. (For preparation details cf. Chapter 3.)

### 2.4.2 Working Principle of Organic Field-effect Transistors

**Figure 2.8b** displays the working principle of an OFET for the case of an n-conductive semiconductor such as PDI1MPCN2, with all relevant voltages. The source electrode is connected to ground, while positive voltages  $V_{\text{DS}}$  and  $V_{\text{GS}}$  are applied to the drain and gate, respectively. The gate voltage injects positive charge carriers into the gate material, and a positive charge sheet builds up at the gate-insulator interface. This induces an electric field in the organic semiconductor that leads to an accumulation of negative charge carriers at the semiconductor-insulator interface. Consequently, the gate-insulator-semiconductor ensemble can be regarded as plate capacitor with the area-normalized capacitance

$$\hat{c} = \frac{\varepsilon_0 \varepsilon_r}{d_{\text{ox}}} \quad (2.21)$$

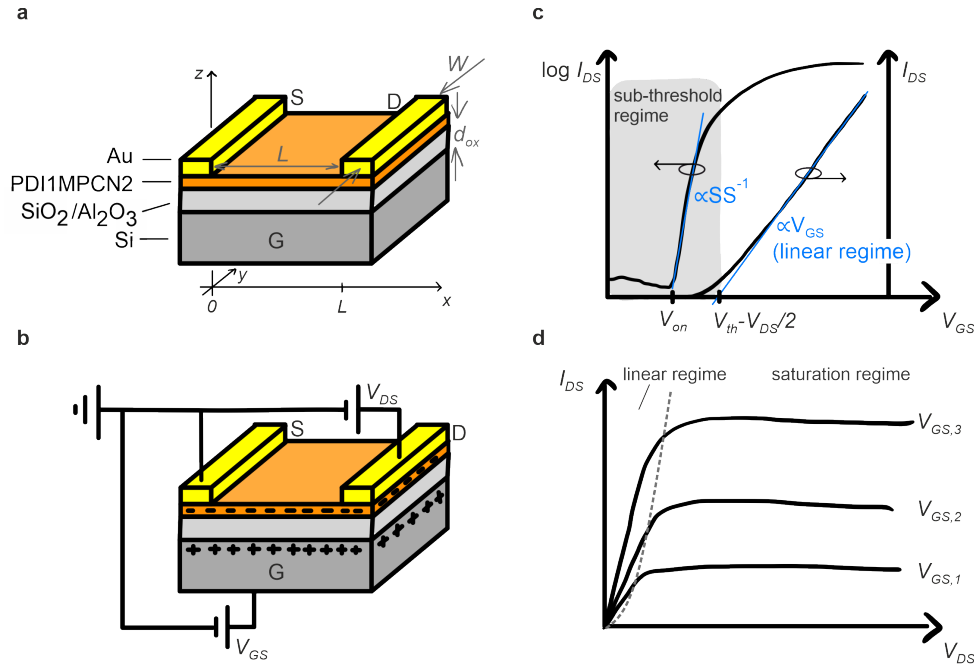


**Figure 2.8** Structure and working principle of an organic-field effect transistor. **a**, Structure of an OFET with all important dimensions and specification of coordination axes. S = source, D = drain, G = gate. **b**, Sketch of the working principle including applied voltages and accumulation of free charges as discussed in the text. **c,d**, Transfer and output curves of an ideal OFET, respectively. The parameters  $SS$  (sub-threshold slope),  $V_{on}$  (turn-on voltage) and  $V_{th}$  (threshold voltage) are discussed in Section 2.4.3. Compare e.g. References [3, 80, 89].

with  $\varepsilon_0$  the vacuum permittivity,  $\varepsilon_r$  the dielectric constant of the insulating layer, and the area-normalized charge in the semiconductor can be written as

$$Q = \hat{c}V_{GS}.$$

If the density of accumulated charge carriers is high enough to form a conductive path, which is represented by a so-called threshold voltage  $V_{th}$  (discussed in Section 2.4.3), a voltage between source and drain  $V_{DS}$  accelerates the charge carriers, leading to a current  $I_{DS}$ . The amount of mobile charge carriers contributing to  $I_{DS}$  can be written as

$$Q(x) = \hat{c}(V_{GS} - V_{th} - V(x)), \quad (2.22)$$

whereby  $V_{th}$  accounts for the fact that not all injected charge-carriers also contribute to a current. Even more,  $Q$  depends on the position within the channel, according to the voltage drop of  $V_{DS}$  from  $|V_{DS}|$  at  $x = L$  to zero at  $x = 0$  (cf. **Figure 2.8a**). This voltage drop can be assumed linear if charge-carrier diffusion is neglected and the electric field induced by the gate is much larger than the drain field (**gradual-channel approximation**). In this case, the absolute drain current is according to Ohm's law

$$I_{DS} = WQ(x)\mu \frac{dV(x)}{dx}. \quad (2.23)$$

Inserting Equation (2.22) and partial integration results in the gradual-channel expression for the drain current

$$\int_0^L I_{\text{DS}} dx = W \mu \hat{c} \int_0^{V_{\text{DS}}} (V_{\text{GS}} - V_{\text{th}} - V(x)) dV$$

$$\Leftrightarrow I_{\text{DS}} = \frac{W}{L} \hat{c} \mu \left[ (V_{\text{GS}} - V_{\text{th}}) V_{\text{DS}} - \frac{1}{2} V_{\text{DS}}^2 \right]. \quad (2.24)$$

Hence, the drain current depends on the interplay of the drain and the gate voltage, which is why two sets of measurements are usually performed to characterize the FET.

On the one hand, the drain current is detected while keeping  $V_{\text{DS}}$  fixed and sweeping  $V_{\text{GS}}$ . This so-called **transfer curve**, whose course is displayed in **Figure 2.8c** allows e.g. to determine the mobility (cf. Section 2.4.3). On the other hand, a sweep of the drain voltage with a set of fixed gate voltages gives the so-called **output characteristics** of the FET, displayed in **Figure 2.8d**. The output curves are usually detected to assess the quality of the FET, e.g. in terms of leakage currents or contact resistance (cf. Section 2.4.4), and to find the different working regimes of a transistor depicted in **Figure 2.8d**. The different regimes are the linear regime and the saturation regime, separated by the so-called pinch-off point, and are defined by the relation between  $V_{\text{GS}}$  and  $V_{\text{DS}}$  as follows:

1. The **linear regime**: If  $V_{\text{DS}} \ll V_{\text{GS}}$ , Equation (2.24) can be approximated to

$$I_{\text{DS}}^{\text{lin}} = \frac{W}{L} \mu \hat{c} (V_{\text{GS}} - V_{\text{th}}) V_{\text{DS}}, \quad (2.25)$$

i.e. the drain current depends linearly on the drain voltage. If additionally  $V_{\text{GS}} > V_{\text{th}}$ , it is also proportional to the gate voltage.

2. The **pinch-off point**: If  $V_{\text{DS}}$  is increased to reach  $V_{\text{DS}} = V_{\text{GS}} - V_{\text{th}}$ , all charges induced by the gate are collected by the drain electrode. The channel is said to be „pinched off“. The pinch-off point denotes the transition from the linear to the saturation regime.
3. The **saturation regime**: If  $V_{\text{DS}}$  is increased above the pinch-off point, the voltage at the drain electrode remains constantly  $V_{\text{GS}} - V_{\text{th}}$  and only the pinch-off position shifts closer to the source electrode, thereby decreasing the effective channel length. Equation (2.24) simplifies to

$$I_{\text{DS}}^{\text{sat}} = \frac{W}{2L} \mu \hat{c} (V_{\text{GS}} - V_{\text{th}})^2, \quad (2.26)$$

i.e. the drain current depends no more on the drain voltage and quadratically on the gate voltage.

### 2.4.3 Device Parameters

Depending on the relation between  $V_{\text{DS}}$  and  $V_{\text{GS}}$ , the transfer curve can be detected in the linear or in the saturation regime. As can be deduced from Equations (2.25) and (2.26), the regime determines how  $I_{\text{DS}}$  depends on  $V_{\text{GS}}$ , and therefore also how the device parameters, such as the aforementioned mobility, are extracted. Hence, all parameters important for this work and how they are calculated from the transport measurements, will be presented and shortly discussed in the following.

### Mobility $\mu$

The mobility is the most common way to describe the quality of a semiconductor [3]. It can be easily extracted from the transfer curves measured in the linear or saturation regime by rearranging Equations (2.25) and (2.26) to

$$\mu_{\text{lin}} = \frac{L}{\hat{c}WV_{\text{DS}}} \cdot \frac{\partial I_{\text{DS}}^{\text{lin}}}{\partial V_{\text{GS}}}, \text{ or} \quad (2.27)$$

$$\mu_{\text{sat}} = \frac{2L}{\hat{c}W} \left( \frac{\partial \sqrt{I_{\text{DS}}^{\text{sat}}}}{\partial V_{\text{GS}}} \right)^2. \quad (2.28)$$

Since  $I_{\text{DS}}^{\text{lin}} \propto V_{\text{GS}}$  and  $I_{\text{DS}}^{\text{sat}} \propto V_{\text{GS}}^2$  in the ideal case, Equations (2.27) and (2.28) indicate that the mobility should be independent of the gate voltage. In real OFETs, however, an increased number of charge carriers induced by an increased gate voltage leads to a change in transport mechanism such as tunneling between localized sites or polaron hopping [85, 90]. This deviation often leads to an overestimation of mobilities [23, 91]. Frisbie, Sirringhaus, Podzorov and coworkers therefore suggest calculating a reliability factor  $r$  to quantify the deviation from the theoretical behavior [92].

For all results presented in this work, the mobility is calculated from the linear regime and compared at fixed charge-carrier densities  $n$ .

### Sub-threshold Slope $SS$ , Turn-on Voltage $V_{\text{on}}$ and Threshold Voltage $V_{\text{th}}$

As long as  $V_{\text{GS}}$  is small enough that no free charge carriers are induced into the semiconductor, the transistor is in its „off“-state. If the gate voltage is increased, the transistor is in its **sub-threshold regime**, which is characterized by an exponential increase over several orders of magnitude of the drain current, as visible if plotted on a logarithmic scale (cf. **Figure 2.8c**). The inverse tangent of this exponential increase is the **sub-threshold slope** [80]

$$SS = \ln 10 \cdot \frac{dV_{\text{GS}}}{d(\ln I_{\text{DS}})} \quad \text{in} \quad \frac{\text{mV}}{\text{decay}}. \quad (2.29)$$

It describes how much voltage has to be applied to increase the drain current by one order of magnitude, i.e. how „fast“ the transistor can be turned on. The intercept of this tangent defines the **turn-on voltage**  $V_{\text{on}}$  [3]. It denotes the gate voltage above which free charge carriers are within the channel. A non-zero turn-on voltage can be attributed to traps at all relevant interfaces, i.e. between the electrodes and the semiconductor, within the semiconductor, and at the semiconductor-insulator interface.

If the gate voltage is increased further and the charge-carrier density is high enough to form a conductive path, the **threshold voltage**  $V_{\text{th}}$  is reached, above which the transistor is in its operation regime. The threshold voltage can be extracted e.g. by extrapolation in the linear regime (ELR). In this method, the linear part of  $I_{\text{DS}}$  is extrapolated to the  $V_{\text{GS}}$ -axis, whose intercept is added to  $V_{\text{DS}}/2$  to determine  $V_{\text{th}}$ , as sketched in **Figure 2.8c**. If the course of the drain voltage is not perfectly linear, due to deviations discussed in Section 2.4.4, the tangent at the maximum slope of  $I_{\text{DS}}$  is taken to find the intercept with the  $V_{\text{GS}}$ -axis [80, 93]. The turn-on and threshold voltage of OFETs made of PDI1MPCN2 are discussed in more detail in Chapter 5.

### Charge-carrier Density $n$

When  $V_{\text{th}}$  is known, the density of charge carriers contributing to the drain current can be calculated using Equation (2.22) to

$$n = \frac{\varepsilon_0 \varepsilon_r}{q d_{\text{ox}}} \cdot (V_{\text{GS}} - V_{\text{th}}) \quad (2.30)$$

with  $q$ , the elementary charge of positive charge carriers.

If the turn-on voltage  $V_{\text{on}}$  is taken as a reference (substitute  $V_{\text{th}}$  by  $V_{\text{on}}$  in Equation (2.30)), the density refers to free charge carriers and is denoted with  $n_{\text{free}}$ .

#### 2.4.4 Deviations from the Ideal Behavior

The transfer and output characteristics introduced in Section 2.4.2 and displayed in **Figure 2.8c,d** represent an ideal FET. In real devices, however, several effects can deviate this ideal behavior, decrease the device performance, and even change the qualitative dependencies of the output and transfer curves. The most important effects for this work are summarized in the following.

#### Contact Resistance

Charge carriers are injected from the electrodes into the semiconductor, whereby the difference between the contact material's Fermi level and the semiconductor's transport level (LUMO for electrons, HOMO for holes) defines the injection barrier. Since it impedes charge-carrier injection, and consequently dampens the drain current, it is related to the **contact resistance**  $R_C$ . In organic semiconductor devices, the contact resistance is one of the main parameters to be minimized to increase the device performance. While investigation or manipulation of the contact resistance is beyond the scope of this thesis, a short summary of the most important properties is presented according to the detailed References [25, 26].

Depending on the relation between the semiconductor's transport level and the metal's Fermi level, the contact can be either Ohmic or Schottky like (cf. **Figure 2.9a,b**). The contact resistance is Schottky like, if the transport level of the semiconductor has a higher energy than the contact material's Fermi level. In this case, the bands bend and form a Schottky barrier, whose width decreases at positive gate voltages, enabling tunneling-mitigated transport through the barrier. This leads to an S-swing at small drain currents (cf. **Figure 2.9a**).

If, on the contrary, the semiconductor's transport level lies energetically below the contact material's Fermi level, the injection barrier is Ohmic, and the linear regime loses its  $V_{\text{GS}}$ -dependence, as displayed in **Figure 2.9b** [88].

A common way to quantify the contact resistance is the so-called transfer-length measurement (TLM). The total resistance  $R_{\text{tot}} = (I_{\text{DS}}/V_{\text{DS}})^{-1}$  is detected at a fixed  $V_{\text{GS}}$  for varying channel lengths  $L$  and extrapolated to  $L = 0$ . This approach makes use of the gradual-channel approximation, within which  $R_{\text{tot}}$  can be regarded as a series connection of the contact resistances of source and drain  $R_C$  and the resistance of the channel, given by the sheet resistance of the organic semiconductor  $R_{\text{ch}} = R_{\text{sh}} \cdot L/W$ . The width-normalized total resistance can therefore be written as

$$R_{\text{tot}} \cdot W = R_{\text{sh}} \cdot L + R_C \cdot W \quad (2.31)$$

and plotted as a function of the channel length  $L$ . The intercept of a linear fit with the  $x$ -axis finally gives  $R_C = R_{\text{tot}}(L = 0) \cdot W/2$  [26]. While the TLM method is easy to conduct on a sample with an assembly of parallel contacts with stepwise increasing distance (TLM

structure), and well established in inorganic materials [94, 95], its usefulness is limited due to a large device-to-device variability that organic devices often suffer from [27, 39, 96].

As a consequence, four-point measurements are often performed, where two probes are used to apply a current and two more probes to detect the voltage drop [97]. This technique allows to extract all influences of the electrodes on the detected current and to investigate solely the semiconducting behavior of the organic film. A specific four-point technique is the so-called van der Pauw method [98], which is introduced in the Supporting Information of Publication **P1** (presented in Chapter 7).

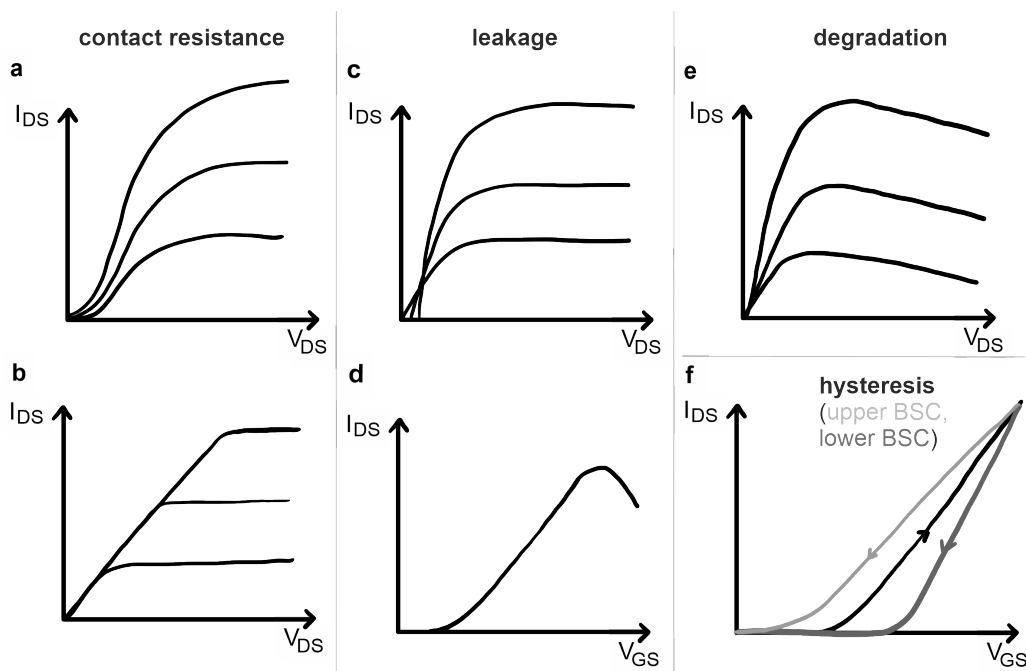


**Figure 2.9** Characteristic output and transfer curves representing deviations from the ideal behavior of an OFET. **a**, Schottky-like contact resistance, **b**, Ohmic contact resistance, **c,d**, leakage currents, **e**, bias-stress or air degradation, **f**, hysteresis (upper and lower back-sweep current (BSC)). Adapted from Reference [88].

## Leakage

The derivation of the expressions for the drain current presented in Section 2.4.2, assumed that the channel has a well-defined length and width. However, the organic semiconductor often surrounds the drain and source contacts (this stems from the processing conditions, cf. Chapter 3), enabling leakage currents to flow at the edges of the electrodes. To reduce them, the semiconductor is usually scratched as close as possible to the electrodes.

While leakage currents between source and drain can easily be reduced, leakage from the gate to the drain is harder to eliminate. It gets visible by a fan structure at small drain voltages in the output characteristics, or a reduction of  $I_{DS}$  at higher gate voltages in the transfer curve, as displayed in **Figure 2.9c,d**. Both effects represent a drain current that is at least partially raised by a gate current  $I_{GS}$  flowing from the gate to the source electrode. A gate current can either be attributed to insufficient thickness or dielectric constant of the FET dielectric, or to cracks and fractures in the dielectric. Hence, the gate current can be minimized by improving the insulating behavior of the dielectric and/or by reducing the contact size of the source and drain electrodes.

## Degradation

An important quality of an electric device is its stability in air, under illumination, as well as under bias stress. Device degradation can be observed as a decreasing current at constant or increasing voltages, as depicted in **Figure 2.9e** [99, 100]. Whether a device is principally stable is mainly defined by the organic material itself. Perylene diimides are in general stable under ambient conditions, which is one of the many advantages of PDI1MPCN2 [60]. However, grain boundaries can reduce the stability of devices and act as degradation sites [40].

## Hysteresis

If the magnitude of  $I_{DS}$  depends on the sweep direction of the gate voltage, one speaks of hysteresis, of which two types can be differed (cf. **Figure 2.9f**). On the one hand, the lower back-sweep current (BSC) hysteresis, which comes in with a decrease in the threshold voltage, is caused by charge-carrier trapping at the semiconductor-insulator interface. On the other hand, the upper BSC hysteresis with a decreased global threshold voltage occurs if free ions in the dielectric are released by increasing gate voltages, which then contribute to the back-sweep current [100].

## 2.5 Introduction to Metal-organic Frameworks

So far, this work only considered charge transport within single grains and across grain boundaries in organic semiconductors. However, grain boundaries are not a feature unique for organic semiconductors, but can be found in nearly all materials that show a specific degree of order, such as inorganic crystals [101–103], perovskites [104], or mixtures of organic and inorganic compounds, e.g. MOFs [105–107].

MOFs are crystals made of building blocks comprised by metal nodes and organic linkers [105]. Since their development in the late 1990s/early 2000s, they have largely increased in interest, because of their tunability in chemical and physical properties. MOFs stand out over e.g. organic materials because they are porous, a property that makes them predestined for applications in e.g. gas sensors or storage [105, 108, 109].

In this work, the structural and charge-transport properties of a newly developed two-dimensional conductive MOF (2D c-MOF) are investigated. Hence, this section will focus on the charge-transport mechanism in MOFs, starting with a short summary on the most important chemical binding mechanisms in Section 2.5.1 (chemists may want to skip this section). The following sections present the structural (Section 2.5.2) and charge-transport properties (Section 2.5.3) of MOFs. Finally, Section 2.5.4 gives a short overview over different synthesis methods and device integration.

### 2.5.1 Binding Mechanisms in Metal-organic Frameworks

The organic components of a MOF are bound by intramolecular covalent and intermolecular van der Waals bonds, as presented for purely organic materials in Section 2.1. In contrast, the organic molecules bind to the metal nodes—this connection is called **linkage**, cf. **Figure 2.10c**—by a special case of a covalent bond, the **coordinate covalent bond** or **coordination bond**. Like in a normal covalent bond, the binding partners share two electrons, but in a coordinate covalent bond both of these electrons are provided by one of the binding partners. The partner that provides the electron is called a **ligand**. If a molecular complex can even offer several electron pairs and thereby bond to a central metal ion via several coordination bonds, one speaks of a **chelating compound** or **chelation** (sketched in **Figure 2.10c**) [83].

## 2.5.2 Structure of Metal-organic Frameworks

In MOFs, the organic linkers are always ligands, that donate an electron pair to a metal cation and form a coordinate covalent bond [109]. MOFs can therefore be defined as „intrinsically porous extended solids formed by coordination bonding between organic ligands and metal ions or clusters“ [108]. The metal nodes usually consist of transition metals such as iron (Fe), cobalt (Co), nickel (Ni), copper (Cu), tin (Zn), palladium (Pd) or platinum (Pt).

Three-dimensional MOFs built by carboxylate linkers were in the focus for the first twenty years after their first development, but since carboxylates lead to nearly ionic bonds and therefore to large band gaps, these MOFs are always insulating [108]. In the last ten years, 2D c-MOFs have attracted more and more interest, where ligands with a good ability to exchange electrons are connected with square-planar complexes of metals [109].

The choice of the metal and organic linker allow to tune the properties of a material, even beyond the electronic properties, such as e.g. the optical band gap, the magnetic properties, or the pore size and geometry, as sketched in **Figure 2.10**. This work has its focus on the transport mechanism in a 2D c-MOF, therefore the impact of the chemical structure on the properties of the MOF crystal will be presented in the following according to Reference [109].

### Influence of the Ligand Choice

As sketched in **Figure 2.10a,b**, the ligand geometry mainly affects the dimensionality and porosity, as well as the shape of the unit cell, and thereby the energy bands of the MOF [109,110]. Even more, its functional groups affect the bond strength and length to the metal nodes, which indirectly also affects the pore size and the crystal geometry.

In two-dimensional MOFs, the interaction of functional groups influence the stacking order (e.g. eclipsed, serrated, inclined, compare **Figure 2.10d**) and distance, thereby changing the band structure with respect to the monolayer band-structure [111]. In a 2D c-MOF, the ligand is mostly chosen such that the  $\pi$  orbitals of the ligands match well with the d orbitals of the transition metals. If the overlap is large enough,  $\pi$ -d hybridization and therefore delocalization of charge carriers is reached, enabling good out-of-plane charge-transport.

### Influence of the Metal Choice

Equivalent to the ligand type, the choice of the metal affects the bond strength and length, the geometries in the MOF, the  $\pi$ -d hybridization, and as a consequence the choice of its binding partner. Tuning the properties of a MOF to specific properties therefore requires good matching of the organic and inorganic parts. The choice of the metal can also affect the spin and magnetic properties of the MOF.

### Influence of Redox-activity in the Linkage

By partial oxidation of organic ligands during the synthesis, the fractional amount of metal nodes can be reduced, which leads to mixed valencies and therefore an increased number of unbound charge carriers in the MOF crystal. If a sufficient amount of charge carriers is provided thereby, the system can even be biased toward the formation of  $\pi$ - $\pi$  or  $\pi$ -d mixed orbitals [108] with delocalized electrons. Partial oxidation of ligands is eased by using redox-active compounds, meaning that the two-electron transfer at a linkage is chemically beneficial.

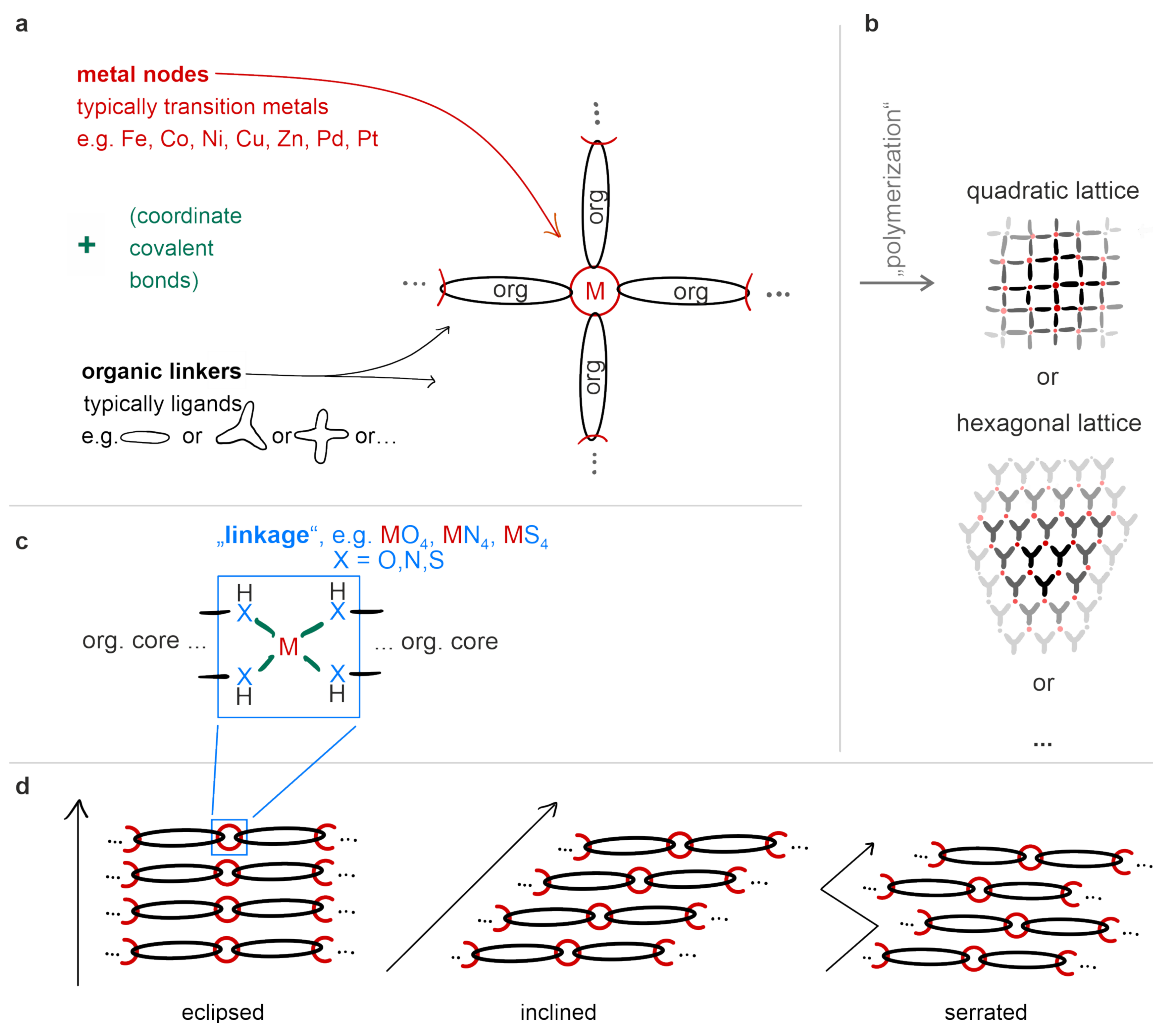


**Figure 2.10 Structure of metal-organic frameworks (MOFs).** **a**, MOFs are always comprised of metal nodes (M) and organic linkers (org) which are connected by coordinate covalent bonds. **b**, The geometry of the linker mainly defines the geometry of the resulting material. **c**, The connection between the organic linker and the metal node is referred to as linkage [109] and is mostly obtained by the metal binding to O = oxygen, N = nitrogen, or S = sulfur. If the organic molecule binds via two or more bonds to the central atom, as shown here, one speaks of chelation. **d**, Different stacking geometries for a simplified 2D c-MOF; eclipsed, inclined, and serrated. Figure inspired by References [109, 110].

### 2.5.3 Charge Transport Models in Metal-organic Frameworks

In MOFs, equivalent to organic crystals, one usually differentiates between hopping and band-like transport (cf. Section 2.3) [108]. For band-like transport a high delocalization of electrons spatially extended over different areas of the crystalline MOF is required. Depending on the extension, the following different pathways have been introduced (also cf. **Figure 2.11a-c**):

- **Through-bond pathways:** Charge transport only takes place between metals and the ligands' functional groups, but not through the organic cores of the linkers, as depicted in **Figure 2.11a**. Only if the network of coordination bonds is dense enough, a continuous route for charge transport can be formed by the linkages.
- **Extended conjugation:** The metal nodes and ligands are chosen such that the  $\pi$ -d conjugation is increased and includes the linkages and the organic cores (cf. **Figure 2.11b**). For this purpose, ligands with chelating functional groups (to increase the number of bonds) and redox-active aromatic cores (to increase the number of free charge carriers) are combined with transition metals.
- **Through-space pathways:** In contrast to the aforementioned pathways, here only the interaction between organic linkers is considered which are assumed to interact by their  $\pi$ - $\pi$ -stacking interaction (cf. **Figure 2.11c**). Hence, the spatial separation determines the transfer integral and therefore the charge mobility. In MOFs where through-space pathways are dominant, e.g. in layer-stacked 2D c-MOFs, charge transport is highly anisotropic, i.e. preferred in the direction perpendicular to the stacks (also cf. Publication **P1** in Chapter 7).

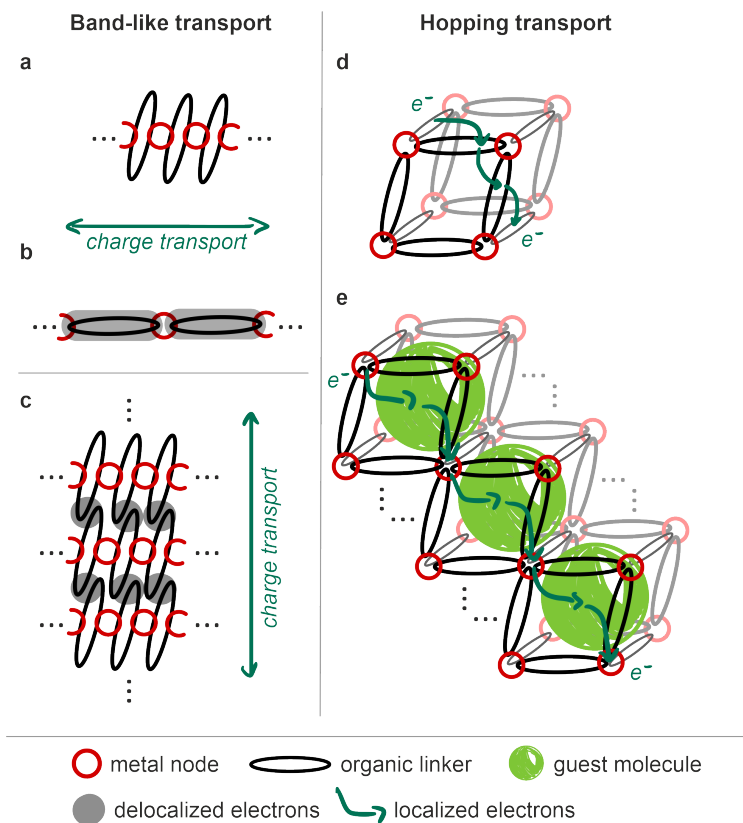


**Figure 2.11** Different transport models for metal-organic frameworks, as discussed in the main text. **a-c** represent band-like transport models, **d,e** represent hopping transport.

Hopping transport is assumed to be predominant in disordered films, at defects (e.g. missing linkers), across grain boundaries [106], as well as at low temperatures [108]. Hopping transport can be provided by the framework itself (so-called redox hopping), or by guests hosted within the framework:

- **Redox-hopping:** If the components of the MOF are redox active, but separated by distances too large to form overlapping orbitals and transport bands, electrons will likely hop from site to site. Depending on which parts of the MOF are redox-active, hopping can occur from metal to metal, from linker to linker (depicted in **Figure 2.11d**), or from metal to linker.
- **Guest-promoted transport:** Hopping can also take place by guest molecules as displayed in **Figure 2.11e**, that are deposited post-synthetically into the MOF, thereby making use of its high porosity. One speaks of guest-promoted transport, if the main transport path is formed by the guest molecules, which can be formed by guest-guest interaction or enabled by guest-framework interaction. The guest materials can be single gas molecules, metals, or even conductive oxides or polymers. Guest-promoted transport makes MOFs especially attractive for application in sensors, since an increase in conductivity of up to 11 orders of magnitude could be demonstrated by introducing fullerene into the pores of a hexa-zirconium(IV) framework [112].

#### 2.5.4 Synthesis and Device Integration

The synthesis of MOFs is still at the heart of the development of new MOF materials. One of the main challenges is to synthesize smooth and thin films on insulating substrates with a low defect and grain-boundary density [105]. Even more, in  $\pi$ -stacked MOFs, where charge transport is anisotropic, the possibility to control the film orientation is highly advantageous. Publication **P1** (Chapter 7) presents a novel approach to synthesize a 2D c-MOF with a predefined stacking direction. Other established methods are shortly introduced in the following, according to Reference [105].

- The most classic way to synthesize a MOF is by **hydro-/solvo-thermal syntheses**, where a substrate is immersed in a precursor solution, if necessary in a washing solution to rinse off solvent residues, and subsequently heated to enable the chemical reaction and film nucleation (compare **Figure 2.12a**) [109].
- **Layer-by-layer growth** or **liquid-phase epitaxy** describes the sequential immersion of a substrate into a solution containing the metal salt, a washing solution to remove excess metal precursor, and a solution containing the organic linker, as depicted in **Figure 2.12b**.
- In **wet-interface assisted syntheses**, the interplay of different interfaces is used to grow films of a MOF on a wet surface (e.g. water). Controlled growth of films with a predefined orientation can be achieved by choosing an organic molecule with a specific combination of hydrophobic and hydrophilic functional groups, as displayed in **Figure 2.12c**. If it is solved in water, the hydrophilic end of the molecule sticks to the water surface, while the hydrophobic end points away from its surface (Langmuir-Blodgett method, cf. e.g. Reference [54]).
- In the **electrochemical approach**, a metal electrode is placed in a linker solution. This solution contains an electrolyte, that dissolves the metal source if an appropriate voltage or current is applied. The metal ions release near the surface of the electrode

and react with the organic linkers in the solution to the desired compound that grows directly on the electrode (compare **Figure 2.12d**).

- Besides synthesis from a solution, MOFs can also be applied by **gas-phase syntheses**. These techniques consist of three steps: (i) precursor vaporization, (ii) precursor transport through the gas phase, and (iii) MOF deposition on the substrate. The most common gas-phase syntheses are chemical vapor deposition (CVD), where the metal and the organic linkers are separately vaporized and the MOF grows during film formation, or physical vapor deposition (PVD), where already-synthesized MOF complexes are applied from the gas phase onto the substrate (cf. **Figure 2.12e**).

After the synthesis, the achieved material is integrated into devices for application in e.g. charge or gas storage, separation, catalysis, proton conduction, and sensors [108, 109]. For charge-transport measurements, MOFs are often used as pellets, since these are easier to synthesize, but also consist of a high defect and grain-boundary density. If charge-transport measurements are performed in electric devices, thin films are integrated into the otherwise equivalent FET structures discussed in Section 2.4 by exfoliating thin nanosheets, or direct growth onto the substrate [109].

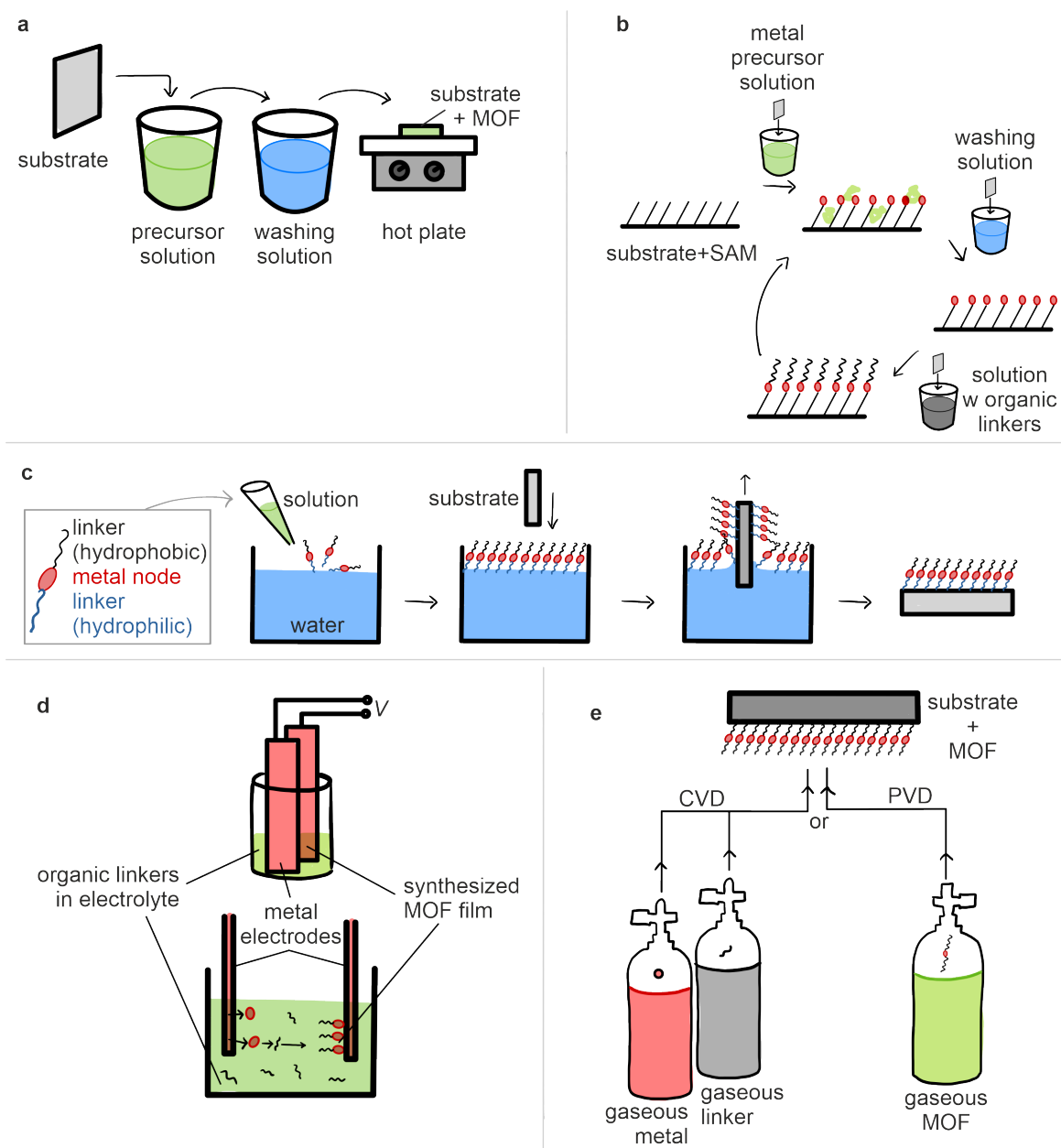


**Figure 2.12 Common syntheses for MOFs**, as described in the main text: **a**, General procedure of hydro-/solvo-thermal syntheses. Adapted from Reference [113]. **b**, Layer-by-layer growth, where the procedure for applying the first monolayer is shown. By repeating the steps, several layers of the MOF can be grown. Inspired by Reference [114]. **c**, Langmuir-Blodgett method as an example for wet-interface assisted syntheses. Adapted from Reference [54]. **d**, Principle of the electrochemical approach. Adapted from Reference [115]. **e**, If grown from the gas phase, MOFs can be either applied via chemical vapor deposition (CVD) or physical vapor deposition (PVD). Adapted from Reference [116].



## 3 Experimental Methods

*This chapter presents the experimental methods used in this work in four sections: First, the different techniques of sample fabrication are presented in Section 3.1. The setups and measurement techniques used to characterize the samples are presented in Section 3.2 (structural characterization), Section 3.3 (electric characterization), and Section 3.4 (characterization by spectroscopic methods).*

### 3.1 Device Fabrication

Organic field-effect transistors with thin films of PDI1MPCN2 are fabricated from bottom to top. In this order the preparation steps to build devices in BGTC structure will be presented, according to the flow chart in **Figure 3.1**. Devices in BGBC structure (cf. Section 2.4) differ from BGTC devices only in the order in which the organic semiconductor and the contacts are applied.

#### 3.1.1 Substrate Preparation

The basis of sample preparation and of the OFET is the substrate. It consists of highly doped silicon, the gate material, and an insulating layer of 30 nm  $\text{Al}_2\text{O}_3$  (BASF or Fraunhofer ISIT) or 300 nm  $\text{SiO}_2$  (ABC GmbH) on top. The substrate is cut or broken from wafers into pieces of  $1 \times 1$  to  $3 \times 3 \text{ cm}^2$  and cleaned successively in acetone and isopropanol in an ultrasonic bath for 7 min each. The substrate surface is functionalized by using an octadecyltrichlorosilane (ODTS) self-assembled monolayer (SAM) on  $\text{SiO}_2$  or a tetradecylphosphonic acid (TDPA) SAM on  $\text{Al}_2\text{O}_3$ . To apply the respective SAM, the wet-cleaning steps are followed by an oxygen-plasma etching step of 7 min at 50 W and 10 sccm gas flow, after which the highly-reactive substrates are immersed into a solution of the desired SAM (compare **Table 3.1**). Afterwards, the substrates are rinsed to get rid of adsorbed molecules, impurities or other residues, and annealed to finalize the bonds between SAM molecules and substrate material [57,117]. Upon SAM functionalization, the substrate's surface gets more hydrophobic, a property that is used to define circular areas for thin-film application on the substrate as displayed in **Figure 3.1**. These areas are obtained by a second plasma-etching step, removing the SAM through a

**Table 3.1 Processing conditions for the different SAMs ODTS and TDPA.** IPA: isopropanol, tol: toluene. For details on SAM application also compare e.g. Thesis **T6** in Appendix H.

SAM molecule	ODTS	TDPA
substrate	$\text{SiO}_2$	$\text{Al}_2\text{O}_3$
solution	1 mM in tol	1 mM in IPA
immersion duration	17 min	$\geq 120$ min
post-processing	rinse with tol & 10 min ultrasonic bath in tol	rinse with IPA
annealing		7 min, $150^\circ\text{C}$

poly(dimethylsiloxane) (PDMS) shadow mask at the desired spots. To keep these spots clean from PDMS residues, the substrates are finally rinsed with acetone, isopropanol and distilled water.

### 3.1.2 Thin-Film Application

In BGTC FETs, the gate and insulating layer are covered by a semiconducting layer. Monolayers of PDI1MPCN2 are applied by a drop-casting method, the theory of which is presented in Section 2.2.1. Since solution-based application methods require good solvability of the material, organic molecules are applied more often from the gas phase, a procedure that has been used within this work to prepare polycrystalline multilayers of PDI1MPCN2. The technical details of both techniques will be presented in the following.

#### Thin-film Application of PDI1MPCN2 From Solution

A 1-mMolar solution of PDI1MPCN2 (obtained from BASF) in dimethylphthalate (DMP) or toluene (Tol) is weighed, stirred at 40 °C and 600 rpm for at least 6 hours, and filtered with 0.2 μm pore size. The solutions are mixed with ratios of DMP:Tol 1:3 or 3:1. 2 μl of the mixtures or pure DMP solutions are drop-cast onto the SAM-free areas of the prepared substrate (compare **Figure 3.1**), which is placed on a hot plate at 70 °C, and let dry overnight. The exact parameters can be varied such that droplets pin on the substrate and dry with a constant contact area (surface structured by SAMs, pure DMP solution) or don't pin and dry with a constant contact angle (drop casting on pure substrates without SAM), described in more detail in the Supporting Information of Publication **P2** (Chapter 4).

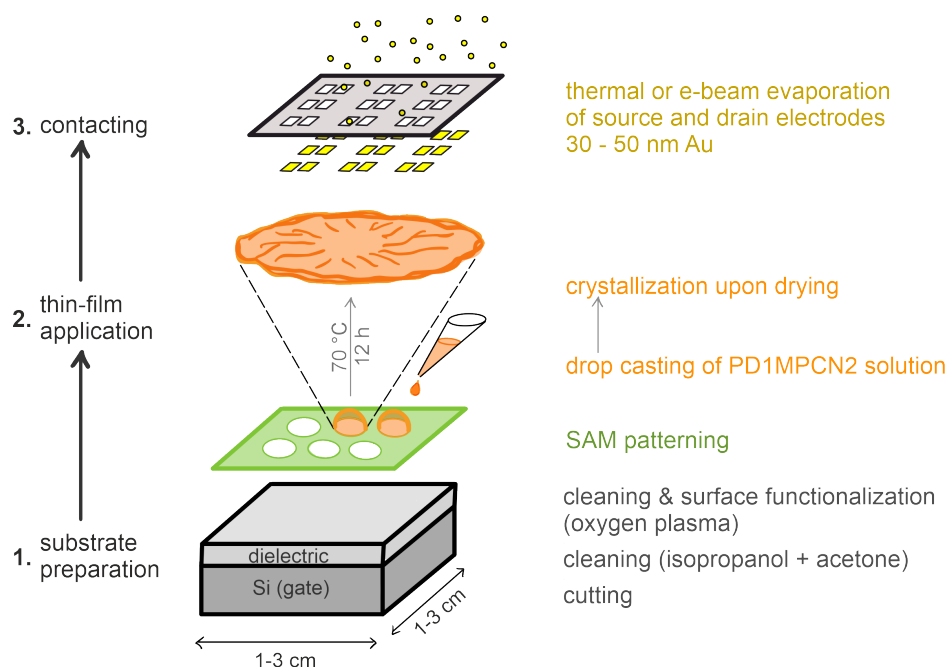


**Figure 3.1** Flow chart for the fabrication of FETs in BGTC structure. The Figure displays the case for devices with monolayers of PDI1MPCN2 applied from solution. More details on sample fabrication are given in Sections 3.1.1 to 3.1.3.

### Application of PDI1MPCN2 from the Gas Phase by Thermal Evaporation

If PDI1MPCN2 is applied from the vapor phase, the substrates are fully coated with the respective SAM (cf. Section 3.1.1 and **Table 3.1**). The SAM saturates dangling bonds and smoothens energetic disorder on the substrate surface and thereby supports a more uniform film growth. Since both effects result in a reduced trap-state density at the insulator-semiconductor interface, it acts as a passivation layer.

The passivated substrates are placed into an evaporation chamber (BesTec) at  $\approx 10^{-6}$  mbar and heated to 90 °C (this temperature has been observed to result in the largest grain sizes for PDI1MPCN2 [61]). Below the substrates, a crucible with the organic molecule in powder form is placed. If an electric current in the order of 50 to 100 A is applied to the crucible, the molecule evaporates and nucleates on the substrates (cf. Section 2.2.1 for a theoretical background). By adjusting the current, the evaporation rate is held constant at  $\approx 0.3$  to  $0.5 \text{ \AA/s}$ , which is monitored by an oscillating quartz crystal. The evaporation time consequently determines the film thickness, which is chosen to  $\approx 25 \text{ nm}$ , if not stated otherwise.

#### 3.1.3 Contacting

The source and drain electrodes are applied via thermal evaporation (BesTec, pressures of approx.  $10^{-6}$  mbar) at currents up to 200 A (i.e. at much higher currents than organic semiconductors), or by electron-beam physical vapor deposition (e-beam PVD) (pressures of approx.  $10^{-7}$  mbar), where the material is not heated by a current, but by a focused electron beam. While the smaller pressure in e-beam PVD is supposed to lead to cleaner contacts, thermal evaporation is assumed to be less destructive on the underneath lying organic semiconductor. A detailed study on this relation is beyond the scope of this thesis, but was investigated for devices with PDI1MPCN2 in Thesis **T5** (Appendix H).

The contacts are evaporated through shadow masks as displayed in **Figure 3.1**. The design of the shadow mask was chosen according to the requirements of the respective experiment. (An overview is given in Appendix B.) For top contacts, 30 to 50 nm gold (Au) are evaporated with a rate of  $1 \text{ \AA/s}$ , while for bottom contacts an additional layer of 1 to 2 nm titanium ( $0.1 \text{ \AA/s}$ ) as adhesion layer between the substrate and the gold contacts is necessary.

A finalized sample in BGTC structure is presented in **Figure 3.2**. For in-operando KPFM measurements presented in Chapter 4, as well as for Fourier transform photoelectric current (FTPC) measurements presented in Chapter 6, the sample is fixed on a mountable sample holder and the source and drain contacts are bonded as shown in **Figure 3.2** to bring them into a closed system (KPFM: glove box; FTPC: vacuum). Since a normal wedge bonding machine was observed to break the underneath lying semiconductor, the top contacts are connected to gold wires with silver (Ag) conductive paint. The other end of the wire is then connected with a sample holder.

#### 3.1.4 Preparation of FETs with MOFs

For the project presented in Chapter 7, FETs with a 2D c-MOF as the active layer are prepared. The films are synthesized as described in Publication **P1** (Chapter 7) and applied on substrates with 300 nm  $\text{SiO}_2$  and flakes of hexagonal boron nitride (hBN). hBN is a two-dimensional insulator with a hexagonal lattice [118, 119] which can be exfoliated onto the substrate to form an atomically-flat surface and reduce the defect density at the insulator-semiconductor interface of the FET.

FETs with PDI1MPCN2 on hBN substrates revealed accordingly higher mobilities compared to hBN-free devices [Publication **P5**], and we implemented hBN into FETs with the 2D

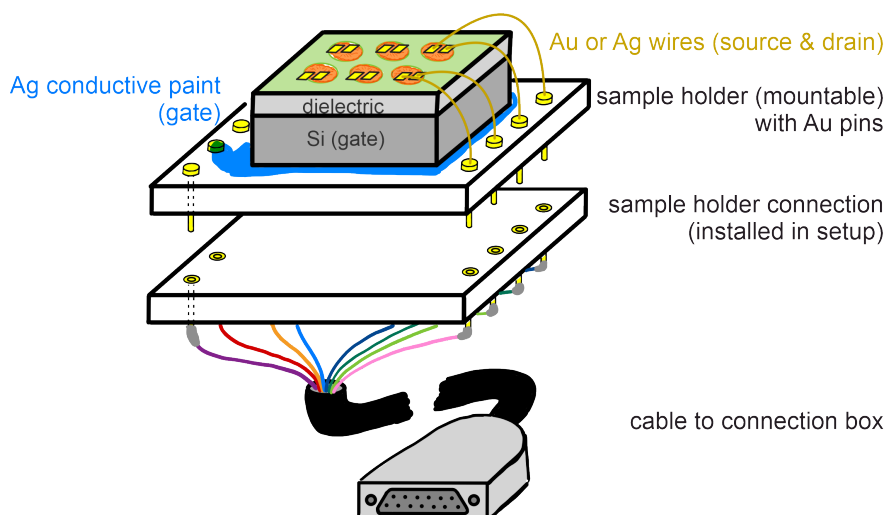


**Figure 3.2 Finalized BGTC OFET on a mountable sample holder to enable electrical connection to a connection box.** The image shows the bonded devices on top of a sample holder that can be mounted to a fixed sample holder and thereby electrically connected to a connection box. The sample is glued with silver (Ag) conductive paint onto the sample holder to connect the gate with one of the gold (Au) pins. A photograph of the real sample holder is presented in **Figure D.6c** in Appendix B.

c-MOF after hBN-free devices broke already at small gate voltages. After applying the MOF film, gold contacts are designed in structures for TLM measurements by electron beam lithography (Raith e-LINE system) in an ultrahigh vacuum.

*The MOF films have been synthesized by cooperation partners from the TU Dresden, exfoliation and contacting of hBN flakes by L. Renn as stated in Publication P5.*

## 3.2 Structural Characterization

The finalized devices are characterized, first structurally, then electrically (cf. Section 3.3) and/or by spectroscopic methods (cf. Section 3.4). Especially in BGTC devices, the structure of the organic films is investigated by optical microscopy after crystallization to localize grain boundaries and contact specific sites right after. Polycrystalline films and contact electrodes were analyzed by AFM, which enables the detection of step heights with a high resolution. This section presents the working principle of both techniques, starting with polarized optical microscopy (POM) in Section 3.2.1, followed by the basics of AFM in Section 3.2.2.

### 3.2.1 Polarized Optical Microscopy

Polarized optical microscopy is a special method of optical microscopy, where a polarizer and an analyzer are included in a standard optical microscope (Zeiss) and set orthogonal to each other as displayed in **Figure 3.3**. Since grains are structurally anisotropic, they reflect incoming polarized light while turning its direction. Therefore, part of the reflected light transmits the analyzer and the grains appear bright (compare **Figure 3.3a,b**), in contrast to the structurally isotropic grain boundaries, which do not turn the polarization direction of the reflected light. Polarized light reflected at grain boundaries therefore is completely filtered out by the analyzer (compare **Figure 3.3c**) and the grain boundaries appear as dark lines [74, 120].

POM allows not only to differentiate between grains and grain boundaries, but also to

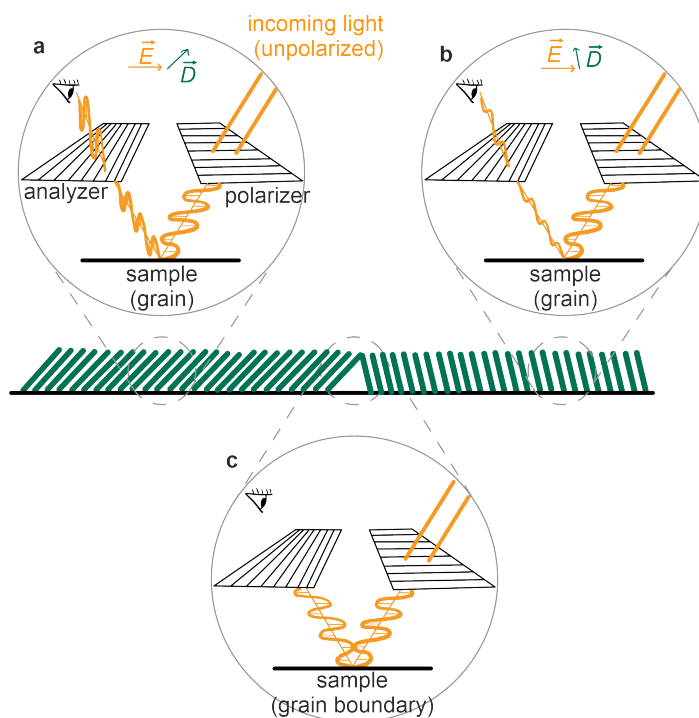


**Figure 3.3 Principle of polarized optical microscopy at grains and grain boundaries.** **a,b,** Optically anisotropic grains turn the direction of polarized light, whereby the absorption intensity is determined by the orientation relation between the electric field of the incoming light  $\vec{E}$  and the molecular dipole moment  $\vec{D}$ . Therefore, grains with different orientations may appear in different brightness. **c,** Optically isotropic grain boundaries do not turn the direction of polarized light and appear as dark lines.

qualitatively investigate the orientation of molecules within a grain [76]. If the molecular dipole moment is parallel to the direction of the incoming light, the absorbed and reflected intensity is increased (cf. Section 2.1) and the respective sites appear brighter, as sketched in **Figure 3.3a** and **b**. Consequently, the continuous transition from bright to dark areas that can be observed within a single grain of PDI1MPCN2 (cf. **Figure 2.5d** in Chapter 2) indicates that the molecules turn from one grain boundary to the next. This behavior is investigated in more detail in Reference [59] by photoluminescence spectroscopy and explained by the molecule's chirality.

### 3.2.2 Atomic Force Microscopy

The centerpiece of an atomic force microscope is a cantilever, fixed at a piezo to move it in  $z$  direction and excite it to an oscillation. The other end of the cantilever is fixed to an (ideally) atomically-sharp tip, whose interaction with a sample surface is used to detect short-range and long-range forces of the sample. The interaction can be measured by a laser beam reflected at the back side of the cantilever onto a four-quadrant diode, which generates no voltage if the cantilever is in its equilibrium state. If, however, the tip is attracted or retracted by the sample-surface, the cantilever bends and the laser beam is displaced, thereby generating a deflection voltage  $U_d$  [121,122].

This is the general working principle of AFM, which will be explained in more detail within this section, and advanced to special AFM techniques, such as conductive AFM and Kelvin probe force microscopy, in Section 3.3. The following description is according to Reference [122].

### Force-distant Curves and Tip Calibration

AFM detects the interaction strength between tip and sample. It can either be detected at constant tip-sample distance while scanning over the surface, or depending on the distance at a fixed position. The latter case is the so-called quasi-static mode, in which force-distance curves are detected by slowly approaching and retracting the tip to/from the surface and measuring the interaction force by the deflection voltage  $U_d$ . The course of a typical force-distance curve is sketched in **Figure 3.4**, which is usually read from right (large distance) to left (tip and sample are in touch).

If the tip and the sample surface are far away from each other, they do not interact and the cantilever deflection does not change, even if the tip is brought closer. However, as soon

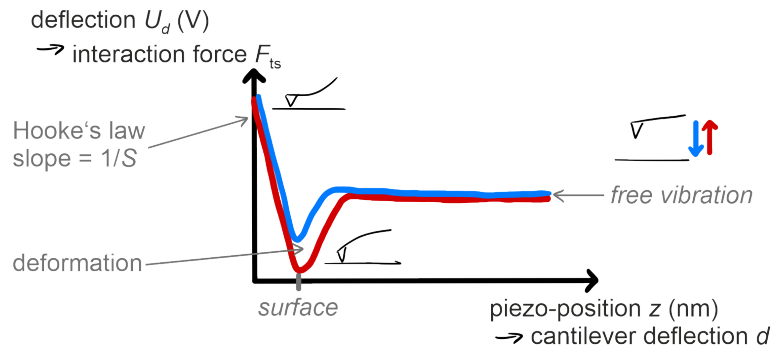


**Figure 3.4 Force-distance curve detected by atomic force microscopy.** The deflection voltage  $U_d$  is a measure of the interaction force  $F_{ts}$  and the piezo-position  $z$  can be translated into the cantilever deflection  $d$ . Figure according to [122].

as the tip-sample distance is small enough, the tip feels the long-range attractive forces of the sample (e.g. capillary forces) and snaps into the surface. This is visible by a sudden decrease of the deflection voltage. From now on, the tip cannot be brought closer to the surface, and moving the  $z$  piezo with the fixed end of the cantilever further down, only bends the cantilever and/or deforms the substrate. This behavior is represented by a linear increase of the deflection voltage. While the cantilever bending is reversible and follows Hooke's law, deformation is non-reversible and makes the deflection voltage dependent on the sweep-direction. The resulting hysteresis is therefore a measure for the dissipative forces on the substrate and can e.g. give information about the mechanical properties of a sample (cf. e.g. Publication **P3** or Reference [59]).

If the sample surface is hard enough to neglect deformation (e.g.  $\text{SiO}_2$ ), the linear dependence between the cantilever deflection  $d$  and the deflection voltage  $U_d$  represents the **optical lever sensitivity**  $S$  in units of  $\text{nm/V}$ . It depends on e.g. the diode, the laser alignment, the piezos, etc., and allows to translate the detected deflection voltage  $U_d$  into the physically more interesting interaction force  $F_{ts}$  between tip and sample. For this purpose, Hooke's law is used with

$$F \stackrel{\text{Hooke's law}}{=} kd = kU_d S, \quad (3.32)$$

where  $k$  is the cantilever's spring constant.

The spring constant can either be calculated from the cantilever's dimensions and using the Young's modulus, which is a simple, but inaccurate method [122], or detected by a so-called „thermal tune“. If the cantilever is far away from any interaction partner, it slightly vibrates due to thermal fluctuations. The oscillation can be described by the simplified equation of

motion

$$m^* \ddot{d}(t) + \eta \dot{d}(t) + kd(t) = F(t) \quad (3.33)$$

with

- $d$  : deflection of the cantilever,
- $m^*$  : effective mass of the cantilever-tip collective,
- $k$  : spring constant of the cantilever,
- $\eta$  : damping coefficient,
- $F(t)$  : the sum of all external forces acting on the tip and the cantilever,

which represents the vibration of a classical harmonic oscillator with the eigenfrequency  $\omega_0$  if  $F(t) = 0$ . According to the equipartition theorem, the mean square deflection  $\langle \Delta d^2 \rangle$  is

$$\frac{1}{2}k \cdot \langle d^2 \rangle = \frac{1}{2}k_B T \Rightarrow k = \frac{k_B T}{\langle d^2 \rangle} \quad (3.34)$$

with  $k_B$  the Boltzmann constant and  $T$  the temperature. Consequently, the intensity of the thermal noise of the tip allows to determine the spring constant  $k$ .

To summarize, detecting the thermal noise and a single force-distance curve on a hard substrate allow to fully calibrate the measurement system and calculate interaction forces acting on the tip.

### Contact Mode vs. Tapping Mode

In the dynamic mode, the tip is scanned over the sample surface, which can be conducted in two different modes, the contact and the tapping mode. In contact mode, the cantilever is approached toward the surface, like in the quasi-static mode, until a predefined maximum interaction force, the **set point**, is reached. This force is held constant by a feedback loop while scanning over the surface. To avoid any impact of the scanning direction on the detected cantilever deflection, contact mode AFM is usually conducted with a scan angle of  $90^\circ$ . Since in contact mode, the tip is constantly in touch with the surface, the topography is detected mainly mechanically, which makes it a technically easy method, but may also damage soft or weakly-bound samples. In contrast, tapping mode AFM is less destructive, but also more complex.

To conduct AFM in tapping mode, the cantilever is excited to an oscillation with a frequency  $\omega_{\text{drive}}$  at or close to its eigenfrequency  $\omega_0$  by an external drive force

$$F(t) = F_{\text{drive}}(t) = A_{\text{drive}} \cdot \sin(\omega_{\text{drive}} t) \quad (3.35)$$

( $A_{\text{drive}}$  is the drive amplitude).

Combining Equations (3.35) and (3.33) results in a differential equation that describes a driven harmonic oscillator and is solved by

$$d(t) = A \cdot \sin(\omega_{\text{drive}} t - \Phi). \quad (3.36)$$

Both, the amplitude  $A$  and phase  $\Phi$  depend on the drive frequency  $\omega_{\text{drive}}$ , whose relation is sketched in **Figure 3.5** and will be discussed in a bit (cf. attractive vs. repulsive regime) [122]. If the tip is brought close enough to the surface, tip and sample interact and the right side of

Equation (3.33) becomes

$$F(t) = F_{\text{drive}}(t) + F_{\text{ts}}(t).$$

$F_{\text{ts}}$  is the sum of all conservative (e.g. electrostatic) and dissipative interaction forces (e.g. damping) between tip and sample. The tip-sample interaction leads to a shift in the resonance frequency  $\omega_0$ , which can be tracked by a feedback system (so-called **frequency modulated (FM)**-AFM). Alternatively, the feedback acts on the amplitude  $A$ . This means that the system tracks the changes in height that have to be applied to keep the amplitude constant (so-called **amplitude modulated (AM)**-AFM).

Usually, when speaking of a set point, one means an amplitude set point that is the reference amplitude one wants to keep constant. The regulation of the  $z$ -piezo then gives the height profile of the detected sample. The phase can be detected simultaneously, which is sensitive on dissipative forces and can give additional information if a sample is smooth but has different mechanical properties.

### Attractive vs. Repulsive Regime

The amplitude  $A(\omega_{\text{drive}})$  and phase  $\Phi(\omega_{\text{drive}})$  sketched in **Figure 3.5** are the solution of Equation (3.35) for a non-interacting tip. An additional force  $F_{\text{ts}}$  shifts these curves, and therefore also the resonance frequency of the driven oscillation. Repulsive forces shift the resonance frequency to higher values, while attractive forces reduce the resonance frequency, as sketched in **Figure 3.5b**. If the drive frequency  $\omega_{\text{drive}}$  is kept constant, the corresponding phase shifts, e.g. to values  $< 90^\circ$ , if the tip feels repulsive forces. In this case, the tip is in (hard) contact with the surface during some time of the oscillation. On the contrary, attractive forces are more gentle to the tip and the sample, but harder to detect, since they are usually very weak and short range [123].

To measure e.g. in the attractive regime, one can either choose the set point such that the phase is constantly above  $90^\circ$ , or choose the drive frequency slightly below resonance, as sketched in **Figure 3.5** [123]. Additionally, the drive frequency should always be chosen slightly different from the resonance frequency, to make sure that the phase does not jump between the different regimes, i.e., to keep the measurement stable. However, it should also still be chosen as close as possible to the resonance frequency to maintain a high amplitude, i.e. measurement signal (cf. **Figure 3.5a**).

Since detecting organic semiconductors is a challenge, because the films are relatively soft and extremely smooth, an instruction on how nice pictures can be obtained is given in Appendix C.

## 3.3 Electric Characterization

In the previous section, the basics of AFM are presented, which is used to characterize the structure of organic films. To investigate the electrical properties, more advanced modes of AFM are used, that is, c-AFM presented in Section 3.3.1 and KPFM presented in Section 3.3.2. Even more, transport measurements of FETs as described in Section 2.4 are conducted at a probe station presented in Section 3.3.3.

### 3.3.1 Conductive Atomic Force Microscopy

c-AFM is a specific contact mode, which allows to simultaneously detect the height and conductivity of each sampling site on the investigated surface. Since the AFM tip acts as one of the electrodes, it has to be conductive, which is achieved e.g. by coating it with a

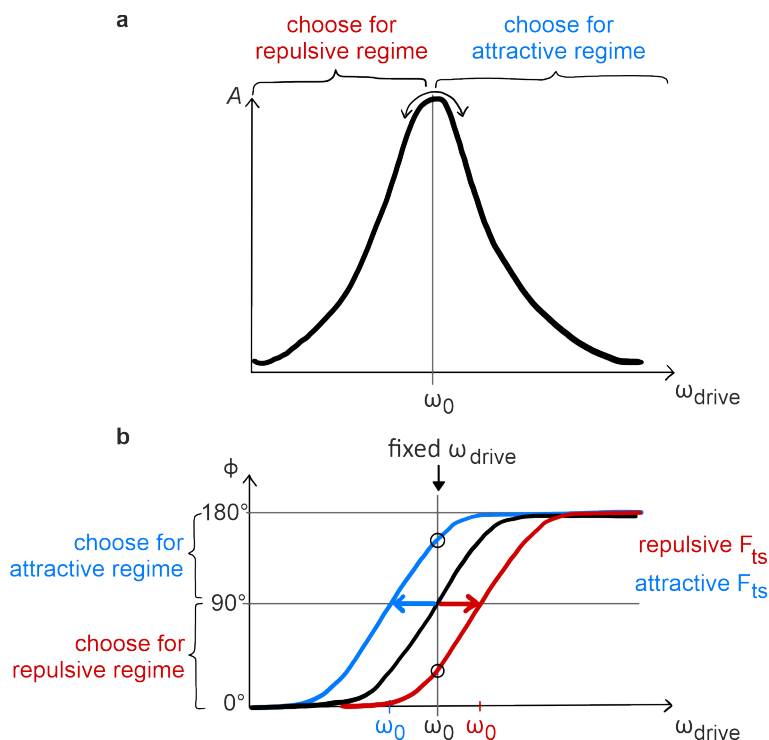


**Figure 3.5 Amplitude  $A$  (a) and phase  $\Phi$  (b) of a driven harmonic oscillator without interaction forces.** The exact relations are given e.g. in Reference [122]. Figure according to Reference [123].

platinum iridium (PtIr) alloy. After the tip is brought into contact with the surface, a voltage is applied between the sample chuck and the tip and the resulting current is detected [124]. c-AFM usually probes the vertical conductivity of samples on a very local area; the resolution is given by the tip diameter which is normally in the range of some nm (cf. **Table C.1** in Appendix C). If the current-voltage dependence is detected between the tip and a second fixed electrode on top of the device, instead of the sample chuck, also horizontal currents can be detected, as e.g. performed across grain boundaries in sexithiophene [125, 126] or triethylsilylethynyl anthradithiophene [42].

In this work, c-AFM has been used to measure the local out-of-plane conductivity of MOF films, the results of which are presented in Publication **P1** (Chapter 7).

### 3.3.2 Kelvin Probe Force Microscopy

In 1898, Lord Kelvin observed that a current flows between two different metals if they are brought into contact [127]. This current flows from the metal with the higher Fermi level to the material with the lower Fermi level, according to the aim of electrons to minimize their energy. This effect is used by a Kelvin probe, a material with a known work function, used to non-destructively measure the work function of a sample [128].

In 1991, Nonnenmacher et al. were the first to use a Kelvin probe as an AFM tip and thereby detect the topography and the work function of a sample surface, which is the concept of Kelvin probe force microscopy [129]. The measurement signal of KPFM is the so-called contact potential difference (CPD) defined as

$$eU_{\text{CPD}} = E_F^{\text{tip}} - E_F^{\text{sample}}, \quad (3.37)$$

which can be understood as the bias voltage to nullify the current between tip and sample [130]. While KPFM was introduced here as a method to detect metallic surfaces in direct contact, actually all kinds of materials can be detected contactless by the measurement techniques introduced in the following according to References [81, 130, 131].

### KPFM modes

The contactless detection of the CPD is based on electrostatic interactions between the sample surface and the vibrating cantilever. The cantilever is excited to an oscillation by applying an alternating current (AC) voltage to the  $z$  piezo at a frequency  $\omega_{\text{drive}}$  (tapping mode, cf. Section 3.2.2). Additionally, an AC voltage with a frequency  $\omega_E$  is applied to the conductive tip, which induces oscillations to the cantilever at  $\omega_E$  if the CPD is non zero. These oscillations depend on the electrostatic interaction strength between tip and sample  $F_E$  and are nullified by an additional direct current (DC) voltage. The total voltage applied to the tip is consequently

$$U_{\text{tip}} = U_{\text{DC}} + U_{\text{AC}} \cdot \sin(\omega_E t) \quad (3.38)$$

and the potential difference between tip and sample is  $\Delta U = U_{\text{tip}} - U_{\text{CPD}}$ , if the sample is set to ground. Note that, if the tip is set to ground and the sample is biased, the definition of the CPD changes in signs and the interpretation of the measurement signal turns around. The potential difference between tip and sample, which act as a plate capacitor with capacitance  $C$  and distance  $z$ , exerts an electrostatic force  $F_E$  on the cantilever:

$$F_E = \frac{1}{2} \frac{\partial C}{\partial z} (\Delta U)^2 = \frac{1}{2} \frac{\partial C}{\partial z} (U_{\text{tip}} - U_{\text{CPD}})^2. \quad (3.39)$$

Inserting Equation (3.38) into Equation (3.39) and expanding it, yields one static and two dynamic modes of the force acting on the cantilever:

$$F_{\text{stat}} = \frac{1}{2} \frac{\partial C}{\partial z} \cdot \left( [U_{\text{DC}} - U_{\text{CPD}}]^2 + \frac{U_{\text{AC}}^2}{2} \right), \quad (3.40)$$

$$F_{\text{dyn}, \omega_E} = \frac{\partial C}{\partial z} \cdot (U_{\text{DC}} - U_{\text{CPD}}) \cdot U_{\text{AC}} \sin(\omega_E t), \quad (3.41)$$

$$F_{\text{dyn}, 2\omega_E} = \frac{1}{4} \frac{\partial C}{\partial z} \cdot U_{\text{AC}}^2 \cos(2\omega_E t). \quad (3.42)$$

Equation (3.41) represents the basic idea of amplitude modulated KPFM, since the amplitude of the response signal at  $\omega_E$  vanishes if  $U_{\text{DC}} = U_{\text{CPD}}$ .

The most common AM-KPFM mode is the so-called **lift mode** (used in the Bruker Icon and Asylum Jupiter, cf. **Table C.1** in Appendix C). Here, each line of the surface is scanned twice: first, the tip detects the topography in usual AFM tapping mode, then it is lifted and scans this topography again from a certain distance (5 to 50 nm). During the second scan, the mechanical excitation is turned off and only the surface potential is detected. This procedure decouples the electrostatic response from any short range interactions, but the resolution and sensitivity are low and the measurement takes twice the time.

A higher sensitivity can be obtained by tracking the frequency instead of the amplitude in FM-KPFM. As depicted in **Figure 3.5b**, the cantilever's eigenfrequency shifts due to the

tip-sample interaction  $F_{ts}$  by

$$\omega_0 \longrightarrow \tilde{\omega}_0 \approx \sqrt{\frac{1}{m} \left( k - \underbrace{\frac{\partial F_{ts}}{\partial z}}_{\propto \partial^2 C / \partial z^2} \right)} \quad (\text{for small amplitudes } A(\omega)). \quad (3.43)$$

Consequently, FM-KPFM detects the force gradient, instead of the absolute interaction force, which is more sensitive to changes in the tip height than AM-KPFM.

The sensitivity increases even further, if sideband frequencies are tracked, which result from mixing of the mechanical drive frequency  $\omega_{\text{drive}}$  and the electric frequency  $\omega_E$  to  $\omega_{\text{drive}} \pm \omega_E$  [131]. Sidebands can easily be separated from the main frequencies and noise bands [130], but have usually also smaller amplitudes.

A special case of sideband detection, that overcomes the problem of reduced signal response, is called **heterodyne** detection [132]. In FM heterodyne KPFM, the cantilever is excited to an oscillation with a frequency close to its eigenfrequency  $\omega_{\text{drive}} \approx \omega_0$  (tapping mode), and the electric excitation is set to  $\omega_E = \omega_1 - \omega_{\text{drive}}$ , where  $\omega_1$  refers to the first overtone of the cantilever vibration. This shifts the sideband frequency into resonance with the first overtone. The resonance amplifies the response signal without limiting the detection bandwidth. This offers a high signal-to-noise ratio (SNR) with high measurement speed at the same time.

So far, the grain boundaries investigated in this work could only be detected using FM heterodyne KPFM while lift mode was not able to display them. Obviously, the measurement requires a high resolution and sensitivity.

### KPFM at Organic Semiconductors

In Chapter 4, the surface potential of organic semiconductors is detected. Usually, the sample is set to ground, and as a consequence the Fermi level is assumed to be constant over the whole measurement system. Equation (3.37) can then be translated into

$$eU_{\text{CPD}} = - \left( W^{\text{tip}} - W^{\text{sample}} \right) = - \left( E_{\text{vac}}^{\text{tip}} - E_{\text{vac}}^{\text{sample}} \right) \quad [46, 133\text{--}135]. \quad (3.44)$$

To determine absolute values for the work function, it is necessary to exactly determine the tip's work function first [136]. Furthermore, measurements in vacuum or at least in an inert atmosphere are advantageous such that the electrical properties of the tip don't change during measurement. For a qualitative description, general knowledge about the work function or Fermi level of the material is required. In the specific case of PDI1MPCN2, which is an n-type semiconductor, the Fermi level is assumed to lie close below the LUMO level and therefore we translate areas with a higher CPD to lower LUMO levels (cf. Chapters 4 and 5).

#### 3.3.3 Probe Station

While KPFM can be used to characterize the LUMO-level distribution of PDI1MPCN2 thin-films, its transport characteristics are detected in FETs using two different probe stations, both following the same principle.

Probe needles are mounted to precision positioners and connected with source-measure units (Keithley 2450). One probe needle is placed on each electrode—source, drain, and gate—to apply  $V_{\text{GS}}$  to the gate and  $V_{\text{DS}}$  to the drain. The voltages are applied using the two source-measure units, which also measure the resulting drain current  $I_{\text{DS}}$  and gate current  $I_{\text{GS}}$ . The source electrode is set to ground.

For standard measurements, a setup at ambient conditions is used, while temperature-

dependent measurements are conducted in a commercial Lakeshore CRX-VF vacuum probe-station. The vacuum probe-station can be pumped down to  $\approx 2 \times 10^{-7}$  mbar and the sample stage can be cooled or heated to temperatures between 5 and 400 K. To improve thermal coupling between the sample stage and the sample, it is glued with silver conductive paint on the sample stage.

### 3.4 Spectroscopic Methods

To detect photocurrents in organic thin-films of PDI1MPCN2, a setup was reassembled from a commercial Fourier transform infrared (FTIR) spectrometer. This section will shortly introduce the general principles of FTIR spectroscopy before describing the modified setup for FTPC spectroscopy.

#### 3.4.1 Fourier Transform Infrared Spectroscopy

A detailed description on FTIR spectrometers and their working is given in References [57,137], on which this section orients contentwise.

FTIR spectroscopy is a special method of IR spectroscopy, which uses light in the range of 780 nm – 1 mm (also compare **Table 3.2** for frequencies or energies). The IR spectrum can be divided into the following subdivisions: the MIR, which corresponds to the energetic range of fundamental vibrational modes of organic molecules, the NIR, corresponding to overtones and combination bands, and the far infrared (FIR), where rotational properties of organic molecules, as well as vibrational modes of inorganic materials lie (compare **Table 3.2** and **Figure 3.8**).

The centerpiece of an FTIR spectrometer is a Michelson interferometer, which transforms the spectrum of a broad-band light-source into an interferogram (the working principle will be presented in the following). After its interaction with the sample, it is detected and translated back using a Fourier Transformation. The use of an interferometer yields an intrinsic higher wavenumber scale („Connes advantage“), higher throughput of radiation („Jacquinot advantage“) and faster measurement („ Fellgett advantage“) than using dispersive methods [137,139]. In this work, a Bruker IFS-66v/S spectrometer was used. Its construction and working principle are sketched in **Figure 3.6** and will be presented in the following in the order of the beam path, which corresponds to the labels in the figure.

#### a) Light-source Compartment

The light source defines the range of the achievable wavelengths. For measurements in the MIR, a silicon carbide (SiC) heating element, called „globar“ (composed of glow + bar) is usually used. If it is heated to temperatures between  $T = 980^\circ\text{C}$  and  $1650^\circ\text{C}$ , it is nearly a perfect black body radiator. Its emission intensity sketched in **Figures 3.6a** and **3.8** can be

**Table 3.2** Definition of the IR spectrum and the subdivisions NIR, MIR and FIR [138] in terms of wavelength  $\lambda$ , frequency  $\nu$ , and photon energy  $E$ .

		$\lambda$	$\nu$	$E$
IR	NIR	780 nm - 3 $\mu\text{m}$	385 THz - 100 THz	1.6 eV - 400 meV
	MIR	3 $\mu\text{m}$ - 50 $\mu\text{m}$	100 THz - 6 THz	400 meV - 25 meV
	FIR	50 $\mu\text{m}$ - 1 mm	6 THz - 300 GHz	25 meV - 1 meV

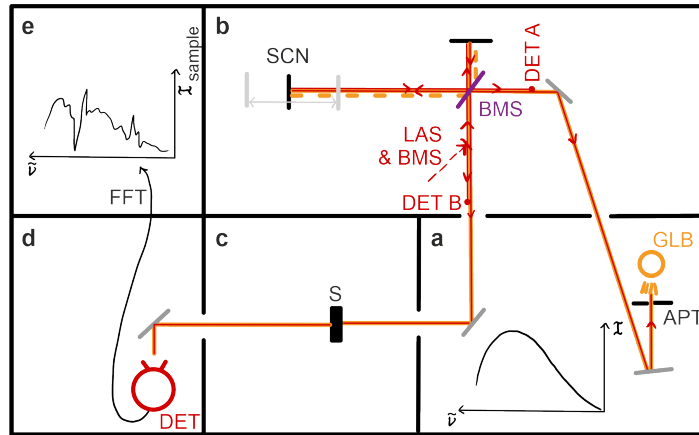


**Figure 3.6 Setup of a Fourier transform infrared spectrometer.** The compartments **a-e** are presented in the corresponding paragraphs in the main text. GLB = Globar, APT = Aperture, SCN = Scanner, BMS = Beamsplitter, LAS = Laser, DET A/B = Laser Detector A/B, S = Sample, DET = Detector, FFT = Fast Fourier transform. The calibration laser is coupled into the spectrometer from its backside (indicated by the dashed arrow) and split by a second beamsplitter into two parts, one reaching for DET A and DET B, the other one following the beam path of the infrared light-source. The inset graphs display the emission (transmission) spectrum of the light source (sample) depending on the wavenumber  $\tilde{\nu} = 1/\lambda$ . Figure inspired by References [57, 139].

described by Planck's law of black-body radiation

$$\mathcal{I}(T) = \frac{2\nu^2}{c^2} \cdot \frac{h\nu}{e^{h\nu/k_B T} - 1} \quad (3.45)$$

with  $h$  Planck's constant,  $c$  the speed of light (in vacuum),  $k_B$  the Boltzmann constant and  $\nu$  the frequency [137]. Behind the light source, an aperture is used to collimate the light beam, whose size determines the illuminated area of the sample. The larger the area, the larger the absorbance, but the higher the influence of random orientation of different grains.

### b) Interferometer Compartment

The spectrum  $\mathcal{I}$  of a broad-band light-source is transformed into an interferogram  $\tilde{\mathcal{I}}$  using a Michelson interferometer. It consists of a beamsplitter, whose material defines the accessible range (compare **Table D.2** in Appendix D), and two mirrors, one of which is movable (called „scanner“, cf. **Figure 3.6b**). The beamsplitter splits the light beam into two parts, and leads them to either one of the mirrors. In their default position, both mirrors have the same distance from the beamsplitter and the reflected beams interfere constructively. If the scanner is displaced by  $\delta$ , the corresponding beam path is increased by  $2\delta$  and the two beams have to travel different distances, leading to destructive or constructive interference depending on the relation between  $2\delta$  and the wavelength. Consequently, by continuously moving the scanner the resulting intensity is modulated to a cosine wave, described by

$$\tilde{\mathcal{I}}(\delta) = \mathcal{I}(\tilde{\nu}) \cos(2\pi\tilde{\nu}\delta) \quad (3.46)$$

with  $\mathcal{I}(\tilde{\nu})$  the intensity of the light source at a specific wavenumber  $\tilde{\nu} = 1/\lambda$  (the wavenumber is more common in IR spectroscopy than wavenumbers or frequencies) [137].

FTIR spectrometers use this modulation of a single wavenumber into a cosine interferogram as depicted in **Figure 3.7b** to detect the exact scanner position at a given time. (For example, a vanishing intensity  $\mathcal{I} = 0$  can be attributed to  $\delta = 0$ .)

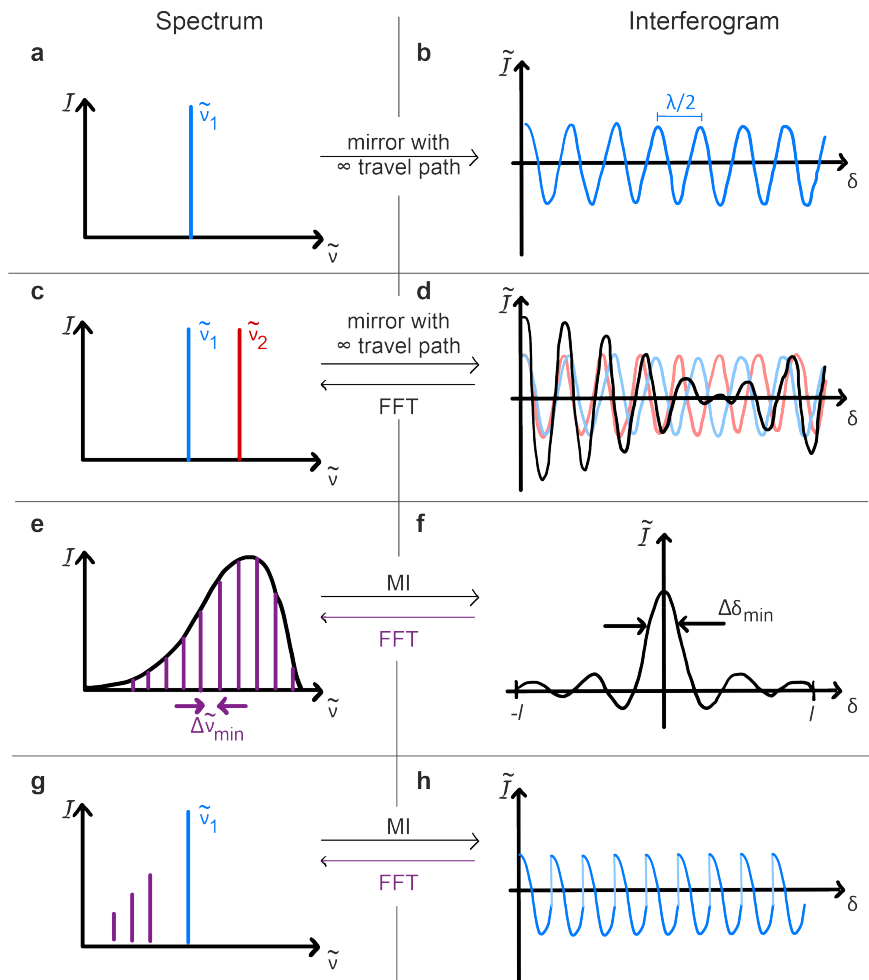


**Figure 3.7** Generation of interferograms of different light sources. **a,b**, Spectrum and interferogram of a monochromatic light source, as e.g. the calibration laser. **c,d** Spectrum and interferogram of a source with two distinct wavelengths. **e,f**, Spectrum and interferogram of a broadband light-source, such as the globar. **g,h**, Spectrum and interferogram of a monochromatic light source for a limited mirror displacement length. MI = Michelson Interferometer, FFT = Fast Fourier Transform. For more details cf. main text. Figure according to Reference [137].

Therefore, a calibration laser (630 nm), is coupled into the spectrometer from its back and divided by a second beamsplitter into two parts. One part follows the beam path of the infrared light-source to ease the calibration of the optics and the sample in the beam path and is used to detect the scanner position. The other part is lead to two photodetectors (DET A and DET B in **Figure 3.6b**), which turn on the mirror movement (driven by air bearing) if the incoming signal is high enough, i.e. when the Michelson interferometer is well aligned.

If a second discrete wavenumber is added to the emission spectrum of an (imaginary) light source, the interferometer modulates both of them by different modulation frequencies, according to Equation (3.46). The resulting interferogram can be modeled as the sum of both cosine waves, as displayed in **Figure 3.7c,d**. If more and more wavelengths are added to the emission spectrum, it becomes clear that the interferometer simply Fourier transforms each spectrum, and the interferogram of a broad-band light-source can be written as

$$\tilde{\mathcal{I}}(\delta) = \int_{-\infty}^{\infty} \mathcal{I}(\tilde{\nu}) \cos(2\pi\tilde{\nu}\delta) d\tilde{\nu}. \quad (3.47)$$

It has its maximum at  $\delta = 0$ , the only mirror position where all wavelengths interfere constructively (compare **Figure 3.7f**).

### c) Sample Compartment

The modulated beam in form of an interferogram is led to the sample, which is, depending on the reflectivity of the substrate, oriented such that either the reflected (e.g. Au) or the transmitted (e.g. glass) interferogram  $\tilde{\mathcal{I}}_{\text{sample}}(\delta)$  can be detected. (The measurement geometry can be varied by several sample holders displayed in Appendix D.) To reduce contributions from air molecules in the detected spectrum, as well as prevent the semiconductor from degradation, the whole FTIR spectrometer is evacuated to approximately 1 mbar.

### d) Detector Compartment

After interaction with the sample, the interferogram  $\tilde{\mathcal{I}}(\tilde{\delta}_{\text{sample}})$  is detected, usually by detectors made of mercury cadmium telluride (MCT) or deuterated L-alanine doped triglycine sulfate (DLATGS). DLATGS detectors are thermal detectors which measure the change in temperature upon absorption. While they show a constant response for each wavelength, the response time is usually too small to resolve high frequencies.

On the other hand, MCT is a mixture of the two semimetals mercury telluride (HgTe) and cadmium telluride (CdTe) which build up a p-n-junction. At this junction, photoexcited excitons can be separated and the resulting photovoltage can be detected. This is the principle of so-called quantum detectors.

MCT detectors have a higher sensitivity than DLATGS detectors, but have to be cooled and show a non-linear behavior (the sensitivity increases with increasing wavelength) which requires additional calibration measurements. The bandgap also defines a certain cut-off wavelength; incoming wavelengths below this value cannot be detected.

### e) Electronics Compartment

The detector signal is finally translated back from an interferogram into the spectrum of the sample by a fast Fourier transform (FFT):

$$\mathcal{F}\mathcal{F}\mathcal{T}(\tilde{\mathcal{I}}_{\text{sample}}(\delta)) = \int_{-\infty}^{\infty} \tilde{\mathcal{I}}_{\text{sample}}(\delta) e^{-2i\pi\tilde{\nu}\delta} d\delta \stackrel{\text{Eq. (3.47)}}{=} \mathcal{I}_{\text{sample}}(\tilde{\nu}).$$

So far, it was assumed that the interferogram reaches from  $\delta = -\infty$  to  $\infty$ , while it is actually cut at  $-l/2$  and  $l/2$  due to the limited range of the movable mirror. To account for this, the detected interferogram is repeated indefinitely often before computing the FFT. However, this procedure leads to discontinuities in the interferogram, which result in additional peaks in the final spectrum, as indicated in **Figure 3.7d**. While these features can be ruled out by an apodization function [137], the limited detection range also cuts certain wavenumbers, and therefore produces a discretized version of the original spectrum with a finite resolution. The resolution of the spectrum is consequently given by  $\Delta\tilde{\nu}_{\min} = 1/l$ . Vice versa, the mirror path  $l$  can be determined from the spectral resolution of the spectrometer. In the Bruker IFS used for this work, the wavenumber resolution can be chosen as low as  $1\text{ cm}^{-1}$ , i.e. the maximum mirror displacement can be determined to  $l = 1\text{ cm}$ .

### 3.4.2 Fourier-Transform Photocurrent Spectroscopy in the Far Infrared

To measure photocurrents in thin films of PDI1MPCN2, the above introduced FTIR spectrometer was modified as described within this section. While the spectrometer is specifically designed to measure vibrational modes in the MIR, the energies relevant for grain boundaries lie in the range of 10 to 100 meV, i.e. in the FIR (cf. **Table 3.2** or **Figure 3.8**). Therefore, the modifications applied to the setup have two aims: First, make the FIR range accessible, while blocking contributions from the MIR range to not enhance vibrational modes that would disturb the current (or at least the analysis). And second, electrically connect the FET devices within the setup such that voltages can be applied and currents can be measured with a high accuracy and sufficient time resolution. All technical changes applied to the spectrometer are summarized at the end of this section in **Figure 3.10**. The measurement concept will be presented in Chapter 6.

#### Detection in the FIR Range

**Figure 3.8** displays an overview of the optical properties for all relevant parts of the photocurrent setup. The different ranges are presented in terms of wavelength  $\lambda$ , wavenumber  $\tilde{\nu}$  (common in IR spectroscopy), and frequency  $\nu$  (common in FIR or terahertz spectroscopy), as well as energy  $E$  (convenient to describe the energetic landscape of the organic film under investigation).

As can be seen from the figure, the emission spectrum of a mercury arc lamp (Hg-arc), which is typically used for measurements in the FIR, fits exactly to the desired range of 10 to 100 meV. However, its intensity is smaller than that of the globar and only yields higher signals at wavenumbers below  $150\text{ cm}^{-1}$  [140]. Since the intensity is expected to be directly correlated with the magnitude of the excited photocurrent, the globar is chosen for photocurrent measurements. On the contrary, KBr is no longer suitable as beamsplitter material and has to be changed to a 6  $\mu$ -Mylar beamsplitter. „Mylar“ is the tradename for thin films of poly(ethylene terephthalate) (PET), where the thickness (here 6  $\mu\text{m}$ ) determines the accessible spectral range [137].

The modulated beam is focused on the sample using a lense made from polymethylpentene (TPX). The choice of TPX as material is stringent, as it is transmittive in the FIR as well as in the visible spectrum [141] and therefore allows precise adjustment of the sample using the beam of the calibration laser at 630 nm. Since the laser beam is needed to start the scanner movement, which produces the interferogram, it cannot be turned off after calibration. However, to rule out undesired interactions with the sample substrate (compare Chapter 6), it is blocked by a 1 nm-thick plate of high-density polyethylene (HD-PE), a material that serves as an optical window for FIR light [141, 142].

Finally, the incoming light is supposed to increase the mobility of the organic semiconductor

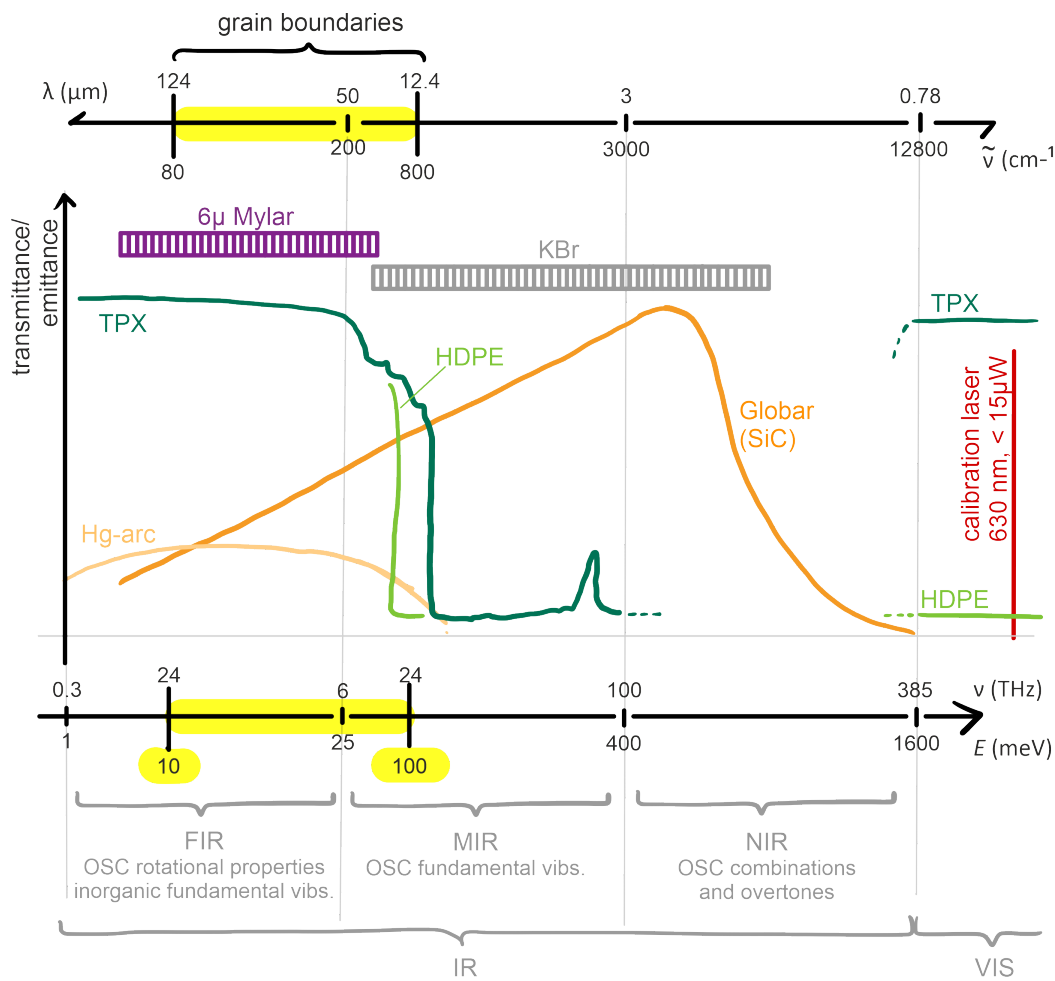


**Figure 3.8 Energetic ranges relevant for infrared spectroscopy and photocurrent spectroscopy across grain boundaries in organic thin-films.** The spectral ranges are according to References [137, 138, 140, 141, 143]. For the beamsplitters the transmittive ranges are indicated according to **Table D.2** in Appendix D.

and therefore the detectable current, such that the sample can be interpreted as the detector for photocurrent measurements. This requires an electrical connection of the sample, which will be explained in the following.

### Electric Acquisition

FTIR spectrometers have been modified for photocurrent measurements and used to analyze a variety of different materials or devices, such as InAs/AlSb quantum dots [144], ZnO films [145], bilayer or trilayer graphene [146, 147], polycrystalline silicon [148, 149], or laser-diode arrays [150]. While the main idea is easy to understand, the electrical and optical properties of the samples lead to specific requirements in sample design and electrical wiring. The samples analyzed in this work contain several field-effect transistors with thin films of PDI1MPCN2 that show lowest degradation and bias stress in vacuum. Therefore, a sample is placed in the evacuable (1 mbar) sample compartment of the spectrometer, in a sample holder that enables electric connection to a connection box and to move it such that each transistor channel can lie in the beam path (compare **Figure 3.2** and **Figure D.6c** in Appendix D). To increase the measurement sensitivity, the beam amplitude is modulated with a frequency  $f_{\text{ch}}$  by an optical chopper that is inserted between the interferometer and the sample.

**Table 3.3 Settings made to the lock-in (LI) amplifier and the SuperFunAnalyzer (SFA) for photocurrent experiments.** The given explanations are according to Reference [152].

name	meaning	chosen setting
Notch filter	removes peaks at 50 and 100 Hz in the incoming signal	ON
Highpass filter	removes DC offsets in the incoming signal	OFF
Synchronous filter	removes outputs at harmonics of the reference frequency	ON
Time constant	defines the bandwidth of the RC filters	$\geq 1/f_{\text{ch}}$
Delay time	SFA: time between applying settings and recording measurement data	$> 10 \times$ time constant

Free charge carriers are induced into the semiconductor by applying a DC voltage  $V_{\text{GS}}$  to the back gate of the sample using a source-measure unit (Keithley 2450). A second source-measure unit (Keithley 2450) is used to apply a DC voltage  $V_{\text{DS}}$  to the drain. The resulting current  $I_{\text{DS}}$  detected at the source electrode, filtered and amplified in a pre-amplifier (Femto, DLPCA-200), and finally analyzed using a lock-in amplifier (Stanford SR860, bandwidth 500 kHz, maximum sampling rate 1.25 MHz) or an oscilloscope (Rohde&Schwarz RTB2000, bandwidth 300 MHz, maximum sampling rate 2.5 GHz).

FTPC spectroscopy is based on the idea that the incoming light in form of an interferogram creates a continuous photocurrent interferogram  $\tilde{I}_{\text{ph}}(\delta)$ . Since each mirror displacement  $\delta$  can be assigned to a certain time, the current interferogram can be measured as a function of time, and transformed back into the contributions of single wavelengths by an FFT. In contrast to normal FTIR spectroscopy, where the originally continuous spectrum gets digitized during the FFT, in FTPC spectroscopy it is the interferogram that gets digitized during the measurement because of the finite time-resolution of the measurement devices:

$$\mathcal{I}_{\text{source}}(\tilde{\nu}) \xrightarrow{\text{MI}} \tilde{\mathcal{I}}_{\text{source}}(\delta) \xrightarrow{\text{sample}} \tilde{I}_{\text{ph}}(\delta) \hat{=} \tilde{I}_{\text{ph}}(t) \xrightarrow{\text{meas.}} \tilde{I}_{\text{ph}}(\Delta t) \xrightarrow{\text{FFT}} I_{\text{ph}}(\Delta\tilde{\nu})$$

**Scheme 3.9 Principle of Fourier transform photocurrent spectroscopy**, according to References [144, 146–148]. MI: Michelson interferometer.

To maintain the shape of  $\tilde{I}_{\text{ph}}$ , the time resolution  $\Delta t$  has to be equal or smaller than the distance (in time) of the narrowest features  $\Delta\delta_{\text{min}}$  (Rayleigh criterion), which originate from the smallest detected wavelength  $\lambda_{\text{min}}$ . With a constant speed of the movable mirror  $v_{\text{mirror}} = 0.633 \text{ cm/s}$  [143] and the minimum desired wavelength  $\lambda_{\text{min}} = 12.4 \mu\text{m}$  (compare **Figure 3.8**), the time resolution has to fulfill the condition

$$\Delta t = \frac{\Delta\delta_{\text{min}}}{v_{\text{mirror}}} \stackrel{!}{\leq} \frac{\lambda_{\text{min}}/4}{v_{\text{mirror}}} = 498.7 \mu\text{s}, \quad (3.48)$$

which corresponds to approximately 2 kHz and can be resolved by both the lock-in amplifier and the oscilloscope.

The lock-in amplifier enables a fully-automated measurement, as it detects, processes (settings are presented in **Table 3.3**) and Fourier transforms the measurement signal [151]. It can be controlled and coordinated with the source-measure units using a home-made python-based

software (SuperFunAnalyzer, [152]). However, the communication with the measurement devices requires additional time (defined by the delay time, cf. **Table 3.3**) and thereby decreases the time-resolution of the measurement procedure.

A faster measurement with a better time resolution can be achieved by a less automated measurement procedure, i.e., without using the SuperFunAnalyzer. In this case, the procedure implemented in the lock-in amplifier is conducted by hand, i.e.,  $V_{GS}$  and  $V_{DS}$  are applied manually to the source-measure units, the time-dependent photocurrent is detected using an oscilloscope and finally transformed by an FFT using the software Origin [153]. The time resolution is then only limited by the bandwidth and the sampling rate of the oscilloscope.

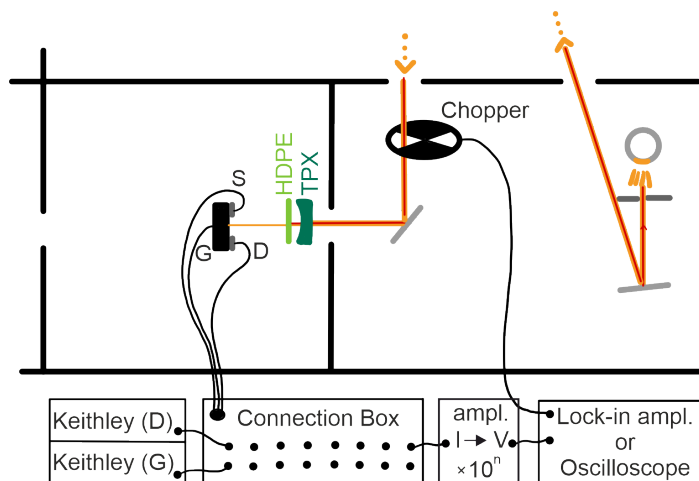


**Figure 3.10** Modified light-source and sample compartment of the FTIR spectrometer displayed in **Figure 3.6a,c** for FTPC spectroscopy at grain boundaries in organic thin-films. S, D, and G refer to source, drain, and gate electrodes, respectively, for the sample only sketched here. (A detailed sample view is e.g. given in **Figure 3.2**, the sample holder is depicted in **Figure D.6c** in Appendix D.)



## 4 Revealing and Controlling Energy Barriers and Valleys at Grain Boundaries in Ultrathin Organic Films

**L.S. Walter**, A. Axt, J.W. Borchert, T. Kammerbauer, F. Winterer, J. Lenz, S.A.L. Weber, and R.T. Weitz

*The previous two chapters presented the theoretical and technical basics of detecting charge transport across grain boundaries in organic thin-films. Grain boundaries in monolayer-thin films of PDI1MPCN2 can be considered as one-dimensional interfaces of grains with different molecular orientations (cf. Chapter 2). Since these structural differences cannot be resolved with standard AFM techniques, in this chapter KPFM is used to investigate the surface-potential difference between grain boundaries and adjacent grains.*

*The chapter starts with a general introduction (1.), and presents the results in four steps, starting with the investigation of the surface potential within a single crystal grain (2.), before presenting the surface potential at grain boundaries (3.). Afterwards, the impact of charge-carrier density on barrier height and valley depth (4.) is presented. Finally, results that lead toward controlling energetics at the grain boundary through processing (5.) are presented, before the results are summarized in a conclusion (6.). The chapter closes with an experimental section (7.).*

*The results presented within this chapter have been published in Publication P2,*

*reprinted on pages 56–64*

with permission from

***Small* 2022, 18, 2200605,**

DOI: [10.1002/sml.202200605](https://doi.org/10.1002/sml.202200605).

Copyright © 1999–2022 John Wiley & Sons, Inc.

Supporting Information reprinted in Appendix E.

# Revealing and Controlling Energy Barriers and Valleys at Grain Boundaries in Ultrathin Organic Films

Lisa S. Walter, Amelie Axt, James W. Borchert, Theresa Kammerbauer, Felix Winterer, Jakob Lenz, Stefan A. L. Weber, and R. Thomas Weitz\*

In organic electronics, local crystalline order is of critical importance for the charge transport. Grain boundaries between molecularly ordered domains are generally known to hamper or completely suppress charge transfer and detailed knowledge of the local electronic nature is critical for future minimization of such malicious defects. However, grain boundaries are typically hidden within the bulk film and consequently escape observation or investigation. Here, a minimal model system in form of monolayer-thin films with sub-nm roughness of a prototypical n-type organic semiconductor is presented. Since these films consist of large crystalline areas, the detailed energy landscape at single grain boundaries can be studied using Kelvin probe force microscopy. By controlling the charge-carrier density in the films electrostatically, the impact of the grain boundaries on charge transport in organic devices is modeled. First, two distinct types of grain boundaries are identified, namely energetic barriers and valleys, which can coexist within the same thin film. Their absolute height is found to be especially pronounced at charge-carrier densities below  $10^{12} \text{ cm}^{-2}$ —the regime at which organic solar cells and light emitting diodes typically operate. Finally, processing conditions by which the type or energetic height of grain boundaries can be controlled are identified.

## 1. Introduction

Organic semiconductors (OSCs) have enabled a variety of (opto-)electronic devices including organic field-effect transistors (OFETs), organic light emitting diodes (OLEDs), and organic photovoltaics (OPV). Critical performance metrics of these devices are strongly affected by the physical processes that occur at interfaces between layers of different materials, or, different phases within the same material. Examples are the interface between the organic layer and contact metal<sup>[1–3]</sup>; between the OSC and the gate insulator in an OFET,<sup>[4]</sup> or between different OSCs at donor–acceptor interfaces in organic solar cells.<sup>[5]</sup> While such interfaces have been studied in great detail, an interface that is comparably not well understood is the interface between individual (nano-)crystalline domains within an OSC layer of an OLED, OFET or organic solar cell, known as grain boundaries. Inevitable defects

at each of these interfaces can act as sources of trap sites for mobile charge carriers,<sup>[6]</sup> leading to losses in efficiency of transformation of energy excitations in devices,<sup>[7–10]</sup> initial and time-dependent degradation,<sup>[11–13]</sup> hysteresis,<sup>[14,15]</sup> and reduced charge-carrier mobilities.<sup>[4,14,16–18]</sup>

Advances in the fundamental understanding of the physical processes at these interfaces and their potential impacts on charge-carrier transport have therefore been essential for enabling improvements to the performance of all optoelectronic devices based on OSCs. However, the detection and simultaneous electrical characterization of grain boundaries has been challenging due to their inherently statistical nature, small scale, and the fact that they are typically hidden within the organic layer.

The most direct impact of grain boundaries on charge transport is typically investigated in FET devices, which is why most impact of grain boundaries on device performance is reported for FETs.

It has been observed that the existence of grain boundaries affects air and bias stability,<sup>[11,13]</sup> the on–off ratio,<sup>[14]</sup> the threshold voltage,<sup>[14,19]</sup> and leads to hysteresis effects.<sup>[14]</sup> However, the greatest consensus is on the finding that grain boundaries lead to charge-carrier density-dependent,<sup>[20,21]</sup> and overall reduced mobilities.<sup>[16–18,22–24]</sup>

L. S. Walter, T. Kammerbauer, F. Winterer, J. Lenz, R. T. Weitz  
Faculty of Physics  
Ludwig-Maximilians-Universität München  
80539 Munich, Germany

L. S. Walter, J. W. Borchert, R. T. Weitz  
I. Institute of Physics  
Georg-August-Universität Göttingen  
37077 Göttingen, Germany  
E-mail: thomas.weitz@uni-goettingen.de

A. Axt, S. A. L. Weber  
Max Planck Institute for Polymer Research  
55128 Mainz, Germany

S. A. L. Weber  
Institute of Physics  
Johannes Gutenberg-Universität Mainz  
55122 Mainz, Germany

R. T. Weitz  
Center for Nanoscience (CeNS)  
Ludwig-Maximilians-Universität München  
80539 Munich, Germany

 The ORCID identification number(s) for the author(s) of this article can be found under <https://doi.org/10.1002/sml.202200605>.

© 2022 The Authors. Small published by Wiley-VCH GmbH. This is an open access article under the terms of the Creative Commons Attribution License, which permits use, distribution and reproduction in any medium, provided the original work is properly cited.

DOI: 10.1002/sml.202200605

Of course, this mobility reduction does not only influence the performance of FETs but also of OLEDs and OPV because here free charge carriers have to diffuse from(to) the electrodes before(after) exciton recombination (dissociation). Moreover, traps in general have been observed to decrease the efficiency of OLEDs by increasing the rate of nonradiative recombination of electron-hole pairs,<sup>[8,10]</sup> and analogously, the efficiency of OPV by increased recombination rates of excitons, i.e., decreased exciton dissociation.<sup>[7,9,12]</sup> While this general impact on recombination rates and device efficiency can likely be attributed to grain boundaries, it is rarely reported<sup>[25–27]</sup> and grain boundaries are mostly avoided in OLEDs and OPV without further explanation.<sup>[28]</sup>

In this work, we present a model system to study the local contribution of grain boundaries in organic semiconducting devices using Kelvin probe force microscopy (KPFM).<sup>[29–31]</sup> KPFM has proven useful to locally characterize grain boundaries both structurally and energetically,<sup>[32–35]</sup> but until now solely applied to films that are several tens of nm thick and/or exhibiting a high density of grain boundaries. Recently, we have demonstrated a drop-casting method for surface-mediated crystallization yielding monolayer-thin films of the prototypical small-molecule OSC *N,N'*-di((*S*)-1-methylpentyl)-1,7(6)-dicyanoperylene-3,4:9,10-bis(dicarboximide) (PDI1MPCN2) with sub-nm roughness even across well-defined grain boundaries and large areas that can be understood as single crystalline thin films.<sup>[36]</sup> While this drop-casting method in its current form is not suitable for large-scale processing, it is sufficient for the current investigations where sample dimensions below 1 cm<sup>2</sup> are required. The high purity of the resulting films is comparable to recent works focusing on low-dimensional organic crystals as the active layer in, e.g., OFETs,<sup>[37–40]</sup> and allows precise examination of the surface potential of individual grain boundaries. In particular, this allows detailed local electrostatic examination of grain boundaries and thereby enables identification of the mechanisms by which grain boundaries can affect charge transport. In addition, using electrostatic gating, the charge-carrier density in the monolayer-thin films can be tuned in situ up to  $\approx 10^{12}$  cm<sup>-2</sup>, allowing measurements of the energetics at grain boundaries at charge-carrier densities relevant in organic solar cells (operated typically at charge-carrier densities of  $10^9$ – $10^{10}$  cm<sup>-2</sup>),<sup>[41,42]</sup> OLEDs ( $10^{10}$ – $10^{11}$  cm<sup>-2</sup>),<sup>[7]</sup> and OFETs ( $10^9$ – $10^{12}$  cm<sup>-2</sup>).<sup>[4]</sup>

## 2. Surface Potential Within A Single Crystal Grain

A schematic of the measurement setup and the devices under investigation is shown in **Figure 1a**. The samples consist of a PDI1MPCN2-covered Si/Al<sub>2</sub>O<sub>3</sub> wafer (see the Experimental Section for fabrication details). The organic films are characterized by large, highly crystalline grains, separated by well-defined grain boundaries (e.g., cf. **Figure 2**).<sup>[36]</sup> According to X-ray diffraction measurements, films of 1.8 nm thickness correspond to monolayers.<sup>[36]</sup> In the shown setup, the charge-carrier density  $n$  in the PDI1MPCN2 thin films can be tuned precisely by the gate voltage  $V_{GS}$ . Its impact on the surface potential  $U_{SP}$  is detected after reaching electrostatic equilibrium, that is, no additional electric field is applied parallel to the molecular layer

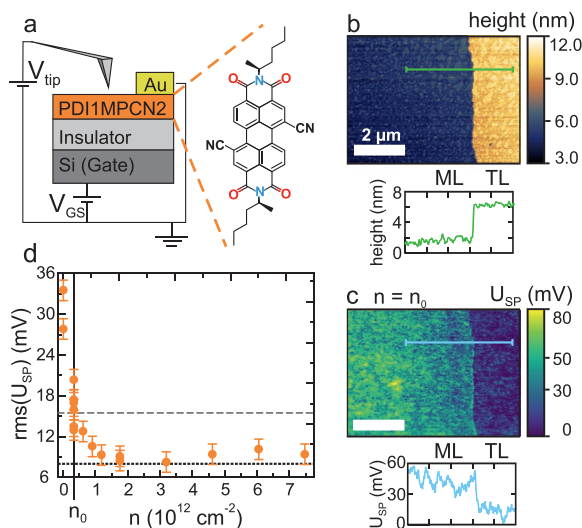


**Figure 1.** Detection of the surface potential under varying charge-carrier density. a) Scheme of the device geometry and the measurement setup. b,c) Topography and surface potential at zero external charge-carrier density  $n_0$ , respectively, with profiles across the indicated lines and indicated position of monolayer (ML) and trilayer (TL). d) Charge-carrier density-dependent rms( $U_{SP}$ ). Data were extracted from the scans shown in Figure S2 in the Supporting Information. The gray dashed line is the mean value of rms( $U_{SP}$ ) at  $n_0$  taken from (c) and serves as a reference. The black dotted line is the resolution limit taken from Figure S1 in the Supporting Information. Data points are the rms value extracted from a slab of 0.5  $\mu\text{m}$  in the  $y$ -direction; the errors are estimated to 1.5 mV due to extraction uncertainties in the choice of the slab width. All scale bars are 2  $\mu\text{m}$ .

and we have not performed time-dependent measurements on electric charging or current flow. The surface potential  $U_{SP}$  is the sum of the potential induced by  $V_{GS}$  and the contact-potential difference (CPD)  $U_{CPD}$  measured at  $V_{GS} = 0$  (see the Supporting Information for details). If  $V_{GS} = 0$ , no external charge carriers are induced in the OSC and we refer to zero external charge-carrier density  $n = n_0$ . In the following, measurements at  $n_0$ , where  $U_{SP} = U_{CPD}$ , serve as reference for measurements with increased charge-carrier density.

As baseline for our measurements, we first discuss the surface potential within a crystalline grain of the PDI1MPCN2 monolayer-thin film. A typical topography and surface-potential map of such a region including a monolayer-trilayer step is shown in **Figure 1b,c**. The topographical smoothness of the clean solution-deposited thin-films can be discerned by the small values for the rms roughness of 0.6 nm. To quantify the variation of the surface potential within a single grain, the rms( $U_{SP}$ ) was extracted, e.g. to 15 mV for the scan at  $n_0$  (dashed line in **Figure 1d**). Since the detected potential landscape does not change during subsequent scans and is well above the noise level of 8 mV (**Figure S1**, Supporting Information), it can be attributed to defects or charge inhomogeneities at the semiconductor-dielectric interface. This is consistent with the observation that OSC films on Al<sub>2</sub>O<sub>3</sub> show smaller rms( $U_{SP}$ ) than films on SiO<sub>2</sub> (see **Table S1**, Supporting Information), highlighting the role of the substrate.

The surface-potential variations can be understood as energetic disorder which may hinder charge-transport even within

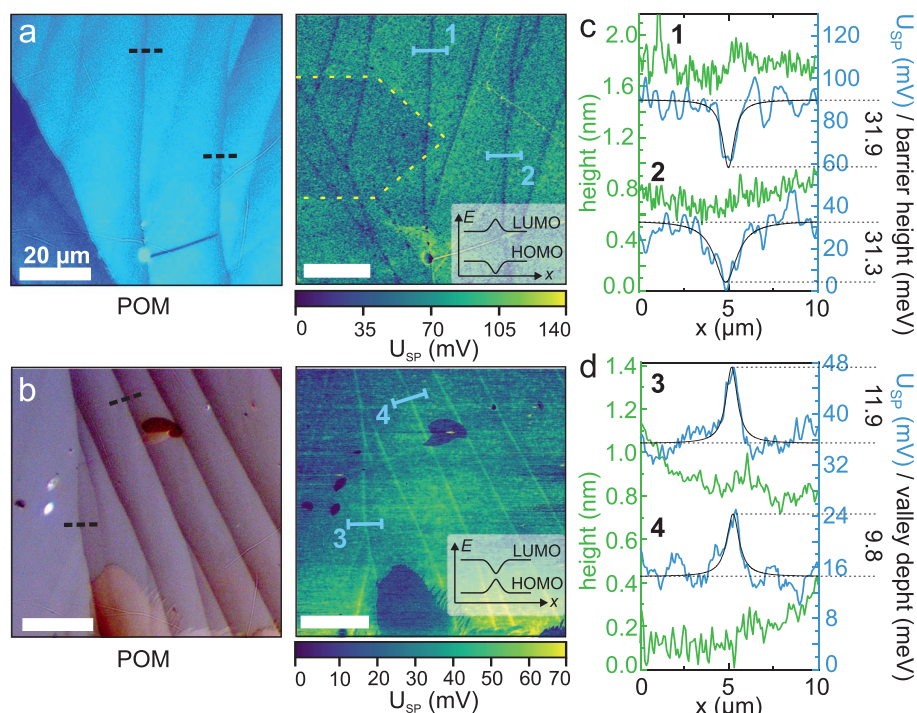


**Figure 2.** Kelvin probe force microscopy at grain boundaries. a,b) POM image (left) and surface potential (right) at two positions of a monolayer film displaying (a) barriers and (b) valleys at  $n_0$ . The insets show the schematic of HOMO and LUMO for the barrier and valley, respectively. The visible shadow of the cantilever highlighted by the yellow dashed line is discussed later in the main text. c,d) Extracted profiles of topography (cf. Figure S5, Supporting Information) and surface potential along the shown lines in (a) and (b), respectively, with Lorentzian fits and calculated barrier heights (fit error 0.7 meV) and valley depths (fit error 2.7 meV), respectively. The graphs are artificially offset for clarity. All scale bars are 20  $\mu\text{m}$ .

single grains and thereby lead to a reduction of charge-carrier mobility. To study the impact of the observed surface-potential variations on charge transport, we increased the charge-carrier density by electrostatic gating and detected the change in  $\text{rms}(U_{\text{SP}})$ , shown in Figure 1d. If  $n$  is increased above  $n_0$  (by application of a positive  $V_{\text{GS}}$ ), the  $\text{rms}(U_{\text{SP}})$  is found to decrease until saturating above  $n \approx 2 \times 10^{12} \text{ cm}^{-2}$  to the resolution limit, while it increases significantly if  $n$  is reduced to zero due to the absence of screening caused by the depletion of charge carriers within the film. Since we are able to tune the charge-carrier density between  $n = 0$  and above  $10^{12} \text{ cm}^{-2}$ , our investigations are performed under conditions in which OLEDs, OFETs and organic solar cells typically operate. Especially in the density region below  $10^{12} \text{ cm}^{-2}$  (typical for OLEDs and organic solar cells), notable surface-potential variations are present, even though our films are highly crystalline. It can be expected that the potential landscape of OSCs in OLEDs and organic solar cells shows even higher energetic disorder and therefore a stronger impact on charge-carrier mobility, as these films are typically disordered.

In passing we note, that at the step edge, no spike in the surface potential is present as has been found by KPFM in bulk single crystals.<sup>[43]</sup> Instead, the trilayer shows an overall smaller surface potential than the monolayer (cf. Figure S4, Supporting Information). This can be attributed to screening of the built-in gate potential by the sheet of mobile charges that forms in the molecular layer close to the insulator.<sup>[44]</sup> This is further

confirmed by the observation that in the absence of screening, i.e., at  $n = 0$ , the potential step at the monolayer-trilayer transition disappears (cf. Figures S2, S4, Supporting Information).

### 3. Surface Potential at Grain Boundaries

In Figure 2, we show a polarized optical microscopy (POM) image and a KPFM scan at  $n_0$  of two exemplary monolayer-thin regions of the PDIIMPCN2 film including grain boundaries. The corresponding topography scans are displayed in Figure S5a,b in the Supporting Information. From the given line profiles in Figure 2c,d across four representative grain boundaries, it becomes clear that the grain boundaries observable in POM are not accompanied by a change in film height. This is in direct contrast to OSC films evaporated onto insulating substrates, which predominantly display some degree of 3D island growth with a high density of step edges during the sub-monolayer growth stage before connected monolayers can grow to cover a significant area.<sup>[32,34,35]</sup> Here, only the KPFM scans in Figure 2 clearly reveal the grain boundaries by a contrast in the CPD and a dip or a peak in the line profile. The CPD contrast can be translated into a local work-function variation and therefore to the bending of the semiconductor's highest occupied molecular orbital (HOMO) and lowest unoccupied molecular orbital (LUMO). Moreover, a clear differentiation can be made between grain boundaries showing a smaller

CPD than surrounding grains (called barriers in the remainder, Figure 2a,c) and those with higher CPD (called valleys, Figure 2b,d). Finally, we would like to point out that in thicker films on the same substrate (bottom of Figure 2b) even though grain boundaries are visible in the POM images, they are not visible in KPFM (compare also Figure S5c, Supporting Information). Hence, grain boundaries in films that are several tens of nm thick and therefore suitable for OLEDs and OPV cells, will likely not be identifiable with this technique. This finding underlines that monolayer films are an ideal model system to investigate energetics at grain boundaries.

Grain boundaries of different type (i.e., barriers and valleys) have been theoretically predicted, e.g., for pentacene thin films,<sup>[45]</sup> and monolayers of PDIIMPCN2,<sup>[46]</sup> but have not been observed in experiment. Specifically, the HOMO and LUMO at grain boundaries bend in an inverted manner,<sup>[46]</sup> i.e., barriers are characterized by upward(downward) bending of the LUMO (HOMO), resulting in an increased band gap (cf. inset of Figure 2a), and vice versa for valleys (inset of Figure 2b). This is the reason for the above assignment of barriers(valleys) to grain boundaries with a smaller(higher) CPD than surrounding grains (see the Supporting Information for a full derivation). In experiments however, it has not been clear if measured differences in CPD at grain boundaries are due to processing conditions,<sup>[6,23,47]</sup> the sign of trapped charges,<sup>[17,19]</sup> the n- or p-type character of the semiconductor,<sup>[32]</sup> or variations in the film thickness.<sup>[34]</sup> Our measurements reveal that none of these conditions can be the only determining factor for the existence of barriers or valleys, since all our films are deposited under similar conditions and are smooth across the grain boundaries. **Figure 3** even displays both types in the same film. To our knowledge, this is the first time that the theoretically predicted coexistence of two distinguishable types of grain boundaries was experimentally proven.

To quantify the differences between valleys and barriers, we determined valley depths and barrier heights by extracting the difference of the CPD between grain boundaries and neigh-

boring grains<sup>[48]</sup> (for evaluation details see Section C in the Supporting Information). While valleys act as traps thereby leading to a reduction of the mobility,<sup>[6,49]</sup> just recently it was shown that barriers impede charge transport more significantly than valleys due to a back-reflection of charges.<sup>[46]</sup> Because of these different mechanisms of trapping and backscattering, previous reports on “barrier heights” or “trap depths” determined by c-AFM,<sup>[19]</sup> or activated charge-transport,<sup>[50]</sup> can only refer to trap-like grain boundaries, that is, valley depths. As indicated in Figure 2 and **Figure 4**, we find valley depths around 10–20 meV and barrier heights from 30 to 60 meV. Note that the valley depths and barrier heights given here, in contrast to transport measurements, do not include transport-limiting factors such as contact resistance or trapping at the semiconductor-insulator interface. Additionally, it is per se unclear how the process of backscattering of charge carriers at barrier-like grain boundaries will show up in activation measurements.

#### 4. Impact of Charge-carrier Density on Barrier Height and Valley Depth

OLEDs and organic solar cells operate at different charge-carrier densities ( $10^9$ – $10^{11}$  cm<sup>-2</sup>),<sup>[7,41,42]</sup> than OFETs ( $10^{12}$  cm<sup>-2</sup>).<sup>[4]</sup> Since absolute values of the observed barrier heights and valley depths have been predicted to decrease with increasing charge-carrier density,<sup>[21]</sup> a careful analysis of the barrier height/valley depth at different charge-carrier densities is required. This investigation will help to assess the respective relevance of grain boundaries for charge transport in the different device types. To this end, we have used two strategies of charge-carrier density control, namely electrostatic gating and photoexcitation. Please note that the influence of only one type of charge carrier is investigated within one experiment (electrons in electrostatic gating and holes via optical excitation, cf. Section D, Supporting Information), so that the results are relevant to transport processes in OFETs and in OLEDs(OPV) before(after) exciton formation(separation). Even more, both injection strategies are assumed to be reversible processes, that is, the surface potential reaches its original distribution after discharging the thin film.

Figure 4 displays KPFM scans of areas with a barrier (Figure 4a) and three valleys (Figure 4c), where the charge-carrier density was increased electrostatically, analogously to the measurements for the single grain shown above. The barrier heights and valley depths clearly decrease with increasing charge-carrier density, and completely disappear in the noise floor at the highest investigated charge-carrier densities. We anticipate that the processes leading to the disappearance of valleys and barriers differ for the two types: In valleys, the electrons are trapped due to the band bending where they act as repulsive sites for subsequently injected electrons,<sup>[45]</sup> thereby making the valley itself energetically less favorable. This is equivalent to the flattening of the LUMO and a decrease of the CPD contrast between grain and grain boundary, i.e., a reduction of the valley depth up to its complete disappearance as seen in Figure 4b,d (for line profiles see Figures S6 and S7, Supporting Information). Conversely, electrons are backscattered from barriers and remain within the energetically more favorable grains,<sup>[21,51]</sup> and raise the LUMO levels of the grains

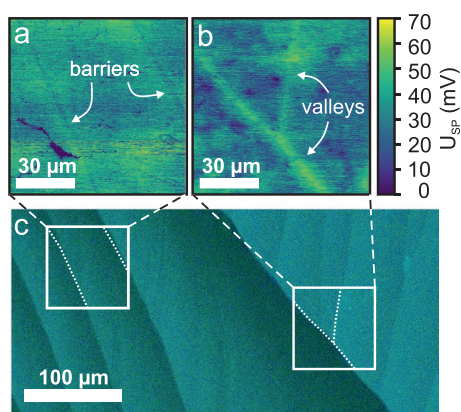


**Figure 3.** Coexistence of barriers and valleys. a) Surface potential of two barriers. b) Surface potential of two valleys. c) POM image of a thin film of PDIIMPCN2, where the areas of (a) and (b) and the courses of the respective grain boundaries are marked. A large-scale scan was performed to exclude degradational effects, shown in Figure S11 in the Supporting Information.

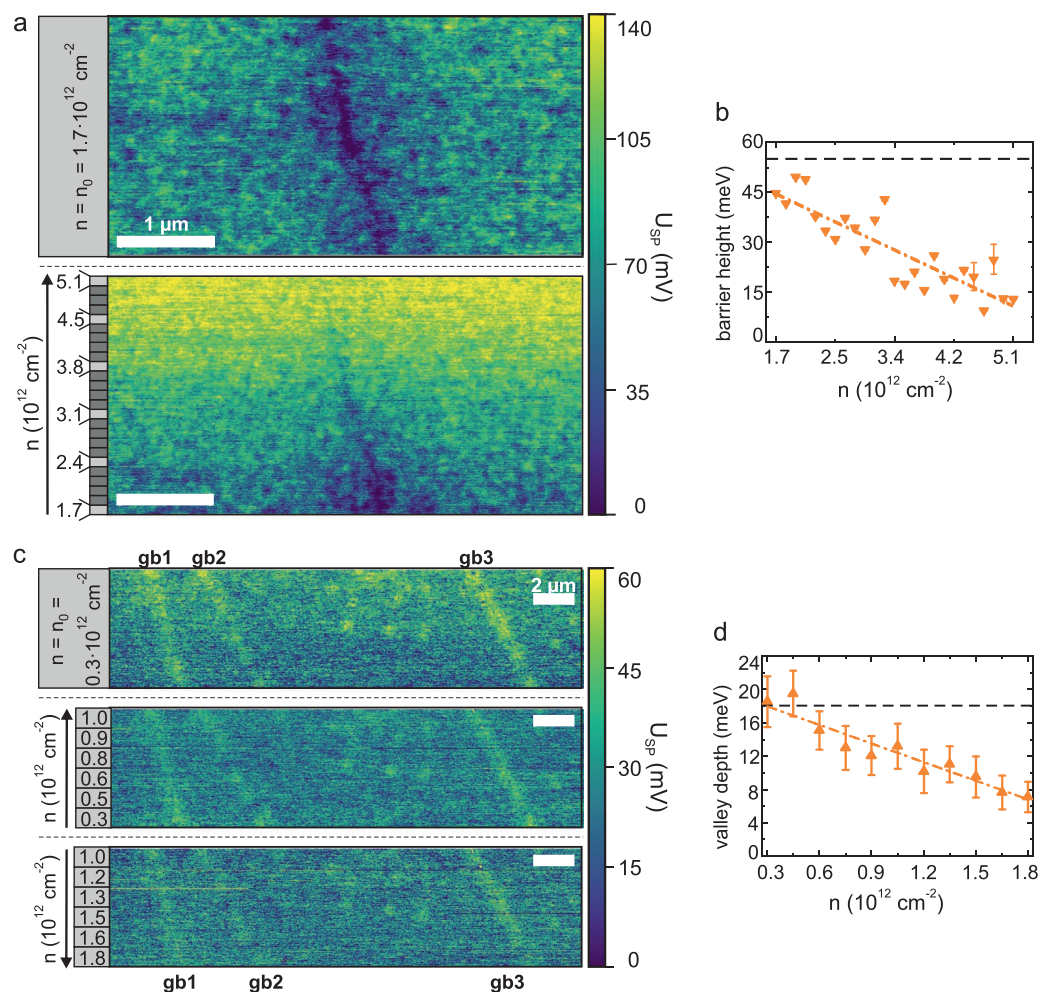


**Figure 4.** Charge-carrier density dependent barrier height and valley depth. a) KPFM scan of a barrier at  $n_0$  (top) and varying electron density as indicated (bottom). The arrow corresponds to the scan direction; scale bars are  $1 \mu\text{m}$ . b) Barrier height extracted from (a) as function of electrostatically induced charge-carrier density. The dashed line is the mean barrier height at  $n_0$ . The dashed-dotted line serves as guide to the eye. c) Surface potential of three valleys at  $n_0$  (top) and varying charge-carrier density as indicated (middle, bottom). Arrows indicate the scan direction; scale bars are  $2 \mu\text{m}$ . A plane level fit was done for the figures with varying  $n$ , but further evaluation was conducted with nonflattened images. d) Valley depth of gb3 as function of electrostatically induced charge carrier density. The dashed line is the mean valley depth at  $n_0$ . The dashed-dotted line serves as guide to the eye. Each data point was extracted from Lorentzian fits at line profiles leveled over a) 15 or c) 35 lines; errors are calculated from fit errors using error propagation. For evaluation details see the Supporting Information.

until the bands are flat,<sup>[52]</sup> and the energetic landscape for all following electrons is the same for grains and valleys.

Notably, the barriers and valleys are only screened if the electrostatically induced charge-carrier density increases to values above  $10^{12} \text{ cm}^{-2}$ . While OFETs are typically operated at such high charge-carrier densities, OLEDs and organic solar cells typically operate at  $n < 10^{11} \text{ cm}^{-2}$  and therefore barriers and valleys, as well as charge inhomogeneities within the film, will significantly impact charge transport in these devices.

So far, we have successfully demonstrated the impact of electrons on the energetic landscape by injecting them electrostatically. Since in OLEDs and organic solar cells it is also possible that small densities of holes accumulate in the electron-conducting film, which then act as recombination sites for subsequently injected electrons, we further studied the impact of a

small density of holes on the potential distribution. However, the electrostatic injection of holes into PDIIMPCN2 is hindered by the high hole-injection barrier of gold, the small HOMO-overlap in PDIIMPCN2, as well as deep hole traps at  $6.0 \text{ eV}$  (the  $E_{\text{HOMO}}$  of PDIIMPCN2 is  $6.74 \text{ eV}$ <sup>[53]</sup>) localized in clusters of residual water,<sup>[54]</sup> small amounts of which can be present in our inert atmosphere.<sup>[55]</sup> Therefore, we illuminated our samples with a standard halogen lamp ( $150 \text{ W}$ ) to form excitons in the OSC thin film (cf. Table S2, Supporting Information), part of which are separated into electrons and holes by the built-in potential at the insulator–semiconductor interface or within the semiconductor. Since our data are consistent with no additional electrons in the film, as we will discuss below, we anticipate that the optically induced electrons are drained by water ions.<sup>[56]</sup> To directly compare the pristine to the slightly hole-doped film,

we have shadowed part of the film with the approached cantilever during illumination and mapped the potential landscape in the dark subsequently (Figure 2a and Figure S8, Supporting Information). Notably, the surface potential increases by 20 mV in the illuminated part, while neither the  $\text{rms}(U_{\text{SP}})$  nor the barrier height seem to be affected by the small density of induced charge carriers (cf. Figure S9, Supporting Information). The increased  $U_{\text{SP}}$ , the sharpness, as well as the observed stability of the potential difference over several hours in the dark, are consistent with an increased density of immobile positive charge carriers generated by light (that are most likely trapped in deep traps in the film). We assume that these hole traps are the same that have previously been identified by transport measurements,<sup>[54]</sup> now first observed in real space by our measurements. Since those traps are presumably located not in the OSC molecules and deeper in energy compared to the potential irregularities within single grains or at grain boundaries, the density of trapped holes increases homogeneously in the entire organic thin film and the barrier heights remain constant. Our measurements thus reveal that while trapped minority carriers will act as recombination sites for majority carriers, they do not change the energetics at the grain boundaries.

## 5. Toward Controlling Energetics at the Grain Boundary Through Processing

A final point pertains the question how the grain boundaries acting as valleys or barriers emerge physically. Identifying the structural cause and/or the parameters in film formation leading to valleys or barriers would be helpful to improve future OSC devices. It is known, that the direct surrounding of each molecule changes its polarization energy,<sup>[6]</sup> and consequently, structural changes such as differences in local packing and/or a change in the distance of the molecules across a grain boundary can lead to locally varying HOMO-LUMO gaps. While the resolution of our measurements is not high enough to resolve the local molecular orientation within a grain, we have found examples in which noticeable dips in the topography of about 0.5 nm were visible (Figure S10, Supporting Information) going along with barriers in the energetic landscape (none were found for valleys). This indicates that larger intermolecular distances can lead to barriers, which is consistent with results obtained by simulations of the polarization field and charge-quadrupole interaction energies across grain boundaries in pentacene films.<sup>[45]</sup> However, we also found barriers in other parts of the film without such dips in the topography, indicating that also changes in molecular orientation, lowering the orbital overlap between neighboring molecules, can lead to both types of grain boundaries as proposed by theoretical calculations.<sup>[45,46]</sup>

In order to find a link between the film formation and the emergence of valleys and barriers, we have investigated the surface potential at 30 positions on 12 individual thin films, and related it to the processing conditions (Section E, Supporting Information). Doing so, we found a relation between the nature of the grain boundaries within a thin film and its shape, emerging from the thin-film fabrication. During the deposition process, a solution of PDI1MPCN2 is drop-cast onto the substrate where the outline of the droplet can pin at its ini-

tial position due to the surface energy contrast on a patterned substrate.<sup>[36]</sup> While circular spots with a homogeneous outline are obtained from such pinned droplets, a smeared noncircular film with wavy or uneven borders can emerge if the droplet does not pin but moves or shrinks while drying. Using these definitions, we found solely valleys in perfectly pinned films and only barriers in depinned (smeared) films. Even more, both types of grain boundaries could be observed within the same organic thin film (Figure 3) in a region between a pinned and a smeared part (cf. Figure S11, Supporting Information). This implies that the complex and not yet fully understood dynamics of thin film crystallization during the PDI1MPCN2 deposition determines the type of the grain boundary. Summarizing, we can a priori control if a thin film will contain only one type of grain boundary by choosing the processing conditions such that the drop-cast solution will pin or smear while drying.

In this context, the substrate only plays a minor role: as mentioned before, we observed that the roughness of the film only impacts the energetic disorder and therefore the  $\text{rms}(U_{\text{SP}})$  of the crystalline areas of the films (also compare Table S1, Supporting Information). However, we could observe both pinned and smeared films, and therefore also the emergence of barriers and valleys, on two different insulators, that is, silicon oxide and aluminum oxide (cf. Table S3, Supporting Information).

Finally, we observed that the solvent choice impacts the energetics at grain boundaries. Overall, less pronounced valleys and barriers at grain boundaries were measured in films produced from toluene-containing solutions (see Figures S12 and S13 and Table S3, Supporting Information).

In passing we note that an idealized thin-film fabrication can be formulated by the aim to achieve films without barriers (as they hinder charge transport more effectively than valleys<sup>[46]</sup>), as few valleys as possible with the smallest possible depth, and as smooth as possible crystal grains. According to our observations, these films are obtained by perfectly pinned droplets containing toluene on smooth substrates. This summary matches with the preparation methods originally suggested for this molecule, as such films have consistently shown increased mobilities.<sup>[36]</sup>

## 6. Conclusion

By using high-sensitivity heterodyne KPFM imaging of grain boundaries within a monolayer thin, highly crystalline organic semiconducting PDI1MPCN2 film, we were able to identify energetic barriers and valleys at grain boundaries, define thin-film processing conditions under which they emerge, and investigate their behavior under electrostatically controlled charge-carrier density. The use of monolayer-thin films was essential to characterize the highly pure, well-defined single grain boundaries in a minimal model system under inert and reversible conditions. By tuning the charge-carrier density electrostatically, we could simulate the impact on charge transport during the operation of organic semiconductor devices. From the different energetic distributions of the two grain-boundary types, we were able to separate the different mechanisms of trapping at valleys and backscattering at barriers at charge-carrier densities less than  $10^{12} \text{ cm}^{-2}$ . This importantly corresponds

to the density range where OLEDs and OPV cells typically operate, thus highlighting the role of grain boundaries as well as potential irregularities in the thin films that lead to a suppression of charge transport in these systems. Likewise, OFETs will be significantly impacted in the transition between the “on” and “off” states of the transistor where low charge-carrier densities are also present.

We have focused our work on a prototypical perylene-diimide semiconductor, an organic dye which is often used in optoelectronic devices, but the general concept of valleys and barriers and their presence in thin films may also hold for other materials used as transport layers in OLEDs, OPV, and OFETs. In addition, the insights from this work may prove useful for researchers investigating charge transport in other optoelectronic materials systems such as perovskites,<sup>[57]</sup> metal oxides,<sup>[58]</sup> and transition metal dichalcogenides,<sup>[59,60]</sup> where grain boundaries might occur and lead to loss in transport or energy transformation processes.

## 7. Experimental Section

**Sample Preparation:** The n-type OSC used in this work is the core cyanated perylene diimide *N,N'*-di((S)-1-methylpentyl)-1,7(6)-dicyanoperylene-3,4,9,10-bis(dicarboximide) (PDI1MPCN2) shown in Figure 1a, whose crystallization behavior, mechanical, and electrical properties have been investigated before.<sup>[4,36,46,61,62]</sup> The preparation of monolayer-thin films by drop-casting was presented and established in previous work<sup>[36]</sup> and accordingly used here as follows: 15 × 20 mm<sup>2</sup>-sized substrates of highly doped silicon with 30 nm Al<sub>2</sub>O<sub>3</sub> or 300 nm SiO<sub>2</sub> were cleaned in acetone and isopropanol for 10 min each and by a subsequent etching step in an oxygen plasma at 50 W for 7 min (Diener Pico Plasmacleaner). The substrates were coated with a tetradecylphosphonic acid (TDPA, used for Al<sub>2</sub>O<sub>3</sub> substrates) or octadecyltrichlorosilane (ODTS, used for SiO<sub>2</sub> substrates) SAM, respectively, from which circles of 5 or 6 mm diameter were etched away using the same conditions as before. A solution of 0.1 wt% PDI1MPCN2 (BASF) in DMP or DMP:Toluene mixtures was dissolved, stirred, filtered, and drop-cast onto the etched circles. The samples were dried on a hotplate at 70 °C over night. Also see Figure S13 and Table S3 in the Supporting Information for details on how to achieve pinned or smeared films. As proposed by previous XRD measurements (cf. the Supporting Information of ref. [36]), to assure mono- (1.8 nm thickness) to bilayer (3.6 nm) thin films, the step height was measured down to the substrate for some samples using AFM (Bruker Dimension 3100) in tapping mode. 40 nm Au were thermally evaporated before(after) dropcasting in order to build bottom gate bottom(top) contact devices.

**Optical Characterization:** Grain boundaries were located using POM (Zeiss Axio Scope.A1) and a complete spot of the organic thin film was mapped. Large crystallites at the border and in the middle of the drops as well as thicker layers served as guides during KPFM measurements and for assembling the taken pictures to the overview images.

**KPFM Measurements:** All KPFM measurements were performed as sketched in Figure 1a in an Argon glove box at 26 °C to avoid bias stress and degradational effects (while perylene diimides are generally known to show minimal air degradation,<sup>[63]</sup> stability under bias stress has been observed to increase with the number of grain boundaries and can be assumed to be small at measurements in solution processed thin films<sup>[11,13]</sup>). An Asylum research MFP3D SFM and a Ptlr coated tip (SCM-PIT-V2, with spring constant  $k = 3.0 \text{ N m}^{-1}$ , tip radius  $r = 25 \text{ nm}$ ) were used. The KPFM signal was detected in FM heterodyne mode using a Zurich Instruments HF2 Lock-in amplifier with AC and DC voltage applied to the tip (tip bias). For the exact circuit diagram cf. ref. [31]. The gate voltage was applied via Output 3 of the HF2 Lock-in

amplifier. Source and drain as well as all outer conductors and the glove box casing were set to the same ground. For measurements at  $n_0$ , the gate was set to ground as well. For the light-dependent measurements, samples were used without evaporated contacts, but grounded by silver paste at the border of the sample. The samples with the built-in halogen lamp (150 W) of the AFM camera were illuminated with the tip approached to the surface, then it was turned off and scanning was started. To reduce effects of the ambient light, the glovebox was covered with a curtain. Impact of the detection laser was excluded with a wavelength of 860 nm, as it was turned on all the time, such that the cantilever shadow would not be observed in Figure 2. An overview over differences in the conducted experiments is shown in Figure S8 in the Supporting Information.

**Statistics:** Within the scope of this work, the surface potential was investigated at 30 positions on 12 individual thin films (Table S3, Supporting Information). All presented AFM data were preprocessed using the software Gwyddion,<sup>[64]</sup> by the following procedure: 1) Rows of KPFM scans were aligned by the mean of differences. If necessary, the plane was leveled additionally by mean plane subtraction for a better view of the scans, but data were extracted from nonleveled scans. The lowest point was set to zero. Line-profiles were extracted with a width slightly smaller than the number of lines with constant gate voltage to account for the time-dependent charging effect of the semiconductor.  $\text{rms}(U_{sp})$  values were extracted using the statistics tool of Gwyddion for areas with a corresponding slab width, by varying this width slightly, the error was estimated to 1.5 mV for all extracted  $\text{rms}(U_{sp})$  values. 2) Topography scans were leveled by mean plane subtraction. For large scans ( $>50 \times 50 \mu\text{m}^2$ ) a polynomial background of 2nd order was subtracted additionally. The rows were aligned by a polynomial of 2nd order while extracting high features by a mask tool. The lowest point was set to zero. Line profiles were extracted at the exact same conditions as for the corresponding KPFM scan and compared to them by position. 3) Extracted line profiles across grain boundaries were fitted by a Lorentzian using the software Origin, the mathematical details are described in Section C in the Supporting Information. The given barrier heights or valley depths refer to the fit values, errors are fit errors using error propagation. 4) Charge-carrier densities have been calculated from the applied gate voltage using a plate capacitor model for the field-effect transistor, detailed in Section B in the Supporting Information.

## Supporting Information

Supporting Information is available from the Wiley Online Library or from the author.

## Acknowledgements

L.S.W. and R.T.W. acknowledge funding from the Center for Nanoscience (CeNS) and the SolarTechnologies go Hybrid (SolTech) initiative. The authors additionally acknowledge funding by the Deutsche Forschungsgemeinschaft (DFG, German Research Foundation) under Germany's Excellence Strategy and “EXC 2089/1–390776260 (e-conversion).” The authors additionally acknowledge insightful discussions with PD Dr. B. Nickel and Prof. P. W. M. Blom.

Open access funding enabled and organized by Projekt DEAL.

## Conflict of Interest

While during the cause of the study A.A. was employed at the Max Planck Institute for Polymer Research, currently she is employee at Oxford, the manufacturer of Asylum AFMs such as the one used for this study.

## Author Contributions

The experiments were conceived and designed by L.S.W. and R.T.W. L.S.W. prepared the samples, conducted the measurements and data analysis. A.A. and S.A.L.W. helped with the measurements, T.K. helped with the sample preparation. All authors discussed the data. L.S.W. and R.T.W. wrote the manuscript with the input of all authors.

## Data Availability Statement

The data that support the findings of this study are available from the corresponding author upon reasonable request.

## Keywords

2D-crystals, energy transformation, grain boundary, Kelvin probe force microscopy, organic semiconductors

Received: February 25, 2022

Revised: July 11, 2022

Published online: July 29, 2022

- [1] M. Waldrip, O. D. Jurchescu, D. J. Gundlach, E. G. Bittle, *Adv. Funct. Mater.* **2019**, *39*, 1904576.
- [2] S. Braun, W. R. Salaneck, M. Fahlman, *Adv. Mater.* **2009**, *21*, 1450.
- [3] N. B. Kotadiya, H. Lu, A. Mondal, Y. Ie, D. Andrienko, P. W. M. Blom, G.-J. A. H. Wetzelaer, *Nat. Mater.* **2018**, *17*, 329.
- [4] I. Vladimirov, S. Müller, R.-P. Baumann, T. Geßner, Z. Molla, S. Grigorian, A. Köhler, H. Bässler, U. Pietsch, R. T. Weitz, *Adv. Funct. Mater.* **2019**, *29*, 1807867.
- [5] R. Steim, F. R. Kogler, C. J. Brabec, *J. Mater. Chem.* **2010**, *20*, 2499.
- [6] H. F. Haneef, A. M. Zeidell, O. D. Jurchescu, *J. Mater. Chem. C* **2020**, *8*, 759.
- [7] M.-J. Tsai, H.-F. Meng, *J. Appl. Phys.* **2005**, *97*, 114502.
- [8] R. A. Street, M. Schoendorf, A. Roy, J. H. Lee, *Phys. Rev. B* **2010**, *81*, 205307.
- [9] M. Kuik, G.-J. A. H. Wetzelaer, H. T. Nicolai, N. I. Craciun, D. M. de Leeuw, P. W. M. Blom, *Adv. Mater.* **2014**, *26*, 512.
- [10] S. R. Cowan, A. Roy, A. J. Heeger, *Phys. Rev. B* **2010**, *82*, 245207.
- [11] S. Müller, R.-P. Baumann, T. Geßner, R. T. Weitz, *Phys. Status Solidi RRL* **2016**, *10*, 339.
- [12] S. Scholz, D. Kondakov, B. Lüssem, K. Leo, *Chem. Rev.* **2015**, *115*, 8449.
- [13] R. T. Weitz, K. Amsharov, U. Zschieschang, M. Burghard, M. Jansen, M. Kelsch, B. Rhamati, P. A. van Aken, K. Kern, H. Klauk, *Chem. Mater.* **2009**, *21*, 4949.
- [14] J. Chen, C. K. Tee, M. Shtein, J. Anthony, D. C. Martin, *J. Appl. Phys.* **2008**, *103*, 114513.
- [15] Y. Sun, L. Zhang, Z. Ahmed, M. Chan, *Org. Electron.* **2015**, *27*, 192.
- [16] A. Di Carlo, F. Piacenza, A. Bolognesi, B. Stadlober, H. Maresch, *Appl. Phys. Lett.* **2005**, *86*, 263501.
- [17] A. B. Chwang, C. D. Frisbie, *J. Appl. Phys.* **2001**, *90*, 1342.
- [18] T. Meier, H. Bässler, A. Köhler, *Adv. Opt. Mater.* **2021**, *9*, 2100115.
- [19] T. W. Kelley, C. D. Frisbie, *J. Phys. Chem. B* **2001**, *105*, 4538.
- [20] A. Bolognesi, M. Berliocchi, M. Manenti, A. DiCarlo, P. Lugli, K. Lmimouni, C. Dufour, *IEEE Trans. Electron Devices* **2004**, *51*, 1997.
- [21] G. Horowitz, *Adv. Funct. Mater.* **2003**, *13*, 53.
- [22] H. Kobayashi, Y. Tokita, *Appl. Phys. Express* **2015**, *8*, 051602.
- [23] S. S. Lee, J. M. Mativetsky, M. A. Loth, J. E. Anthony, Y.-L. Loo, *ACS Nano* **2012**, *6*, 9879.
- [24] S. Wo, R. L. Headrick, J. E. Anthony, *J. Appl. Phys.* **2012**, *111*, 073716.
- [25] R. R. Lunt, J. B. Benziger, S. R. Forrest, *Adv. Mater.* **2010**, *22*, 1233.
- [26] K. Shi, A. T. Healy, I. J. Curtin, T. Zhang, D. A. Blank, R. J. Holmes, *J. Phys. Chem. C* **2022**, *126*, 4792.
- [27] S. Caria, E. Da Como, M. Murgia, R. Zamboni, P. Melpignano, V. Biondo, *J. Phys.: Condens. Matter* **2006**, *18*, S2139.
- [28] X. Zhang, H. Dong, W. Hu, *Adv. Mater.* **2018**, *30*, 1801048.
- [29] M. Nonnenmacher, M. P. O' Boyle, H. K. Wickramasinghe, *Appl. Phys. Lett.* **1991**, *58*, 2921.
- [30] V. Palermo, M. Palma, P. Samori, *Adv. Mater.* **2006**, *18*, 145.
- [31] A. Axt, I. M. Hermes, V. W. Bergmann, N. Tausendpfund, S. A. L. Weber, *Beilstein J. Nanotechnol.* **2018**, *9*, 1809.
- [32] K. Puntambekar, J. Dong, G. Haugstad, C. D. Frisbie, *Adv. Funct. Mater.* **2006**, *16*, 879.
- [33] H. Huang, H. Wang, J. Zhang, D. Yan, *Appl. Phys. A* **2009**, *95*, 125.
- [34] S. Yogeve, R. Matsubara, M. Nakamura, Y. Rosenwaks, *Org. Electron.* **2010**, *11*, 1729.
- [35] M. Tello, M. Chiesa, C. M. Duffy, H. Siringhaus, *Adv. Funct. Mater.* **2008**, *18*, 3907.
- [36] I. Vladimirov, M. Kellermeier, T. Geßner, Z. Molla, S. Grigorian, U. Pietsch, L. S. Schaffroth, M. Kühn, F. May, R. T. Weitz, *Nano Lett.* **2018**, *18*, 9.
- [37] S. K. Park, J. H. Kim, S. Y. Park, *Adv. Mater.* **2018**, *30*, 1704759.
- [38] H. Yan, Y. Li, J.-K. Qin, B. Xu, P.-A. Hu, L. Zhen, C.-Y. Xu, *Small* **2021**, *17*, 2007739.
- [39] P. Hu, X. He, H. Jiang, *InfoMat* **2021**, *3*, 613.
- [40] X. Zhang, X. Zhao, L. Rao, J. Zhang, M. Xiao, D. Zhu, C. Li, X. Shi, J. Liu, L. Jiang, *Nano Res.* **2022**, *15*, 858.
- [41] S. Schiefer, B. Zimmermann, U. Würfel, *J. Appl. Phys.* **2014**, *115*, 044506.
- [42] K. Nakano, Y. Chen, K. Tajima, *AIP Adv.* **2019**, *9*, 125205.
- [43] T. He, Y. Wu, G. D'Avino, E. Schmidt, M. Stolte, J. Cornil, D. Beljonne, P. P. Ruden, F. Würthner, C. D. Frisbie, *Nat. Commun.* **2018**, *9*, 2141.
- [44] Y. M. Lee, J. W. Kim, H. Min, T. G. Lee, Y. Park, *Curr. Appl. Phys.* **2011**, *11*, 1168.
- [45] S. Verlaak, P. Heremans, *Phys. Rev. B* **2007**, *75*, 115127.
- [46] I. Vladimirov, M. Kühn, T. Geßner, F. May, R. T. Weitz, *Sci. Rep.* **2018**, *8*, 14868.
- [47] L. H. Jimison, M. F. Toney, I. McCulloch, M. Heeney, A. Salleo, *Adv. Mater.* **2009**, *21*, 1568.
- [48] J. W. Orton, M. J. Powell, *Rep. Prog. Phys.* **1980**, *43*, 1263.
- [49] R. T. Weitz, K. Amsharov, U. Zschieschang, E. B. Villas, D. K. Goswami, M. Burghard, H. Dosch, M. Jansen, K. Kern, H. Klauk, *J. Am. Chem. Soc.* **2008**, *130*, 4637.
- [50] A. K. Hailey, S.-Y. Wang, Y. Chen, M. M. Payne, J. E. Anthony, V. Podzorov, Y.-L. Loo, *Adv. Funct. Mater.* **2015**, *25*, 5662.
- [51] L. G. Kaake, P. F. Barbara, X.-Y. Zhu, *J. Phys. Chem. Lett.* **2010**, *1*, 628.
- [52] X. Li, A. Kadashchuk, I. I. Fishchuk, W. T. T. Smaal, G. Gelinck, D. J. Broer, J. Genoe, P. Heremans, H. Bässler, *Phys. Rev. Lett.* **2012**, *108*, 66601.
- [53] I. Vladimirov, Dissertation, Technische Universität Braunschweig, Braunschweig, Germany **2016**.
- [54] N. B. Kotadiya, A. Mondal, P. W. M. Blom, D. Andrienko, G.-J. A. H. Wetzelaer, *Nat. Mater.* **2019**, *18*, 1182.
- [55] M. Kettner, M. Zhou, J. Brill, P. W. M. Blom, R. T. Weitz, *ACS Appl. Mater. Interfaces* **2018**, *10*, 35449.
- [56] U. Zschieschang, K. Amsharov, M. Jansen, K. Kern, H. Klauk, R. T. Weitz, *Org. Electron.* **2015**, *26*, 340.
- [57] Y. Gao, W. Xu, S.-W. Zhang, T. Fan, M. Zhang, A. Ran, X. Zhang, F. Kang, G. Wei, *Small* **2022**, *18*, 2106083.
- [58] K. Liang, D. Li, H. Ren, M. Zhao, H. Wang, M. Ding, G. Xu, X. Zhao, S. Long, S. Zhu, P. Sheng, W. Li, X. Lin, B. Zhu, *Nano-Micro Lett.* **2021**, *13*, 164. Published Online: Aug. 3, 2021.
- [59] S. Zhang, J. Pang, Q. Cheng, F. Yang, Y. Chen, Y. Liu, Y. Li, T. Gemming, X. Liu, B. Ibarlucea, J. Yang, H. Liu, W. Zhou, G. Cuniberti, M. H. Rummeli, *InfoMat* **2021**, *3*, 1455.

- [60] Y. Wang, J. Pang, Q. Cheng, L. Han, Y. Li, X. Meng, B. Ibarlucea, H. Zhao, F. Yang, H. Liu, H. Liu, W. Zhou, X. Wang, M. H. Rummeli, Y. Zhang, G. Cuniberti, *Nano-Micro Lett.* **2021**, *13*, 143.
- [61] L. S. Schaffroth, J. Lenz, V. Giegold, M. Kögl, A. Hartschuh, R. T. Weitz, *Adv. Mater.* **2019**, *31*, 1808309.
- [62] L. Renn, L. S. Walter, K. Watanabe, T. Taniguchi, R. T. Weitz, *Adv. Mater. Inter.* **2022**, *9*, 2101701.
- [63] C. D. Dimitrakopoulos, P. Malenfant, *Adv. Mater.* **2002**, *14*, 99.
- [64] D. Nečas, P. Klapetek, *Cent. Eur. J. Phys.* **2012**, *10*, 181.

## 5 Grain Boundaries Influence Global Device Parameters of Organic Thin-film Transistors

*The previous chapter presented the finding that grain boundaries in thin films of PDI1MPCN2 can act as energy barriers, that backscatter electrons, or energy valleys, that trap electrons (compare Chapter 4). This chapter investigates the impact of both grain-boundary types on FET device-parameters, such as the turn-on and threshold voltage, as well as hysteresis effects by time-resolved KPFM. It is structured as follows:*

*Section 5.1 introduces and motivates the time-dependent surface-potential measurements, while Section 5.2 presents experimental details on sample fabrication and the measurement setup. Section 5.3 presents and discusses the results in four steps, which are concluded and put into the context of future experiments in Section 5.4. Supporting Information are presented in Appendix F.*

*The experiments and results of this chapter were prepared in collaboration with A. Art, J.W. Borchert, J. Pöhls, S.A.L. Weber, and R.T. Weitz.*

### 5.1 Motivation

Organic semiconductors have been implemented in a wide variety of optoelectronic devices, such as OLEDs [10], organic solar cells [7,8], and organic field-effect transistors [5,6]. The performance of these devices strongly depends on the intrinsic and extrinsic properties of the organic semiconductor(s) used as the active layers. The charge transport in organic semiconductors, in particular, is sensitive to the morphological properties, e.g. crystallization, and the energetic properties, i.e. the frontier highest occupied molecular orbital (HOMO) and lowest unoccupied molecular orbital (LUMO) levels. It is often very difficult to control these properties precisely, leading to a notable persistent challenge in device-to-device reproducibility and variability [27–29]. This can be drawn back to a variety of imperfections, including local variations such as inhomogeneities or grain boundaries between crystallites in a thin film, which can adversely change the energetic landscape in an uncontrollable way [39,96]. Particularly notable examples of the effects of morphology arise in organic transistors in the form of significant threshold voltages and turn-on voltages, both in magnitude and variability, and poor charge-carrier injection into the semiconductor [39,43,154,155]. Detailed characterization of the microscopic properties that lead to these effects is essential for advancing the efficiency of organic electronics and for expanding them into greater varieties of applications.

We recently presented a method for characterizing the detailed effects that grain boundaries have on the energetic landscape in highly-crystalline monolayer organic semiconductors using Kelvin Probe Force Microscopy [Publication **P2**]. Here, we present an expansion of this method to include local, time-resolved measurements that allow the observation of the charging and discharging at different sites in the organic semiconductor.

Our measurements give a first indication that grain boundaries act as deep traps, independent of them being a valley or a barrier. While valleys mainly trap charge carriers within the organic semiconductor due to their smaller LUMO level compared to their surrounding, barriers, that were so-far only assumed to backscatter electrons, trap charge carriers due to band bending at the semiconductor-insulator interface. However, it is mainly the lower-lying LUMO levels of

valleys that are found to influence the global device parameters, mainly the turn-on voltage, since they form an energetically favored pathway in the channel. Hence, we propose that it is not the number of grain boundaries that affects the device performance [39, 40, 70, 156], but the type and depth (or height). To support these findings, more measurements are needed, and we conclude this chapter with an outlook on possible investigations in the future.

## 5.2 Experimental Details

Organic thin-film transistors (TFTs) of PDI1MPCN2 were prepared in a BGBC structure as displayed in **Figure 5.1a**. Substrates of highly-doped silicon and an aluminum oxide layer with a thickness of 30 nm acted as global back-gate electrode and insulating layer, respectively. Gold source and drain contacts were thermally evaporated (BesTec) through a shadow mask. Highly-crystalline monolayers of the organic semiconductor small molecule N,N'-di((S)-1-methylpentyl)-1,7(6)-dicyano-perylene-3,4:9,10-bis-(dicarboximide) (PDI1MPCN2) were deposited from solution using a drop casting method described in previous work [53]. PDI1MPCN2 is an n-type semiconductor that has shown maximum mobilities up to  $4 \text{ cm}^2/\text{Vs}$  [53], [Publication **P5**]. The finalized TFTs are tested in a probe station at ambient to evaluate the global device parameters (results are presented in supplementary **Table F.3**, Appendix F).

To determine the local surface potential  $U_{\text{SP}}$  in the channel region of the organic TFTs, KPFM was detected using an Asylum research MFP3D SFM and a PtIr coated tip (SCM-PIT-V2), compare **Table C.1** in Appendix C. The circuit diagram for frequency-modulated heterodyne KPFM is displayed in Reference [131]. In previous work, we have presented the local surface potential of PDI1MPCN2 at electrostatically or optically injected, varying charge-carrier densities, but in the electrostatic equilibrium [Publication **P2**]. In this work, we present time-dependent measurements to account for the charging and discharging effect in TFTs and their dependence on local impurities and grain boundaries. For this purpose, the AFM tip was held at a constant position, i.e. scanning was turned off, and the time-resolved (resolution 1 second) change of the surface potential upon different gate voltages was detected. All measurements were taken in an Argon glove box to avoid bias stress or degradation effects [40, 41].

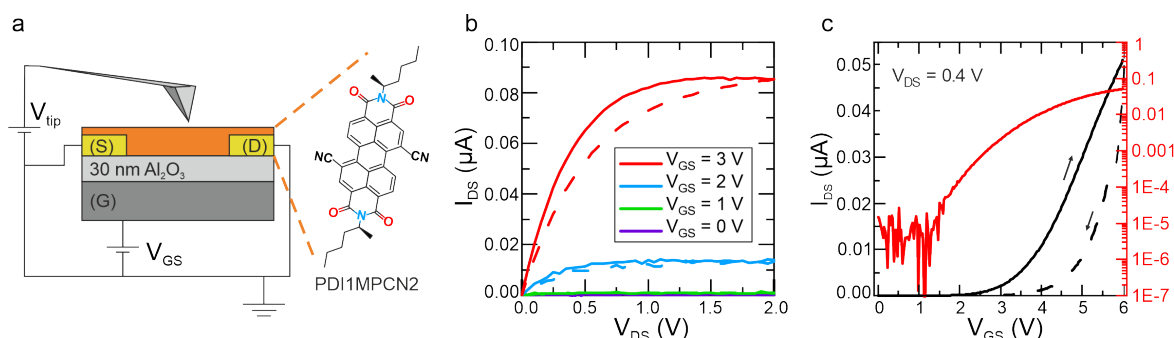


**Figure 5.1 Measurement setup and electric characterization.** **a**, Scheme of the KPFM measurement setup at a BGBC device with source (S), drain (D) and gate (G) electrode, built of the organic small molecule PDI1MPCN2. **b,c**, Output and transfer characteristics of a device identical in construction.

## 5.3 Results and Discussion

### 5.3.1 Time Dependence of the Surface Potential as a Function of Gate Voltage

The surface potential  $U_{\text{SP}}$  was detected for three different classes of sites within the channel region of an organic TFT, which were chosen according to the findings of our previous work: We showed that crystalline grains are characterized by medium and relatively uniform surface potential, separated by grain boundaries that can either act as energetic valleys or barriers. While energy valleys are defined by smaller LUMO levels and higher surface potentials than the grain regions, barriers act vice versa. Regions of different surface potential can also be distinguished in the representative potential scan shown in **Figure 5.2a**, taken at a gate voltage of zero volts, i.e. with no external charges in the semiconductor. Within this scan, we chose three representative sites; one within a grain, a valley and a local impurity with a smaller surface potential than its surrounding, i.e. acting like a barrier for charge carriers.

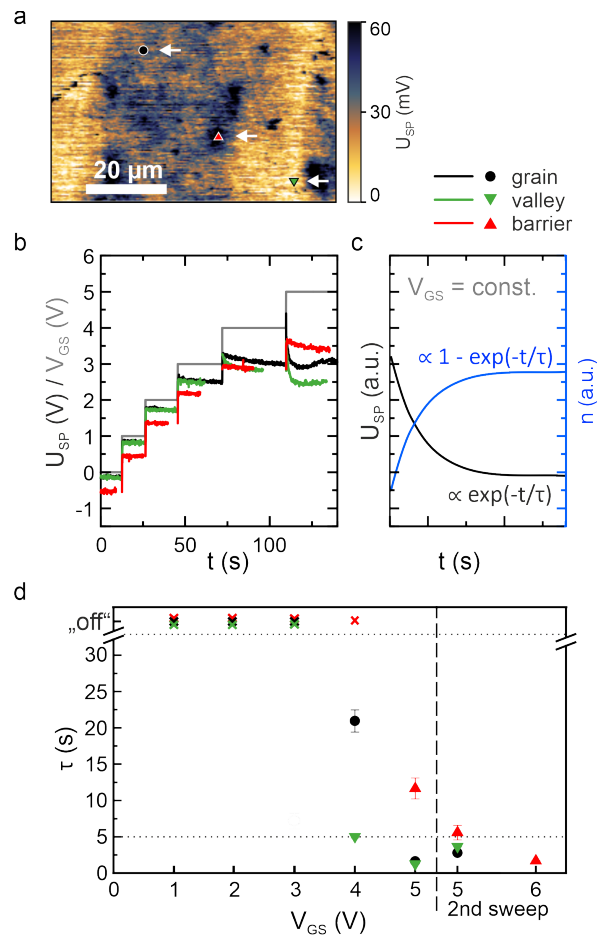


**Figure 5.2** Time dependent surface potential of three different sites and at varying gate voltage. **a** KPFM scan at  $V_{\text{GS}} = 0\text{V}$  displaying the positions of the three different sites investigated within this work. The image was leveled by a plane fit for the ease of view. **b**, Surface potential  $U_{\text{SP}}$  at different gate voltages  $V_{\text{GS}}$  (grey) detected within a grain (black), at an energy valley (green) and an energy barrier (red). **c**, Schematic course of the detected surface potential (black) and the corresponding density of electrically induced free charges  $n$  (blue) as response to a changing gate voltage. **d**, Screening times  $\tau$  extracted from exponential curves in **b** and the curves shown in supplementary **Figure F.7** at  $400 < t < 500\text{s}$ . Constant curves without definable screening time are considered by crosses to visualize the transition between the different time dependencies.

The density of (negative) charge carriers in the semiconductor can be increased by applying a (positive) gate voltage  $V_{GS}$ , which allows to investigate the process of charging/discharging at the different sites within the semiconductor channel. We applied gate voltages between 0 and 7 V and detected the surface potential until it stabilized, then increased/decreased the gate voltage in steps of 1 V. The complete measurement took 750 seconds, within which we applied two cycles of increasing and decreasing gate voltages. Supplementary **Figure F.7** displays the complete measurement as well as the simultaneously detected signal noise (corresponds to the resolution limit) and height, which underline the stability and precision of the procedure. First, we investigate the transition from the „off“ to the „on“ state of the TFT, represented by a successive increase of the gate potential within the first 160 seconds. The measured surface potentials are presented in **Figure 5.2b**, revealing not only an increase in absolute value, but also a change in the time dependence for increasing gate voltages at all three sites. At gate voltages below 3 V, the surface potential is nearly constant and increases by steps of approximately 1 V, in accordance with the increasing gate voltage. On the contrary, gate voltages above 3 V reveal an exponential behavior at each site analogous to the response of an  $RC$ -circuit. Such an  $RC$ -like behavior represents the charging of a plate capacitor, a common model to explain the working principle of field-effect transistors [85]. Hence, the exponential time dependence of the surface potential as a response to the increasing gate potential displays the charging of the semiconducting layer by the induced charge carriers. This behavior is in clear contrast to the observed time independence at small gate voltages, which represents the off-state of the TFT. In this operation regime, the gate potential is completely detected by the AFM tip, since no free charge carriers are induced into the semiconductor to screen the gate potential. The absence of charge carriers can be due to contact resistance [25], mismatch between the gate’s work function and the transport level of the semiconductor [58], and/or (positively charged) traps at the interfaces between layers or in the semiconductor itself [39]. In organic TFTs, these effects are summarized in a turn-on voltage  $V_{on}$ , which has to be overcome by a sufficient  $V_{GS}$  to induce free charge carriers into the semiconductor, and a threshold voltage  $V_{th}$ , above which a conductive channel is formed between source and drain [90, 154, 155, 157]. Analogously, we introduce a local turn-on voltage  $V_{on}^{local}$  and a local threshold voltage  $V_{th}^{local}$  for each site to describe the transition from no charge carriers (i.e. constant surface potential) to accumulated charges within the channel. In our previous work, we observed that electrostatically-injected charge carriers smoothen the energetic distribution at gate voltages above the threshold voltage, resulting in a constant surface potential across grain boundaries and impurities. Since remarkable differences between the grain, the valley and the barrier are visible in **Figure 5.2b**, we attribute the transition from constant surface potential to  $RC$ -like time-dependence to a local turn-on voltage  $V_{on}^{local}$  as

$$U_{SP}(t, V_{GS}) \propto \begin{cases} t : & V_{GS} < V_{on}^{local}, \\ \exp(-\frac{t}{\tau}) : & V_{GS} > V_{on}^{local}. \end{cases} \quad (5.49)$$

The time constant  $\tau$  can be regarded as „screening time“ and corresponds to the time-dependent density of charge carriers in the channel as  $n \propto 1 - \exp(-\frac{t}{\tau})$  (sketched in **Figure 5.2c**).

### 5.3.2 Extraction of Screening Times and Local Threshold Voltages

Different time dependencies of the surface potential could be observed previously by KPFM in polymer transistors [158], but were not explicitly investigated for energetically different sites. To describe the site and time dependence of the surface potential, and to extract values

for  $V_{\text{on}}^{\text{local}}$  and/or  $V_{\text{th}}^{\text{local}}$ , we introduce a „screening factor“  $\beta$  with  $0 \leq \beta \leq 1$  and express the surface potential by

$$U_{\text{SP}} = U_{\text{CPD}} + (1 - \beta)V_{\text{GS}}. \quad (5.50)$$

$U_{\text{CPD}}$  is the contact potential difference (CPD) arising from different work functions of the AFM tip and the organic semiconductor [131,134,135], while the second term of Equation (5.50) describes the unscreened part of the back-gate potential [135,159,160]. The gate potential is completely detected by the AFM tip if no external charge carriers are within the semiconductor and  $\beta = 0$ , while its contribution vanishes if  $\beta = 1$ , and charges are accumulated within the transistor channel, i.e.  $V_{\text{GS}} > V_{\text{th}}^{\text{local}}$ . While we have introduced  $\beta$  as site-dependent parameter, it also contains global device parameters, such as contact resistance, capacitive effects or trapping at the semiconductor-insulator interface, which suppress optimal charge injection and screening. The ideal case of  $\beta = 1$  is therefore unlikely in real devices and  $\beta$  will more likely remain at values below 1.

Since  $\beta$  is related with the charge-carrier density, it exhibits the same time and  $V_{\text{GS}}$  dependence and the above introduced values have to be understood as saturation values reached after the screening time  $\tau$ . This screening time can only be defined reasonably if  $V_{\text{GS}} > V_{\text{on}}^{\text{local}}$  (according to Equation (5.49)), and we expect it to decrease with increasing  $V_{\text{GS}}$  down to a minimum value reached as soon as  $V_{\text{GS}} > V_{\text{th}}^{\text{local}}$  and  $\beta = \beta_{\text{max}}$ .

We used these relationships (summarized by supplementary **Figure F.8**) and extracted the screening times for each curve of the surface potential at a constant gate voltage by an exponential fit using the software Origin. The extracted screening times are plotted for different gate voltages in **Figure 5.2d**, where we additionally indicated gate voltages at which no exponential distribution could be fitted to the surface potential. Since these curves, characterized by a constant behavior, represent the off state of the transistor ( $V_{\text{GS}} < V_{\text{on}}^{\text{local}}$ ), the corresponding data points are labeled „off“. Smallest screening times, representing gate voltages above the local threshold voltage ( $V_{\text{GS}} > V_{\text{th}}^{\text{local}}$ ), are found at approximately 5 seconds, since  $\tau$  does not fall below this value once reached, even if the gate voltage is increased further.

The presentation in **Figure 5.2d** allows a rough estimation for the local turn-on and threshold voltages. While we can observe the expected transition from non-defined to medium to minimal time constants for the grain and the barrier, the resolution of the gate voltage is not sufficiently small as to extract exact values for  $V_{\text{on}}^{\text{local}}$  and  $V_{\text{th}}^{\text{local}}$ . However, we clearly find the smallest global turn-on and threshold voltage at the valley, since it reaches its minimal screening time already at  $V_{\text{GS}} = 4 \text{ V}$ , where the grain is still represented by a medium screening time and the barrier’s surface potential is even time independent.

To place the local parameters in a context of global device performance, we compared the data in **Figure 5.2d** to global turn-on and threshold voltages. These were extracted from twelve devices identical in construction on three different semiconducting films to  $V_{\text{on}} = (1.9 \pm 1.4) \text{ V}$  and  $V_{\text{th}} = (2.9 \pm 0.8) \text{ V}$  (mean value and standard deviation). While the large deviations underline the poor reproducibility of device performance, the single data points (listed in supplementary **Table F.3**) reveal that devices on the same semiconducting film vary much less. Hence, better statistics and comparability will be achieved if global and local measurements are performed on the same organic thin-film, which has so far not been possible due to restrictions on the sample design (cf. Supporting Information, Appendix F).

Apart from these technical details, comparing the local and global device parameters indicates that the local threshold voltage of the valley fits best to the global threshold voltage, leading to the assumption that the global threshold voltage mostly detects the electrical properties of the more conductive points (i.e. valleys) and disguises variations in the energetic landscape.

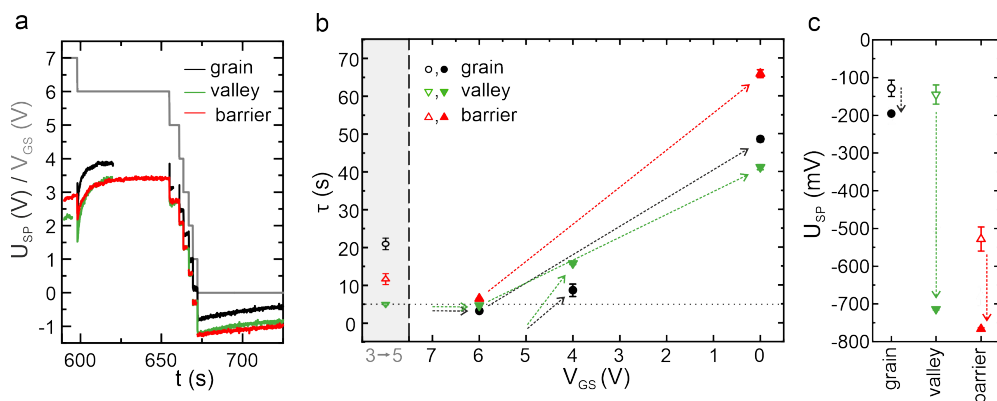


**Figure 5.3** Trapping and detrapping of charge carriers at different investigated by the time-dependent local surface potential. **a**, Surface potential  $U_{SP}$  at decreasing gate voltages  $V_{GS}$  (grey) detected within a grain (black), at an energetic valley (green) and an energetic barrier (red). **b**, Screening times  $\tau$  extracted from the surface potential detected at 6 V and 0 V in **a** and from the surface potential detected at 4 V ( $160\text{ s} < t < 200\text{ s}$ ) in supplementary **Figure F.7**. The arrows indicate the corresponding change in gate voltage. Open symbols repeat the maximum screening times at increasing gate voltages displayed in **Figure 5.2**. **c**, Shift of the contact potential difference (corresponds to  $U_{SP}(V_{GS} = 0)$ ) before (open symbols) and after (filled symbols) two complete cycles of applied gate voltages.

However, measurements at more sites within a channel region and with a smaller resolution in  $V_{GS}$  are necessary to clearly prove the first indication that valleys have the smallest local threshold voltage and mainly define the global threshold voltage.

### 5.3.3 Charge-carrier Detrapping at Zero Gate Voltage

After two cycles of increasing and decreasing gate voltages (cf. supplementary **Figure F.7**), we set the gate voltage back to 0 V and detected the surface potential, as displayed in **Figure 5.3a** at  $t > 675$  seconds. Since a gate voltage of 0 V induces no more external charge carriers in the organic semiconductor, the time dependence of the surface potential now represents withdrawing charges from traps in the channel region. The discharging-time constants of approximately 40, 50, and 65 s for the valley, the grain, and the barrier, respectively, are much higher than all time constants found for the charging process (cf. **Figure 5.3b**). This implies that charge carriers escape from deep traps—independent of the energetic distribution at the specific site.

Besides the time dependence, also the absolute value of the surface potential is affected by the previously applied gate voltages. **Figure 5.3c** displays the initial and final surface potential (i.e. before and after the gate-voltage sweeps) for each site, revealing a downshift of the surface potential, which represents, in the case of  $V_{GS} = 0$  V a change of  $U_{CPD}$  (compare Equation (5.50)). Since we exclude any degradation effects due to the inert atmosphere, the change in the CPD can be attributed to an additionally detected potential induced by the trapped charges. Using the relationship

$$n_t = \hat{c} \cdot \Delta U_{CPD}, \quad (5.51)$$

and the width-normalized capacitance of the insulating layer  $\hat{c}$  (here  $229 \frac{\text{nF}}{\text{cm}^2}$ ), the trap-state density  $n_t$  of the different sites can be calculated [158]. We result with  $(1.3 \pm 0.5) \cdot 10^{11} \text{ cm}^{-2}$  for the grain,  $(10.6 \pm 0.5) \cdot 10^{11} \text{ cm}^{-2}$  for the valley, and  $(4.4 \pm 0.6) \cdot 10^{11} \text{ cm}^{-2}$  for the barrier. These trap-state densities have to be interpret by two different effects, namely trapping within the organic semiconductor due to the band bending at grain boundaries and impurities

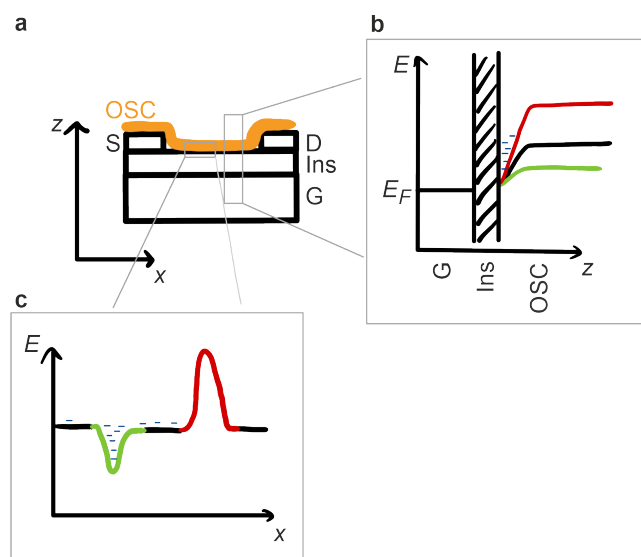


**Figure 5.4** Scheme of two different trapping mechanisms within organic TFTs. **a**, Sketch of a TFT defining the directions of  $x$  and  $z$ . **b**, Trapping within the organic semiconductor due to the band bending at grain boundaries or impurities, which may act as energetic valleys (green) or barriers (red). Electrons (blue) get mainly trapped within valleys or at impurities within grains. **c**, Trapping at the semiconductor-insulator interface for sites with different LUMO levels (black: grains, red: barriers, green: valleys). S = source, D = drain, G = gate, OSC = organic semiconductor, Ins = insulator.

[Publication **P2**], and trapping at the semiconductor-insulator interface [58], [Publication **P5**] (compare **Figure 5.4**). Trapping within the organic semiconductor was investigated by electrostatic KPFM [Publication **P2**], finding that valleys trap electrons, while barriers backscatter them, such that no trapped charges should be detected at the barrier at all. We conclude that trapping at the semiconductor-insulator interface has to play a similarly important role, defined by the different transport levels of grains, barriers and valleys. The energy mismatch between the transport levels and the Fermi level of the gate material thereby lead to a trap-state density that is highest for barriers and smallest for valleys (**Figure 5.4c**). The above calculated local trap-state densities therefore add up from both contributions, i.e. trapping at the interface and within the organic semiconductor,

$$n_t^i = n_{t,\text{interface}}^i + n_{t,\text{semiconductor}}^i,$$

where  $i$  denotes the specific site.

In passing we note that the CPD of the valley is close to the one for the grain in the beginning, and close to the CPD of the barrier in the end, indicating that trapped charges act as repulsive sites on additional charge carriers, in accordance with theoretical predictions [45, 51].

### 5.3.4 Investigation of Hysteresis Effects

To investigate whether and how trapped charges within the semiconductor and at the semiconductor-insulator interface influence the local threshold voltages, we finally analyze the transition from the „on“ to the „off“ state of the TFT. Successively decreasing gate voltages are thereby interpreted as a down-sweep, analogous to the dashed current in **Figure 5.1c**. The resulting surface potentials and related time constants are displayed in **Figure 5.3a** and **b**, respectively.

Decreasing the gate voltage from 7 to 6 V maintains the minimal time constants we found

for the turning-on process, since the gate voltage is still above the respective local threshold voltage at all three sites. Differences for the different sites can be observed for the step from 5 to 4 V, where the time constants for the barrier and the valley start to increase to medium values. However, while the time constant at the grain remains smaller for the turning-off than for the turning-on process (displayed by open symbols), the valley shows a time constant increased by more than three times. These changes of the time constants suggest a downshift of the grain's local threshold voltage and an upshift of the valley's local threshold voltage. This contradictive behavior of the two sites can be explained by hysteresis effects of which two different types exist, that is, the lower back-sweep current (BSC) hysteresis caused by trapped charges which increase the global threshold voltage, and the upper BSC hysteresis with a decreased global threshold voltage caused by free ions in the dielectric [100]. The lower BSC hysteresis is observed in electrical measurements in TFTs of PDI1MPCN2 with a shifting global threshold voltage from 3.4 to 5.3 V (compare **Figure 5.1c**), which again mainly represents the local behavior at the valley. In contrast, we assume that free ions decrease the local threshold voltage at the barrier, since **Figure 5.3b** reveals a decrease of its local threshold voltage from approximately 5 V to below.

We conclude that locally trapped charge carriers shift the local threshold voltage and thereby influence the global threshold voltage and/or global turn-on voltage, whereby again, the valley represents the global device performance best.

## 5.4 Conclusion and Outlook

Time-resolved, local KPFM measurements were performed on monolayer-thin organic films implemented in field-effect transistors to investigate the impact of charge-carrier trapping and detrapping at local impurities, such as grain boundaries, and their impact on global device parameters. While grain boundaries generally act as deep traps, the different LUMO level distributions for energy valleys and barriers are responsible for different trapping processes. Energy valleys are assumed to trap charge carriers within the semiconducting layer due to their smaller LUMO level compared to their surrounding; barriers trap them due to the presence of the semiconductor-insulator interface. However, energetic barriers and valleys do not equally influence the global threshold voltage or turn-on voltage, but the global device parameters resemble more to the smallest local threshold voltages which are defined by valleys, i.e. sites with the smallest LUMO level. We assume that this relation is specific for the here-investigated n-type semiconductor, where electrons aim to find the energetically most favorable way into and through the semiconductor as previously proposed by conductive AFM measurements [126] and theoretical simulations [52]. In this case, not the number of grain boundaries, but their type and depth define the global device parameters.

However, especially the device-to-device variability, responsible for the large errors in the stated global threshold and turn-on voltages, demand for more measurements on an increased number of samples and sites, with an improved device design as suggested in supplementary **Figure F.9**, as well as with a lower resolution in the gate voltage sweeps. Additional measurements could also help to test whether the turn-on or threshold voltage can be decreased by including sites with a smaller (higher) LUMO level into an n-type (p-type) semiconductor. The findings on how local distributions such as grain boundaries or impurities define the global device parameters will then help to understand the origin of variations in the device-to-device performance.

## 6 Can Charge Transport Across Grain Boundaries Be Manipulated with Light?

*In the last two chapters, the influence of grain boundaries on charge-carrier transport (Chapter 4) and device parameters (Chapter 5) have been presented. While energy barriers seem to limit charge transport more effectively than valleys (they have a larger absolute barrier height, cf. Chapter 4, and a larger trap-state density, cf. Chapter 5), valleys are assumed to define e.g. the global threshold and turn-on voltage of OFETs (cf. Chapter 5). As a consequence, controlling the density, type, and absolute height of grain boundaries plays an important role for high mobilities, device efficiencies, and small device-to-device variations. However, since controlling the emergence of grain boundaries still remains a challenge, this chapter presents an alternative by introducing a technique to manipulate charge transport across grain boundaries: Trapped electrons are expected to be excited over grain boundaries upon illumination with light from the FIR and to contribute to a photocurrent.*

*This chapter presents the motivation and basic principles for measurements of this photocurrent in Section 6.1. Details on the sample fabrication and characterization prior to photocurrent measurements are presented in Section 6.2. Section 6.3 presents and discusses preliminary results, while Section 6.4 presents further steps that have to be taken to realize their detection.*

*The results presented in this chapter were prepared with the help from C. Eckel, L. Kühner, A. Seiler, F. Geisenhof, and F. Winterer.*

### 6.1 Motivation

Organic semiconductors are built of organic molecules weakly bound by van der Waals interactions [54]. The weak binding forces allow to process organic semiconductors from solution or thermal evaporation at much smaller energies than inorganic materials, which increases their economical and ecological advantages [163,164]. Especially thermal evaporation is often the method of choice for large-scale applications, since the film thickness and morphology can be tuned easily [3,84]. However, films prepared from the gas phase always consist of a high density of grain boundaries and these mainly affect the device performance of organic field-effect transistors (OFETs), organic light-emitting diodes (OLEDs), and organic solar cells, since they reduce, among others, the effective mobility of charge carriers [39,42,68,156,165,166]. While this impact of grain boundaries on charge transport is a fundamental property of grain boundaries, independent of the material class [104,167,168], just recently a decrease in grain-boundary resistance upon illumination with above-bandgap light could be observed in polycrystalline ceramics [169]. This observation was explained by enhanced ionic transport due to interband absorption at the grain boundaries. In organic semiconductors, on the contrary, hopping between localized states is assumed to be the prevailing transport mechanism across grain boundaries [45,49,51,52] (also cf. Section 2.3). We suggest the hopping rate to equivalently increase upon illumination with light at or above the lowest unoccupied molecular orbital (LUMO)-level difference between grains and grain boundaries.

We use the results of Chapter 4 (Publication **P2**), where this LUMO-level difference was

quantified in terms of barrier heights or valley depths using Kelvin probe force microscopy. Since they were found to range from approximately 10 to 100 meV, which corresponds to light in the far infrared (FIR), the light source of a Fourier transform infrared spectrometer and the setup is modified for Fourier transform photocurrent spectroscopy (FTPC). This technique has already been proven powerful to investigate a variety of different materials, such as InAs/AlSb quantum dots [144], ZnO films [145], bilayer or trilayer graphene [146,147], or polycrystalline silicon [148,149].

Here, we present the necessary modifications to the setup for Fourier transform photocurrent (FTPC) spectroscopy in monolayer-thin crystalline films and thicker polycrystalline films of PDI1MPCN2, implemented in OFETs. We aim for investigating the photocurrent at different charge-carrier densities, tuned by electrostatic gating in the sub-threshold regime, the range where charge transport takes place, but energy barriers or valleys at grain boundaries are still present [Publication **P2**].

With these investigations we hope to be able to answer the following questions in the future:

1. Can FTPC spectroscopy be used to identify grain boundaries and quantify their impact on charge transport, especially in bulk-like materials, where grain boundaries typically act as „hidden interfaces“? If yes, FTPC spectroscopy could support Kelvin probe force microscopy (KPFM), which is able to detect grain boundaries, but only at the surface of bulk materials or in thin layers. FTPC spectroscopy will then also be complementary to KPFM, since it probes the optical properties of grain boundaries, especially the existence and lifetime of excited states.
2. What are the prevalent excitation and transport mechanisms? The temperature dependence of photoexcitation could give information about whether the states near grain boundaries are really localized, as widely assumed, or if intraband absorption takes place.
3. Can the resistance of grain boundaries effectively be manipulated similar to the observations made in the polyceramic material [169], and as a consequence, can light from the FIR help to tune a device’s threshold voltage, mobility, stability, and/or efficiency?

## 6.2 Experimental Details

### Sample Preparation

Monolayer-thin films of PDI1MPCN2 applied from solution or 25 nm-thick polycrystalline layers of PDI1MPCN2 applied via thermal evaporation were integrated into bottom-gate top-contact (BGTC) FETs as presented in Section 3.1. The extreme differences in grain size of approximately three orders of magnitude between the two preparation methods are visible in **Figure 6.1**. The large grain sizes in monolayer-thin films allow to apply source and drain contacts such that a specific number of grain boundaries lies within the channel orthogonal to the charge-transport direction, that is, zero, one, or several grain boundaries.

### Electrical Characterization

The finalized samples were mounted on a sample holder, bonded and inserted into the sample compartment of the spectrometer. After evacuating the sample compartment (approx. 1 mbar), the transfer curves were detected without illumination (i.e. the spectrometer light beam was blocked) up to five times until the currents were stabilized and charges possibly induced by the room light were extracted.

The following devices were used for electrical and photocurrent measurements: Two source-measure units Keithley 2450 were used to apply DC voltages and measure small DC currents down to  $10^{-10}$  A. A preamplifier (Femto, DLPCA-200) was used to transform small currents

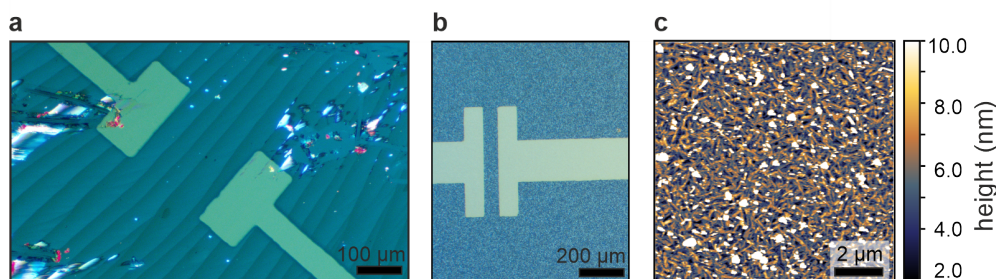


**Figure 6.1** Transistor channels of two selected devices. **a**, Polarized optical microscope (POM) image of a monolayer-thin film applied from solution with 4 grain boundaries within the channel. **b**, Polarized optical microscope image of a 25 nm-thick film applied via thermal evaporation. **c**, Atomic force microscope image of the film shown in **b**.

into voltages with amplifications of  $10^3$  to  $10^6 \frac{\text{V}}{\text{A}}$ . Either the full bandwidth of the signal can be amplified, or frequencies above 10 Hz can be cut off by a low-pass filter. Even more, DC offsets can be filtered out (so-called AC coupling). A lock-in amplifier (Stanford SR860) was used to apply, measure and analyze alternating voltages, with possible frequencies up to 500 kHz. Alternatively, an oscilloscope (Rohde&Schwarz RTB2000) was used to detect time-dependent voltages with possible frequencies up to 300 MHz. Finally, an optical chopper (Thorlabs MC2000B-EC) was used to modulate the intensity of the Fourier transform infrared (FTIR) spectrometer's light source with possible frequencies between 4 Hz and 10 kHz. The electric setup for photocurrent measurements is presented in Section 6.3.

### FTIR Spectroscopy

In this work, the light source and interferometer of a Bruker IFS66v/S were used and the spectrometer was modified for photocurrent spectroscopy measurements as presented before [144–150]. Its main principle, explicitly the generation of an interferogram, is described in Section 3.4. For all FTIR and photocurrent measurements, a mirror velocity  $v_{\text{mirror}} = 0.633 \text{ cm/s}$ , spectral resolution of  $1 \text{ cm}^{-1}$  and aperture diameter of 12 mm was chosen. The modifications applied to the setup are part of this work and presented in the following.

## 6.3 Toward Photocurrent Spectroscopy of Grain Boundaries in Organic Thin-films

The principle of Fourier transform photocurrent spectroscopy is described in Section 3.4. It is based on the assumption that a light beam modulated by an interferometer interacts with the sample and thereby increases its conductivity. If the resulting increase in current is detected and Fourier transformed, the resulting spectrum displays the wavelengths at which light-matter interaction has taken place [144–150].

We will present the experiments conducted, aiming for measuring photocurrent spectroscopy in organic thin-films in three steps: preliminary tests of isolated parts of the final experiment, restrictions for device design and electrical wiring, and the development of an optimized setup and measurement procedure.

### 6.3.1 Preliminary Measurements

For a beginning, we checked whether the FTIR spectrometer was working at all by detecting the spectrum of a known sample (air). The spectrum of air with its specific absorption peaks at approx.  $2300\text{ cm}^{-1}$  (contribution of  $\text{CO}_2$  vibrations) or between  $3500$  and  $4000\text{ cm}^{-1}$  ( $\text{H}_2\text{O}$ ) [170] is displayed in **Figure 6.2a** and proof enough that the light source is emitting in its typical range and the generation of an interferogram is possible. For measurements in the FIR, a Mylar beamsplitter was used, which still yields a spectrum, proving the successful recalibration after the beamsplitter change. However, at wavenumbers  $> 700\text{ cm}^{-1}$ , the detected spectrum visualizes that the Mylar absorbs most of the wavelengths and the KBr beamsplitter has to be used, while the Mylar shows superior performance at wavenumbers  $< 700\text{ cm}^{-1}$ , the range in which the excitation of photocurrents is expected. We want to emphasize that especially at wavenumbers below  $300\text{ cm}^{-1}$ , the deuterated L-alanine doped triglycine sulfate (DLATGS) detector cuts off, which distorts the real transmission intensity of the Mylar beamsplitter.

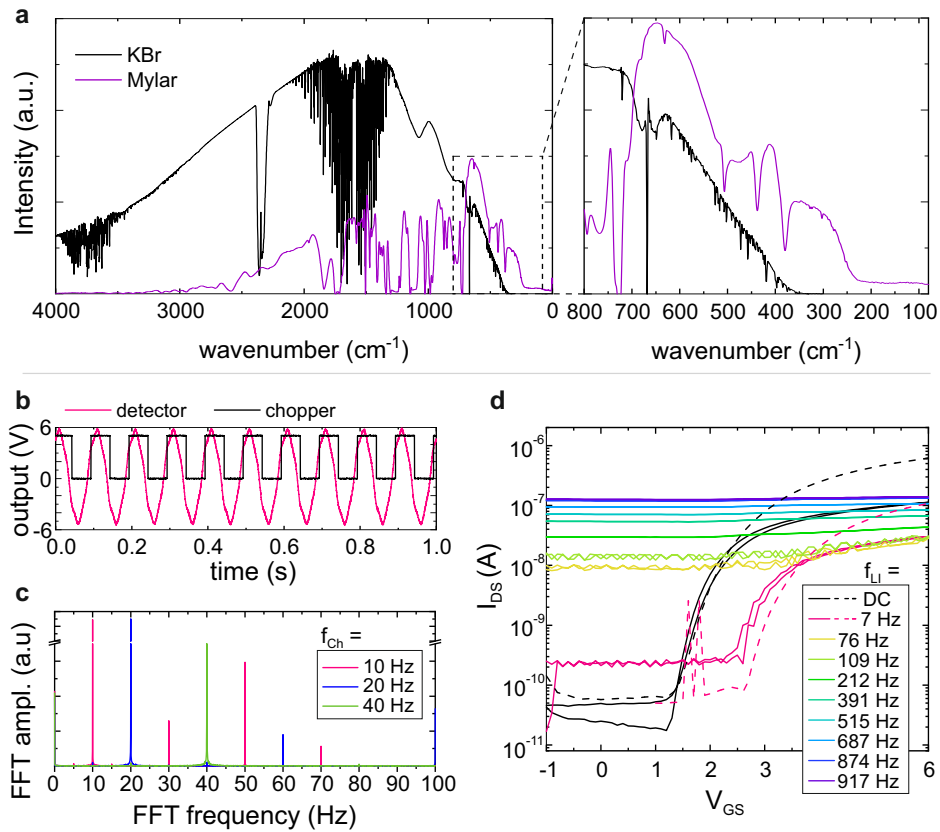


**Figure 6.2 Preliminary measurements to check the working principle of different parts of the FTIR setup.** **a**, Vibration spectrum of air detected using beamsplitters made of KBr or Mylar. Due to the absorption bands of the Mylar at wavenumbers  $> 700\text{ cm}^{-1}$ , the KBr beamsplitter shows superior performance within this range, while at wavenumbers below  $700\text{ cm}^{-1}$ , the Mylar transmits more light. Note that the detector cuts off small wavenumbers below  $300\text{ cm}^{-1}$ . **b**, Output signal of the DLATGS detector and the optical chopper for a chopper frequency of  $f_{\text{ch}} = 10\text{ Hz}$ , detected with an oscilloscope, time resolution  $200\text{ }\mu\text{s}$ . **c**, Fast Fourier transform (FFT) amplitude of the detector signal shown in **a** and two more measurements at chopper frequencies  $f_{\text{ch}} = 20, 40\text{ Hz}$ . **d**, Transfer curves for two different devices performed at AC  $V_{\text{DS}}$  with varying frequencies  $f_{\text{LI}}$ . Settings for device 1 ( $L = 50\text{ }\mu\text{m}$ ,  $W = 500\text{ }\mu\text{m}$ , compact lines):  $V_{\text{DS}} = 0.5\text{ V(DC)} + 0.1\text{ V(AC)}$ , time constant  $100\text{ ms}$ , delay  $0.1\text{ s}$ . Settings for device 2 ( $L = 200\text{ }\mu\text{m}$ ,  $W = 500\text{ }\mu\text{m}$ , dashed lines):  $V_{\text{DS}} = 1.5\text{ V(DC)} + 0.5\text{ V(AC)}$ , time constant  $1\text{ s}$ , delay  $0.10\text{ s}$ .

As the photocurrent in organic thin films is expected to be rather small, the measurement sensitivity is increased by including an optical chopper into the beam path and analyzing the electric current at the chopper frequency  $f_{\text{ch}}$ . We first detected the resulting signal of a known sample, namely the DLATGS detector, which creates a voltage upon illumination. The time-dependent detector output (cf. **Figure 6.2b**) was recorded using an oscilloscope and transformed by an FFT into the spectra displayed in **Figure 6.2c**. The spectra show the most pronounced peaks at 10, 20, or 40 Hz depending on the chosen  $f_{\text{ch}}$ , proving the working principle of modulating, detecting and transforming the light-source emission-spectrum. After having tested the individual parts of the setup, we checked whether the devices in principal work at alternating currents, like they are induced by a modulated light beam. Therefore, we detected transfer curves with alternating drain voltages  $V_{\text{DS}}$  at varying frequencies  $f_{\text{LI}}$ , presented in **Figure 6.2c**. As can be seen, small frequencies imitate the transfer curves at DC voltages  $V_{\text{DS}}$  best. This observation is independent of the DC offset of  $V_{\text{DS}}$ , the time constant, or the delay time (compare devices 1 and 2 in **Figure 6.2**). As a consequence, we chose a chopper frequency of  $f_{\text{ch}} = 7$  Hz for the following measurements.

### 6.3.2 Restrictions for Device and Experiment Design

First photocurrent measurements were performed on samples with an insulating layer of 300 nm  $\text{SiO}_2$  and PDI1MPCN2 monolayers, where a finite photocurrent in the range of  $10^{-9}$  A can be observed at small  $V_{\text{GS}}$  (**Figure 6.3a**). The photocurrent decreases with increasing  $V_{\text{GS}}$ , which fits to the expectation that an increasing charge-carrier density decreases grain-boundary barrier-heights (or valley depths) [Publication **P2**] and thereby suppresses excitation across them. However, a photocurrent could no longer be detected when the laser beam was blocked, leading to the conclusion that it is actually induced by the calibration-laser beam rather than by the infrared light. To identify the absorbing material, we prepared substrates without a semiconducting layer, but with evaporated source and drain contacts. These devices (**Figure 6.3b**) yield even higher photocurrents, provided the substrates contain a layer of silicon dioxide. On substrates with aluminum oxide, however, no detectable photocurrent is generated, and the same holds when the laser is turned off. We conclude that the observed photocurrent is neither generated by an increased transfer rate of charge carriers nor originated in the organic semiconductor or the infrared light, but induced by the interaction of the silicon dioxide with the laser beam. To eliminate this undesired interaction, only samples with  $\text{Al}_2\text{O}_3$  were prepared in the following, and/or the laser beam was blocked right in front of the sample by a 1 mm-thick plate of high-density polyethylene (HD-PE), which still transmits most of the desired wavenumbers between 80 and  $800\text{ cm}^{-1}$  [141, 142], also compare **Figure 6.3c**.

While HD-PE blocks the laser beam and thereby eliminates undesired light-matter interactions, it also decreases the transmitted FIR intensity. As a consequence, the photocurrent amplitude decreases, leading to a smaller signal-to-noise ratio. To compensate this drawback, three measures that increase the signal-to-noise level have been taken: first, we focused the light beam onto the transistor channel and thereby increased the number of incoming photons. Second, we increased the total absorption of the organic layer according to Beer's law [3, 144] by investigating thicker layers of PDI1MPCN2 applied via thermal evaporation in the following. Third, we used that the signal-to-noise ratio depends on the scan number  $n$  as  $\sqrt{n}$  [144] and increased the number of detected modulation periods.

When speaking of modulation periods, we have to discuss all relevant time scales in FT-PC spectroscopy. Provided that the signal with respect to the noise level is high enough to be detectable, the required time-resolution for the measurement devices is given by the smallest features of the current interferogram, and these are in turn defined by the minimal wavelength

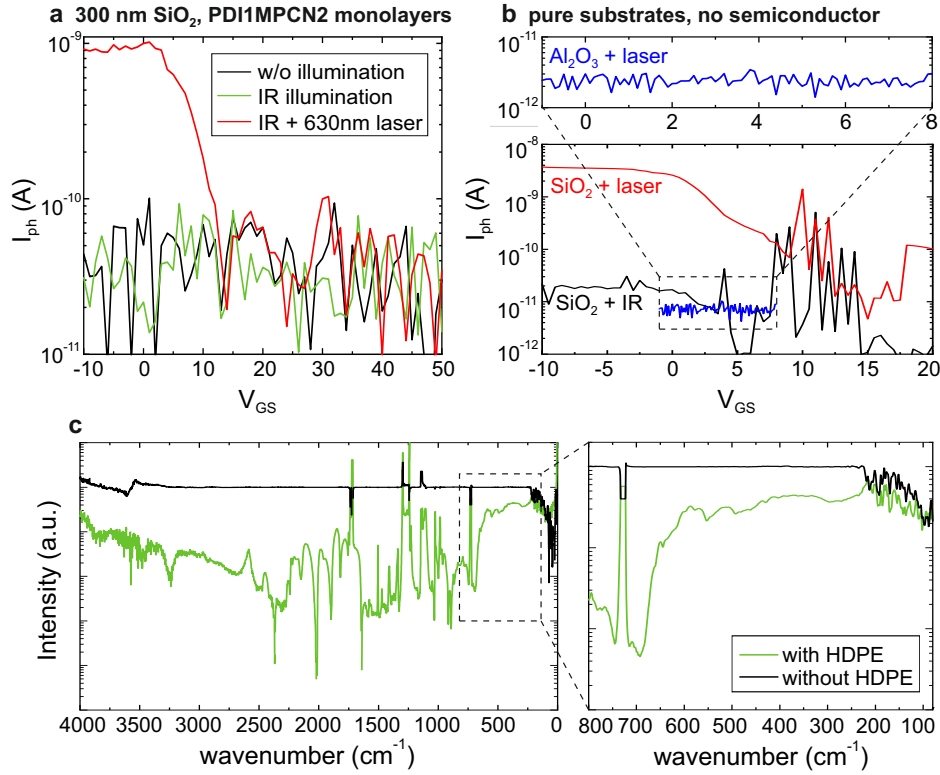


**Figure 6.3 Eliminating visible-light interaction with the sample substrate.** **a**, Detected photocurrent under different conditions of illumination on transistors with monolayers of PDI1MPCN2 and SiO<sub>2</sub>,  $L = 20 \mu\text{m}$ ,  $W = 200 \mu\text{m}$ . **b**, Detected photocurrent on pure substrates with different insulating layers (300 nm SiO<sub>2</sub> or 30 nm Al<sub>2</sub>O<sub>3</sub>), for both devices  $L = 50 \mu\text{m}$ ,  $W = 500 \mu\text{m}$ . **c**, FTIR transmission spectrum in vacuum with and without HD-PE window. Note the logarithmic scale on the  $y$ -axis.

(or the maximum energy) that shall be detected (also compare Equation (3.48) in Section 3.4):

$$\Delta t \stackrel{!}{\leq} \frac{hc}{4E_{\text{max}} \cdot v_{\text{mirror}}} = 498.7 \mu\text{s}$$

with  $h$  Planck's constant,  $c$  the speed of light, and a maximum barrier height of 100 meV [Publication **P2**], this resolution corresponds to approximately 2 kHz and can, from a technical point of view, easily be resolved by the lock-in amplifier or the oscilloscope.

When additionally the amplitude of the interferogram is chopped (to exclude noise contributions in the detected current),  $f_{\text{ch}}$  has to be chosen such that at least one, preferably several, interferograms are included within one illumination period. While one illumination period duration is given by  $1/f_{\text{ch}}$ , the time needed to detect one interferogram corresponds to the time needed by the movable mirror to move between its maximum displacement positions. With a mirror path length of  $l = 1/\Delta\tilde{\nu}_{\text{min}} = 1 \text{ cm}$  (cf. Section 3.4), the interferogram is found to be repeated after each 1.6 s. This means that, if the chopper frequency is in the order of 1 to 10 Hz, it always cuts part of the interferogram rather than including several periods of it. Hence, the mirror velocity has to be increased to make spectroscopic measurements possible at all.

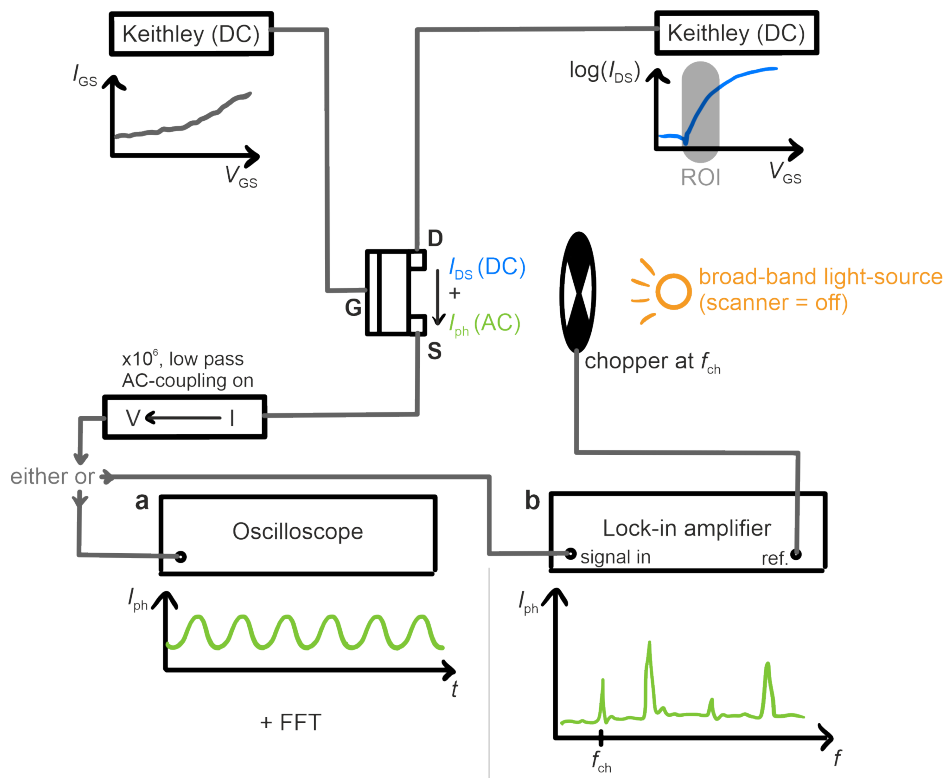


**Figure 6.4** Setup and measurement principle of FTPC spectroscopy in operating FETs. For details cf. main text.

### 6.3.3 Absolute Photocurrent in Polycrystalline Films

To take a step back, we now concentrate on simplified photocurrent measurements, in which the light beam is not modulated into an interferogram (the scanner of the interferometer is turned off), and only the absolute increase in the resulting current is detected. We use the optimized setup and measurement principle displayed in **Figure 6.4**, which was developed as a summary of all previous findings:

Transistors with 25 nm-thick, polycrystalline films of PDI1MPCN2 are connected to two source-measure units Keithley 2450 to apply DC voltages  $V_{GS}$  and  $V_{DS}$  to the gate (G) and drain (D), respectively. The gate and drain voltages are chosen such that a sufficient charge-carrier density is induced into the channel to generate a small current flow, but not so high as to decrease grain-boundary barrier-heights (or valley depths). This balance for the charge-carrier density is equivalent to the sub-threshold region of the OFETs [Publication **P2**]. A constant gate voltage within this regime is applied while the channel of the transistor is illuminated with a modulation frequency of 7 Hz (chopped to increase the measurement sensitivity) for at least 10 s. Within this duration, several modulation periods of the resulting current, composed of a DC ( $I_{DS}$ ) and an AC part ( $I_{ph}$ ), are detected at the source electrode. From the source, the signal is led to a preamplifier, freed from DC contributions and frequencies above 10 Hz, amplified, and finally analyzed by a lock-in amplifier (Stanford SR860) or an oscilloscope (Rohde&Schwarz RTB2000). If the oscilloscope is used to detect the time-dependent current,  $V_{DS}$  and  $V_{GS}$  are applied manually, the time-dependent current is detected, and afterwards Fourier transformed using the software Origin (for an exemplary set of data cf. **Figure 6.5a**). The obtained FFT amplitude at  $f_{ch}$  was extracted and plotted for the corresponding gate voltage, as displayed in **Figure 6.5b**. As this procedure corresponds to the principle of a lock-in amplifier, its use offers a fully-automated analysis of photocurrent, albeit at the

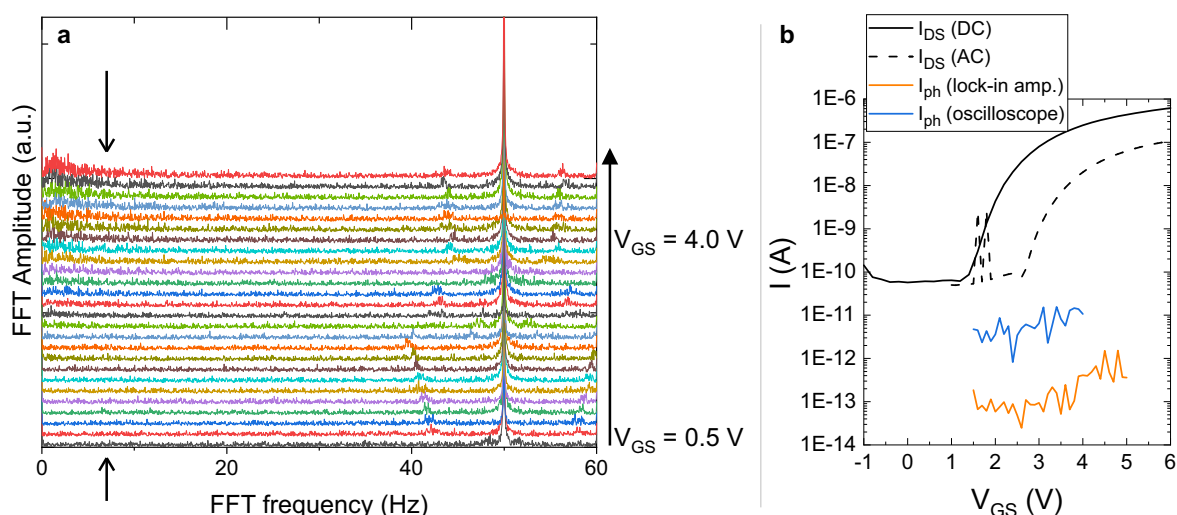


**Figure 6.5** (Photo)current detected in a FET with a 25 nm-thick polycrystalline film and  $L = 200 \mu\text{m}$ ,  $W = 500 \mu\text{m}$ . **a**, Fourier transformations of raw data detected by the oscilloscope, from which the amplitude at  $f_{\text{ch}} = 7 \text{ Hz}$  was extracted and plotted in **b**. **b** Currents detected without illumination (black) at constant  $V_{\text{DS}} = 1.5 \text{ V}$  (compact line) and alternating  $V_{\text{DS}} = 1.5 V_{\text{DC}} + 0.5 V_{\text{AC}}$  (dashed line), as well as with light modulation, detected using the lock-in amplifier (orange) and the oscilloscope (blue).

expense of measurement time, because it needs additional communication time between the devices and the measurement software.

Despite all achievements made so far, no photocurrent can be seen in **Figure 6.5b**. A possible explanation is given by the polycrystallinity of the films with a high density of grain boundaries that an electron has to overcome. Since grain boundaries are supposed to be the location where photocurrent is generated, at first intuition more grain boundaries should lead to a higher photocurrent. However, the opposite can also be the case, since more grain boundaries can lead to higher contact resistances [35], thereby dampening the measurement signal, an increased impact of random molecular orientation (whose contribution on light absorption has not been considered yet), and an increase in required particle-particle interactions.

To account for these effects, we also detected photocurrents in monolayer-thin films with 4 grain boundaries as well as in reference films without grain boundaries, displayed in **Figure 6.6**. Since no difference for samples with **(a)** and without **(b)** grain boundaries can be observed (other than a higher signal in a film with less grain boundaries if only the lock-in measurements are compared), we will conclude this part with suggestions for further improvements of our experiment.

## 6.4 Conclusion and Outlook

Many steps have been taken toward photocurrent spectroscopy in organic thin-films since the beginning of this work, most of which are not presented here. These include mainly technical details of the Fourier spectrometer, which had to be repaired after a long time of no usage before the presented preliminary measurements could be performed. The achievements made so far now allow to focus on further improvements in device and experimental design and especially to concentrate on the underlying physics.

The next step that has to be taken is to increase the signal-to-noise ratio such that photocurrents can be measured. A very promising possibility is to perform a specific mode of IR

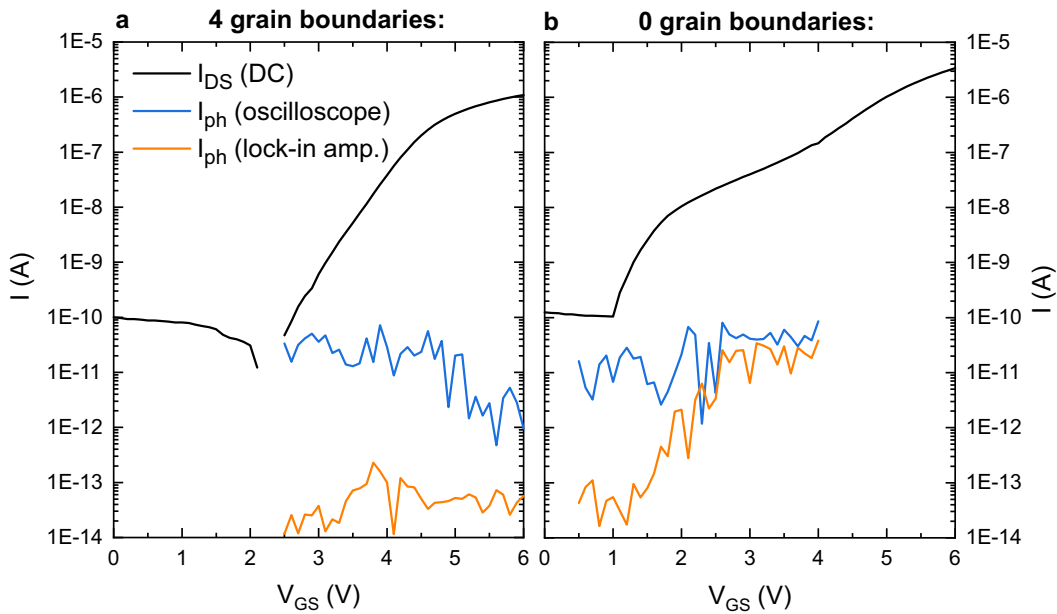


**Figure 6.6** (Photo)current detected in two different FETs with monolayer-thin films comprising of a) 4 or b) no grain boundaries. Currents were detected without illumination at constant  $V_{DS} = 1.5$  V (black), as well as with light modulation, detected using the lock-in amplifier (orange) and the oscilloscope (blue). **a**,  $L = 200$   $\mu\text{m}$ ,  $W = 200$   $\mu\text{m}$ . **b**,  $L = 30$   $\mu\text{m}$ ,  $W = 500$   $\mu\text{m}$ .

spectroscopy, the so-called attenuated total reflection (ATR), with which vibrational modes of a small-molecule self-assembled monolayer (SAM) could already be detected [57]. ATR is a very surface-sensitive method, since it induces evanescent modes at the interface between the sample surface and a waveguide. The material of the waveguide thereby defines the accessible light range; for FIR silicon crystals are typically used [139]. The detailed principles of ATR are beyond the scope of this work but can be read in detail e.g. in the textbook by Griffiths and de Haseth [137].

While performing photocurrent spectroscopy under ATR is most promising, it also increases the demands on device design. Easier ways to increase the signal-to-noise ratio are to increase the scan number by increasing the mirror velocity, decreasing the global temperature to shift its emission spectrum to larger wavelengths (compare Equation (3.45)), or to test whether a Hg-arc lamp offers better results.

Besides increasing the signal-to-noise ratio, one main question that should be addressed in future experiments is, what are the physical processes possibly leading to a photocurrent across grain boundaries? In this regard, the proposed excitation across grain boundaries differs fundamentally from all existing models of photocurrent (cf. Section 2.3), such as the inner photoelectric effect, where excitation across the optical band-gap upon absorption of visible light takes place, or photoionization, which probes the work function or ionization potential by ultraviolet light or X-rays. Photocurrents across grain boundaries, however, do not probe a band edge, but excite electrons into energetically higher states, presumably localized states. Since this idea is based on the assumption that hopping transport takes place across grain boundaries, which is facilitated by higher temperatures and/or smaller grain-boundary densities, it will be interesting to detect photocurrents at varying temperatures and varying densities of grain boundaries. The latter can be tuned in evaporated films by varying the evaporation conditions [53, 61].

On the other hand, temperature-dependent photocurrent-measurements could prove if energetic excited states near grain boundaries are really localized and hopping occurs across

grain boundaries, or if intraband absorption takes place.

To prove that illumination with far infrared light does not heat the semiconductor, lattice and molecular vibrations have to be investigated using Raman spectroscopy or FTIR spectroscopy, which would be especially interesting if performed simultaneously to photocurrent spectroscopy. This, however, requires an optical detector working in a very broad wavenumber range from  $80\text{ cm}^{-1}$  (lower limit of photocurrent spectroscopy) to  $4000\text{ cm}^{-1}$  (upper limit of IR spectroscopy), as well as a substrate that is either transmittive or reflective within this range.

We see that, once we make it work, photocurrent spectroscopy is likely to be a powerful tool to deepen the understanding on the fundamental transport mechanisms across grain boundaries in organic semiconductors.

## 7 Interfacial Synthesis of Layer-Oriented 2D Conjugated Metal-Organic Framework Films toward Directional Charge Transport

Z. Wang\*, **L.S. Walter\***, M. Wang\*, P.S. Petkov, B. Liang, H. Qi, N.N. Nguyen, M. Hamsch, H. Zhong, M. Wang, S.W. Park, L. Renn, K. Watanabe, T. Taniguchi, S.C.B. Mannsfeld, T. Heine, U. Kaiser, S. Zhou, R.T. Weitz, X. Feng, and R. Dong

\* These authors contributed equally.

*So far, the role of grain boundaries in organic semiconductors have been investigated (Chapters 4-6). However, grain boundaries can be found in all types of well-ordered, crystalline materials, as e.g. MOFs (cf. Section 2.5). This chapter presents the structural, optical, and transport properties of a novel 2D c-MOF, that can be synthesized with a predefined stacking direction. This allows for directional charge-transport measurements, which have been conducted globally and locally, as well as in FET, four-point structure, and using c-AFM, to investigate the importance of the stacking direction, contact resistance, and grain boundaries. This work is a collaborative work: the synthesis and characterization of the MOF, as well as global charge-transport measurements have been performed by the chemist group of the Technische Universität Dresden. Devices for local charge transport were prepared by L. Renn. The contribution of the author of this thesis was to conduct local transport measurements in FETs and using c-AFM, to interpret the measurements and write the respective part of the manuscript with a contribution of all other authors.*

*After an introduction into the state of the art, the results in this chapter are structured as follows: First, the design, synthesis and characterization of the novel 2D c-MOF are presented, followed by a discussion on crystallinity and molecular orientation. Afterwards, charge-transport properties and a theoretical calculation of electronic structures are presented. The chapter closes with a conclusion and supporting information.*

*The results presented within this chapter have been published in Publication P1,*

*reprinted on pages 84–92*

with permission from

***J. Am. Chem. Soc.* 2021, 143, 34, 13624—13632,**

DOI: [10.1021/jacs.1c05051](https://doi.org/10.1021/jacs.1c05051).

Copyright © 2021 American Chemical Society

Supporting Information reprinted in Appendix G.

# Interfacial Synthesis of Layer-Oriented 2D Conjugated Metal–Organic Framework Films toward Directional Charge Transport

Zhiyong Wang,<sup>▲</sup> Lisa S. Walter,<sup>▲</sup> Mao Wang,<sup>▲</sup> Petko St. Petkov, Baokun Liang, Haoyuan Qi, Nguyen Ngan Nguyen, Mike Hamsch, Haixia Zhong, Mingchao Wang, SangWook Park, Lukas Renn, Kenji Watanabe, Takashi Taniguchi, Stefan C. B. Mannsfeld, Thomas Heine, Ute Kaiser, Shengqiang Zhou, Ralf Thomas Weitz,\* Xinliang Feng,\* and Renhao Dong\*

Cite This: *J. Am. Chem. Soc.* 2021, 143, 13624–13632

Read Online

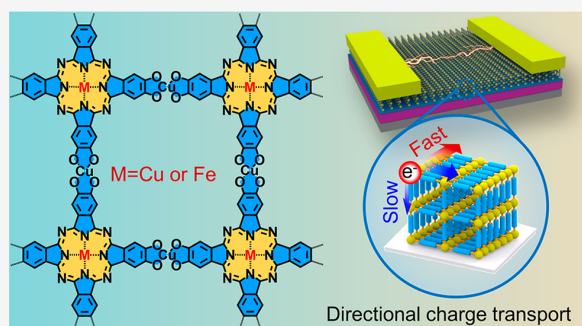
ACCESS |

Metrics & More

Article Recommendations

Supporting Information

**ABSTRACT:** The development of layer-oriented two-dimensional conjugated metal–organic frameworks (2D c-MOFs) enables access to direct charge transport, dial-in lateral/vertical electronic devices, and the unveiling of transport mechanisms but remains a significant synthetic challenge. Here we report the novel synthesis of metal-phthalocyanine-based p-type semiconducting 2D c-MOF films ( $\text{Cu}_2[\text{PcM}-\text{O}_8]$ ,  $M = \text{Cu}$  or  $\text{Fe}$ ) with an unprecedented edge-on layer orientation at the air/water interface. The edge-on structure formation is guided by the preorganization of metal-phthalocyanine ligands, whose basal plane is perpendicular to the water surface due to their  $\pi$ – $\pi$  interaction and hydrophobicity. Benefiting from the unique layer orientation, we are able to investigate the lateral and vertical conductivities by DC methods and thus demonstrate an anisotropic charge transport in the resulting  $\text{Cu}_2[\text{PcCu}-\text{O}_8]$  film. The directional conductivity studies combined with theoretical calculation identify that the intrinsic conductivity is dominated by charge transfer along the interlayer pathway. Moreover, a macroscopic ( $\text{cm}^2$  size) Hall-effect measurement reveals a Hall mobility of  $\sim 4.4 \text{ cm}^2 \text{ V}^{-1} \text{ s}^{-1}$  for the obtained  $\text{Cu}_2[\text{PcCu}-\text{O}_8]$  film. The orientation control in semiconducting 2D c-MOFs will enable the development of various optoelectronic applications and the exploration of unique transport properties.



## INTRODUCTION

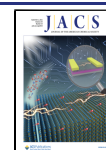
Layered two-dimensional conjugated metal–organic frameworks (2D c-MOFs) have emerged as a new generation of MOF materials featured with strong in-plane conjugation and weak out-of-plane van der Waals force.<sup>1–4</sup> The current development of 2D c-MOFs with conjugated redox-active ligands (e.g., benzene, triphenylene, coronene, and phthalocyanine (Pc) derivatives) and square planar metal-complex linkages (e.g.,  $\text{MNH}_4$ ,  $\text{MO}_4$ ,  $\text{MS}_4$ , and  $\text{M}_3\text{S}_3$ ;  $M$  is metal)<sup>5,5–7</sup> has demonstrated that the electrical conductivities and charge mobilities could reach up to  $10^2 \text{ S cm}^{-1}$  and  $\sim 220 \text{ cm}^2 \text{ V}^{-1} \text{ s}^{-1}$  at room temperature, respectively.<sup>8,9</sup> These results highlight the potential for high electrical conductivity or high mobility 2D c-MOFs as attractive active layers in electronic and spintronic devices, such as field-effect transistors (FETs),<sup>10</sup> superconductors,<sup>11</sup> chemiresistive sensors,<sup>12</sup> thermoelectronics,<sup>13</sup> photodetectors,<sup>14</sup> battery electrodes,<sup>15</sup> capacitor electrodes,<sup>16</sup> ferromagnetic semiconductors,<sup>17,18</sup> and non-magnetic spacers in spin valves.<sup>19</sup>

Despite extensive progress in this field, the nature of charge transport that mainly refers to the structure and electrical property relationship has remained elusive.<sup>20,21</sup> Particularly,

the fundamental understanding of the anisotropic transport mechanism in these van der Waals conducting materials is still ambiguous. In the previous reports, a great effort was devoted to exploring electronic properties via the intralayer (basal plane) pathway because it was believed that the high conductivity of 2D c-MOFs depended critically on the full  $\pi$ -electron delocalization in the 2D conjugated plane.<sup>2,22–25</sup> In this context, the contribution from interlayer coupling ( $\pi$ – $\pi$  stacking) received much less attention. However, recent advances demonstrated that long-range charge transport in these layer-stacked framework materials could be primarily mediated via  $\pi$ – $\pi$  stacking order.<sup>8,26</sup> Therefore, the observation of  $\pi$ – $\pi$  stacking contributions to efficient charge transport in 2D c-MOFs has opened yet other pathways to explore the

Received: May 16, 2021

Published: August 3, 2021



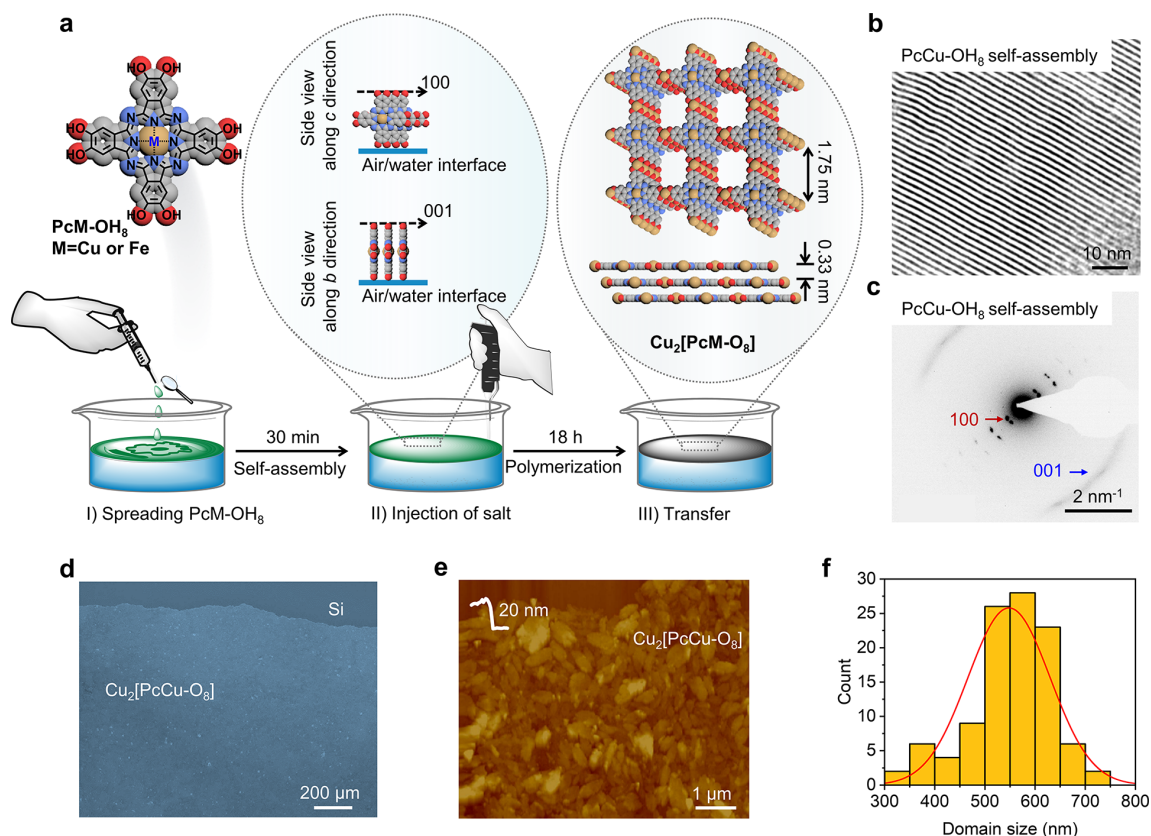


**Figure 1.** Synthesis and morphology of  $\text{Cu}_2[\text{PcM}-\text{O}_8]$ . (a) Synthetic scheme and atomic model of  $\text{Cu}_2[\text{PcM}-\text{O}_8]$  ( $M = \text{Cu}$  or  $\text{Fe}$ ). Gray, red, blue, and white spheres represent  $\text{Cu}$ ,  $\text{O}$ ,  $\text{N}$ , and  $\text{C}$  atoms, respectively. (b) HRTEM image of the self-assembly of  $\text{PcCu}-\text{OH}_8$ . (c) SAED pattern of the self-assembly of  $\text{PcCu}-\text{OH}_8$ . (d) SEM image of the  $\text{Cu}_2[\text{PcCu}-\text{O}_8]$  film. (e) AFM image of the  $\text{Cu}_2[\text{PcCu}-\text{O}_8]$  film. (f) Size distribution of  $\text{Cu}_2[\text{PcCu}-\text{O}_8]$  crystals. Over 100 crystals were used for statistical analysis.

nature of charge transport and improve their electronic properties.<sup>27–29</sup> Nevertheless, the control of the layer orientation in 2D  $c$ -MOF film by exploiting the anisotropic character is urgently needed to direct the charge transport along the interlayer or intralayer pathway and dial-in lateral/vertical electronic devices as well as further unveil the transport mechanism but has so far remained unexplored due to the challenge in synthesis.<sup>30,31</sup>

In this work, we demonstrate a novel strategy for the synthesis of unprecedented edge-on layer-oriented  $\text{Cu}_2[\text{PcM}-\text{O}_8]$  ( $M = \text{Cu}$  or  $\text{Fe}$ ) 2D  $c$ -MOF films at an air/water interface by employing (2,3,9,10,16,17,23,24-octahydroxy phthalocyaninato)metal ( $\text{PcCu}-\text{OH}_8$  or  $\text{PcFe}-\text{OH}_8$ ) as ligands and square planar metal–bis(dihydroxy) complex as a linkage. The  $\pi$ – $\pi$  stacking and hydrophobic interaction could induce an ordered preorganization of the ligands with an edge-on geometry on the water surface, which is crucial to enable the 2D coordination to the water surface. The resulting  $\text{Cu}_2[\text{PcCu}-\text{O}_8]$  film with edge-on structure exhibits a thickness of  $\sim 20$  nm and  $\sim 600$  nm sized crystal domains and shows a room temperature conductivity of  $\sim 5.6 \times 10^{-4} \text{ S cm}^{-1}$  and a Hall mobility of  $\sim 4.4 \text{ cm}^2 \text{ V}^{-1} \text{ s}^{-1}$  based on a macroscopic van der Pauw pattern. Lateral and vertical measurements further reveal the directional charge transport feature in this edge-on 2D  $c$ -MOF film; i.e., the lateral conductivity ( $\sim 2 \times 10^{-3} \text{ S cm}^{-1}$  by two-probe) is 2–3 orders of magnitude higher than the vertical one ( $10^{-6}$ – $10^{-5} \text{ S cm}^{-1}$

by conducting atomic force microscopy and two-probe). The theoretical calculation for  $\text{Cu}_2[\text{PcCu}-\text{O}_8]$  shows that a higher dispersion of the valence bands is determined along the interlayer pathway compared with that along the intralayer pathway, supporting that the intrinsic conductivity is dominated by the charge transfer along the interlayer pathway. This work sheds light on controlling the crystalline orientation of 2D  $c$ -MOF films toward future high-performance optoelectronic devices as well as exploring unique charge transport properties.

## RESULTS AND DISCUSSION

**Design, Synthesis, and Characterization.** The first step in our study was to select suitable organic ligands to fulfill the criteria that their molecular orientations can be controlled on the water surface. In principle, the molecular packing of metal-phthalocyanine ( $\text{PcM}$ ) on the water surface can be precisely controlled by considering the intermolecular distance and molecular orientations through the modification of the substituents.<sup>32,33</sup> Thereby, we consider that the combination of the supramolecular chemistry of  $\text{PcM}$  with the interface-assisted polymerization<sup>9,34</sup> would provide a possible strategy to prepare oriented 2D  $c$ -MOFs films. Toward this end, a ligand of (2,3,9,10,16,17,23,24-octahydroxy phthalocyaninato)copper ( $\text{PcCu}-\text{OH}_8$ ) was employed for the synthesis of edge-on layer-oriented  $\text{Cu}_2[\text{PcCu}-\text{O}_8]$  film at the air/water interface, as illustrated in Figure 1a. The surface pressure–mean

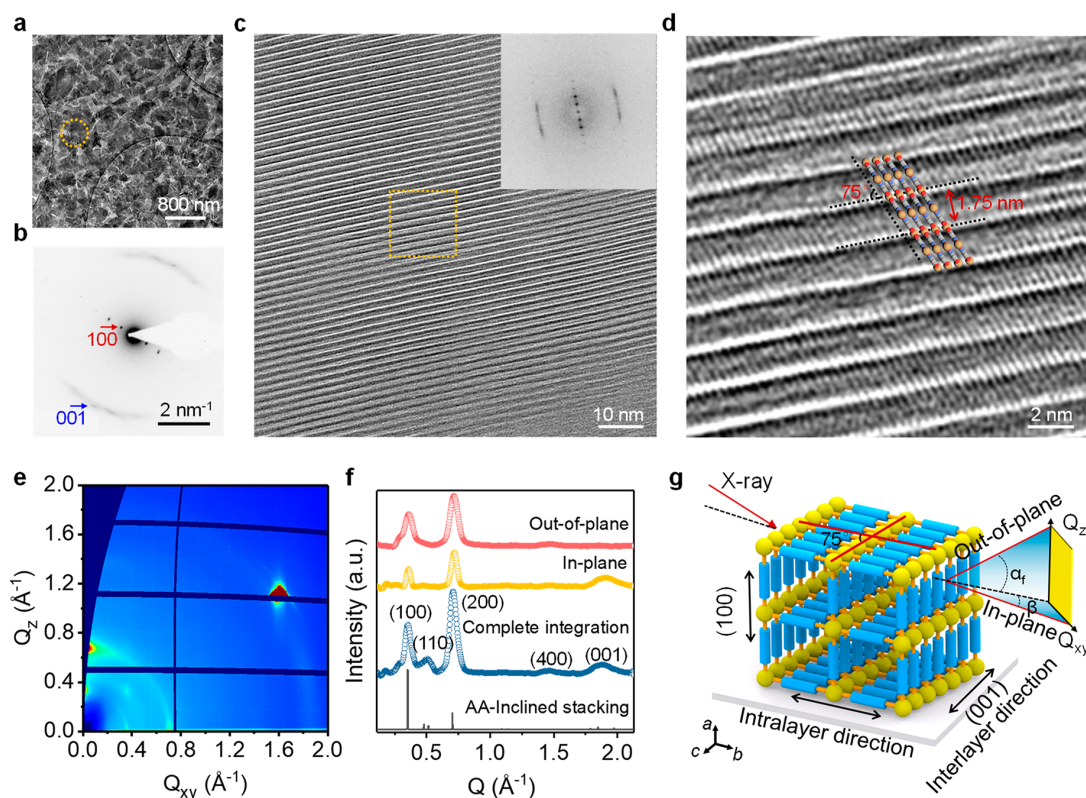


**Figure 2.** Structural characterization of  $\text{Cu}_2[\text{PcCu}-\text{O}_8]$ . (a) TEM image of the  $\text{Cu}_2[\text{PcCu}-\text{O}_8]$  film. The yellow circle marks the position of the selected-area aperture. (b) SAED pattern from the circular region. (c) AC-HRTEM image of  $\text{Cu}_2[\text{PcCu}-\text{O}_8]$ . Inset: fast Fourier transform (FFT) image. (d) Enlarged image of (c) with the structure model overlaid. (e) GIWAXS diffraction pattern of  $\text{Cu}_2[\text{PcCu}-\text{O}_8]$  film. (f) Experimental and calculated GIWAXS intensity profiles of  $\text{Cu}_2[\text{PcCu}-\text{O}_8]$ . (g) The proposed model and GIWAXS measurement geometry.  $\alpha_i$ : exit angle;  $\beta$ : in-plane angle. The model shows the preferential edge-on orientation and AA-inclined stacking of  $\text{Cu}_2[\text{PcCu}-\text{O}_8]$  on the substrate.

molecular area ( $\pi$ -A) isotherm was first recorded by the Langmuir–Blodgett (LB) technique to understand the molecular packing of  $\text{PcCu}-\text{OH}_8$  through compression on the water surface. As shown in Figure S1, through the compression, we observed a sharp rising of surface pressure when the mean molecular area reached  $\sim 36 \text{ \AA}^2$ , revealing a transformation of molecular packing from the gas phase to the crystal phase.<sup>33</sup> To our delight, this achieved average space per molecule is consistent with the theoretical cross-section area per  $\text{PcCu}-\text{OH}_8$  ( $35.7 \text{ \AA}^2$ ),<sup>35</sup> which strongly suggests that the  $\text{PcCu}-\text{OH}_8$  molecules are arranged with the basal plane perpendicular to the water surface.<sup>36,37</sup> One would expect that part of the hydrophilic ( $-\text{OH}$ ) groups orient toward the water surface, while the hydrophobic phthalocyanine macrocycles tend to leave out of the subphase, thereby forcing the  $\text{PcCu}-\text{OH}_8$  molecules to energy-favorably stand on the water surface.<sup>38,39</sup>

Subsequently, we explored the self-assembly of  $\text{PcCu}-\text{OH}_8$  ligands at higher density on the water surface. Typically, a volume of  $200 \mu\text{L}$  of freshly prepared solution of  $\text{PcCu}-\text{OH}_8$  ( $0.47 \text{ mM}$ ) in chloroform/DMF (2:1 in volume) was spread onto the water surface in a  $28 \text{ cm}^2$  sized beaker under ambient conditions. The density of  $\text{PcCu}-\text{OH}_8$  molecules in the beaker reached  $\sim 3.4 \times 10^{-6} \text{ mmol cm}^{-2}$ , which is  $\sim 7.8$ -fold higher than that of the LB monolayer ( $4.37 \times 10^{-7} \text{ mmol cm}^{-2}$ ). After 30 min self-assembly of  $\text{PcCu}-\text{OH}_8$ , a green film was formed on the water surface, which could be readily transferred onto

other substrates (Figure S2a). Remarkably enough, transmission electron microscopy (TEM) images reveal an ordered 2D network with a linear lattice (Figure 1b and Figure S2b). The selected-area electron diffraction (SAED) patterns display diffraction dots with the nearest reflection at  $0.58 \text{ nm}^{-1}$  and diffusive arcs at  $3.0 \text{ nm}^{-1}$ , corresponding to  $\sim 1.73$  and  $0.33 \text{ nm}$  in real space, respectively (Figure 1c). These results manifest that, before the coordination polymerization, the  $\text{PcCu}-\text{OH}_8$  ligands were preorganized into ordered 2D networks with edge-on stacking on the water surface.

Encouraged by the above result, we then performed the coordination polymerization of preorganized  $\text{PcCu}-\text{OH}_8$  ligands on the water surface by adding the solution of copper(II) acetate and sodium acetate into the water subphase. The coordination polymerization was kept at  $20 \text{ }^\circ\text{C}$  under ambient conditions for 18 h, affording a black film on the water surface. The achieved  $\text{Cu}_2[\text{PcCu}-\text{O}_8]$  film on the water surface was transferred horizontally onto various substrates (e.g., *h*-BN,  $\text{SiO}_2/\text{Si}$ , TEM grid) for morphological and structural characterizations. The scanning electron microscopy (SEM) and optical microscopy (OM) images show a macroscopically homogeneous film with a size over  $\text{cm}^2$  (Figure 1d and Figure S3). Atomic force microscopy (AFM) (Figure 1e) and TEM images (Figure 2a and Figure S4) demonstrate that the resultant films are composed of flat crystalline nanosheets with a thickness of  $\sim 20 \text{ nm}$  and the lateral size of hundreds of nanometers (Figure 1f).

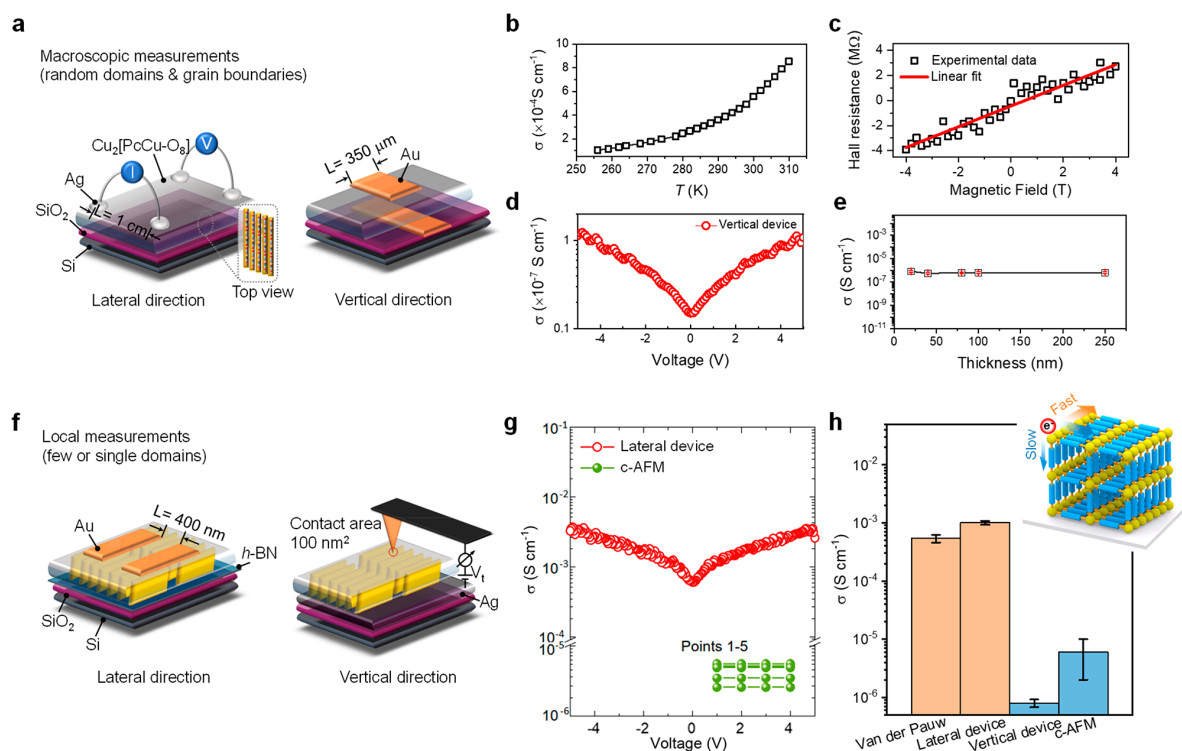


**Figure 3.** Directional charge transport measurement of  $\text{Cu}_2[\text{PcCu}-\text{O}_8]$  films using different configurations of measurement techniques. (a) Schematic diagrams of electrical conductivity measurements on  $\text{Cu}_2[\text{PcCu}-\text{O}_8]$  in macroscopic devices via van der Pauw geometry (left) and in the vertical direction (right). The lateral contact separation for the van der Pauw device was  $\sim 1$  cm, and the contact area in the vertical device was  $\sim 1.3 \times 10^{-3} \text{ cm}^2$ . (b) Electrical conductivity of  $\text{Cu}_2[\text{PcCu}-\text{O}_8]$  as a function of temperature ranging from 256 to 310 K measured by the van der Pauw method. (c) Magnetic field dependence of the Hall resistance by measuring the changes of the electrical resistance in an applied field (from  $-4$  to  $4$  T) at 300 K. (d) Conductivity derived from the vertical device. (e) Plot of the conductivity vs film thickness for vertical devices. (f) Schematic diagram of the device for local lateral (left) and vertical c-AFM measurements (right). (g) Conductivity derived from the local measurements. (h) Direction-dependent electrical conductivity of  $\text{Cu}_2[\text{PcCu}-\text{O}_8]$  at 300 K.

Attenuated total reflection Fourier transform infrared (ATR-FTIR) spectroscopy of the  $\text{Cu}_2[\text{PcCu}-\text{O}_8]$  film reveals a full vanishing of the OH modes ( $\sim 3200 \text{ cm}^{-1}$ ) from  $\text{PcCu}-\text{OH}_8$ , indicating high conversion of the monomer (Figure S5a). The Raman spectra of  $\text{Cu}_2[\text{PcCu}-\text{O}_8]$  manifest the absence of OH peaks in the range of  $2900\text{--}3200 \text{ cm}^{-1}$ , which suggests the efficient coordination between Cu and O ions (Figure S5b). The high degree of copper–oxygen coordination was further demonstrated by X-ray photoelectron spectroscopy (XPS) and SEM-energy dispersed X-ray spectroscopy mapping (SEM-EDX) studies, which show a Cu:O ratio of 1:2.6 (Figure S6) and 1:2.5 (Figure S7), respectively, corresponding to the ideal composition (Cu:O = 1:2.67). X-ray absorption near-edge structure (XANES) was employed to further analyze the chemical state of Cu atoms in  $\text{Cu}_2[\text{PcCu}-\text{O}_8]$  (Figure S8a). The Cu K-edge of XANES in  $\text{Cu}_2[\text{PcCu}-\text{O}_8]$  is different from those of CuO,  $\text{Cu}_2\text{O}$ , and Cu foil. The pre-edge feature in  $\text{Cu}_2[\text{PcCu}-\text{O}_8]$  originates from the transition of 1s core electrons to hybridized orbitals of 3d. The recorded extended X-ray absorption fine structure (EXAFS) spectra show that there is one prominent peak at  $\sim 1.52 \text{ \AA}$  from the Cu–O contribution in  $\text{Cu}_2[\text{PcCu}-\text{O}_8]$  (Figure S8b). Another contrast sample CuO exhibits two different predominant peaks at  $\sim 1.56$  and  $\sim 2.49 \text{ \AA}$ , which arise from Cu–O and Cu–Cu bonds, respectively. These results prove the formation of square planar complexes through the coordination of PcCu–

$\text{OH}_8$  and Cu ions, and the presence of metal oxides (such as CuO) in the  $\text{Cu}_2[\text{PcCu}-\text{O}_8]$  can be excluded. The UV/vis spectra of the  $\text{Cu}_2[\text{PcCu}-\text{O}_8]$  film on a quartz substrate reveal an optical band gap of  $\sim 1.17 \text{ eV}$  (also see Tauc plots of  $(\alpha h\nu)^2$  vs  $h\nu$ , Figure S9).

**Crystallinity and Molecular Orientation.** Detailed insight into the local crystallinity and molecular orientation of the  $\text{Cu}_2[\text{PcCu}-\text{O}_8]$  film was achieved from the SAED and aberration-corrected high-resolution transmission electron microscopy (AC-HRTEM) imaging. The SAED pattern displays a line of sharp reflections and two diffusive arcs (Figure 2a, b). The nearest reflections were found at  $0.57 \text{ nm}^{-1}$  corresponding to  $1.75 \text{ nm}$  in real space, agreeing with the AA-inclined atomic models of  $\text{Cu}_2[\text{PcCu}-\text{O}_8]$  derived by density functional theory (DFT) calculations (Figures S10 and S11). The diffusive arcs fit nicely into a ring with a radius of  $3.0 \text{ nm}^{-1}$ , i.e.,  $0.33 \text{ nm}$ , which is in agreement with the  $\pi$ – $\pi$  stacking distance. The SAED patterns acquired on isolated flat domains illustrate well-defined crystallographic orientation (Figure S12), revealing the crystalline nature of the  $\sim 600 \text{ nm}$  sized nanosheets. As shown in Figure 2c, the AC-HRTEM image presents a highly ordered linear arrangement with a lattice distance of  $1.75 \text{ nm}$ . In the enlarged image, fine fringes with a distance of  $0.33 \text{ nm}$  have been observed, corresponding well to the  $\pi$ – $\pi$  stacking distance (Figure 2d). The FFT pattern is in excellent agreement with the SAED pattern

measured on different crystal domains, suggesting that there is a preferential interlayer  $\pi$ - $\pi$  stacking direction with an angle of  $75^\circ$  relative to the intralayer conjugation direction.

To probe the layer orientation and stacking of the  $\text{Cu}_2[\text{PcCu}-\text{O}_8]$  film on a macroscopic scale, we further performed a grazing incidence wide-angle X-ray scattering (GIWAXS) analysis. Figure 2e shows the 2D GIWAXS pattern of a  $\text{Cu}_2[\text{PcCu}-\text{O}_8]$  film. The in-plane intensity profile reveals a  $\pi$ - $\pi$  stacking peak (001) at  $1.90 \text{ \AA}^{-1}$  (Figure 2f), indicating a preference of  $\text{Cu}_2[\text{PcCu}-\text{O}_8]$  for the edge-on orientation (Table S1). Furthermore, in the out-of-plane direction, three Bragg diffraction peaks with higher scattering intensities are observed at  $Q_z = 0.36, 0.72,$  and  $1.43 \text{ \AA}^{-1}$  ((100), (200), and (400)). The intensity profile resolved in the samples supports the AA-inclined stacking (Figure 2g). Thus, the measured GIWAXS data combined with DFT calculations confirm that  $\text{Cu}_2[\text{PcCu}-\text{O}_8]$  has square unit cells with  $a = b = 1.81 \text{ nm}$  ( $1.75/\sin(75^\circ)$ ) and an interlayer distance of  $\sim 0.33 \text{ nm}$ .

Inspired by the above success, we further extended the synthetic strategy toward another edge-on layer-oriented  $\text{Cu}_2[\text{PcFe}-\text{O}_8]$  film using the (2,3,9,10,16,17,23,24-octahydroxy phthalocyaninato)iron ( $\text{PcFe}-\text{OH}_8$ ) ligand. The preparation condition is identical to the synthesis of the  $\text{Cu}_2[\text{PcCu}-\text{O}_8]$  film. As shown in Figure S13, the measured  $\pi$ -A isotherm for  $\text{PcFe}-\text{OH}_8$  is consistent with that for  $\text{PcCu}-\text{OH}_8$ , revealing that the molecules are vertically oriented on the water surface. The crystallinity and preferred orientation of the as-prepared  $\text{Cu}_2[\text{PcFe}-\text{O}_8]$  film are confirmed from the analysis by TEM imaging and SAED pattern (Figure S14). The results elucidate unambiguously that the crystalline  $\text{Cu}_2[\text{PcFe}-\text{O}_8]$  film exhibits a preferred edge-on orientation with a  $\pi$ - $\pi$  stacking distance of  $0.31 \text{ nm}$ .

**Charge Transport Properties.** Benefiting from the achieved edge-on orientation in the layered  $\text{Cu}_2[\text{PcCu}-\text{O}_8]$  film, we investigated the charge transport properties along the lateral and vertical directions. Figure 3a presents the electrical measurements performed on a macroscopic  $\text{Cu}_2[\text{PcCu}-\text{O}_8]$  film (thickness  $\sim 100 \text{ nm}$ ) along the lateral direction through the van der Pauw method (Schemes S1 and S2). The linear  $I$ - $V$  curve was recorded to verify the Ohmic contact (Figure S15). From those measurements, the lateral conductivity was derived to be  $5.6 \times 10^{-4} \text{ S cm}^{-1}$  at  $300 \text{ K}$  (Figure 3b). Variable-temperature conductivity measurements show a nonlinear increase of electrical conductivity from  $256$  to  $310 \text{ K}$ . The conductivity ( $\sigma$ ) plotted versus  $T^{-1}$  presents a nonlinear relationship at this temperature range (Figure S16), which reveals thermal activation contributions to the conductivity. Activation energies ( $E_a$ ) were derived from fitting the Arrhenius plot, which is expressed as  $\sigma(T) = \sigma_0 \exp[-(E_a/k_B T)]$  ( $k_B$  is the Boltzmann constant). The fitted result for  $E_a$  of the measurement is determined to be  $\sim 285 \text{ meV}$ , indicating a typical semiconducting feature of  $\text{Cu}_2[\text{PcCu}-\text{O}_8]$  films. The charge carrier mobility was further evaluated by measuring the Hall resistance ( $R_{\text{Hall}}$ ) under magnetic field ( $H$ ) based on the van der Pauw pattern (method seen in the Supporting Information and Schemes S3 and S4). As shown in Figure 3c, the Hall effect measurement shows a linear relationship of the Hall resistance  $R_{\text{Hall}}$  vs the perpendicular magnetic field  $H$ . Moreover, the polarity of the Hall coefficient indicates a p-type semiconducting behavior of  $\text{Cu}_2[\text{PcCu}-\text{O}_8]$ . The hole concentration is calculated as  $\sim 7.33 \times 10^{14} \text{ cm}^{-3}$ , and the corresponding Hall mobility reaches  $4.4 \pm 0.7 \text{ cm}^2 \text{ V}^{-1} \text{ s}^{-1}$ . Note that the arrangement of the edge-on oriented

$\text{Cu}_2[\text{PcCu}-\text{O}_8]$  nanosheets in the horizontal direction is random. To elucidate the influence of such anisotropic nature on the charge transport in the lateral direction, we measured 10 two-probe devices with a channel length of  $300 \mu\text{m}$ . As shown in Figure S17, all the contrast samples display consistent conductivity values ( $\sim 3 \times 10^{-4} \text{ S cm}^{-1}$ ).

We further fabricated vertical devices and investigated the charge transport along the vertical direction as shown in Figure 3a (right) and Figure S18. For better comparability, the contact resistance was determined by transmission line measurements to  $\sim 2600 \Omega \text{ cm}$  and extracted from the detected data. The resulting conductivity of the  $\text{Cu}_2[\text{PcCu}-\text{O}_8]$  film in the vertical direction is on the order of  $\sim 10^{-6} \text{ S cm}^{-1}$  and therefore 2 orders of magnitude smaller than in the lateral direction as detected by the van der Pauw measurements (Figure 3d). Besides, to exclude that shorts are measured between the top and bottom contacts with a contact area of  $1.3 \times 10^{-3} \text{ cm}^2$ , the film thickness was varied between  $20$  and  $250 \text{ nm}$ , and all the contrast samples provided consistent conductivity values (Figure 3e).

To reduce the impact of grain boundaries on the long-range transport, we built devices with smaller dimensions (sub-micrometers). For the analysis of transport in the lateral direction, FET devices were fabricated with  $h$ -BN as part of the gate dielectric as shown in Figure 3f (left). Here, the contacts with distances between  $100$  and  $500 \text{ nm}$  and widths of  $8 \mu\text{m}$  were patterned using electron-beam lithography (Figure S19 and Scheme S5). Figure 3g (red circles) shows the resulting conductivity of one representative contact pair ( $400 \text{ nm}$ ) on the order of  $2 \times 10^{-3} \text{ S cm}^{-1}$ , representing charge transport through only very few domains and grain boundaries.

For the analysis of local charge transport in the vertical direction, conductive AFM (c-AFM) was conducted on  $20 \text{ nm}$  thick  $\text{Cu}_2[\text{PcCu}-\text{O}_8]$  films applied on a silver substrate (Figure 3f (right), Schemes S6 and S7). Again, this technique was chosen to prevent short currents from being measured. Voltages of  $1, 2, 3,$  and  $4 \text{ V}$  were applied to the tip, and the resulting local current in the contact area of  $\sim 100 \text{ nm}^2$  (ref 40) was recorded simultaneously with the film topography (Figure S20). To estimate an upper value for the conductivity, only the highest positions within a scan were evaluated. Here, the least steep curvature guarantees good contact, and the film thickness can be determined by the detected height with a smaller uncertainty compared to lower-lying positions. The resulting vertical conductivities are on the order of  $10^{-6}$ - $10^{-5} \text{ S cm}^{-1}$  (Figure 3g, green balls). The local measurements, while including contact resistances, are consistent with the macroscopic measurements, as both suggest that the lateral conductivity is  $10^2$ - $10^3$ -fold higher than that along the vertical direction (Figure 3h). Therefore, it can be concluded that neither grain boundaries nor contact resistance is the main limiting factor for determining the charge transport of  $\text{Cu}_2[\text{PcCu}-\text{O}_8]$  film but that it stems from its intrinsic anisotropic charge transport feature. Clearly, we can attribute such anisotropic behavior to the preferential charge transport along the layer-stacking direction. These results highlight the importance of controlling the stacking direction in MOF films for the implementation in electrical devices.

**Theoretical Calculation of Electronic Structures.** To further understand the charge transport nature and the structure-charge transport correlation, we employed DFT to calculate the electronic structures of  $\text{Cu}_2[\text{PcCu}-\text{O}_8]$ . The charge density difference map of monolayer and multilayer

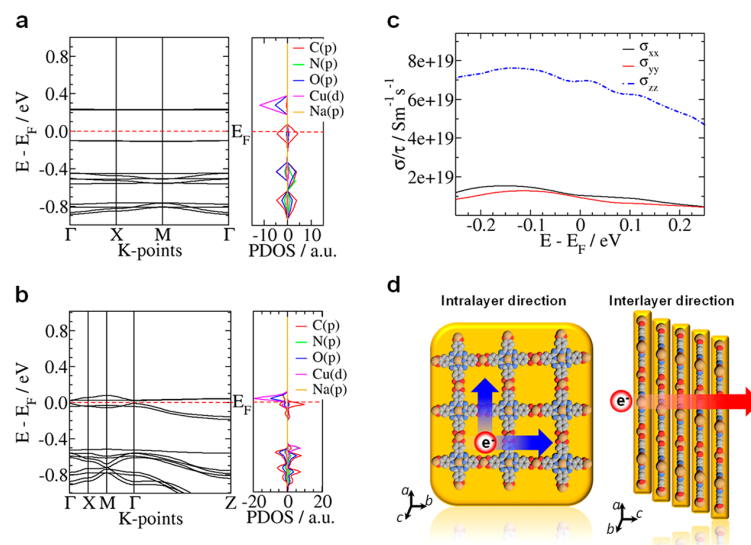


**Figure 4.** Modeling of the electronic structures of  $\text{Cu}_2[\text{PcCu}-\text{O}_8]$ . Calculated electronic band structure of a monolayer (a) and multilayered  $\text{Cu}_2[\text{PcCu}-\text{O}_8]$  (b). (c) Calculated electrical conductivity within the constant-relaxation-time approximation of the Boltzmann transport equation using the BoltzTraP2 code. The k grid of the VASP calculations was interpolated onto a 7 times denser grid. (d) Schematic illustration of the correlation between the  $\text{Cu}_2[\text{PcCu}-\text{O}_8]$  structure and the anisotropic charge transport.

$\text{Cu}_2[\text{PcCu}-\text{O}_8]$ , combined with Bader charge analysis, demonstrates that the main charge density redistribution happens at the  $\text{Cu}-\text{O}_4$  moiety (Figures S21 and S22). As shown in Figure 4a and 4b, the calculated electronic band structures for the monolayer and multilayer  $\text{Cu}_2[\text{PcCu}-\text{O}_8]$  present notable differences along the intralayer and interlayer directions. The band structure of a monolayer  $\text{Cu}_2[\text{PcCu}-\text{O}_8]$  with optimized geometry shows no dispersion in both conduction and valence bands near the Fermi level, implying that charge transport for the monolayer is practically null because of an extremely large effective mass for charge carriers. The  $\pi$ -electrons are trapped within the  $\text{PcCu}-\text{OH}_8$  moiety. In addition, the presence of defects originating from the uncoordinated Cu-site at the edge of  $\text{Cu}_2[\text{PcCu}-\text{O}_8]$  also contributes to breaking the electron delocalization (Figure S23).<sup>41</sup> The localization of electron density causes flat bands and thus hampers the charge transport within the monolayer. Besides, the bands near to the Fermi level could be easily thermally populated with holes, indicating a typical p-type semiconducting behavior with a bandgap of  $\sim 0.35$  eV. Contrary to the monolayer, the energy band diagram of the AA-inclined stacking  $\text{Cu}_2[\text{PcCu}-\text{O}_8]$  shows a small bandgap of 0.03 eV and a band dispersion of 0.19 eV along the interlayer direction ( $\Gamma$ -Z direction). The higher dispersion of the valence bands indicates a higher hole mobility along the interlayer direction compared with the intralayer direction. As shown in Figure 4c, the plot of the conductivity at constant relaxation time reveals that the intralayer conductivity is much lower than the interlayer one, thus further supporting the anisotropic transport property.<sup>42</sup> In association with the DFT calculations and the experimental finding, we conclude that the charge transport of the  $\text{Cu}_2[\text{PcCu}-\text{O}_8]$  film is preferential along the interlayer direction and essentially limited along the intralayer direction, as illustrated in Figure 4d.

## CONCLUSION

In summary, we have demonstrated a novel strategy for the synthesis of edge-on layer-oriented 2D c-MOF films employing the preorganized PcM ligands at the air/water interface. The macroscopic Hall effect and vertical device measurements as well as local charge transport studies by two-probe and c-AFM methods were employed for unveiling the anisotropic charge transport feature of  $\text{Cu}_2[\text{PcCu}-\text{O}_8]$ . Notably, a Hall mobility of  $4.4 \pm 0.7 \text{ cm}^2 \text{ V}^{-1} \text{ s}^{-1}$  was determined, and the resolved lateral conductivity was 2–3 orders of magnitude higher than the vertical one, revealing that the electrical transport of  $\text{Cu}_2[\text{PcCu}-\text{O}_8]$  is dominated primarily by the stacking direction. The strategy of combining the ligand design and interface-assisted synthesis provides a unique route to control the layer orientation in conducting 2D c-MOFs, which can allow directional charge transport studies and the development of specific optoelectronic devices.

## ASSOCIATED CONTENT

### Supporting Information

The Supporting Information is available free of charge at <https://pubs.acs.org/doi/10.1021/jacs.1c05051>.

Experimental methods, SAED patterns, TEM images, XPS spectra, XANES spectra, EXAFS spectra, DFT calculations, conductivity measurements, and c-AFM experiments (PDF)

## AUTHOR INFORMATION

### Corresponding Authors

Ralf Thomas Weitz – I. Physical Institute, Faculty of Physics, Georg-August-University Göttingen, 37077 Göttingen, Germany; Physics of Nanosystems, Department of Physics, Ludwig-Maximilians-University München, 80799 Munich, Germany; [orcid.org/0000-0001-5404-7355](https://orcid.org/0000-0001-5404-7355); Email: [thomas.weitz@uni-goettingen.de](mailto:thomas.weitz@uni-goettingen.de)

**Xinliang Feng** – Center for Advancing Electronics Dresden (cfaed) and Faculty of Chemistry and Food Chemistry, Technische Universität Dresden, 01062 Dresden, Germany; Max Planck Institute for Microstructure Physics, Halle (Saale) D-06120, Germany; [orcid.org/0000-0003-3885-2703](https://orcid.org/0000-0003-3885-2703); Email: [xinliang.feng@tu-dresden.de](mailto:xinliang.feng@tu-dresden.de)

**Renhao Dong** – Center for Advancing Electronics Dresden (cfaed) and Faculty of Chemistry and Food Chemistry, Technische Universität Dresden, 01062 Dresden, Germany; [orcid.org/0000-0002-4125-9284](https://orcid.org/0000-0002-4125-9284); Email: [renhao.dong@tu-dresden.de](mailto:renhao.dong@tu-dresden.de)

## Authors

**Zhiyong Wang** – Center for Advancing Electronics Dresden (cfaed) and Faculty of Chemistry and Food Chemistry, Technische Universität Dresden, 01062 Dresden, Germany

**Lisa S. Walter** – I. Physical Institute, Faculty of Physics, Georg-August-University Göttingen, 37077 Göttingen, Germany; Physics of Nanosystems, Department of Physics, Ludwig-Maximilians-University München, 80799 Munich, Germany

**Mao Wang** – Helmholtz-Zentrum Dresden-Rossendorf, Institute of Ion Beam Physics and Materials Research, 01328 Dresden, Germany

**Petko St. Petkov** – Faculty of Chemistry and Pharmacy, University of Sofia, 1164 Sofia, Bulgaria

**Baokun Liang** – Central Facility for Electron Microscopy, Electron Microscopy of Materials Science Central, Facility for Electron Microscopy, Ulm University, 89081 Ulm, Germany

**Haoyuan Qi** – Center for Advancing Electronics Dresden (cfaed) and Faculty of Chemistry and Food Chemistry, Technische Universität Dresden, 01062 Dresden, Germany; Central Facility for Electron Microscopy, Electron Microscopy of Materials Science Central, Facility for Electron Microscopy, Ulm University, 89081 Ulm, Germany; [orcid.org/0000-0002-6684-7074](https://orcid.org/0000-0002-6684-7074)

**Nguyen Ngan Nguyen** – Center for Advancing Electronics Dresden (cfaed) and Faculty of Chemistry and Food Chemistry, Technische Universität Dresden, 01062 Dresden, Germany

**Mike Hambsch** – Center for Advancing Electronics Dresden (cfaed) and Faculty of Electrical and Computer Engineering, Technische Universität Dresden, 01062 Dresden, Germany; [orcid.org/0000-0002-8487-0972](https://orcid.org/0000-0002-8487-0972)

**Haixia Zhong** – Center for Advancing Electronics Dresden (cfaed) and Faculty of Chemistry and Food Chemistry, Technische Universität Dresden, 01062 Dresden, Germany

**Mingchao Wang** – Center for Advancing Electronics Dresden (cfaed) and Faculty of Chemistry and Food Chemistry, Technische Universität Dresden, 01062 Dresden, Germany

**SangWook Park** – Center for Advancing Electronics Dresden (cfaed) and Faculty of Chemistry and Food Chemistry, Technische Universität Dresden, 01062 Dresden, Germany; [orcid.org/0000-0002-2834-5700](https://orcid.org/0000-0002-2834-5700)

**Lukas Renn** – I. Physical Institute, Faculty of Physics, Georg-August-University Göttingen, 37077 Göttingen, Germany; Physics of Nanosystems, Department of Physics, Ludwig-Maximilians-University München, 80799 Munich, Germany

**Kenji Watanabe** – National Institute for Materials Science, 305-0047 Tsukuba, Japan; [orcid.org/0000-0003-3701-8119](https://orcid.org/0000-0003-3701-8119)

**Takashi Taniguchi** – National Institute for Materials Science, 305-0047 Tsukuba, Japan; [orcid.org/0000-0002-1467-3105](https://orcid.org/0000-0002-1467-3105)

**Stefan C. B. Mannsfeld** – Center for Advancing Electronics Dresden (cfaed) and Faculty of Electrical and Computer Engineering, Technische Universität Dresden, 01062 Dresden, Germany; [orcid.org/0000-0003-0268-519X](https://orcid.org/0000-0003-0268-519X)

**Thomas Heine** – Center for Advancing Electronics Dresden (cfaed) and Faculty of Chemistry and Food Chemistry, Technische Universität Dresden, 01062 Dresden, Germany; Helmholtz-Zentrum Dresden-Rossendorf, Institute of Resource Ecology, 04316 Leipzig, Germany; Department of Chemistry, Yonsei University, Seoul 03722, Korea; [orcid.org/0000-0003-2379-6251](https://orcid.org/0000-0003-2379-6251)

**Ute Kaiser** – Central Facility for Electron Microscopy, Electron Microscopy of Materials Science Central, Facility for Electron Microscopy, Ulm University, 89081 Ulm, Germany

**Shengqiang Zhou** – Helmholtz-Zentrum Dresden-Rossendorf, Institute of Ion Beam Physics and Materials Research, 01328 Dresden, Germany; [orcid.org/0000-0002-4885-799X](https://orcid.org/0000-0002-4885-799X)

Complete contact information is available at:  
<https://pubs.acs.org/10.1021/jacs.1c05051>

## Author Contributions

The manuscript was written through contributions of all authors. All authors have given approval to the final version of the manuscript.

## Author Contributions

▲These authors contributed equally.

## Notes

The authors declare no competing financial interest.

## ACKNOWLEDGMENTS

The authors thank Dr. Markus Löffler, Dr. Petr Formanek, Dr. Jichao Zhang, Prof. Xiaodong Zhuang, and Dr. Tao Zhang for SEM, TEM, XANES, XPS, and Raman measurements. The authors acknowledge cfaed and Dresden Center for Nano-analysis (DCN) at TUD. This work is financially supported by EU Graphene Flagship (Core3, No. 881603), ERC starting grant (FC2DMOF, No. 852909), ERC Consolidator Grant (T2DCP), DFG projects (SFB-1415, No. 417590517, SPP 1928, WE 4893/6-1, COORNET), H2020-MSCA-ITN (ULTIMATE, No. 813036), as well as the German Science Council and Center of Advancing Electronics Dresden (cfaed). Z.W. gratefully acknowledges funding from the China Scholarship Council. R.T.W. acknowledges funding from the Center for Nanoscience (CeNS) and the Solar Technologies go Hybrid (SolTech) initiative as well as funding by the Deutsche Forschungsgemeinschaft (DFG, German Research Foundation) under Germany's Excellence Strategy-EXC-2111-390814868 (MCQST) and EXC 2089/1-390776260 (e-conversion). K.W. and T.T. acknowledge support from the Elemental Strategy Initiative conducted by the MEXT, Japan, A3 Foresight by JSPS, and the CREST (JPMJCR15F3), JST. K.W. and T.T. acknowledge support from the EMEXT Element Strategy Initiative to Form Core Research Center, Grant Number JPMXP0112101001 and the CREST (JPMJCR15F3), JST. P.S.P. and T.H. thank ZIH Dresden for providing high-performance computing facilities. We acknowledge Elettra Sincrotrone Trieste for providing access to its synchrotron radiation facilities and we thank Luisa Barba for assistance in using beamline XRD1. The research leading to this result has been supported by the project CALIPSOplus under Grant Agreement 730872 from the EU Framework Programme for Research and Innovation HORIZON 2020.

## REFERENCES

- (1) Hmadeh, M.; Lu, Z.; Liu, Z.; Gándara, F.; Furukawa, H.; Wan, S.; Augustyn, V.; Chang, R.; Liao, L.; Zhou, F.; Perre, E.; Ozolins, V.; Suenaga, K.; Duan, X.; Dunn, B.; Yamamoto, Y.; Terasaki, O.; Yaghi, O. M. New porous crystals of extended metal-catecholates. *Chem. Mater.* **2012**, *24* (18), 3511–3513.
- (2) Kambe, T.; Sakamoto, R.; Kusamoto, T.; Pal, T.; Fukui, N.; Hoshiko, K.; Shimojima, T.; Wang, Z.; Hirahara, T.; Ishizaka, K.; Hasegawa, S.; Liu, F.; Nishihara, H. Redox control and high conductivity of nickel bis (dithiolene) complex  $\pi$ -nanosheet: a potential organic two-dimensional topological insulator. *J. Am. Chem. Soc.* **2014**, *136* (41), 14357–14360.
- (3) Huang, X.; Sheng, P.; Tu, Z.; Zhang, F.; Wang, J.; Geng, H.; Zou, Y.; Di, C.; Yi, Y.; Sun, Y.; Xu, W.; Zhu, D. A two-dimensional  $\pi$ -d conjugated coordination polymer with extremely high electrical conductivity and ambipolar transport behaviour. *Nat. Commun.* **2015**, *6*, 7408.
- (4) Zhao, M.; Huang, Y.; Peng, Y.; Huang, Z.; Ma, Q.; Zhang, H. Two-dimensional metal–organic framework nanosheets: synthesis and applications. *Chem. Soc. Rev.* **2018**, *47* (16), 6267–6295.
- (5) Feng, D.; Lei, T.; Lukatskaya, M. R.; Park, J.; Huang, Z.; Lee, M.; Shaw, L.; Chen, S.; Yakovenko, A. A.; Kulkarni, A.; Xiao, J.; Fredrickson, K.; Tok, J. B.; Zou, X.; Cui, Y.; Bao, Z. Robust and conductive two-dimensional metal–organic frameworks with exceptionally high volumetric and areal capacitance. *Nat. Energy* **2018**, *3* (1), 30–36.
- (6) Sheberla, D.; Bachman, J. C.; Elias, J. S.; Sun, C.; ShaoHorn, Y.; Dincă, M. Conductive MOF electrodes for stable supercapacitors with high areal capacitance. *Nat. Mater.* **2017**, *16* (2), 220–224.
- (7) Mähringer, A.; Jakowetz, A. C.; Rotter, J. M.; Bohn, B. J.; Stolarczyk, J. K.; Feldmann, J.; Bein, T.; Medina, D. D. Oriented thin films of electroactive triphenylene catecholate-based two-dimensional metal–organic frameworks. *ACS Nano* **2019**, *13* (6), 6711–6719.
- (8) Day, R. W.; Bediako, D. K.; Rezaee, M.; Parent, L. R.; Skorupskii, G.; Arguilla, M. Q.; Hendon, C. H.; Stassen, I.; Gianneschi, N. C.; Kim, P.; Dincă, M. Single crystals of electrically conductive two-dimensional metal–organic frameworks: dstructural and electrical transport properties. *ACS Cent. Sci.* **2019**, *5* (12), 1959–1964.
- (9) Dong, R.; Han, P.; Arora, H.; Ballabio, M.; Karakus, M.; Zhang, Z.; Shekhar, C.; Adler, P.; Petkov, P. S.; Erbe, A.; Mannsfeld, S. C. B.; Felser, C.; Heine, T.; Bonn, M.; Feng, X.; Cánovas, E. High-mobility band-like charge transport in a semiconducting two-dimensional metal–organic framework. *Nat. Mater.* **2018**, *17* (11), 1027–1032.
- (10) Wu, G.; Huang, J.; Zang, Y.; He, J.; Xu, G. Porous field-effect transistors based on a semiconductive metal–organic framework. *J. Am. Chem. Soc.* **2017**, *139* (4), 1360–1363.
- (11) Huang, X.; Zhang, S.; Liu, L.; Yu, L.; Chen, G.; Xu, W.; Zhu, D. Superconductivity in a copper (II)-based coordination polymer with perfect kagome structure. *Angew. Chem.* **2018**, *130* (1), 152–156.
- (12) Meng, Z.; Stolz, R. M.; Mendecki, L.; Mirica, K. A. Electrically-transduced chemical sensors based on two-dimensional nanomaterials. *Chem. Rev.* **2019**, *119* (1), 478–598.
- (13) Sun, L.; Liao, B.; Sheberla, D.; Kraemer, D.; Zhou, J.; Stach, E. A.; Zakharov, D.; Stavila, V.; Talin, A. A.; Ge, Y.; Allendorf, M. D.; Chen, G.; Léonard, F.; Dincă, M. A microporous and naturally nanostructured thermoelectric metal–organic framework with ultralow thermal conductivity. *Joule* **2017**, *1* (1), 168–177.
- (14) Arora, H.; Dong, R.; Venanzi, T.; Zscharschuch, J.; Schneider, H.; Helm, M.; Feng, X.; Cánovas, E.; Erbe, A. Demonstration of a broadband photodetector based on a two-dimensional metal–organic framework. *Adv. Mater.* **2020**, *32* (9), 1907063.
- (15) Wang, Z.; Wang, G.; Qi, H.; Wang, M.; Wang, M.; Park, S.; Wang, H.; Yu, M.; Kaiser, U.; Fery, A.; Zhou, S.; Dong, R.; Feng, X. Ultrathin two-dimensional conjugated metal–organic framework single-crystalline nanosheets enabled by surfactant-assisted synthesis. *Chem. Sci.* **2020**, *11* (29), 7665–7671.
- (16) Nam, K. W.; Park, S. S.; dos Reis, R.; Dravid, V. P.; Kim, H.; Mirkin, C. A.; Stoddart, J. F. Conductive 2D metal–organic framework for high-performance cathodes in aqueous rechargeable zinc batteries. *Nat. Commun.* **2019**, *10* (1), 4948.
- (17) Yang, C.; Dong, R.; Wang, M.; Petkov, P. S.; Zhang, Z.; Wang, M.; Han, P.; Ballabio, M.; Bräuningner, S. A.; Liao, Z.; Zhang, J.; Schwotzer, F.; Zschech, E.; Klaus, H.-H.; Cánovas, E.; Kaskel, S.; Bonn, M.; Zhou, S.; Heine, T.; Feng, X. A semiconducting layered metal–organic framework magnet. *Nat. Commun.* **2019**, *10* (1), 3260.
- (18) León-Alcaide, L.; López-Cabrelles, J.; Mínguez Espallargas, G.; Coronado, E. 2D magnetic MOFs with micron-lateral size by liquid exfoliation. *Chem. Commun.* **2020**, *56* (55), 7657–7660.
- (19) Song, X.; Wang, X.; Li, Y.; Zheng, C.; Zhang, B.; Di, C.-a.; Li, F.; Jin, C.; Mi, W.; Chen, L.; Hu, W. 2D semiconducting metal–organic framework thin films for organic spin valves. *Angew. Chem., Int. Ed.* **2020**, *59* (3), 1118–1123.
- (20) Talin, A. A.; Centrone, A.; Ford, A. C.; Foster, M. E.; Stavila, V.; Haney, P.; Kinney, R. A.; Szalai, V.; El Gabaly, F.; Yoon, H. P.; Léonard, F.; Allendorf, M. D. Tunable electrical conductivity in metal–organic framework thin-film devices. *Science* **2014**, *343* (6166), 66–69.
- (21) Dong, R.; Zhang, Z.; Tranca, D. C.; Zhou, S.; Wang, M.; Adler, P.; Liao, Z.; Liu, F.; Sun, Y.; Shi, W.; Zhang, Z.; Zschech, E.; Mannsfeld, S. C. B.; Felser, C.; Feng, X. A coronene-based semiconducting two-dimensional metal–organic framework with ferromagnetic behavior. *Nat. Commun.* **2018**, *9* (1), 2637.
- (22) Yao, M.; Xiu, J.-W.; Huang, Q.-Q.; Li, W.-H.; Wu, W.-W.; Wu, A.-Q.; Cao, L.-A.; Deng, W.-H.; Wang, G.-E.; Xu, G. Van der waals hetero-structured MOF-on-MOF thin films: cascading various functions to realize advanced chemiresistive sensing. *Angew. Chem., Int. Ed.* **2019**, *58* (42), 14915–14919.
- (23) Stavila, V.; Talin, A. A.; Allendorf, M. D. MOF-based electronic and opto-electronic devices. *Chem. Soc. Rev.* **2014**, *43* (16), 5994–6010.
- (24) Sheberla, D.; Sun, L.; Blood-Forsythe, M. A.; Er, S.; Wade, C. R.; Brozek, C. K.; Aspuru-Guzik, A.; Dincă, M. High electrical conductivity in  $\text{Ni}_3(2,3,6,7,10,11\text{-hexaminotriphenylene})_2$ , a semiconducting metal–organic graphene analogue. *J. Am. Chem. Soc.* **2014**, *136* (25), 8859–8862.
- (25) Zhang, R.; Liu, J.; Gao, Y.; Hua, M.; Xia, B.; Knecht, P.; Papageorgiou, A. C.; Reichert, J.; Barth, J. V.; Xu, H.; Huang, L.; Lin, N. On-surface synthesis of a semiconducting 2D metal–organic framework  $\text{Cu}_3(\text{C}_6\text{O}_6)$  exhibiting dispersive electronic bands. *Angew. Chem.* **2020**, *132* (7), 2691–2695.
- (26) Skorupskii, G.; Trumpf, B. A.; Kassel, T. W.; Brown, C. M.; Hendon, C. H.; Dincă, M. Efficient and tunable one-dimensional charge transport in layered lanthanide metal–organic frameworks. *Nat. Chem.* **2020**, *12* (2), 131–136.
- (27) Qu, L.; Iguchi, H.; Takaiishi, S.; Habib, F.; Leong, C. F.; D’Alessandro, D. M.; Yoshida, T.; Abe, H.; Nishibori, E.; Yamashita, M. Porous molecular conductor: electrochemical fabrication of through-space conduction pathways among linear coordination polymers. *J. Am. Chem. Soc.* **2019**, *141* (17), 6802–6806.
- (28) Haider, G.; Usman, M.; Chen, T.-P.; Perumal, P.; Lu, K.-L.; Chen, Y.-F. Electrically driven white light emission from intrinsic metal–organic framework. *ACS Nano* **2016**, *10* (9), 8366–8375.
- (29) Xie, L. S.; Alexandrov, E. V.; Skorupskii, G.; Proserpio, D. M.; Dincă, M. Diverse  $\pi$ - $\pi$  stacking motifs modulate electrical conductivity in tetrathiafulvalene-based metal–organic frameworks. *Chem. Sci.* **2019**, *10* (37), 8558–8565.
- (30) Kung, C.-W.; Goswami, S.; Hod, I.; Wang, T. C.; Duan, J.; Farha, O. K.; Hupp, J. T. Charge transport in zirconium-based metal–organic frameworks. *Acc. Chem. Res.* **2020**, *53* (6), 1187–1195.
- (31) Goswami, S.; Hod, I.; Duan, J. D.; Kung, C.-W.; Rimoldi, M.; Malliakas, C. D.; Palmer, R. H.; Farha, O. K.; Hupp, J. T. Anisotropic redox conductivity within a metal–organic framework material. *J. Am. Chem. Soc.* **2019**, *141* (44), 17696–17702.
- (32) Yoneyama, M.; Sugi, M.; Saito, M.; Ikegami, K.; Kuroda, S.-i.; Iizima, S. Photoelectric properties of copper phthalocyanine Langmuir-Blodgett film. *Jpn. J. Appl. Phys.* **1986**, *25* (Part 1, No. 7), 961–965.

- (33) Hua, Y.; Roberts, G.; Ahmad, M.; Petty, M.; Hanack, M.; Rein, M. Monolayer films of a substituted silicon phthalocyanine. *Philos. Mag. B* **1986**, *53* (2), 105–113.
- (34) Liu, K.; Qi, H.; Dong, R.; Shivhare, R.; Addicoat, M.; Zhang, T.; Sahabudeen, H.; Heine, T.; Mannsfeld, S.; Kaiser, U.; Zheng, Z.; Feng, X. On-water surface synthesis of crystalline, few-layer two-dimensional polymers assisted by surfactant monolayers. *Nat. Chem.* **2019**, *11* (11), 994–1000.
- (35) Xiao, K.; Liu, Y.; Huang, X.; Xu, Y.; Yu, G.; Zhu, D. Field-effect transistors based on Langmuir-Blodgett films of phthalocyanine derivatives as semiconductor layers. *J. Phys. Chem. B* **2003**, *107* (35), 9226–9230.
- (36) Makiura, R.; Motoyama, S.; Umemura, Y.; Yamanaka, H.; Sakata, O.; Kitagawa, H. Surface nano-architecture of a metal-organic framework. *Nat. Mater.* **2010**, *9* (7), 565–571.
- (37) Motoyama, S.; Makiura, R.; Sakata, O.; Kitagawa, H. Highly crystalline nanofilm by layering of porphyrin metal-organic framework sheets. *J. Am. Chem. Soc.* **2011**, *133* (15), 5640–5643.
- (38) Cook, M. J.; McMurdo, J.; Miles, D. A.; Poynter, R. H.; Simmons, J. M.; Haslam, S. D.; Richardson, R. M.; Welford, K. Monolayer behaviour and Langmuir-Blodgett film properties of some amphiphilic phthalocyanines: factors influencing molecular organisation within the film assembly. *J. Mater. Chem.* **1994**, *4* (8), 1205–1213.
- (39) Fujiki, M.; Tabei, H.; Kurihara, T. In-plane dichroisms of phthalocyanine Langmuir-Blodgett films. *Langmuir* **1988**, *4* (5), 1123–1128.
- (40) Jiang, L.; Weber, J.; Puglisi, F. M.; Pavan, P.; Larcher, L.; Frammelsberger, W.; Benstetter, G.; Lanza, M. Understanding current instabilities in conductive atomic force microscopy. *Materials* **2019**, *12* (3), 459.
- (41) Foster, M. E.; Sohlberg, K.; Allendorf, M. D.; Talin, A. A. Unraveling the semiconducting/metallic discrepancy in Ni<sub>3</sub>(HITP)<sub>2</sub>. *J. Phys. Chem. Lett.* **2018**, *9* (3), 481–486.
- (42) Madsen, G. K. H.; Carrete, J.; Verstraete, M. J. BoltzTraP2, a program for interpolating band structures and calculating semi-classical transport coefficients. *Comput. Phys. Commun.* **2018**, *231*, 140–145.

## 8 Conclusion and Outlook

Due to their detrimental effect on the performance of semiconductor devices, grain boundaries in organic semiconductors have received significant research attention over the last years. While the direct relation between the number of grain boundaries (or the grain size) and the device efficiency and charge-carrier mobility is nowadays widely acknowledged [36–38, 40, 156], the fundamental processes of charge-carrier trapping and detrapping, exciton recombination and site degradation are still not well understood. To shed more light onto the intrinsic nature of grain boundaries, their emergence, electric and opto-electronic properties, and how they affect device parameters, this work presented a summary of the state of the art, followed by the investigation of grain boundaries in a specific organic semiconductor.

From a structural point of view, grain boundaries are mostly assumed to be accompanied by a change in molecular orientation. However, depending on the film thickness, such grain-grain interfaces can either be one-dimensional in two-dimensional organic films—in this case, the grain boundaries are thin and not accompanied by a change in film thickness—, two-dimensional (referred to as „void“), or three-dimensional („crevice“) [42, 51].

This work concentrates on grain boundaries in mono- to bilayer-thin films of the n-type organic semiconductor PDI1MPCN2 [53]. These films are atomically flat, even across grain boundaries, which leads to the conclusion that most grain boundaries are one-dimensional meeting points of grains with different molecular orientations. This demands a measurement technique other than AFM in tapping mode to localize and quantify grain boundaries. Therefore, we used KPFM in the first part of this work and investigated the locally-resolved surface potential of single grains and grain boundaries. Depending on their surface-potential distribution with respect to the surrounding grains, the grain boundaries could be divided into two energetically different types, namely barriers and valleys.

By comparing variations in thin-film application, films with only barriers or valleys could be applied. As a consequence, it will be possible in the future to control the prevalent energy landscape within a semiconducting film of PDI1MPCN2. A mixture of the modified preparation techniques even resulted in films with both types of grain boundaries, which was the first experimental proof that energy barriers and valleys can coexist in the same film. This coexistence is not only notable as it implies that the processing conditions alone do not define the energetic appearance of grain boundaries, but it also underlines the necessity to differ between grain boundaries that trap and grain boundaries that backscatter charge carriers (in this case electrons).

Finally, we investigated the barrier height / valley depth for different charge-carrier densities in the semiconductor, which we tuned by electrostatic gating (electrons) and optical excitation (holes). It could be observed that barriers and valleys, as well as energetic variations within single grains, vanish in the potential of trapped charges if the charge-carrier density is increased toward the operation regime of field-effect transistors. However, in the working regime of OLEDs or organic solar-cells, grain boundaries are still significant, which demands for further investigation of grain boundaries.

The second part of this thesis advanced from electrostatic to time-dependent KPFM at three different classes of sites, namely a grain, a valley and a barrier. At each site, the

evolution of the surface potential was detected while successively increasing (decreasing) the gate voltage in an OFET, thereby simulating the transition from its „off“ state to its „on“ state (from „on“ to „off“). The related transition from a time-independent to exponentially time-dependent surface potential allowed to extract local turn-on and threshold voltages for each of the sites and to compare it to global device parameters.

While the experiments presented in this chapter need repetition on more samples for reasonable statistics, the results give first evidence that single local impurities define the properties of the whole device, especially hysteresis effects and the turn-on and threshold voltages. However, not all impurities affect these global device parameters to the same extent, but they depend more on the properties detected at valleys. This observation fits well to the suggestions made from simulations and conductive AFM, which proposed that (deep) valleys form a conductive path through which charge transport takes place. The results may also help to understand device-to-device variabilities typical for organic-semiconductor devices, since not only the number of grain boundaries, but also their type and depth/height has to be controlled.

Controlling the emergence of grain boundaries, their type and especially their height, however, still poses one of the main challenges in the field of organic semiconductors. Therefore, the third chapter of this work proposed an alternative to eliminating grain boundaries in organic thin-films by manipulating charge transport across grain boundaries by illumination. Similar to the photoexcitation of currents in optically-active devices, photons with energies corresponding to the barrier height or valley depth may be absorbed and provide the energy needed to excite an electron out of a valley or over a barrier. In this case, the electric current across grain boundaries can not only be enhanced, but this method will also help to localize and quantify grain boundaries, even in bulk-like materials where KPFM fails since it is a surface-sensitive technique.

With this aim, a setup was built for photocurrent-spectroscopy measurements, starting from a commercial Fourier transform infrared spectrometer. Its working principle and light source were used, because the absolute height of grain boundaries corresponds to the energy of the far-infrared range.

Their preliminary results show that the setup is working, while absolute photocurrents, not to mention photocurrent spectra, could not be measured yet. Since the photocurrents are expected to lie below the noise level, the conclusion and outlook of this chapter present several suggestions to improve the signal-to-noise ratio and make photocurrents detectable.

Besides the concrete suggestions for further experiments made in the respective chapters, the results demand further investigations of grain boundaries in monolayer thin-films of PDI1MPCN2.

The first and most important question to be addressed is: Why and how do energy barriers and valleys emerge? This question includes structural differences between energy barriers and valleys. As an example, it is widely accepted that the change in molecular orientation determines the grain-boundary resistance, or valley depth, respectively [42, 48]. However, this relationship could not be verified by simulations on energetic barriers [48]. To address this question, experiments beyond the ones presented in this work are necessary, since KPFM was not able to simultaneously detect the surface potential of grain boundaries and the molecular orientation within surrounding grains. Combined experiments of KPFM and confocal photo-luminescence microscopy as presented in Reference [59] at the very same grain boundaries should help to examine the impact of the orientation change on the absolute and relative grain-boundary height (or depth).

KPFM could also be used to investigate the mechanisms of device degradation at grain boundaries, since the surface potential is expected to change if impurities are trapped within the

semiconductor, or molecules are oxidized. In a simple experiment, transport measurements and KPFM measurements could be alternated with storage in air, vacuum or nitrogen atmosphere.

As a next step, it will be interesting to investigate which device parameters other than the threshold voltage are determined by local impurities. Specific focus should lie on the activation energy, which is typically measured in global transport measurements, but defined as the energy to excite an electron out of a localized state. Recent simulations by Meier et al. [52] suggest that the activation energy is less affected by the type than by the grain-boundary depth/height, since deep valleys lead to a different pathway through the semiconductor than shallow valleys. Even more, data simulated by coworkers, as well as first temperature-dependent transport-measurements, presented in the Appendix of this work, suggest that the number of grain boundaries also plays an important role. These data are given as a starting point for promising examinations of the impact of grain boundaries on the activation energy in the future.

Finally, similar investigations as shown within this work on another semiconductor molecule would be interesting to conduct. If one or several findings of this work can be reproduced in films of a different molecule, their general interest for the field of organic electronics will be further supported.



# Appendix

## A Influence of Grain Boundaries on the Activation Energy

This section presents a project that aims to investigate the impact of grain boundaries on the activation energy in thin-film transistors of PDI1MPCN2. The project was started, but could not be finished due to difficulties in sample preparation and out of personal reasons. However, the work done so far will be summarized here as a give-away for future researchers in this project.

### A.1 Motivation

As we have seen, it is widely accepted that grain boundaries affect the performance of semiconducting devices, above all the mobility [156,171], but also the on-off ratio [68], turn-on and threshold voltages [68,126,154,155], as well as the channel and contact resistance [42,43,126,165]. Few works also report that the activation energy is affected [68]. However, it is so-far unclear, whether the number, the type, the height, or a combination of all influence the activation energy. Simulations on the activation energy reveal a clear correlation with the number of grain boundaries, as long as all grain boundaries act as valleys (cf. **Figure A.1b**). This finding also fits with recently published simulations by Meier et al. [52]. The results of these simulations serve as a starting point for the measurements presented in this section, where the number of grain boundaries within the conductive channel of TFTs was varied and the activation energy was determined.

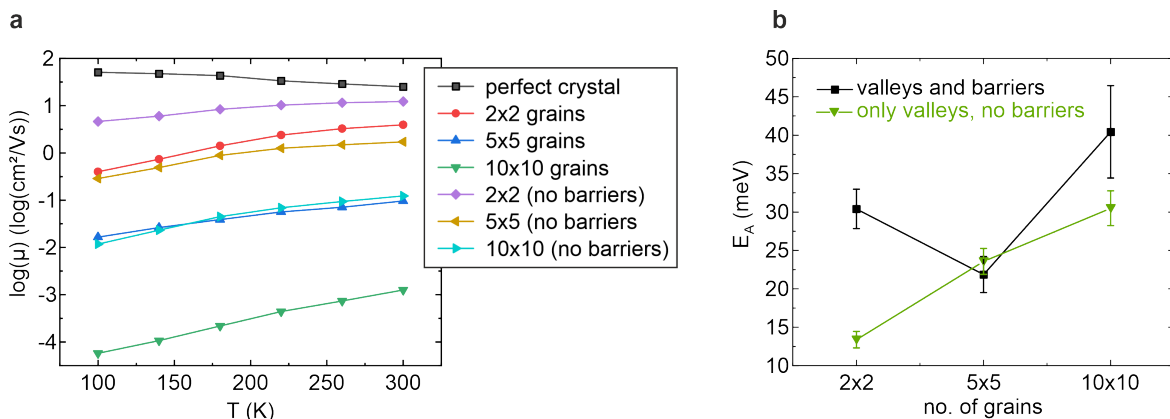


**Figure A.1 Simulated mobilities (a) and activation energies (b) for varying grain-boundary densities.** The number of grains is increased within a fixed area of the conductive channel. The grains are either valleys and barriers, or only valleys, as denoted in the legends. The data were simulated by Michael Kühn, details on the simulations are presented in the Supporting Information of Reference [48].

## A.2 Technical Details

### Sample Preparation

Samples were prepared as presented in Section 3.1 in the main text on substrates with 30 nm of  $\text{Al}_2\text{O}_3$ . Shadow masks with channel lengths of  $L = 20\ \mu\text{m}$  or  $L = 200\ \mu\text{m}$  were applied after solution-based thin-film formation. Using POM, the shadow masks were placed such that either one or no grain boundaries are located within the channel. Since this requires precise work, each shadow mask consists of only one electrode pair (cf. **Figure B.4**), which is placed twice on each sample. Hence, each sample consists of two transistors with a different amount of grain boundaries within the channel (preferably zero or one), as displayed in **Figure A.2d,e**.

Since the samples were supposed to be used for FTPC measurements (cf. Chapter 6) afterwards, the contacts have to be bondable. This means that 1. the contacts have to be connected to pads large enough that they can be covered with a droplet of silver conductive paint and 2. those pads have to be far enough apart from the channel that the droplet of silver conductive paint cannot touch the channel. The masks shown in **Figure B.4** fulfill these conditions, but the bridges of the contacts usually cross the border of the organic thin-film spot, where the molecule agglomerates in high, bulk-like structures that may break the contacts. Therefore, all agglomerations on the thin-film spot, especially at its border, were scratched away before placing the shadow mask.

After contact evaporation and prior to measurements, the organic film was scratched around source and drain prior to reduce leakage currents at the edges of the electrodes (cf. Section 2.4). The backside of the samples was scratched and glued with silver conductive paint onto the sample stage of the vacuum probe-station to enable good electric and thermal coupling.

Within this project, many more samples than presented in Section A.3 have been prepared and evaluated. However, the contact geometry and the thinness of the organic semiconductor make the samples extremely fragile. Hence, samples tend to break already during fabrication, or during the measurements (most likely the channels or contacts are scratched by the probe needles). Even more, placing the masks by hand on top of the semiconductor and fixing them such that they stay at the desired position during evaporation is extremely prone to errors. Therefore, only the three samples presented in **Figure A.3** remained.

### Measurements

The samples were examined in a vacuum probe-station at temperatures between 40 and 400 K in steps of 40 K. For each temperature, the output characteristics, and transfer curves in the linear ( $V_{\text{DS}} = 1\ \text{V}$ ) and the saturation ( $V_{\text{DS}} = 4\ \text{V}$ ) regime were recorded.

### Evaluation

The transfer curves in the linear regime were plotted as a function of the density of free charge-carriers  $n_{\text{free}}$  as displayed in **Figure A.2a** and **f** for two exemplary devices on one sample. The mobility was calculated as described in Section 2.4 (**Figure A.2b,g**) and extracted at fixed values for  $n_{\text{free}}$ . The mobility at fixed free-charge-carrier densities can then be plotted as a function of temperature, as can be the threshold voltage (**Figure A.2c,h**). We extracted the mobility at values for  $n_{\text{free}}$  between  $1 \cdot 10^{12}\ \text{cm}^{-2}$  and  $1 \cdot 10^{13}\ \text{cm}^{-2}$  in steps of  $1 \cdot 10^{12}\ \text{cm}^{-2}$  to extract the activation energy from an Arrhenius plot (described in Section 2.3). The resulting activation energies at different values for  $n_{\text{free}}$  and for varying numbers of grain boundaries in the channel are presented in Section A.3.

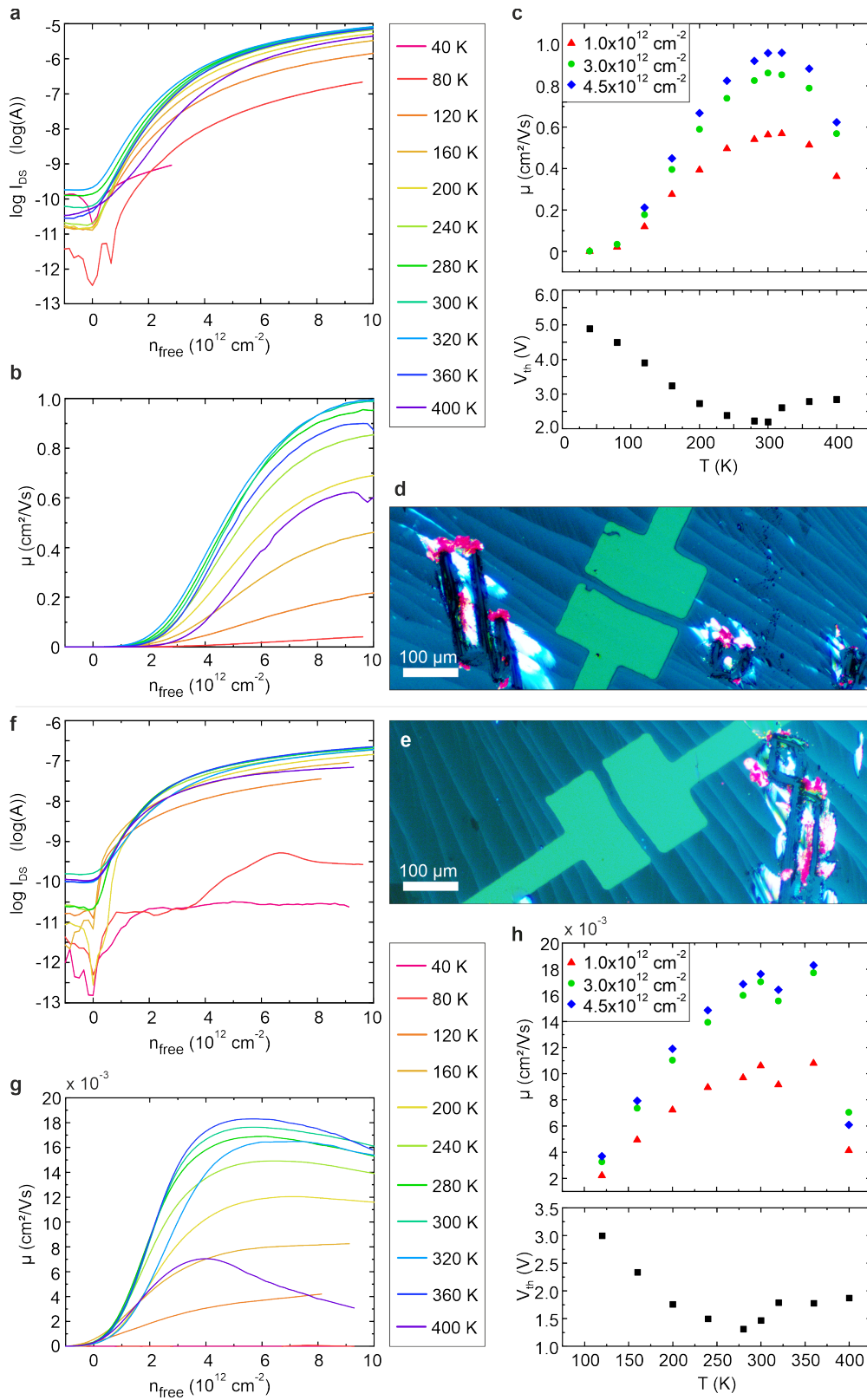


**Figure A.2** Measurement data for one representative sample consisting of two TFT devices. **a,b**, Drain-source current  $I_{DS}$  and mobility  $\mu$  for the device shown in **d**). **c**, Temperature-dependent mobility and threshold voltage for the device shown in **d**). **d,e**, The devices of one sample have either one or no grain boundary within the channel. **f-h**, Drain-source current  $I_{DS}$ , mobility  $\mu$ , and temperature-dependent mobility and threshold voltage for the device shown in **e**).

### A.3 Results

**Figure A.3** depicts the results obtained so-far for temperature-dependent transport-measurements in devices with varying numbers of grain boundaries. Since the device-to-device variability is larger than the differences observed between devices with or without grain boundaries in the channel, we plotted the results for each sample in a single graph **a-c**.

The data show clear evidence that the existence of one grain boundary raises the activation energy, consistently at all evaluated charge-carrier densities. This observation also holds for increasing the number of grain boundaries from 4 to 6 (cf. **Figure A.3c**). However, more data are needed for reasonable statistics.

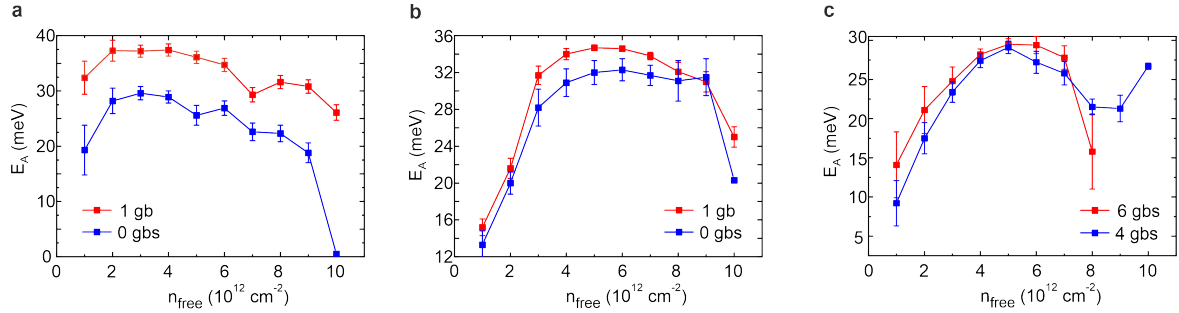


**Figure A.3** Activation energy  $E_A$  as a function of the density of free charges  $n_{\text{free}}$  detected on three different samples. Each sample consists of two devices with a different number of grain boundaries in the conductive channel: **a,b**, One or no grain boundary, **c**, 6 or 4 grain boundaries.

### A.4 Discussion and Outlook

The activation energy is originally defined for the multiple-trapping-and-release model, which assumes that the trap-state density is significantly smaller than the total density of states [51, 85]. Here, we investigate the activation energy of areas that can be regarded as highly crystalline, if no grain boundaries are within the channel. For devices with one or few grain boundaries within the channel, the condition has to be taken with care. Since the grain boundaries are assumed to be infinitesimally thin, the grains still make the largest portion of the channel area. However, as we can see in KPFM measurements, the surface potential is affected over a wider range around the grain boundaries (compare Publication **P2** in Chapter 4), which is why we also have consider pure hopping transport in these devices. Another limitation for the presented results is the Arrhenius approach, which only holds in the gradual-channel approximation. It is of great importance to check whether this condition is fulfilled close to the potential of single grain boundaries, or if the band bending leads to further restrictions.

So-far, we have only prepared samples that are assumed to consist of grain boundaries that act as valleys. The results obtained and presented in **Figure A.3** therefore can be well compared to the simulations presented in **Figure A.1**. It would be, however, of large interest if the same holds when devices with barriers in the channel are prepared using the processing conditions presented in Publication **P2** (Chapter 4).

## B Technical Details on Shadow Masks

This section presents an overview of the used masks within this work. Depending on the respective experiments, the following mask was used:

- standard transistors with varying channel lengths, to check if transistors work at all (cf. **Figure B.4a**)
- ring-like contacts for the investigation of directional charge transport (e.g. Thesis **T1**, cf. **Figure B.4b**).
- single transistors to contact single grain boundaries and bond the electrodes afterwards (e.g. Chapter 6, Section A, cf. **Figure B.4c**)
- standard transistors with varying channel lengths, to check if transistors work at all and to investigate the influence of the channel area on the absorbance (e.g. Chapter 6, cf. **Figure B.5d**)
- mask for contacting single grain boundaries in the KPFM setup and to ground the semiconducting film close to these grain boundaries (e.g. Chapter 4, Chapter 5, cf. **Figure B.5e**)

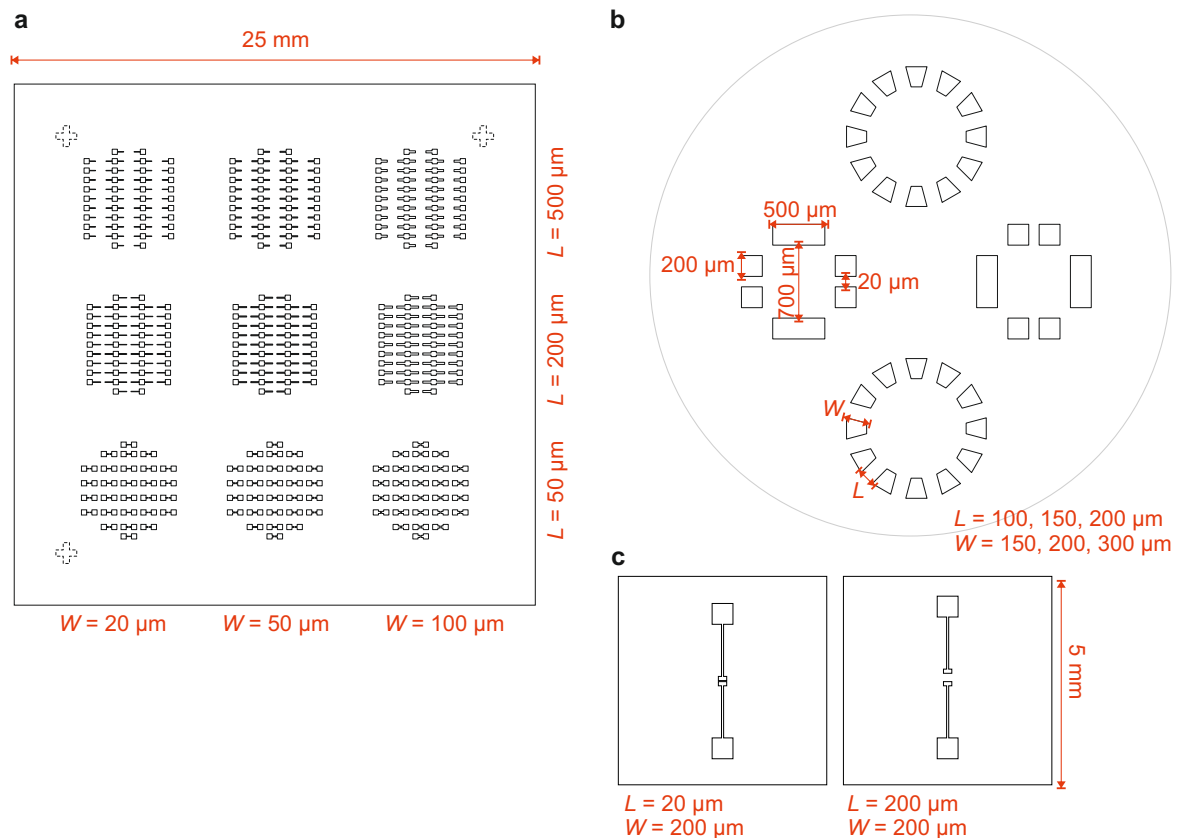


**Figure B.4 Overview over the shadow masks used within this work (part 1).** **a**, Mask named „transistors“ with varying channel lengths and widths, as denoted. Each group of contacts is supposed to be placed onto one organic thin-film spot. The dashed lines mark contacts used for mask calibration. **b**, Part of a mask named „pie“. This mask has the same structure as the mask shown in **a**), with varying channel lengths and widths, which is why only one contact group is shown in detail. **c**, Masks named „20  $\mu\text{m}$ -transistor“ or „200  $\mu\text{m}$ -transistor“, depending on the channel length.

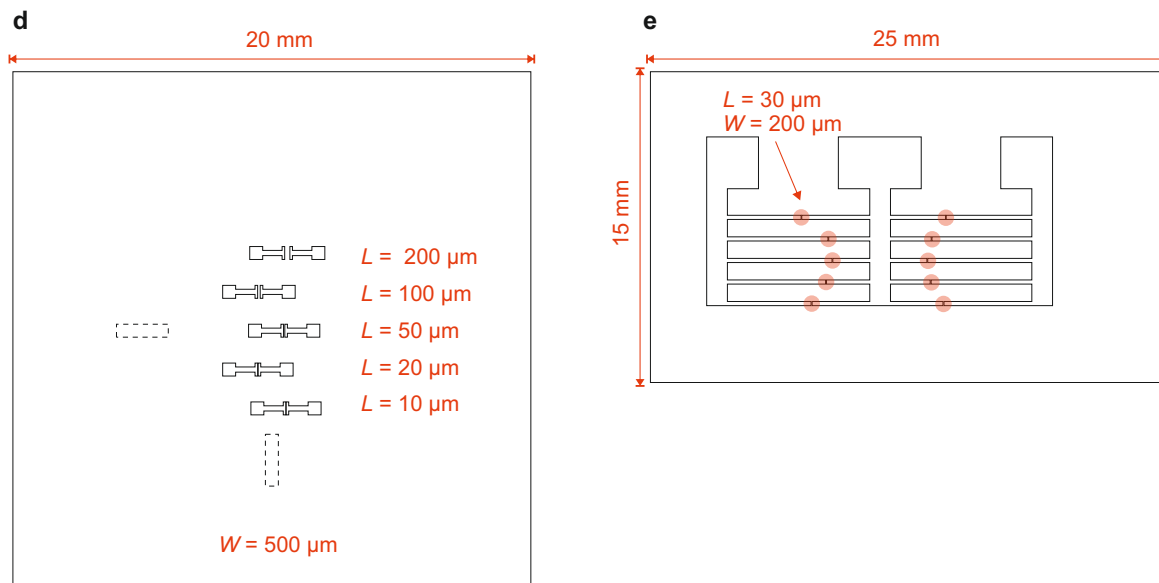


**Figure B.5 Overview over the shadow masks used within this work (part 2).** d, Mask named „lab course“ with increasing channel lengths and constant channel width. e, Mask named „KPFM“. The position of the channels with fixed channel length and width are marked by red spots.

## C Technical Details on Atomic Force Microscopy

To take a nice picture of organic thin-films, the following procedure has proven successful (valid for the setups and corresponding tips presented in **Table C.1**):

1. Check if the tip is still good on a small area of a clean, hard surface, e.g. a gold contact. (Tips can be „cleaned“ by setting the tip hard on the measured surface, i.e. decreasing the amplitude set point for all used devices and choosing a very high scan rate. Then let the tip run over the surface for some time.)
2. Choose the area you want to detect, accept a bad quality and low resolution.
3. Increase the amplitude set-point until the tip loses contact, i.e. trace and retrace show a free oscillation.
4. Decrease the amplitude set point until trace and retrace resemble to each other. Decrease it a little further. Have a look on the detected phase. If it shows stripes or gets unstable, the set point is too low.
5. Increase the integral gain until the trace and retrace look identical and sharp. If very smooth areas get noisy, also increase the proportional gain.
6. Correct the amplitude set-point and the gains iteratively.
7. If the images don't get nice, change the drive frequency slightly above resonance, that is, into the attractive regime (be super careful with this change!). Then repeat steps 3-7.

However, note that every instruction can only be a rough guide. You yourself as a user have to find out the best options depending on your sample and the setup you are using.

**Table C.1** Overview over the used setups to measure AFM and AFM-related modes. An 'x' denotes that the respective mode has been used and data are shown within this work. The used tips (italic) refer to: *Tap300Al-G*:  $k = 40 \text{ N/m}$ ,  $\omega_0 = 300 \text{ kHz}$ , *tip radius = 10 nm*, *Aluminum reflex coating on detector side*; *SCM-PIT*:  $k = 2.8 \text{ N/m}$ ,  $\omega_0 = 75 \text{ kHz}$ , *tip radius < 25 nm*, *PtIr coating on both sides*; *Asyelec01*:  $k = 2.8 \text{ N/m}$ ,  $\omega_0 = 75 \text{ kHz}$ , *tip radius = 25 nm*, *TiIr coating on both sides*. [172,173]

	topography	c-AFM	KPFM	atmosphere
<b>Bruker Dimension3100</b>	x <i>Tap300Al-G</i>			ambient (clean room)
<b>Bruker Icon</b>	x <i>Tap300Al-G</i>	x <i>SCM-PIT</i>	x (lift mode) <i>SCM-PIT</i>	ambient (clean room)
<b>Asylum Jupiter</b>	x <i>Tap300Al-G</i>	x <i>SCM-PIT</i> or <i>Asyelec01</i>	x (lift mode) <i>SCM-PIT</i>	ambient
<b>Asylum MFP-3D</b>	(simultaneously w KPFM)		x (FM heterodyne) <i>SCM-PIT</i>	glovebox (N <sub>2</sub> )

## D Technical Details on FTIR Spectroscopy

**Table D.2** denotes the ranges of different beamsplitter materials. **Figure D.6** displays different units that can be inserted into the sample chamber of the FTIR spectrometer. Thereby, the FTIR spectra can either be detected in transmission (the sample is simply placed in the beam path, not shown here), reflection (a) or under grazing incidence (b). **Figure D.6c** displays the modifications made to the transmission unit, where a sample holder with a connection to an electrical feed-through was implemented for photocurrent measurements.

**Table D.2** Ranges of typical beamsplitter materials. [143]

KBr	7500 cm <sup>-1</sup> - 370 cm <sup>-1</sup>	6 $\mu$ -Mylar	480 cm <sup>-1</sup> - 60 cm <sup>-1</sup>
CaF <sub>2</sub>	10 000 cm <sup>-1</sup> - 1850 cm <sup>-1</sup>	Quartz	14 000 cm <sup>-1</sup> - 5500 cm <sup>-1</sup>

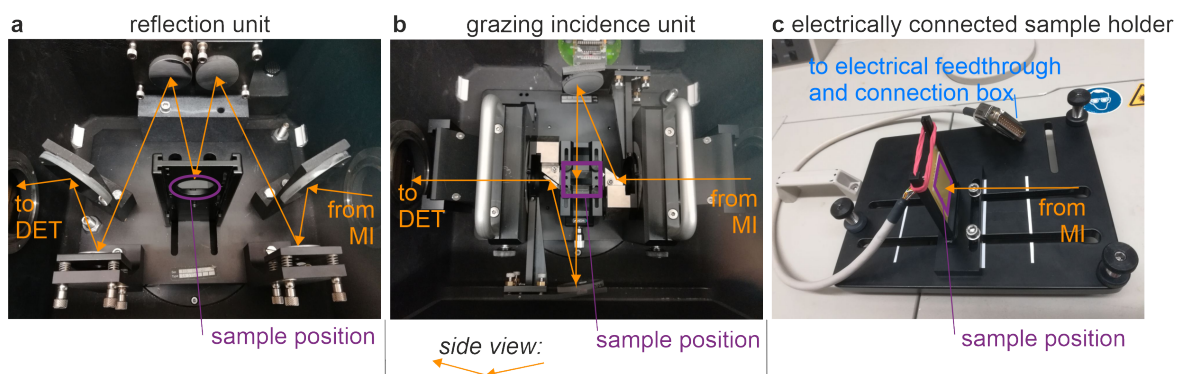


**Figure D.6** Different sample units for the FTIR spectrometer. If the transmission spectrum of the sample is supposed to be measured, it is just placed into the beam path. **a,b** Units for reflective measurements under small incident angles (a) or grazing incidence (b, top and side view). **c**, For photocurrent measurements, an electrically connected sample holder is placed into the beam path. It can be connected to a bonded sample as shown in **Figure 3.2** in Chapter 3.

## E Supporting Information to Chapter 4



### Supporting Information

for *Small*, DOI: 10.1002/sml.202200605

Revealing and Controlling Energy Barriers and Valleys at  
Grain Boundaries in Ultrathin Organic Films

*Lisa S. Walter, Amelie Axt, James W. Borchert, Theresa  
Kammerbauer, Felix Winterer, Jakob Lenz, Stefan A. L.  
Weber, and R. Thomas Weitz\**

## Supporting information

for

### Revealing and controlling energy barriers and valleys at grain boundaries in ultrathin organic films

L.S. Walter<sup>1,2</sup>, A. Axt<sup>3</sup>, J.W. Borchert<sup>2</sup>, T. Kammerbauer<sup>1</sup>, F. Winterer<sup>1</sup>, J. Lenz<sup>1</sup>, S.A.L. Weber<sup>3,4</sup>,

R.T. Weitz<sup>\*1,2,5</sup>

<sup>1</sup> Faculty of Physics, Ludwig-Maximilians-Universität München, Munich, Germany

<sup>2</sup> I. Institute of Physics, Georg-August-Universität Göttingen, Göttingen, Germany

<sup>3</sup> Max Planck Institute for Polymer Research, Mainz, Germany

<sup>4</sup> Institute of Physics, Johannes Gutenberg-Universität Mainz, Mainz, Germany

<sup>5</sup> Center for Nanoscience (CeNS), Ludwig-Maximilians-Universität München, Munich, Germany

\* [thomas.weitz@uni-goettingen.de](mailto:thomas.weitz@uni-goettingen.de)

## A. Interpretation of the measurement signal

Kelvin probe force microscopy (KPFM) measures the local contact-potential difference (CPD)<sup>1</sup> which can be defined as

$$eU_{CPD} \equiv W^{OSC} - W^{tip}, \quad (\text{A.1})$$

where  $W^{OSC}, W^{tip}$  is the work function of the organic semiconductor (OSC) or the tip, respectively. Under the assumption of the Fermi energy being constant over the whole system, this expression is equivalent to the definition given by Tal et al.<sup>2,3</sup> and Roelofs et al.<sup>4</sup>

$$eU_{CPD} = E_{vac}^{OSC} - E_{vac}^{tip}. \quad (\text{A.2})$$

On the other hand, if we assume constant vacuum levels, we result with the definition given by e.g. Axt et al.<sup>5</sup> to

$$eU_{CPD} = E_F^{tip} - E_F^{OSC}. \quad (\text{A.3})$$

For equation (A.2) and (A.3) we used  $W = E_{vac} - E_F$  for both, tip and organic semiconductor. We emphasize the difference between both formulas in order to show that the expressions are consistent, but only if the right conditions are chosen. For the following description, we choose  $E_{vac}(z) = const.$ , i.e. in the direction out of plane of the semiconductor surface.

As found from the measurements presented in **Figure 2** in the main text, the CPD differs for grains and grain boundaries. For “positive” (+) and “negative” (-) grain boundaries we find with equation (A.1)

$$U_{CPD}^+ > U_{CPD}^{grain} > U_{CPD}^- \Leftrightarrow W^+ > W^{grain} > W^- \Leftrightarrow E_A^+ > E_A^{grain} > E_A^-, \quad (\text{A.4})$$

where  $E_A = E_{vac} - E_{LUMO}$  is the electron affinity, i.e. the difference between the vacuum energy and the lowest unoccupied molecular orbital (LUMO), and therefore

$$U_{CPD}^+ > U_{CPD}^{grain} > U_{CPD}^- \Leftrightarrow E_{LUMO}^+ < E_{LUMO}^{grain} < E_{LUMO}^-. \quad (\text{A.5})$$

Therefore, “positive” grain boundaries can be related to a downwards-bending LUMO at the grain-grain interface, that is, an energetic valley and *vice versa* for barriers.

If a gate voltage  $V_{GS} > 0$  is applied, positive charges accumulate at the gate-insulator interface and electrons are injected from the metal contact into the OSC. Due to the accumulation of electrons with density  $n$  at the insulator-semiconductor interface<sup>6</sup>, the detected CPD changes. The energy relations in  $z$ -direction, that is, the gate-insulator-semiconductor-air-tip collective is sketched in detail for a p-type OSC in ref. <sup>2</sup> ( $E_F(z) = const.$ ) or ref. <sup>4</sup> ( $E_{vac}(z) = const.$ ). The latter can directly be applied to our case if changing signs for  $V_{GS}$ , in order to account for an n-type OSC.

As a consequence of increasing charge-carrier density, the CPD changes corresponding to the shift of the LUMO (and the HOMO):

$$e\Delta U_{CPD} = \Delta E_F^{tip} = \Delta E_{vac}^{OSC} = \Delta E_{LUMO} = \Delta E_{HOMO} \quad (A.1)$$

As, in this model, the LUMO shifts to smaller energies (according to an increased number of electrons in the OSC), we should also find

$$\Delta E_{LUMO} = E_{LUMO}(V_{GS} > 0) - E_{LUMO}(V_{GS} = 0) < 0. \quad (A.2)$$

However, as we measure the opposite sign (compare **Figure S6** and **Figure S7**), we have to consider that the injected electrons in the semiconductor do not completely screen the gate potential as long as the FETs are performed in the subthreshold region<sup>6-8</sup> (we determined the threshold voltage of corresponding transistors to approximately 3 V). Consequently, we measure the unscreened part of the gate potential additionally to the CPD<sup>4,9,10</sup> and we have to rewrite the detected signal to

$$U_{SP} = (1 - \beta)V_{GS} + U_{CPD}. \quad (A.3)$$

Here, the first term is the sum of the potential at the gate-insulator interface  $\Phi_G = V_{GS}$  and the potential at the insulator-semiconductor interface  $\Phi_S = -\beta V_{GS}$  with  $0 \leq \beta \leq 1$ . The factor  $\beta$  includes all screening-suppressing effects such as capacitive effects of the gate dielectric, contact resistances, or trap states at the interfaces<sup>11,12</sup>, and therefore depends on position, time and  $V_{GS}$ . This leads to two important requirements for the evaluation of our measurements (also cf. Section C): First, for each area detected at a certain  $|V_{GS}| > 0$ , we detected an additional reference measurement with  $V_{GS} = 0$  at the very same position. Second, we extracted values from such areas excluding the first and last two scan lines, in order to eliminate any time-dependencies of the charging of the semiconductor.

**Figure S1** displays the signal noise of the setup at zero, positive and negative gate voltages. As can be observed, the measurement resolution is not affected by crosstalk or capacitive effect due to the applied gate voltages. This observation validates the use of the measurement technique for the investigation of surface potentials in monolayer-thin semiconducting films also at higher voltages.

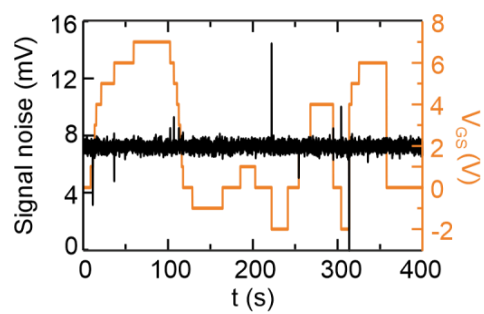


**Figure S1 Signal noise of the measurement.** Different gate voltages between -2 and 7 V were applied during measurement in order to show that they do not affect the measurement resolution. The signal noise is constantly slightly below 8 mV.

## B. Surface potential variations as a measure of charge-carrier density

As described in the main text, the surface-potential distribution within single grains of the OSC thin-film can be attributed to defects or charge inhomogeneities at the semiconductor-dielectric interface. **Table S1** summarizes rms values for the topography and the surface potential of thin films on different substrates; indicating that topographically rougher insulators lead to higher surface potential variations in the OSC thin-films.

**Table S1 rms values for substrates with different insulators.** The given values are mean values and standard deviations out of 5 measurements (for the thin film on Al<sub>2</sub>O<sub>3</sub>, only 4 measurements were evaluated).

	Al <sub>2</sub> O <sub>3</sub>	SiO <sub>2</sub>
rms roughness of clean substrate (pm)	96.0 ± 4.0	159.0 ± 31.0
rms( $U_{SP}$ ) of clean substrate (mV)	2.1 ± 0.3	2.4 ± 0.2
rms( $U_{SP}$ ) of thin film PDI1MPCN2 (mV)	10.3 ± 4.5	18.3 ± 1.6

Furthermore, it was found that this potential distribution can be screened by injecting charge carriers of a density  $n$  into the organic semiconductor by applying a gate voltage  $V_{GS}$ . While we discussed the direct influence of  $V_{GS}$  on the measurement signal in the previous section, we will describe the translation from the gate voltage to the charge-carrier density and its impact on rms( $U_{SP}$ ) in more detail in the following.

The charge-carrier density  $n$  in the organic semiconductor can be calculated by

$$n = \frac{C_i}{e} \cdot (V_{GS} - V_0),$$

where  $C_i$  is the capacitance per unit area of the insulator (measured to 229 nF/cm<sup>2</sup> for substrates with aluminum oxide),  $e$  the elementary charge,  $V_{GS}$  the applied gate voltage and  $V_0$  an onset voltage. The latter cannot directly be measured, since this would require to build a local field-effect transistor, and is consequently determined from the measurement data. For this purpose, the surface potential of the organic thin film was detected within the same area for different gate voltages as shown in **Figure S2**. From each area, the rms( $U_{SP}$ ) was extracted using the software Gwyddion<sup>13</sup> and plotted as shown in **Figure S3** for two different samples. As can be consistently observed, rms( $U_{SP}$ ) decreases for positive gate voltages and increases rapidly for negative gate voltages. Therefore, the data within the range of positive  $V_{GS}$  were fitted by a function of exponential decay. The crossing point with the mean value of the data for negative  $V_{GS}$  where the film is completely depleted of free charge carriers gives  $V_0$ , as graphically shown in **Figure S3**.

We end up with  $V_0 = -0.2 \pm 0.1$  V for the sample shown in **Figure 1** and **4b** of the main text (**Figure S3a**) and  $V_0 = -1.2 \pm 0.2$  V for the sample shown in **Figure 4a** of the main text (mean of **Figure S3b** and **c**). Please note, that these onset voltages are not necessarily the same as the ones that could possibly be determined from electrical measurements on field-effect transistors. Rather, the here-given onset voltages describe the voltage at which the organic semiconductor is completely free of excess charge carriers. Finally, the charge-carrier density at which no *external* charge-carriers are induced, is given by  $n_0 = n(V_{GS} = 0)$ .

From **Figure S4** it can be observed, that the surface potential of mono- and trilayers differ for finite charge-carrier densities, and equalizes if the semiconductor is free of excess charge carriers, i.e.  $n = 0$ , as discussed in the main text.

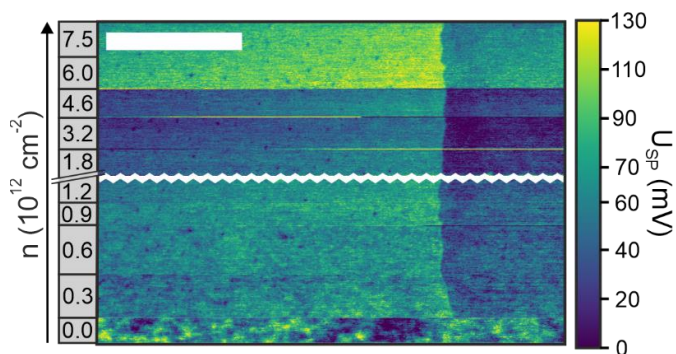


**Figure S2 Surface potential for varying charge-carrier density  $n$ .** The figure is a combination of several scans taken in the same spatial region as the scan in Figure 1b,c (main text), while holding  $n$  constant over several lines (slab of  $0.5 \mu\text{m}$  in the  $y$ -direction).

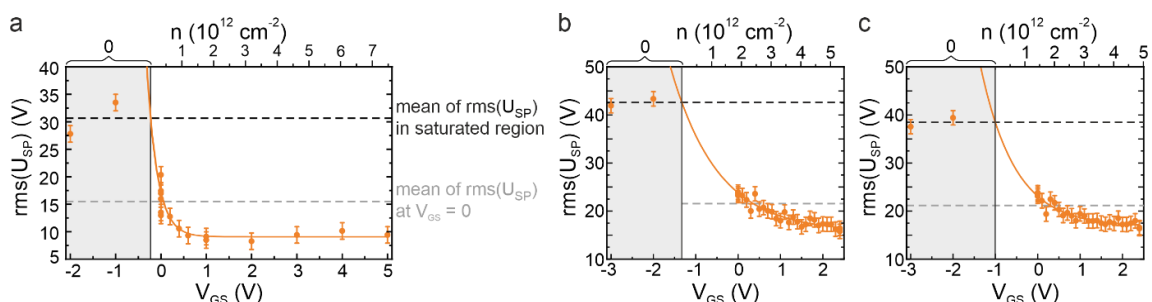


**Figure S3 Extraction method of the charge carrier density from in-operando KPFM measurements.** The procedure is described in the text. **a**,  $\text{rms}(U_{SP})$  extracted from the scan shown in Figure 1 and 4b of the main text. **b,c**,  $\text{rms}(U_{SP})$  extracted from the scan shown in Figure 3a of the main text, where b) refers to the part on the left of grain boundary and c) on the part on the right of the grain boundary. For the plots shown in the main text, all values for  $n = 0$  were set to the same value on the x-axis.

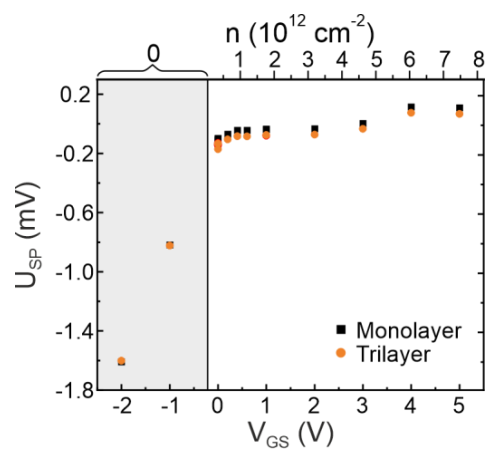


**Figure S4 Gate-dependent surface potential for mono- and trilayer.** At negative gate voltages, i.e. zero charge-carrier density, mono- and bilayers have the same surface potential and the step disappears as visible in Figure 1 of the main text.

### C. Surface potential at grain boundaries – detection and evaluation

**Figure S5a** and **b** display the topography images of two exemplary monolayer-thin regions of the PDI1MPCN2 film including grain boundaries. As can be seen, the grain boundaries are not visible in the topography scans, which we discuss in more detail in the main text.

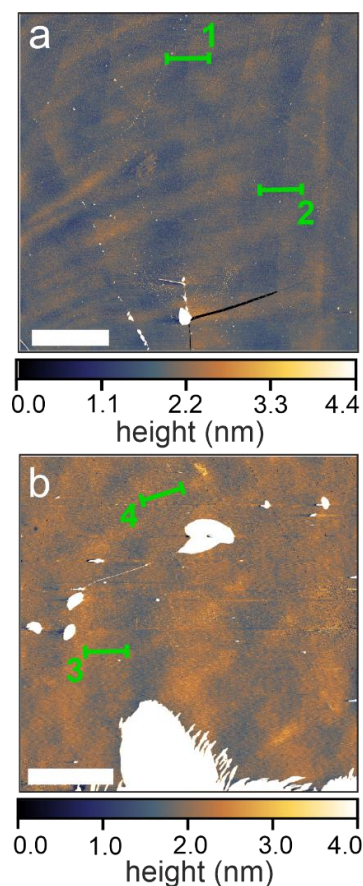


**Figure S5a,b** Topography scans at monolayer-thin films including grain boundaries. The images correspond to the areas shown in Figure 2 of the main text. The given lines indicate the positions where the line profiles shown in Figure 2c,d were extracted.

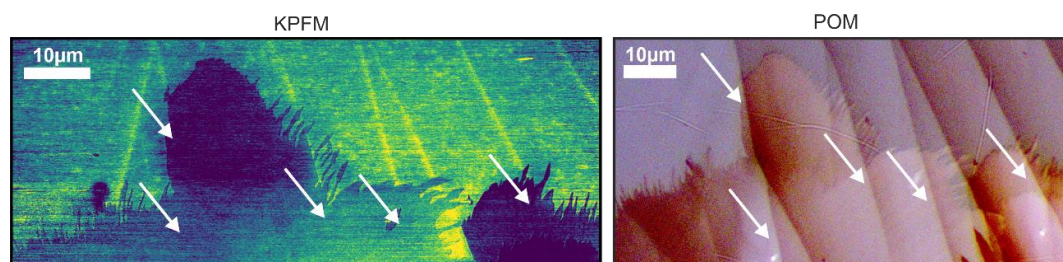


**Figure S5c** KPFM and POM image of a monolayer-trilayer and monolayer-fourlayer step. The grain boundaries visible in POM are not visible in KPFM, if more than one layer is present on the surface.

All presented AFM data were manipulated using the software Gwyddion<sup>13</sup> as described in the Experimental Section of the main text. Afterwards, the extracted line profiles of the KPFM scans were fitted by a Lorentzian<sup>14</sup> (cf. **Figure S6**, **Figure S7**) of the form

$$y = y_0 + \frac{2A}{\pi} \cdot \frac{w}{4(x-x_c)^2+w^2}, \quad (\text{C.1})$$

where  $y_0$  is the potential far away from the peak position,  $A$  is an amplitude factor giving  $y_c = y_0 + \frac{2A}{w\pi}$ , the global minimum/maximum,  $x_c$  the peak position and  $w$  the full width at half maximum (FWHM). Consequently, we interpret  $y_0$  as surface potential within the grains,  $y_c$  as the grain boundary potential, and  $|y_c - y_0| = \left| \frac{2A}{w\pi} \right|$  the barrier height or valley depth, respectively. Errors were calculated from fit errors using error propagation.

For in-operando measurements, we first detected a small area of a grain boundary where it was approximately constant in width and barrier height or valley depth (judged by eye) at zero gate voltage after the sample had been under measurement for several hours so that thermal drift can be neglected. Afterwards, we scanned the same spot with the same scanning direction and scan rate, while applying a constant gate voltage for several lines. We increased  $V_{GS}$  in steps of 0.1 V after each 20<sup>th</sup> line up to 2.4 V for the data shown in **Figure S6** (barrier) and after each 42<sup>nd</sup> line up to 1.0 V for the data shown in **Figure S7** (valleys).

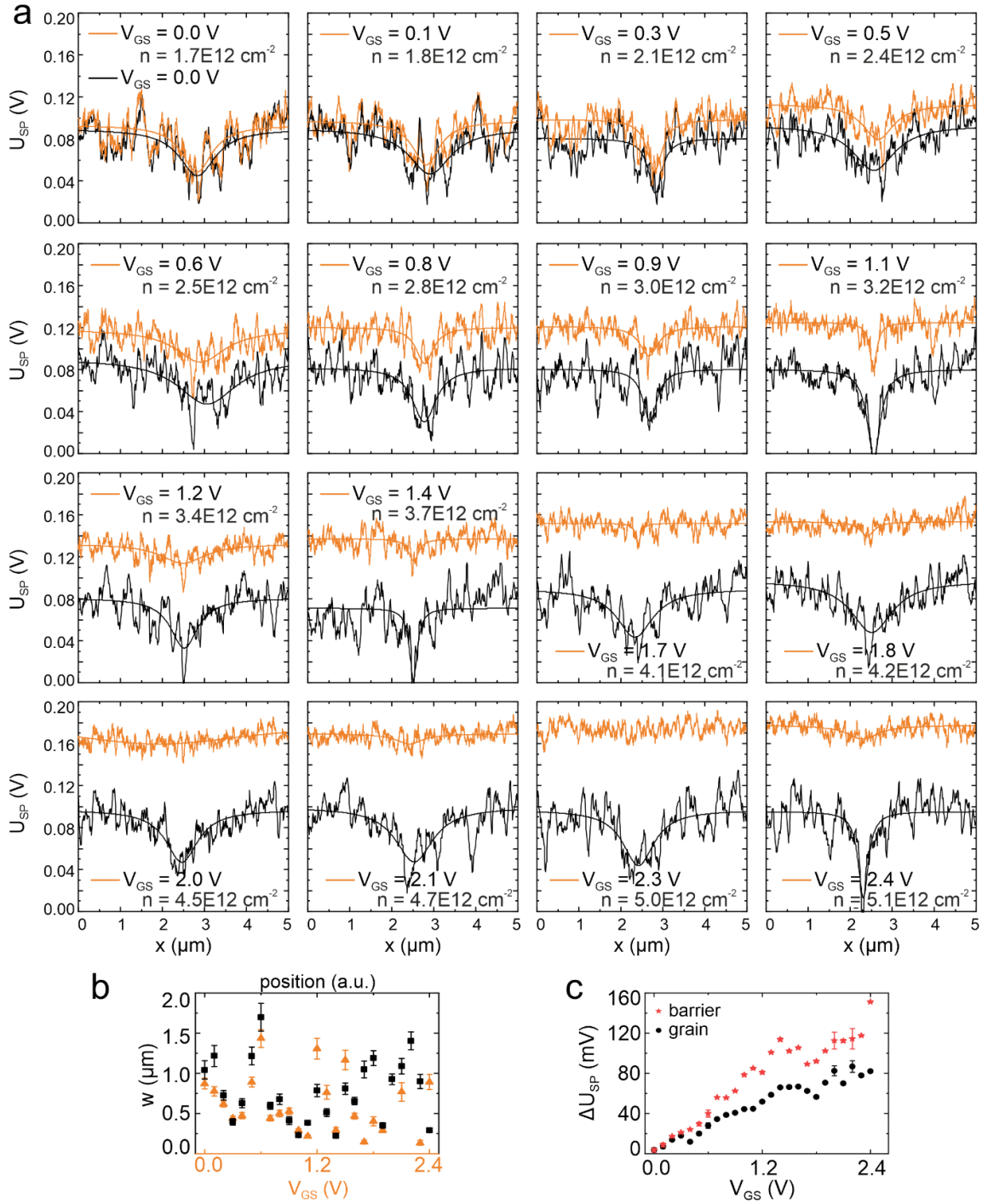


**Figure S6 Gate-voltage dependent surface potential at a barrier.** **a**, Selection of extracted profiles at zero (black) and varying back gate voltage  $V_{GS}$  (orange) with Lorentzian fits according to equation (C.1). **b**, Extracted grain boundary widths ( $w$ ) from Lorentz fits for zero (black) and varying  $V_{GS}$  (orange). **c**, Change of measured surface potential  $\Delta U_{SP} = U_{SP}(V_{GS} > 0) - U_{SP}(V_{GS} = 0) = (1 - \beta)V_{GS}$  for the barrier and the surrounding grains.

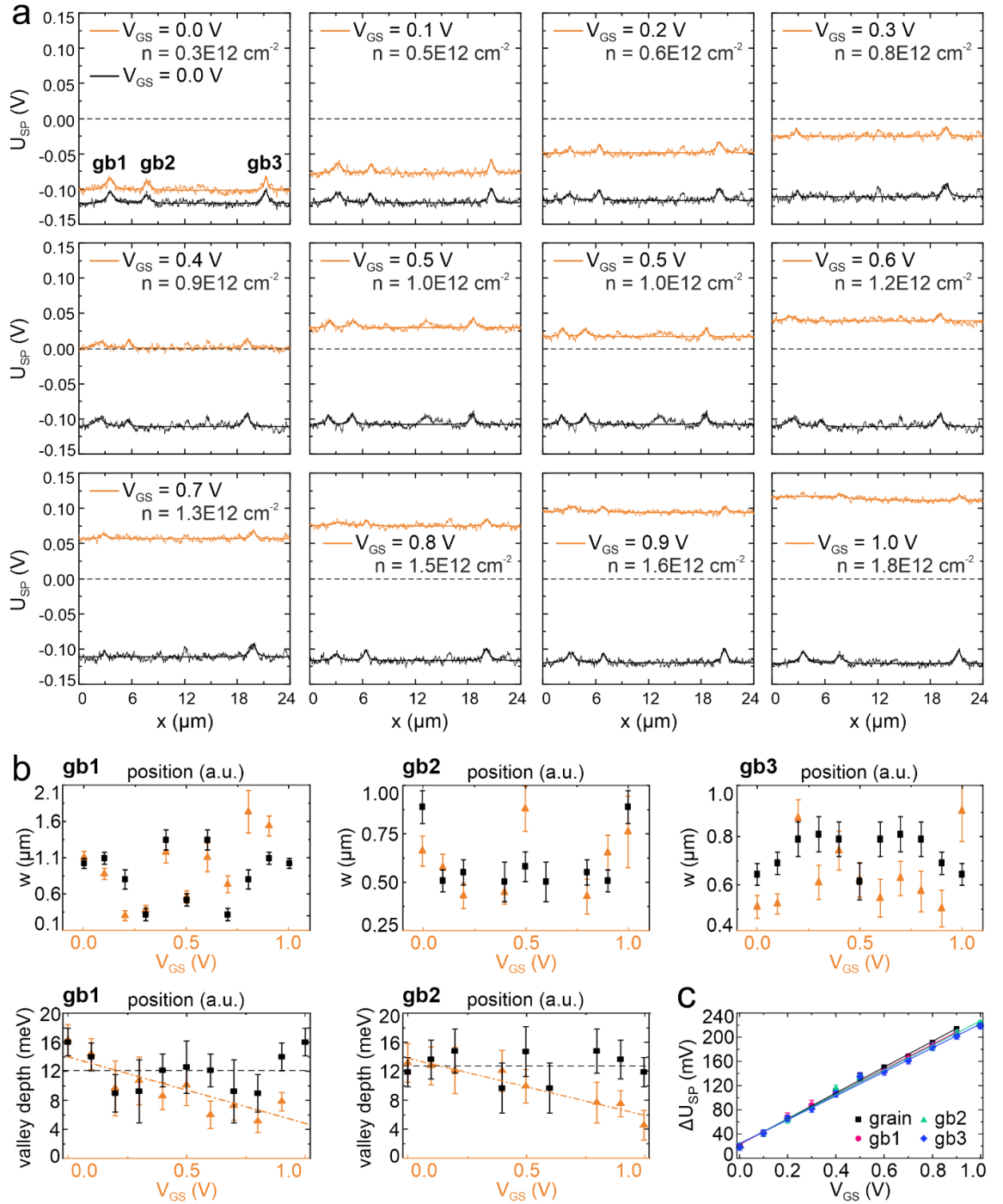


**Figure S7 Gate-voltage dependent surface potential at valleys.** **a**, Selection of extracted profiles at zero (black) and varying back gate voltage  $V_{GS}$  (orange) with Lorentzian fits according to equation (C.1). **b**, Extracted grain boundary widths and valley depths from Lorentz fits for zero (black) and varying  $V_{GS}$  (orange). The valley-depth dependence for gb3 is presented in Figure 4d in the main text. The dashed lines are the mean values for zero gate voltage, the dashed-dotted lines a linear fit for varying gate voltage, both serve as guide to the eye. **c**, Change of measured surface potential  $\Delta U_{SP} = U_{SP}(V_{GS} > 0) - U_{SP}(V_{GS} = 0) = (1 - \beta)V_{GS}$  for grain and valleys (gb1-3). The linear fits serve as guide to the eye.

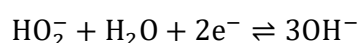
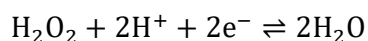
## D. Interaction with light

As described in the main text, an increase of the CPD was observed under constant illumination (cf. Experimental Section and **Figure S8**), while barrier heights and the  $\text{rms}(U_{SP})$  are not affected (**Figure S9**). **Table S2** summarizes the optical properties of all materials used in our devices from which can be deduced that indeed the organic semiconductor absorbs the spectrum of the halogen lamp.

Since our results are consistent with no electrons remaining in the semiconductor after absorption of light and formation of electron-hole pairs, we anticipate that optically-induced electrons are drained by water ions.<sup>15</sup> The first redox potential of PDI1MPCN2 can be estimated due to its structural similarity with PDI-CN2<sup>16</sup> to



and by the autoionization process of water resulting ions may react as



Therefore, the probability for one electron to transfer to a water ion is higher than to remain on the ionized organic molecule.

The effect of water ions on electronic properties of OSC devices has been observed before even at low densities of  $7.2 \cdot 10^8$  water molecules per  $\text{cm}^3$ .<sup>18</sup> Our measurements are taken in an argon-atmosphere with a pressure of  $\sim 1$  bar and a humidity of  $< 1\%$ , i.e.  $2.4 \cdot 10^{17}$  water molecules per  $\text{cm}^3$ , which is why its presence has to be considered here as well.

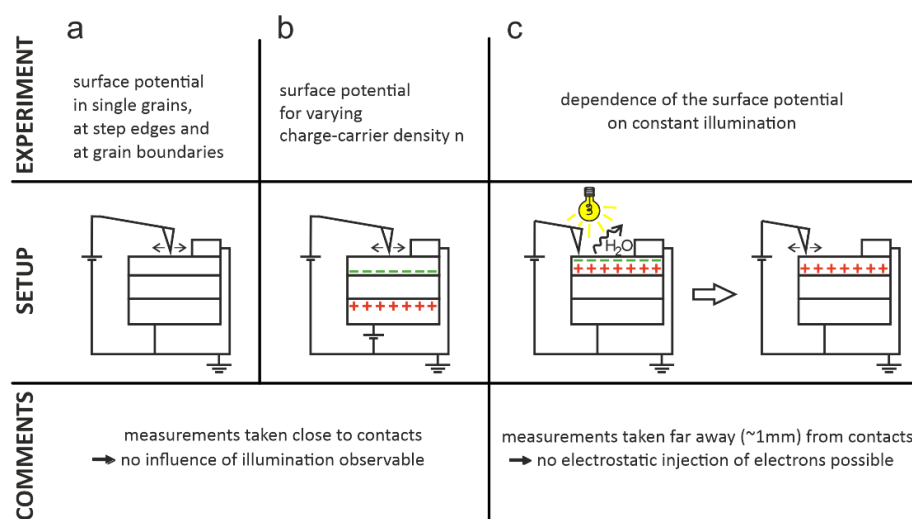


**Figure S8 Summary of the different setups and conducted experiments.**

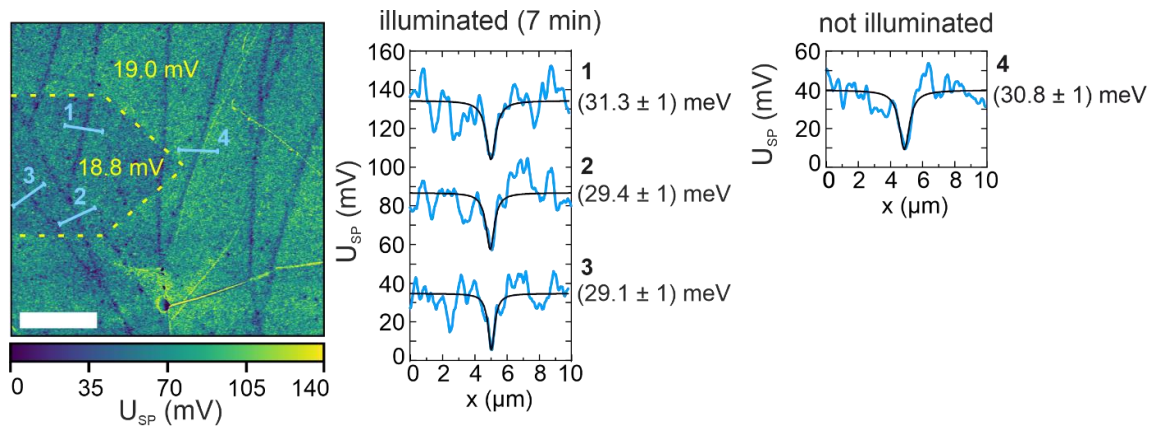


**Figure S9** Line profiles and  $\text{rms}(U_{sp})$  at barriers in illuminated and non-illuminated areas. The line profiles (blue) have been extracted according to **Figure 2** in the main text. The Lorentzian fits (black) provide the given barrier heights. Profile 4 is given as a reference for the non-illuminated part. The yellow numbers are the  $\text{rms}(U_{sp})$ -values for the respective areas. The scalebar is  $20 \mu\text{m}$ .

**Table S2** Optical properties of device materials for light absorption analysis.

Band gap	[eV]
$\text{Al}_2\text{O}_3$	$8.8^{19}$
$\text{SiO}_2$	$8.2^{20}$
Si (undoped)	$1.12^{21}$
Si (doping concentration $10^{18} - 10^{19} \text{ cm}^{-3}$ )	$1.08 - 1.04^{22}$
PDI1MPCN2	$2.6^{23}$
Spectrum of halogen lamp	$3.5 - 1.3^{24}$ ( $350 - 950 \text{ nm} \gg \text{OSC layer thickness}$ )

### E. Impact of processing conditions on the existence of valleys and barriers

**Figure S10** displays a close-up image of a spot where an energetic barrier at a grain boundary coincides with a dip in the topography. Other correspondences than that could not be found for barriers and valleys in the topography scans.

In **Table S3**, we present an overview of all spots detected by KPFM including the main processing conditions such as the chosen substrate, the device structure and the solution. As can be seen, there is no simple global correlation between processing parameters and the occurrence of valleys and barriers. Furthermore, neither the film thickness<sup>25</sup>, nor the size of adjacent grains<sup>26</sup> could be found to be responsible for the grain-boundary type. Moreover, we checked if valleys and barriers can be differentiated by cross-polarized optical microscopy (POM). For this instance, we investigated the change of molecular orientation at the grain boundaries by contrast change<sup>27</sup>:

$$C = \frac{D_{OSC} - D_{Substrate}}{D_{Substrate}} \quad (\text{E.1})$$

Here,  $D$  is “a digital value calculated from the microscope image”<sup>27</sup>. We chose the green part of the rgb-value due to the green emission of the organic molecule. The obtained values are summarized in **Table S3** showing that the change in orientation (i.e. the difference between the given contrast values at a certain gb) does not correlate with the grain boundary type.

Even more, the right- or left-handedness turning direction of molecules within the grains<sup>28</sup> with respect to the grain boundaries shows no correlation (e.g. **Figure S12c**).

As described in the main text, we could however find a correlation between the shape of a thin film spot and the occurrence of a certain grain-boundary type (**Table S3**). Here, we used the differentiation between spots of circular shape with a straight border (“pinned” droplets (P)), in contrast to non-circular films with a smeared out, wavy border (“shrunk” or “smeared” droplets (S)). While we could achieve good pinning by structuring the oxides using hydrophobic SAMs as described in the Experimental section, the droplets extremely shrunk if no SAM was applied. By using structured SAMs and adding toluene to the drop-cast solution, we achieved mixed P/S behavior (i.e. part of the droplet remained pinned and other parts smeared) where both, valleys and barriers could be detected as shown in **Figure S11** (**Figure 3** in the main text). An overview over the different procedures is shown in **Figure S13**. In one measurement out of 30, we even managed to detect both types of grain boundaries within one scan (**Figure S12b**). This case is, however, extremely rare, for three reasons. First, we observed grain boundaries in films out of toluene containing solutions to be less pronounced

than in films of pure DMP solutions (cf. **Figure S12d**). This explains on one hand their major performance in electric measurements<sup>29</sup>, but also complicates their detection and interpretation. Second, barriers and valleys seem to be spatially separated from each other, meaning that there are areas with only valleys or only barriers and in between, grain boundaries are less pronounced; possibly because effects of non-pinning and pinning areas interfere with each other. Third, due to the spatial separation, the combination of the grain size and the maximum scan size of 90  $\mu\text{m}$  limit the possibility to observe both, valleys and barriers, within one scan.

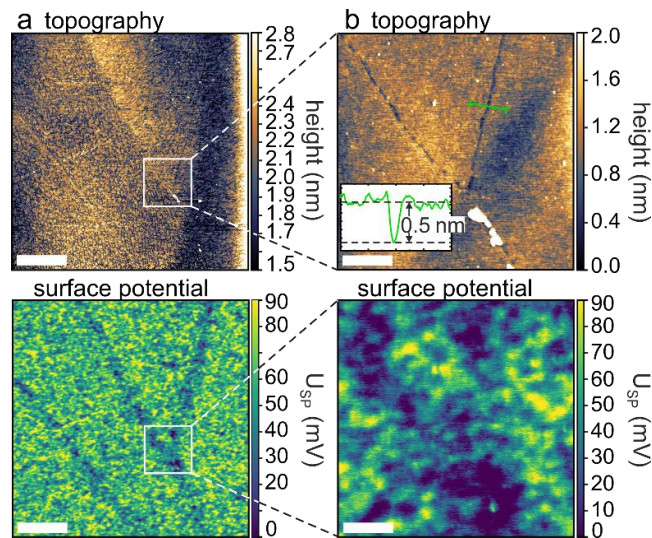


**Figure S10 Zoom into a barrier.** **a**, Detail of **Figure 2a** in the main text, scalebars are 5  $\mu\text{m}$ . **b**, Detail of **a**), scalebars are 1  $\mu\text{m}$ . Inset: height profile along the given line giving the depth of the visible dip at the grain boundary of 0.5 nm.

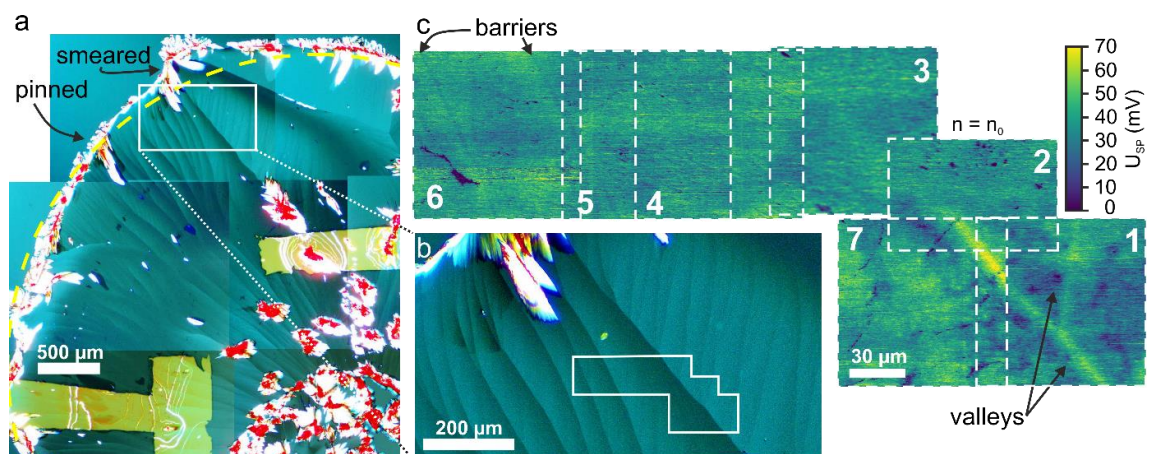


**Figure S11 Coexistence of valleys and barriers.** **a**, Part of a spot of a thin film of PDI1MPCN2, composed of several POM images. The yellow dashed circle with 5 mm diameter serves as guide to the eye to underline the difference between pinned areas (circular shape with straight border) and smeared areas. **b**, Zoom into marked area in **a**. **c**, Composition of KPFM

scans within the marked area in b. The numbers indicate the chronological order of scans to exclude degradation effects.

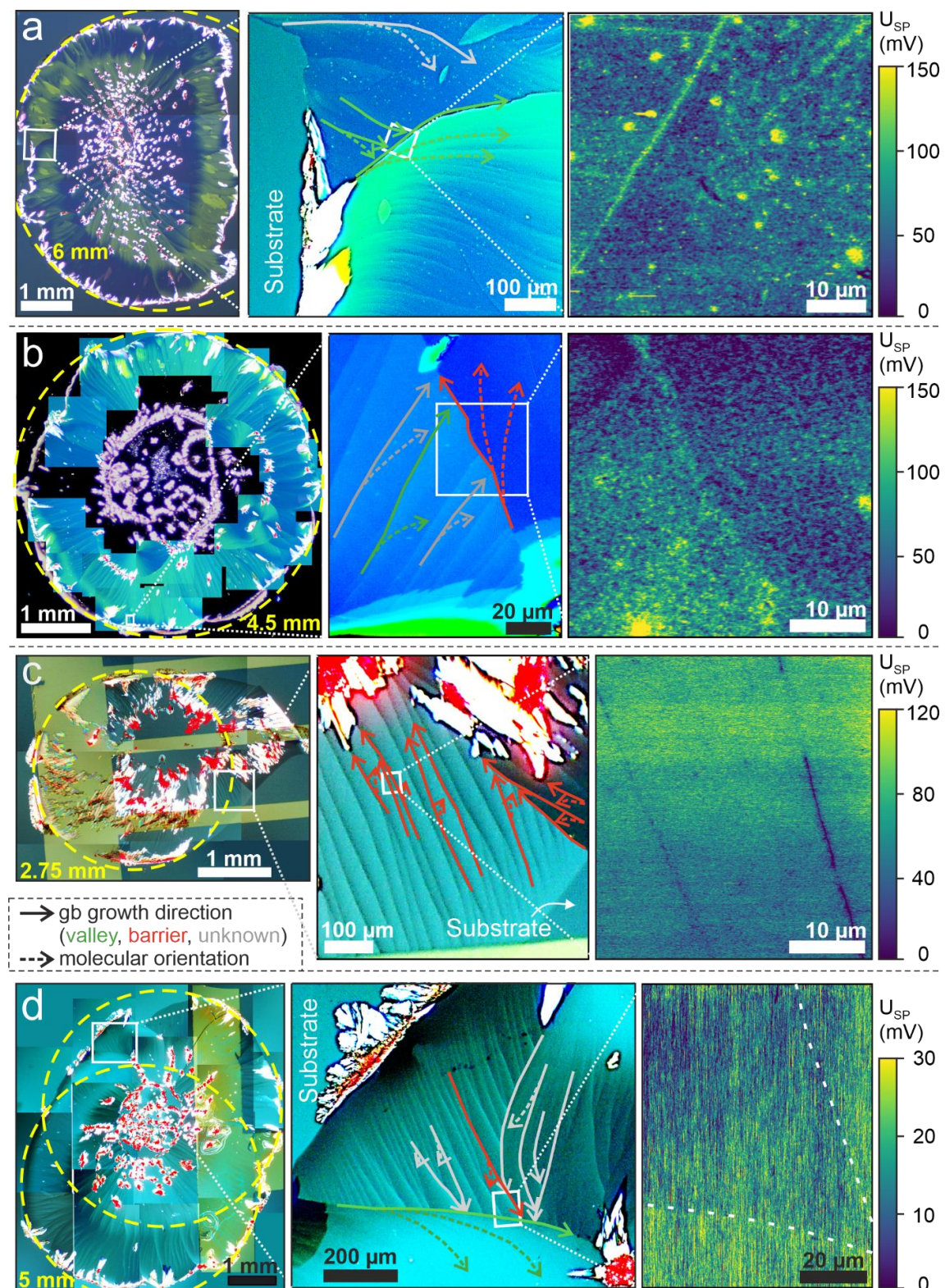


**Figure S12 Overview of four investigated thin-film spots. a,** Left: Spot of a thin film of PDI1MPCN2, composition of POM images. The yellow dashed circle indicates the etched spot of 6 mm diameter and underlines the different parts of pinned and non-pinned (smeared)

area. Middle: Zoom into white box in the left picture. The solid lines indicate the growth direction of the grain boundaries, the dashed lines the assumed turning of the molecules within the grains (judged by color). Right: KPFM measurement of indicated area in the middle picture. **b,c**, Analogous; for experimental details cf. **Table S3**. For both droplets a mask with 5 mm diameter was used. In **b,c**, droplets shrunk to sizes of the indicated 4.5 mm and 2.75 mm, respectively, while drying. **d**, Analogous; for experimental details cf. **Table S3**. The substrate was etched twice with slightly misaligned masks leading to the overlap of two different circles of 5 mm diameter each. Therefore, the droplet slightly smeared into a non-circular shape. Since toluene was added to the solvent, the grain boundaries are only slightly observable in the KPFM scan (marked by white dashed lines).

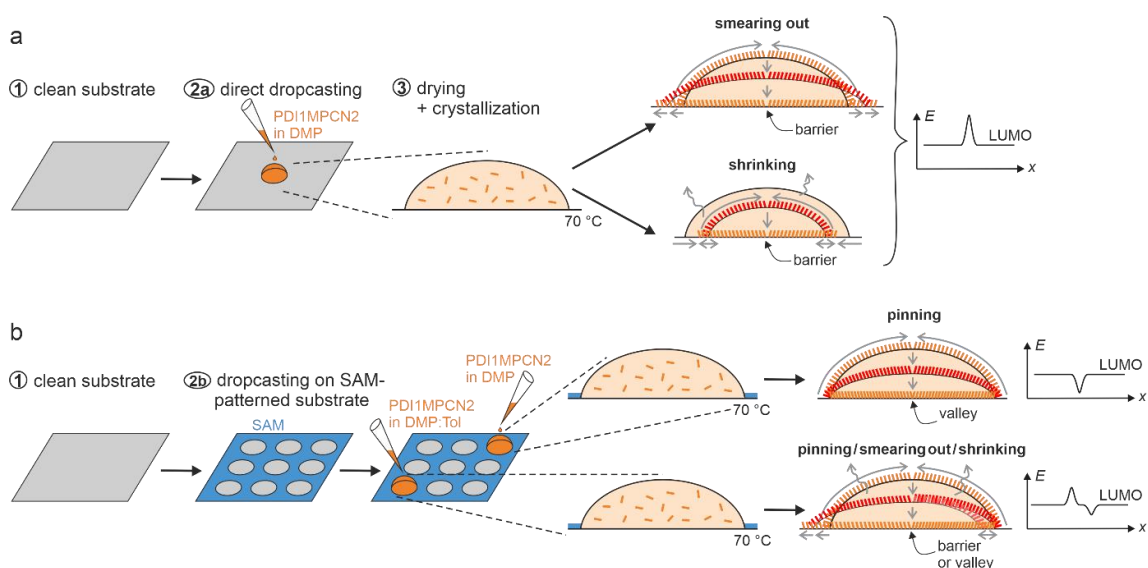


**Figure S13 Process diagram of the thin-film formation and crystallization determining the growth of different grain boundary types and heights.** **a**, The substrate is cleaned and a solution of the molecule PDI1MPCN2 in dimethylphthalate (DMP) is drop-cast on the substrate. In this case, the edges of the droplet do not pin to the substrate but the droplet outline smears or shrinks while drying, resulting only in barriers at grain boundaries. **b**, A SAM is applied on the substrate and patterned by plasma etching. The solution is then drop-cast onto the circular areas without SAM. If the standard DMP solution is used, the droplet pins while drying and the grain boundaries appear as valleys. If the solution is mixed with toluene (Tol), a mixture of the pinning and smearing/shrinking process is achieved and both, barriers and valleys can be observed in the resulting thin film. Even more, the addition of toluene results in less-pronounced grain boundary heights/depths. Please note, that the combination of SAM patterning and use of a DMP:Tol solution is not the only way to achieve mixed pinning/smearing behavior, but our method to force it. We have also observed mixed pinning/smearing behavior on samples with insufficient SAMs and even on substrates without SAMs.

**Table S3 Overview of detected barriers and valleys on different samples.** In sum, 30 measurements on 12 different thin-film spots on 9 samples were investigated. One sample, consisting of one and the same substrate, can comprise of several spots of the organic film named by greek letters. The solutions used for sample preparation (cf. Experimental section)

were prepared from two different molecule batches 1 and 2. DMP: Dimethylphthalate, Tol: Toluene. P: pinned droplet, S: smeared out droplet, using the definitions given in the text. Several “X” within one cell represent several measurements on the same spot. (X): very weak grain boundary whose type is hardly recognizable. The named figures show data of the corresponding spots. The absolute value of the contrast change at grain boundaries  $|\Delta C|$  was calculated via equation (E.1). The colors are for simplicity of reading.

Substrate	Device structure	Spot	Solution (Batch, Solvent)	Spot shape	Detected Barriers	Detected Valleys	Figure	$ \Delta C $
SiO <sub>2</sub>	w/o contacts	$\gamma$	L0 (1,DMP)	P / S		X	S12a	0.9
SiO <sub>2</sub>	w/o contacts	$\alpha$	L4 (2,DMP)	S	X		2a	0.1
		$\beta$	L4	P / S	XXX	X		0.3 / 5.0
		$\delta\epsilon$	L4	S	X			0.5
SiO <sub>2</sub>	w/o contacts	$\beta$	L3 (1+2, DMP:Tol=1:3)	P / S	X	XX	S12b	0.2 0.7
SiO <sub>2</sub>	BGBC	$\beta$	L30 (2,DMP)	P / S	X			
Al <sub>2</sub> O <sub>3</sub>	BGTC	$\gamma$	L30	S	XXX		S12c	0.3
Al <sub>2</sub> O <sub>3</sub>	BGBC	$\alpha$	L30	P		X	2b	0.3 / 0.5
Al <sub>2</sub> O <sub>3</sub>	BGBC	$\alpha$	L2 (1+2, DMP:Tol=3:1)	P / S	(X)	X(X)	S12d	0.1 0.5
		$\alpha$	L2	P		X		0.2
Al <sub>2</sub> O <sub>3</sub>	BGBC	$\beta$	L2	P / S	X	X	3	0.4 0.5
		$\alpha$	L3	P		X		0.1 / 0.2

## References

- (1) Palermo, V.; Palma, M.; Samorì, P. Electronic Characterization of Organic Thin Films by Kelvin Probe Force Microscopy. *Adv. Mater.* **2006**, *18* (2), 145–164. DOI: 10.1002/adma.200501394.
- (2) Tal, O.; Rosenwaks, Y. Electronic properties of doped molecular thin films measured by Kelvin probe force microscopy. *The journal of physical chemistry. B* **2006**, *110* (50), 25521–25524. DOI: 10.1021/jp065246q.
- (3) Tal, O.; Rosenwaks, Y.; Preezant, Y.; Tessler, N.; Chan, C. K.; Kahn, A. Direct determination of the hole density of states in undoped and doped amorphous organic films with high lateral resolution. *Phys. Rev. Lett.* **2005**, *95* (25), 256405. DOI: 10.1103/PhysRevLett.95.256405.
- (4) Roelofs, W. S. C.; Mathijssen, S. G. J.; Janssen, R. A. J.; Leeuw, D. M. de; Kemerink, M. Accurate description of charge transport in organic field effect transistors using an experimentally extracted density of states. *Phys. Rev. B* **2012**, *85* (8). DOI: 10.1103/PhysRevB.85.085202.
- (5) Axt, A.; Hermes, I. M.; Bergmann, V. W.; Tausendpfund, N.; Weber, S. A. L. Know your full potential: Quantitative Kelvin probe force microscopy on nanoscale electrical devices. *Beilstein journal of nanotechnology* **2018**, *9*, 1809–1819. DOI: 10.3762/bjnano.9.172.
- (6) Horowitz, G.; Hajlaoui, R.; Bouchriha, H.; Bourguiga, R.; Hajlaoui, M. The Concept of “Threshold Voltage” in Organic Field-Effect Transistors. *Adv. Mater.* **1998**, *10* (12), 923–927. DOI: 10.1002/(SICI)1521-4095(199808)10:12<923:AID-ADMA923>3.0.CO;2-W.
- (7) Dagan, R.; Vaknin, Y.; Weisman, D.; Amit, I.; Rosenwaks, Y. Accurate Method To Determine the Mobility of Transition-Metal Dichalcogenides with Incomplete Gate Screening. *ACS applied materials & interfaces* **2019**, *11* (47), 44406–44412. DOI: 10.1021/acsami.9b12611.
- (8) Braga, D.; Horowitz, G. Subthreshold regime in rubrene single-crystal organic transistors. *Appl. Phys. A* **2009**, *95* (1), 193–201. DOI: 10.1007/s00339-008-5008-y.
- (9) Puntambekar, K. P.; Pesavento, P. V.; Frisbie, C. D. Surface potential profiling and contact resistance measurements on operating pentacene thin-film transistors by Kelvin probe force microscopy. *Appl. Phys. Lett.* **2003**, *83* (26), 5539–5541. DOI: 10.1063/1.1637443.
- (10) Bürgi, L.; Sirringhaus, H.; Friend, R. H. Noncontact potentiometry of polymer field-effect transistors. *Appl. Phys. Lett.* **2002**, *80* (16), 2913–2915. DOI: 10.1063/1.1470702.
- (11) Murawski, J.; Mönch, T.; Milde, P.; Hein, M. P.; Nicht, S.; Zerweck-Trogisch, U.; Eng, L. M. Tracking speed bumps in organic field-effect transistors via pump-probe Kelvin-probe force microscopy. *Journal of Applied Physics* **2015**, *118* (24), 244502. DOI: 10.1063/1.4938529.
- (12) Henriksen, E. A.; Eisenstein, J. P. Measurement of the electronic compressibility of bilayer graphene. *Phys. Rev. B* **2010**, *82* (4). DOI: 10.1103/PhysRevB.82.041412.
- (13) Nečas, D.; Klapetek, P. Gwyddion Version 2.50: An open-source software for SPM data analysis. *Central European Journal of Physics* **2012**, *10* (1), 181–188. DOI: 10.2478/s11534-011-0096-2.
- (14) Kalinin, S. V.; Bonnell, D. A. Surface potential at surface-interface junctions in SrTiO<sub>3</sub> bicrystals. *Phys. Rev. B* **2000**, *62* (15), 10419–10430. DOI: 10.1103/PhysRevB.62.10419.
- (15) Zschieschang, U.; Amsharov, K.; Jansen, M.; Kern, K.; Klauk, H.; Weitz, R. T. Separating the impact of oxygen and water on the long-term stability of n-channel perylene diimide thin-film transistors. *Organic Electronics* **2015**, *26*, 340–344. DOI: 10.1016/j.orgel.2015.07.060.
- (16) Jones, B. A.; Facchetti, A.; Wasielewski, M. R.; Marks, T. J. Tuning orbital energetics in arylene diimide semiconductors. materials design for ambient stability of n-type charge transport. *Journal of the American Chemical Society* **2007**, *129* (49), 15259–15278. DOI: 10.1021/ja075242e. Published Online: Nov. 14, 2007.
- (17) Leeuw, D. M. de; Simenon, M.; Brown, A. R.; Einerhand, R. Stability of n-type doped conducting polymers and consequences for polymeric microelectronic devices. *Synthetic Metals* **1997**, *87* (1), 53–59. DOI: 10.1016/S0379-6779(97)80097-5.
- (18) Kettner, M.; Zhou, M.; Brill, J.; Blom, P. W. M.; Weitz, R. T. Complete Suppression of Bias-Induced Threshold Voltage Shift below 273 K in Solution-Processed High-Performance Organic Transistors. *ACS applied materials & interfaces* **2018**, *10* (41), 35449–35454. DOI: 10.1021/acsami.8b13035.
- (19) French, R. H. Electronic Band Structure of Al<sub>2</sub>O<sub>3</sub>, with Comparison to Alon and AlN. *J American Ceramic Society* **1990**, *73* (3), 477–489. DOI: 10.1111/j.1151-2916.1990.tb06541.x.
- (20) Nekrashevich, S. S.; Gritsenko, V. A. Electronic structure of silicon dioxide (a review). *Phys. Solid State* **2014**, *56* (2), 207–222. DOI: 10.1134/S106378341402022X.
- (21) Sze, S. M.; Ng, K. K. *Physics of semiconductor devices*, 3. ed.; Wiley-Interscience, 2007. DOI: 10.1002/0470068329.
- (22) Dhariwal, S. R.; Ojha, V. N. Band gap narrowing in heavily doped silicon. *Solid-State Electronics* **1982**, *25* (9), 909–911. DOI: 10.1016/0038-1101(82)90180-0.

- (23) Vladimirov, I. Crystallization Behavior and Charge Transport of Organic Semiconductors. Dissertation, Technische Universität Carolo-Wilhelmina zu Braunschweig, Braunschweig, 2016.
- (24) Thoms, L.-J.; Girwidz, R. Experimenting from a Distance: Optical Spectrometry via the Internet. In *MPTL, At Madrid, Volume: 18*.
- (25) Yogev, S.; Matsubara, R.; Nakamura, M.; Rosenwaks, Y. Local charge accumulation and trapping in grain boundaries of pentacene thin film transistors. *Organic Electronics* **2010**, *11* (11), 1729–1735. DOI: 10.1016/j.orgel.2010.07.021.
- (26) Horowitz, G. Tunneling Current in Polycrystalline Organic Thin-Film Transistors. *Adv. Funct. Mater.* **2003**, *13* (1), 53–60. DOI: 10.1002/adfm.200390006.
- (27) Hattori, Y.; Kitamura, M. Crystal orientation imaging of organic monolayer islands by polarized light microscopy. *ACS applied materials & interfaces* **2020**. DOI: 10.1021/acsami.0c08672.
- (28) Schaffroth, L. S.; Lenz, J.; Giegold, V.; Kögl, M.; Hartschuh, A.; Weitz, R. T. Freely Suspended, van der Waals Bound Organic Nanometer-Thin Functional Films: Mechanical and Electronic Characterization. *Advanced materials (Deerfield Beach, Fla.)* **2019**, *31* (16). DOI: 10.1002/adma.201808309.
- (29) Vladimirov, I.; Kellermeier, M.; Geßner, T.; Molla, Z.; Grigorian, S.; Pietsch, U.; Schaffroth, L. S.; Kühn, M.; May, F.; Weitz, R. T. High-Mobility, Ultrathin Organic Semiconducting Films Realized by Surface-Mediated Crystallization. *Nano letters* **2018**, *18* (1), 9–14. DOI: 10.1021/acs.nanolett.7b03789.

## F Supporting Information to Chapter 5

### F.1 Supplementary Data

**Figure F.7** shows the complete measurement of local, time-dependent surface-potentials at a grain, a valley and a barrier (the position of the sites are displayed in **Figure 5.2a** in the main text). **Table F.3** summarizes the global turn-on and threshold voltages extracted from transfer measurements at devices identical in construction.

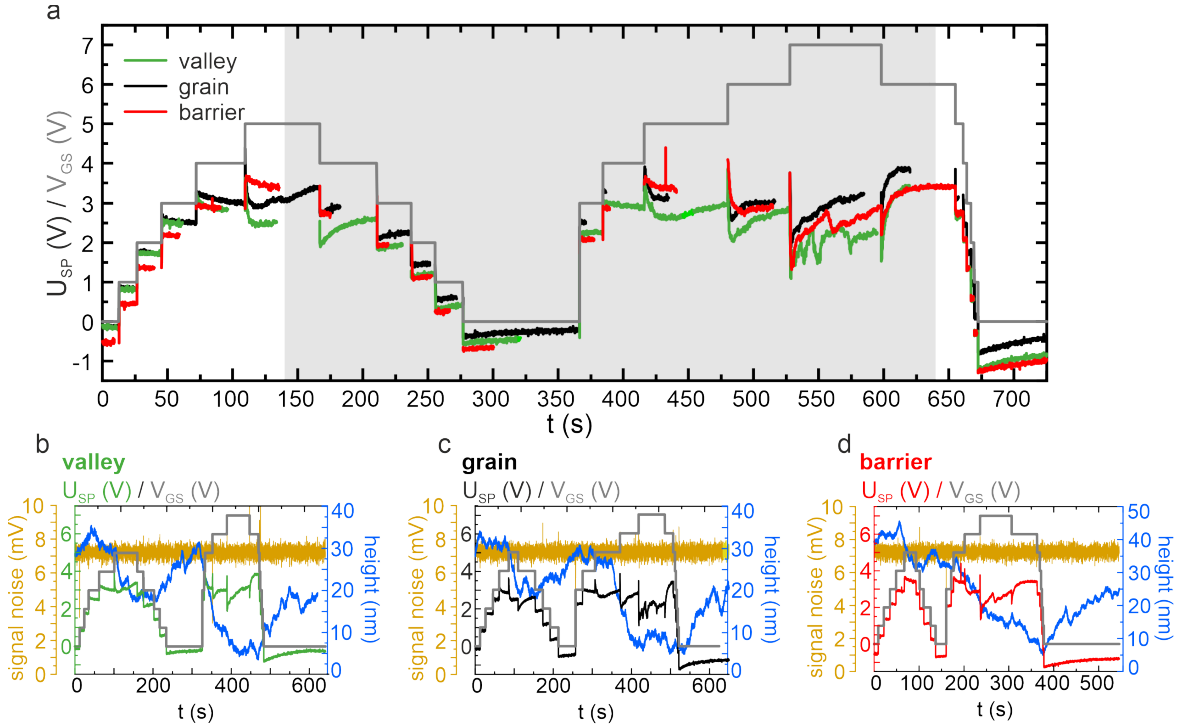


**Figure F.7 Complete measurement of the surface potential depending on gate voltage and time.** **a**, Detected surface potential for the grain (black), valley (green) and barrier (red) as displayed in **Figure 5.1** and discussed in the main text. The grey marked area displays the data not shown in **Figure 5.2** or **Figure 5.3**. **b-d**, Signal noise and tip height as a measure for the measurement stability in combination with the surface potential and the applied gate voltage for **b** the valley, **c** the grain, **d** the barrier. The surface potentials correspond to the data shown in **a**.

### F.2 Extraction of the Screening Factor $\beta$

As discussed in the main text, the measurement signal includes a gate-voltage dependent term (cf. Equation (5.50) and **Figure F.8**) which accounts for imperfect screening of  $V_{GS}$  at small charge-carrier densities. While we discussed the time dependence of  $\beta$ , we abstained from presenting exact values for its saturation value  $\beta_{max}$ , since we expect it to depend on many different local and global parameters (e.g. the used insulator, the sample geometry, the quality of all interfaces, ...). However, we will shortly present two possible methods to extract a value for  $\beta_{max}$  to enable a more detailed analysis in the future.

#### Extraction from Time-dependent Measurements

If we assume the CPD to be independent of time, we can extract the surface potentials for  $t = 0$  and  $t \rightarrow \infty$  detected at a constant gate voltage. According to Equation (5.50),  $\beta_{max}$

**Table F.3 Global device parameters extracted from transfer curves in the linear regime ( $V_{DS} = 0.5$  V) detected on 12 devices a-l, defined by a pair of source and drain electrode.** The threshold and turn-on voltages were extracted as described in References [93,157].  $L$  and  $W$  denote the channel length and width, respectively.

OSC spot	Transistor	$L$ ( $\mu\text{m}$ )	$W$ ( $\mu\text{m}$ )	$V_{\text{on}}$ (V)	$V_{\text{th}}$ (V)
1	a	100	200	1.3	2.7
1	b	100	200	0.9	2.5
2	c	100	200	1.0	2.3
2	d	100	200	0.4	1.9
2	e	100	200	0.4	2.1
2	f	100	200	1.0	1.4
3	g	17	44	2.8	3.3
3	h	21	44	2.7	3.7
3	i	27	44	3.4	3.5
3	j	33	44	3.4	3.7
3	k	39	44	3.5	3.7
3	l	44	44	3.5	3.6
medium and standard deviation of spot 1				$1.1 \pm 0.3$	$2.6 \pm 1.0$
medium and standard deviation of spot 2				$0.5 \pm 0.4$	$1.9 \pm 0.4$
medium and standard deviation of spot 3				$3.2 \pm 0.1$	$3.6 \pm 0.4$

then calculates to

$$\begin{aligned}
 t = 0 &\rightarrow \beta = 0 &\Rightarrow U_{\text{SP}}^0 = U_{\text{CPD}} + V_{\text{GS}} \\
 t = \infty &\rightarrow \beta = \beta_{\text{max}} &\Rightarrow U_{\text{SP}}^\infty = U_{\text{CPD}} + V_{\text{GS}} - \beta_{\text{max}} V_{\text{GS}} \\
 &&\Leftrightarrow \beta_{\text{max}} = \frac{U_{\text{SP}}^0 - U_{\text{SP}}^\infty}{V_{\text{GS}}}.
 \end{aligned}$$

### Extraction from the Sub-threshold Slope of Transfer Measurements

If the incomplete gate screening is mainly caused by capacitive effects,  $\beta_{\text{max}}$  can be related to the gate-coupling factor

$$\alpha = \frac{\hat{c}_D}{n_{it}e^2 + \hat{c}_C + \hat{c}_D}$$

with  $\hat{c}_D$  the capacitance of the gate dielectric per unit area,  $\hat{c}_C$  the capacitance of the charges in the channel per unit area,  $e$ , the elemental charge, and  $n_{it}$  the density of fixed charges at the semiconductor-insulator interface [161,162]. Assuming negligibly small  $\hat{c}_D$  (which is reasonable for small  $V_{\text{GS}}$ ),  $\alpha$  can be deduced from the sub-threshold slope using [161,162]

$$SS = \left[ \frac{d \log(I_{\text{DS}})}{dV_{\text{GS}}} \right]^{-1} = \frac{k_B T}{e} \cdot \ln \alpha^{-1}.$$

The assumption that only the substrate, device structure and contact quality are responsible for  $\beta_{\text{max}} < 1$ , is equivalent to assume that  $\alpha$  and  $\beta_{\text{max}}$  are the same for grains and grain boundaries. Since this makes the introduction of the screening factor  $\beta_{\text{max}}$  as a site-dependent parameter unreasonable, this extraction method can of course only give a rough estimation for  $\beta_{\text{max}}$ .

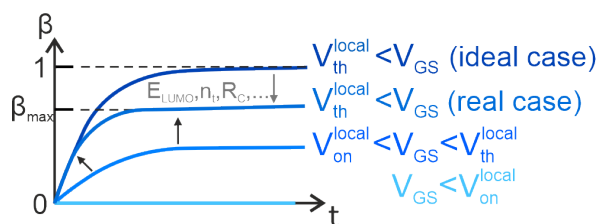


**Figure F.8 Time and gate voltage dependence of the screening factor  $\beta$ .** The graphic shows a case distinction for different gate voltages relative to the local threshold voltage. For a detailed description see main text.

### F.3 Suggestions for an Improved Device Design

Up to now, local KPFM measurements and global electrical measurements have been performed on different devices. As we have discussed in the main text, the extracted parameters can only be compared well if measured on the same semiconducting layer. The following challenges have to be overcome to make KPFM and electrical measurements possible.

- Heterodyne KPFM measurements cannot be performed in the channel of a TFT, since the proximity of source and drain contacts have been observed to shadow the small potential variations at grain boundaries or impurities by much larger potential variations. Therefore, source and drain electrodes have to be in a sufficient distance from the spots at which KPFM measurements are performed, but close enough to enable sufficient charge-carrier injection.
- The cantilever should not be placed above a contact to avoid crosstalk or capacitive effects.
- Source and drain contacts have to be contacted with an external voltage source. However, the wires have to be as flat as possible to prevent the AFM head, the cantilever and the tip from interacting with the wires. While evaporated contacts would fulfill this criterion best, very long contacts would also increase the contact area between contacts and insulating layer, and thereby leakage currents from the gate to source and drain.
- The contact width can only be decreased (e.g. to reduce the electrode-insulator interface) up to a certain extent, since narrow contacts are extremely vulnerable and may break, especially during approaching the cantilever head, which is done manually in the used setup.

The device design displayed in **Figure F.9** aims to overcome all of the stated challenges. It consists of a monolayer-thin film of PDI1MPCN2 applied on a substrate consisting of a silicon gate and a 30 nm-thick layer  $\text{Al}_2\text{O}_3$ , glued onto a glass plate by silver conductive paint. Four long and spatially separated source/drain electrodes are applied such that they can be contacted via wire bonds to the outer edge of the glass plate. At this position, the wire bonds can be connected to the cables of the voltage source e.g. by a copper tape.

The gate electrode of the substrate is connected from the back side via the silver conductive paint. The substrate is shifted to the very edge of the glass plate to protect the wires from interactions with the AFM head.

Additional source and drain contacts with smaller dimensions are evaporated for transport measurements. Even more, we keep the option to evaporate source and drain contacts on top of the existing KPFM contacts, to elongate them and enable transfer measurements at the region where KPFM measurements have been performed before, as indicated by the dashed lines in **Figure F.9b**.

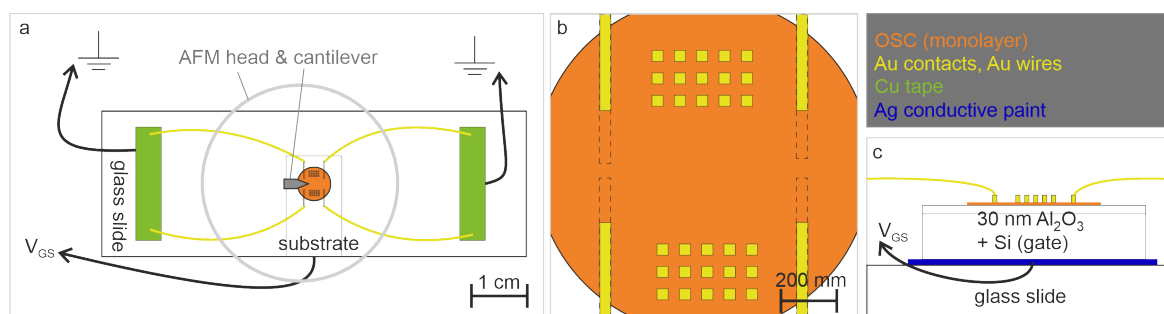


**Figure F.9 Suggestion for an improved device design for local KPFM measurements and global transport measurements on the same organic semiconducting layer.** **a**, Overview of the sample consisting of a monolayer-thin organic film on a substrate, glued on a glass plate, and contacted by gold wires. The size of the AFM head is indicated and the direction of the cantilever (the size of the cantilever is not to scale.) **b**, Zoom into the contact geometry. The large contacts enclose possible areas for local KPFM measurements, while the smaller squares enable transport measurements. The dashed lines indicate the areas on which source and drain electrode can be elongated by a second evaporation for additional transport measurements after the local KPFM measurements. **c**, Side view of the glass slide and the sample (the height is not to scale).

## G Supporting Information to Chapter 7

Supporting Information for

### **Interfacial Synthesis of Layer-Oriented 2D Conjugated Metal-Organic Framework Films toward Directional Charge Transport**

Zhiyong Wang<sup>1</sup>, Lisa S. Walter<sup>2,7</sup>, Mao Wang<sup>3</sup>, Petko St. Petkov<sup>4</sup>, Baokun Liang<sup>5</sup>, Haoyuan Qi<sup>1,5</sup>, Nguyen Ngan Nguyen<sup>1</sup>, Mike Hamsch<sup>11</sup>, Haixia Zhong<sup>1</sup>, Mingchao Wang<sup>1</sup>, SangWook Park<sup>1</sup>, Lukas Renn<sup>2,7</sup>, Kenji Watanabe<sup>6</sup>, Takashi Taniguchi<sup>6</sup>, Stefan C. B. Mannsfeld<sup>11</sup>, Thomas Heine<sup>1,9,10</sup>, Ute Kaiser<sup>5</sup>, Shengqiang Zhou<sup>3</sup>, Ralf Thomas Weitz<sup>2,7,\*</sup>, Xinliang Feng<sup>1,8,\*</sup> and Renhao Dong<sup>1\*</sup>

<sup>1</sup>Center for Advancing Electronics Dresden (cfaed) and Faculty of Chemistry and Food Chemistry, Technische Universität Dresden, 01062 Dresden, Germany

<sup>2</sup>I. Physical Institute, Faculty of Physics, Georg-August-University Göttingen, 37077 Göttingen, Germany

<sup>3</sup>Helmholtz-Zentrum Dresden-Rossendorf, Institute of Ion Beam Physics and Materials Research, 01328 Dresden, Germany

<sup>4</sup>Faculty of Chemistry and Pharmacy, University of Sofia, 1164 Sofia, Bulgaria

<sup>5</sup>Central Facility for Electron Microscopy, Electron Microscopy of Materials Science Central, Facility for Electron Microscopy, Ulm University, 89081 Ulm, Germany

<sup>6</sup>National Institute for Materials Science, 305-0047 Tsukuba, Japan

<sup>7</sup>Physics of Nanosystems, Department of Physics, Ludwig-Maximilians-University München, 80799 Munich, Germany

<sup>8</sup>Max Planck Institute for Microstructure Physics, Weinberg 2, Halle (Saale), D-06120 Germany

<sup>9</sup>Helmholtz-Zentrum Dresden-Rossendorf, Institute of Resource Ecology, Leipzig Research Branch, 04316 Leipzig, Germany

<sup>10</sup>Department of Chemistry, Yonsei University, 50 Yonsei-ro, Seodaemun-gu, Seoul, 03722 Korea

<sup>11</sup>Center for Advancing Electronics Dresden (cfaed) and Faculty of Electrical and Computer Engineering, Technische Universität Dresden, 01062 Dresden, Germany

#### **Corresponding Author**

\*Ralf Thomas Weitz (thomas.weitz@uni-goettingen.de)

\*Xinliang Feng (xinliang.feng@tu-dresden.de)

\*Renhao Dong (renhao.dong@tu-dresden.de)

## Table of Contents

<b>Materials and methods</b> .....	4
Materials .....	4
Methods.....	4
General characterizations .....	4
AC-HRTEM measurements .....	4
GIWAXS measurements.....	4
Modeling and electronic structure .....	5
Variable-temperature conductivity and Hall effect measurements in macroscopic devices for lateral direction .....	5
Macroscopic vertical devices .....	9
Local characterization of directional charge transport .....	9
<b>Synthetic Procedures</b> .....	12
Synthesis of PcM-OH <sub>8</sub> .....	12
Synthesis of Cu <sub>2</sub> [PcCu-O <sub>8</sub> ] MOF film .....	13
Synthesis of Cu <sub>2</sub> [PcFe-O <sub>8</sub> ] MOF film .....	13
<b>Supporting Figures and Tables</b> .....	14
Figure S1 .....	14
Figure S2 .....	15
Figure S3.....	16
Figure S4.....	17
Figure S5 .....	18
Figure S6.....	19
Figure S7.....	20
Figure S8.....	21
Figure S9.....	22
Figure S10.....	23
Figure S11 .....	24
Figure S12 .....	25
Figure S13.....	26
Figure S14.....	27
Figure S15 .....	28
Figure S16.....	29
Figure S17 .....	30
Figure S18.....	31
Figure S19.....	32
Figure S20.....	33
Figure S21 .....	34
Figure S22 .....	35
Figure S23.....	36

Table S1 .....	37
Table S2 .....	38
<b>Reference</b> .....	<b>41</b>

## Materials and methods

### Materials

Chemicals (e.g., copper (II) acetate and sodium acetate) and solvents (e.g., N,N-Dimethylformamide (DMF) and chloroform) were purchased from PorphyChem and Sigma-Aldrich, and used directly without further purification. Water was purified using a Milli-Q purification system (Merck KGaA). All the reactions were carried out under an ambient atmosphere. Substrates (e.g., 300 nm SiO<sub>2</sub>/Si wafer, quartz glass, and copper grids) were obtained from Plano GmbH.

### Methods

#### General characterizations.

Optical microscopy (Zeiss), Atomic force microscopy (AFM) (NT-MDT), transmission electron microscopy (TEM, Zeiss, Libra 200 KV), and scanning electron microscopy (SEM, Zeiss Gemini 500) equipped with EDX was used to investigate the morphology and structure of the samples. Two-dimensional metal-organic frameworks (2D MOFs) films were deposited on Si substrate for SEM, and copper grids for TEM characterizations. All optical microscopy and AFM images were recorded on a 300-nm SiO<sub>2</sub>/Si substrate. UV-visible spectra were measured on a UV-vis-NIR Spectrophotometer Cary 5000 at room temperature using a 3×3 cm quartz wafer. FTIR spectra were collected using Tensor II (Bruker) with an attenuated total reflection (ATR) unit. The samples were prepared by depositing the films onto a copper foil. X-ray photoelectron spectroscopy (XPS) measurements were carried out using an AXIS Ultra DLD system. Both survey and high-resolution spectra were collected using a beam diameter of 100 μm. All displayed binding energy values are calibrated to the graphitic C1s peak with a value of 284.6 eV.

#### AC-HRTEM measurements.

AC-HRTEM imaging and selected area electron diffraction (SAED) were conducted on an image-side C<sub>s</sub>-corrected FEI Titan 80-300 microscope operated at 300 kV. The low-dose technique was applied to preserve the pristine structure of the 2D *c*-MOFs. The electron dose rate for AC-HRTEM and SAED were as low as 200 e<sup>-</sup> Å<sup>-2</sup>s<sup>-1</sup> and 0.15 e<sup>-</sup> Å<sup>-2</sup>s<sup>-1</sup>, respectively. For AC-HRTEM imaging, the spherical aberration coefficient C<sub>s</sub> was tuned to approx. -15 μm and the images were acquired using over-focus conditions. To maximize the contrast transfer for low spatial frequencies, relative large defocus values (20-200 nm) were selected.

#### GIWAXS measurements.

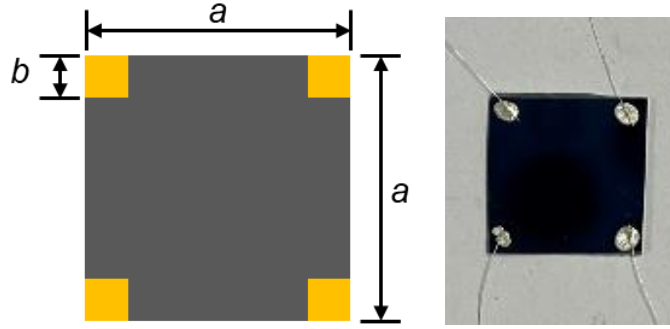
The GIWAXS measurements were performed at the XRD1 beamline at ELETTRA, Trieste, Italy. The detector was a Dectris Pilatus 2M and the photon beam energy was 12.398 keV (λ = 1 Å). The sample-to-detector distance was 350.2 mm and was verified using a lanthanhexaborid (LaB6) calibration standard.

The grazing incidence angle was chosen to be  $0.13^\circ$  and the sample exposure time was 180 s. The scattering data were then analyzed with WxDiff.

### **Modeling and electronic structure.**

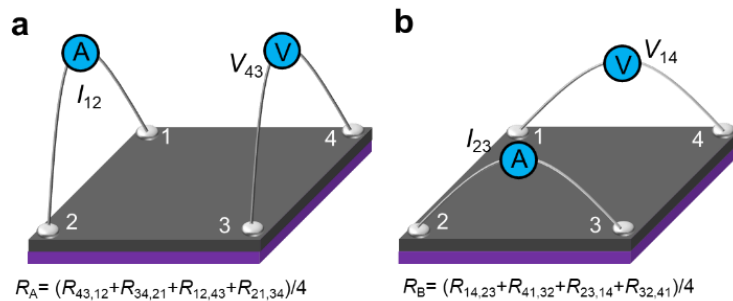
DFT calculations were carried out using the Vienna ab-initio Simulation Package (VASP)<sup>1</sup> version 5.4.1. The electronic wave-functions were expanded in a plane-wave basis set with a kinetic energy cutoff of 400 eV. The energy stopping criterion was set to EDIFF = 1E-6 eV. The lattice constants for the monolayer  $\text{Cu}_2[\text{PcCu-O}_8]$  was optimized with PBE-D2 and SCAN functionals respectively. Both functionals fall to the local minima at difference of 0.04 Å. The PBE-D2 predicts the minima at  $a=b=18.36$  Å, while SCAN at 18.40 Å (0.2% discrepancy in a and b lattice vectors). In the case of MOFs, HSE06, known as one of the most accurate hybrid XC-functional for band gap calculations, is more than 100 times slower than one of the best local functionals HLE17 for band gaps in MOFs.<sup>2</sup> Unfortunately, using of HLE17 needs some code modifications and recompilation of VASP. According to the recent research in ref.<sup>2</sup> the mean unsigned error of PBE+U, HSE06 and HLE17 are 0.49, 0.32, and 0.35 eV, respectively over 32 semiconductors including MOFs. Thus we conclude that PBE+U still remains the best compromise for band gap accuracy concerning the feasibility of these calculations. The geometry optimization convergence was set to forces acting on the ions were smaller than  $0.03 \text{ eV \AA}^{-1}$ . Electron-ion interactions were described using the projector augmented wave (PAW) method.<sup>3</sup> Generalized gradient approximation (GGA)<sup>4</sup> of the exchange-correlation energy in the form of Perdew-Burke-Ernzerhof (PBE) was applied.<sup>5</sup> We used DFT+U approach to describe the localized d-orbitals of Cu ions. The effective Coulomb (U) and exchange (J) terms were set to 4 and 1 eV, respectively.<sup>6</sup> Such a combination of U and J are already successfully applied for very similar systems.<sup>7</sup> The  $\text{Cu}_2[\text{PcCu-O}_8]$  monolayer was modeled by adding a large vacuum space, 10 Å, in the direction normal to the monolayer. Monkhorst-Pack Gamma-centered grid<sup>8</sup> with  $3 \times 3 \times 1$  dimension was used for K-point sampling of the Brillouin zone for the monolayer during the geometry optimization and  $9 \times 9 \times 1$  for band structure calculations. In the computational protocol for the 3D stacking of  $\text{Cu}_2[\text{PcCu-O}_8]$  the K-point grid dimension was changed to  $2 \times 2 \times 4$  for the geometry optimization and  $4 \times 4 \times 6$  for the band structure calculations and Grimme-D2 correction for the dispersion interlayer interactions was applied.<sup>9</sup> In order to estimate the possible charge transfer between the layers of  $\text{Cu}_2[\text{PcCu-O}_8]$ , a Bader analysis was performed.<sup>10</sup>

### **Variable-temperature conductivity and Hall effect measurements in macroscopic devices for lateral direction.**



**Scheme S1.** Van der Pauw sample geometry in square shape. Contacts are orange.  $a$  represents the sample size of 1 cm while  $b$  is the contact size of 0.1 cm. Typically,  $a$  should be much larger than  $b$ .

The macroscopic electrical measurements, i.e., temperature-dependent conductivity, carrier concentration, and Hall mobility are characterized in the van der Pauw geometry (Scheme S1) using a commercial Lakeshore Hall System (9700A). This fully integrated Hall measurement system is capable to detect the resistance ranging from 0.04 m $\Omega$  to 200 G $\Omega$ . Moreover, it can set a magnetic field of up to  $\pm 9$  T by a superconducting magnet, and the temperature is varied from 1.8 to 400 K by heating and liquid helium cooling. Silver-conductive glue paste was used to contact the silver wires to the samples. The insulating substrate hereby prevents that shorts are detected even if the silver conductive glue percolates through gaps in the Cu<sub>2</sub>[PcCu-O<sub>8</sub>] films. For the electrical conductivity measurements, samples were measured in the temperature range from 256 K to 310 K. After confirming the Ohmic contact at different temperatures, we collected an  $I$ - $V$  curve by scanning the current from -10 nA to 10 nA and measuring the voltage at each step at every certain temperature. For the Hall effect measurements, samples were measured at room temperature (300 K) and a magnetic field perpendicular to the sample plane was swept from -4 T to 4 T. A schematic of a square van der Pauw configuration is shown in Scheme S1. The detailed procedures to carry out resistivity and Hall measurements using the van der Pauw technique are described in the following.



**Scheme S2.** Schematic view of a van der Pauw configuration used in the determination of the two characteristic resistances  $R_A$  and  $R_B$ .<sup>11-12</sup> Contacts are labeled 1, 2, 3, and 4 counterclockwise.

**Resistivity measurements.** Van der Pauw method demonstrates that there are two characteristic resistances  $R_A$  and  $R_B$ , associated with the corresponding terminals shown in Scheme S2. In the basic van der Pauw contact arrangement, the four contacts on the sample are numbered in ascending order. It is important to use the same batch of wire for all four leads to minimizing thermoelectric effects. Similarly, all contacts should consist of the same material.

To obtain the two characteristic resistances, one applies a DC current into contact 1 and out of contact 2 and measures the voltage  $V_{43}$  from contact 4 to contact 3 as shown in Scheme S2a. Next, the current  $I$  is applied into contact 2 and out of contact 3 while measuring the voltage  $V_{14}$  from contact 1 to contact 4 (shown in Scheme S2b). Then, one should reverse the polarity of the current  $I_{21}$  ( $I_{32}$ ) and measure  $V_{34}$  ( $V_{41}$ ). After that, the same process will repeat for the remaining voltage values. Eight measurements of voltage yield the following eight values of resistance, all of which must be positive:

$$R_{21,34} = \frac{V_{34}}{I_{21}}, R_{12,43} = \frac{V_{43}}{I_{12}}, \quad (1.1)$$

$$R_{32,41} = \frac{V_{41}}{I_{32}}, R_{23,14} = \frac{V_{14}}{I_{23}}, \quad (1.2)$$

$$R_{43,12} = \frac{V_{12}}{I_{43}}, R_{34,32} = \frac{V_{21}}{I_{34}}, \quad (1.3)$$

$$R_{14,23} = \frac{V_{23}}{I_{14}}, R_{41,32} = \frac{V_{32}}{I_{41}}, \quad (1.4)$$

Thus, the characteristic resistances  $R_A$  and  $R_B$  are calculated using the following expressions:

$$R_A = \frac{R_{43,12} + R_{34,21} + R_{12,43} + R_{21,34}}{4} \quad (1.5)$$

$$R_B = \frac{R_{14,23} + R_{41,32} + R_{23,14} + R_{32,41}}{4} \quad (1.6)$$

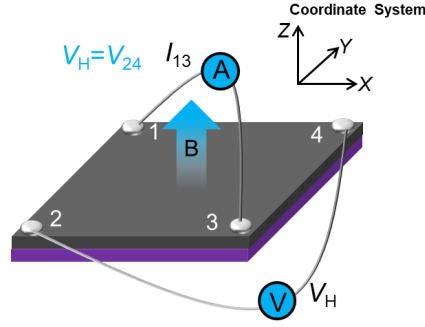
The sheet resistance  $R_s$  can be determined numerically from the two characteristic resistances  $R_A$  and  $R_B$  through the van der Pauw equation:

$$\exp\left(\frac{-\pi R_A}{R_s}\right) + \exp\left(\frac{-\pi R_B}{R_s}\right) = 1 \quad (1.7)$$

Therefore, the bulk electrical resistivity  $\rho$  can be calculated using

$$\rho = R_s d \quad (1.8)$$

where  $d$  is the thickness of the  $\text{Cu}_2[\text{PcCu-O}_8]$  sample.



**Scheme S3.** Schematic of a van der Pauw configuration used in the determination of the Hall voltage  $V_H$ .

**Hall measurements.** The objective of the Hall measurement by the van der Pauw technique is to determine the sheet carrier density ( $n_s$ ) by measuring the Hall voltage ( $V_H$ ). The Hall voltage measurement consists of a series of voltage measurements with a constant current  $I$  and a constant magnetic field  $B$  applied perpendicular to the plane of the sample. An example is shown in Scheme S3. To measure the Hall voltage  $V_H$ , a current  $I$  is forced through the opposing pair of contacts 1 and 3 and the Hall voltage  $V_H = V_{24}$  is measured across the remaining pair of contacts 2 and 4. Once the Hall voltage  $V_H$  is acquired, the sheet carrier density  $n_s$  can be calculated via

$$n_s = \frac{IB}{e\gamma V_H} \quad (1.9)$$

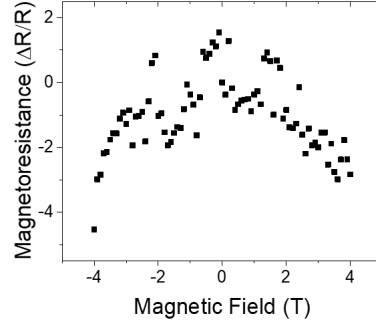
where  $I$  is current,  $B$  is the magnetic field,  $V_H$  is the Hall voltage,  $e$  ( $1.602 \times 10^{-19}$  C) is the elementary charge and  $\gamma$  is the Hall scattering factor (generally assumed to be 1 in heavily doped Si system)<sup>13-14</sup>. If the effective thickness of the conducting layer  $d$  is known, the bulk density ( $N$ ) can be determined as:

$$N = \frac{n_s}{d} \quad (1.10)$$

Besides, the polarity of the Hall voltage indicates which type of carrier dominates the conducting behavior of the sample, and the Hall voltage is negative for  $n$ -type semiconductors (electron) and positive for  $p$ -type semiconductors (hole). As described before, the sheet resistance  $R_s$  of the semiconductor can be conveniently determined by using the van der Pauw resistivity measurement technique. Since sheet resistance involves both sheet density and mobility, the Hall mobility can be obtained via the equation below:

$$\mu = \frac{|V_H|}{IBR_s} = \frac{1}{qn_s R_s} \quad (1.11)$$

Normally, the unit of the Hall mobility is  $\text{cm}^2\text{V}^{-1}\text{s}^{-1}$ .



**Scheme S4.** Magnetoresistance as a function of the magnetic field.

The magnetoresistance as the function of the magnetic field is shown in Scheme S4. The magnetoresistance is in the order of  $10^8 \Omega/\text{sq}$ , and the line shape is relatively symmetric. Therefore, the influence of magnetoresistance on Hall resistance can be neglected.

### Macroscopic vertical devices.

For the vertical devices as shown in Figure 3a (right), gold contacts with sizes of  $350 \mu\text{m}$  were evaporated through shadow masks, resulting in the structure shown in Figure S18. The channel length ( $L$ ) is the thickness of the sample, which was varied between 20 and 250 nm, and the channel area ( $A$ ) is  $\sim 1.3 \times 10^{-3} \text{ cm}^2$ . The conductivity was calculated with the equation:

$$\sigma = \frac{1}{R_{\text{sample}}} \cdot \frac{L}{A}$$

where  $R_{\text{sample}} = V/I$ .

We calculated the conductivity in Figure 3d by  $R = \left(\frac{\partial I}{\partial V}\right)^{-1}$  and the conductivity using  $\sigma = \rho^{-1} = \left(R \cdot \frac{A}{L}\right)^{-1}$  with  $A$ ,  $L$ , the channel area, and length, respectively.

The values of conductivity as presented in Figure 3d and Figure 3e were calculated after excluding the contact resistance ( $2R_c$ ).

$$R_{\text{sample}} = R_{\text{total}} - 2R_c,$$

where  $R_{\text{total}}$  was resolved by linear fitting the  $I$ - $V$  curve in the voltage range from -1 to 1 V; and  $2R_c$  was extracted with the use of transmission line measurement (TLM) to be  $\sim 2600 \Omega \cdot \text{cm}$  in vertical devices.

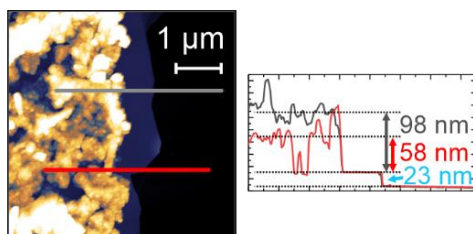
### Local characterization of directional charge transport.

**Lateral transport.** Field-effect transistors (FETs) for local lateral transport measurements were fabricated on substrates of highly doped Si with 300 nm  $\text{SiO}_2$ . Hexagonal boron nitride ( $h$ -BN) flakes were exfoliated and the  $\text{Cu}_2[\text{PcCu-O}_8]$  film was applied on top, as described in the main text. Suitable flakes were located using an optical microscope (Zeiss) and electrical contacts were structured using

electron beam lithography (Raith e-LINE system) in an ultrahigh vacuum. Contacts of 0.5 nm titanium (at  $0.1 \text{ \AA s}^{-1}$ ) and 60 nm gold (at  $1.0 \text{ \AA s}^{-1}$ ) were evaporated in an UHV evaporation chamber (BesTec) at  $\sim 10^{-7}$  mbar. In this manner, transistor geometries with several contacts per flake were obtained (e.g. six in Figure S19). By detecting  $I$ - $V$  curves for each pair of neighboring contacts, in sum 15 measurements were taken.

The electrical measurements were taken in a LakeShore Probe station CRX-VF at room temperature and  $3 \times 10^{-5}$  mbar using two Keithley Sourcemeters 2450. We detected no field effect, presumably due to a significant amount of charge trapping in the thin film, even by applying gate voltages up to  $\pm 120$  V. However, the use of  $h$ -BN was observed to increase the detected current in two-point measurements and the stability against degradation, compared to  $h$ -BN free substrates. Due to its two-dimensional nature, the roughness of the underneath lying substrate is minimized, and trapping at the insulator- $\text{Cu}_2[\text{PcCu-O}_8]$ -interface is suppressed.

From the detected currents, we calculated the resistance by  $R = \left(\frac{\partial I}{\partial V}\right)^{-1}$  and the conductivity using  $\sigma = \rho^{-1} = \left(R \cdot \frac{Wd}{L}\right)^{-1}$  with  $W$ ,  $L$ , the channel width and length, respectively. The film thickness,  $d$ , was measured by the step height at a scratch in the film down to the substrate using a Bruker Icon AFM in tapping mode, exemplarily shown for one device in Scheme S5.

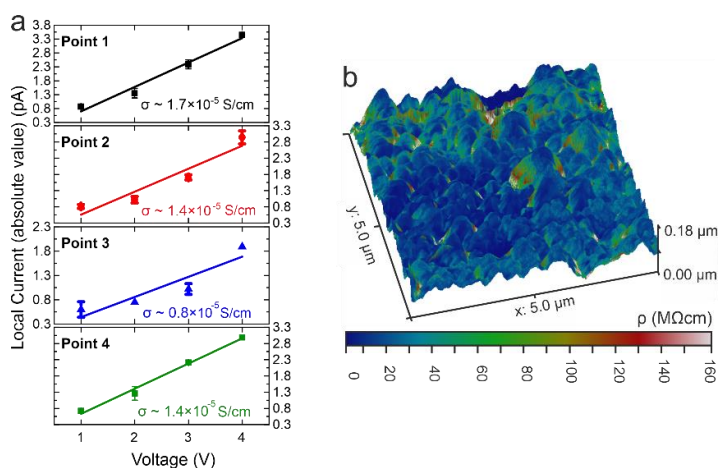


**Scheme S5.** Measurement of mean film thickness at an arbitrarily chosen spot by AFM step height down to the substrate. Red and grey denote the detected film height for the  $\text{Cu}_2[\text{PcCu-O}_8]$  film at two different positions, blue is the height of the  $h$ -BN.

Besides the conductivity, the total resistance  $R$  was plotted for increasing channel lengths  $L$  to estimate the contact resistance of the nanoscopic gold contacts. However, no  $R(L)$  dependence could be observed. This might be drawn back to the inhomogeneity of the  $\text{Cu}_2[\text{PcCu-O}_8]$  film within the size of one  $h$ -BN flake.

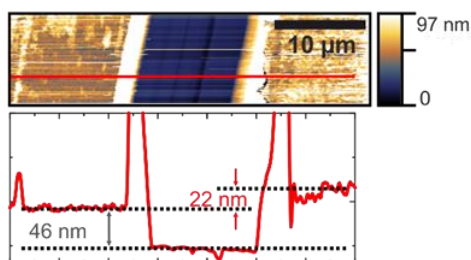
**Vertical transport.** For the local electrical measurements in the vertical direction,  $\text{Cu}_2[\text{PcCu-O}_8]$  films were applied on substrates with a 50 nm thick layer of silver. c-AFM measurements were taken, as it was observed before, that the evaporation of gold on very thin films of  $\text{Cu}_2[\text{PcCu-O}_8]$  film on top of conductive substrates may lead to shorts, due to percolating contact material or because the

evaporation of gold destroys the  $\text{Cu}_2[\text{PcCu-O}_8]$  film. The measurements were taken using the c-AFM mode of an Icon AFM (Bruker) at ambient pressure and room temperature. The tip used is an SCM-PIT-V2 ( $k=2.8 \text{ N m}^{-1}$ , PtIr coating), at which we applied voltages between 1 and 4 V, while keeping the silver layer grounded. The contact area between tip and film is estimated to  $100 \text{ nm}^2$ .<sup>15</sup> This measurement setup corresponds to the suggested setup by Jiang, Weber, et al. to prevent local anodic oxidation, and we can exclude degradation of the tip due to the small number of scans we have made (ten in total for each of two different positions on the film).<sup>15</sup> To calculate the local conductivity of the film in the intralayer direction, we extracted the absolute current values at the highest points within one scan (compare Figure S20) for the reasons given in the main text and below. The resulting plots for the first four points are presented in Scheme S6a. From fitting a linear curve for each data set, the resistivity and conductivity are calculated as presented for the lateral transport measurements (with  $R=1/\text{slope}$  and  $wd=A=100 \text{ nm}^2$ ).



**Scheme S6.** (a) Extracted currents from the four highest points detected in Figure S20a with a linear fit and the resulting conductivity, calculated as explained in the text. (b) 3D topography plot of the spot shown in Figure S20c with the local resistivity in the color scale.

For the calculation of the film thickness, we determined the mean thickness of the  $\text{Cu}_2[\text{PcCu-O}_8]$  film to  $d = 19 \pm 3 \text{ nm}$  by measuring the step height to the substrate, as shown in Scheme S7. However, this value cannot be used for local resistivity/conductivity calculations, as both topography scans at the two arbitrarily chosen spots (Figure S20) show that the film height varies by about 90 to 160 nm. Hence, the detected height of a certain position with respect to the lowest point within one scan is taken as effective film thickness  $d_{\text{eff}}$ . By only analyzing the highest points, the error according to the unknown underneath lying film thickness will thereby be reduced.



**Scheme S7.** Measurement of mean film thickness at an arbitrarily chosen spot by AFM step height down to the substrate. In red, the average thickness of the  $\text{Cu}_2[\text{PcCu-O}_8]$  film is given, grey denotes the thickness of the silver layer.

Another way to calculate the resistivity without the use of a fit function is given in Scheme S6b. Here, we directly calculated and plotted the resistivity  $\rho = \frac{4V}{I(x,y)} \cdot \frac{A_{eff}}{d_{eff}(x,y)}$  from the c-AFM plot taken at  $V_t = 4 \text{ V}$  and the topography scan using the arithmetic function of Gwydion.<sup>16</sup> We did this to prove if the deviation of the  $I$ - $V$ -dependence from the Ohmic law has a high impact on the resistivity values. From the three dimensional (3D) plot correlating the topography (z-axis) and resistivity (color scale), we can conclude that: (1) the resistivity is mostly independent of the film height; (2) at steep flanks the resistivity takes the highest values, presumably due to bending of the AFM tip or decreased contact between tip and sample (the resistivity values were consequently extracted at positions of flat geometry), and (3) the resistivity values calculated from the  $I$ - $V$  dependence as explained above tend to be underestimated (and therefore the conductivities in the main text are overestimated), but the results go along with the previously made observation, that the resistivity of the  $\text{Cu}_2[\text{PcCu-O}_8]$  film along the intralayer direction is much higher than along interlayer direction.

## Synthetic Procedures

### Synthesis of PcM-OH<sub>8</sub>

**PcCu-OMe<sub>8</sub>:** The synthesis was adopted from reported literature procedures.<sup>17-19</sup> 1, 2-dibromo-4, 5-dimethoxybenzene (8.87 g, 0.03 mol), and 8.06 g (0.09 mol) of CuCN was refluxed in DMF at 165 °C for 5 h. After cooling at room temperature, 300 ml of concentrated ammonium hydroxide was added into the above reaction mixture and it was stirred at room temperature for 12 h under air. Then the green solid was obtained by filtration and washed with a copious amount of diluted ammonium hydroxide and water. The dry, crude olive-green product was placed in the thimble of a Soxhlet extractor and extracted with methanol and acetone for 1 day. Then, the green solid was collected.

**PcCu-OH<sub>8</sub>:** 2 g as-prepared PcCu-OMe was dissolved into 300 ml of dry dichloromethane, and boron tribromide (4.8 ml) was added under Ar atmosphere. After stirring at room temperature for 2 h, the mixture was refluxed for 20 h. After cooling down, 50 ml of methanol was slowly added to the mixture.

Then the precipitates were filtered and washed with MeOH, water, and dichloromethane, centrifuged many times with water, MeOH, and dichloromethane until the supernatant became almost transparent, as well as dried under vacuum.

**PcFe-OH<sub>8</sub>:** PcCu-OH<sub>8</sub> (0.005 mmol) was well dispersed into DMF (25 ml). After adding 2.2 ml of NH<sub>3</sub> H<sub>2</sub>O (v/v: 50%), the PcCu-OH<sub>8</sub> solution was diluted with 30 ml of H<sub>2</sub>O. After sonication for 5 min, 5 ml of Fe(acac)<sub>2</sub> (0.01 mmol) solution was added to the above mixture. This mixture was transferred into the autoclave and heated at 120 °C for 40 h. Finally, the solid was obtained by filtration, washed with DMF, H<sub>2</sub>O, and acetone, and vacuum dried at room temperature.

**Reagents:** All solvents, reagents, and chemicals were purchased from commercial suppliers (Sigma-Aldrich, TCI, and abcr GmbH.) and used without further purification unless specially addressed. All the reactions were performed using the standard vacuum-line and Schleck techniques under argon or vacuum.

**Synthesis of Cu<sub>2</sub>[PcCu-O<sub>8</sub>] MOF film.** PcCu-OH<sub>8</sub> (1 mg) was dissolved in 3 ml of mixed chloroform/DMF solvent (2:1, in volume). A beaker (80 ml, diameter = 6 cm) was filled with 40 ml Milli-Q water under the ambient condition to form a static air/water interface. 200 µl of a freshly prepared PcCu-OH<sub>8</sub> solution was carefully spread drop-by-drop onto the water surface with a syringe. The solvent was allowed to evaporate for 30 minutes. Then, 5 ml copper(II) acetate (1 mg ml<sup>-1</sup>) and 2 ml sodium acetate (1 mg ml<sup>-1</sup>) were subsequently added to the subphase. The reaction system was left undisturbed under an ambient atmosphere for 18 h to obtain a film on the water surface. The as-prepared film was then transferred onto substrates.

**Synthesis of Cu<sub>2</sub>[PcFe-O<sub>8</sub>] MOF film.** PcFe-OH<sub>8</sub> (1 mg) was dissolved in 3 ml of mixed chloroform/DMF solvent (2:1, in volume). A beaker (80 ml, diameter = 6 cm) was filled with 40 ml Milli-Q water under the ambient condition to form a static air/water interface. 200 µl of a freshly prepared PcCu-OH<sub>8</sub> solution was carefully spread drop-by-drop onto the water surface with a syringe. The solvent was allowed to evaporate for 30 minutes. Then, 5 ml copper(II) acetate (1 mg ml<sup>-1</sup>) and 2 ml sodium acetate (1 mg ml<sup>-1</sup>) were subsequently added to the subphase. The reaction system was left undisturbed under an ambient atmosphere for 18 h to obtain a film on the water surface. The as-prepared film was then transferred onto substrates.

## Supporting Figures and Tables

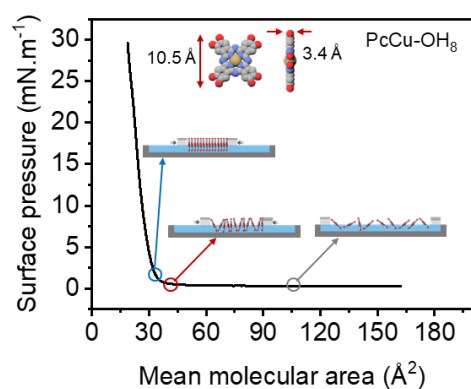


**Figure S1.** Surface pressure-mean molecular area ( $\pi$ -A) isotherm for PcCu-OH<sub>8</sub>. 50  $\mu$ l freshly prepared solution of PcCu-OH<sub>8</sub> (0.47 mM) in chloroform/DMF (2:1 in volume) was spread onto the water surface. After 10 min evaporation of the solvent, the Delrin barriers were driven forward to compress PcCu-OH<sub>8</sub> on the water surface at a rate of 5 mm min<sup>-1</sup> until the surface pressure reaching 30 mN m<sup>-1</sup>. The small molecular area implies that the PcCu-OH<sub>8</sub> molecules stand vertically on the water surface.

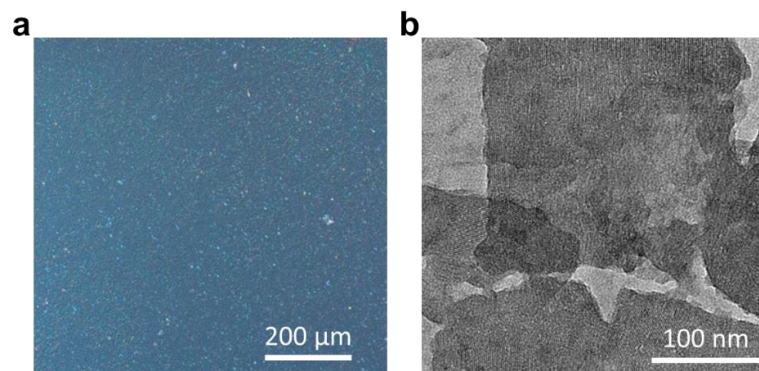


**Figure S2.** Structural characterization of the PcCu-OH<sub>8</sub> ligand self-assembly. Optical microscopy (OM) (a) and (b) TEM images of the self-assembly PcCu-OH<sub>8</sub>.

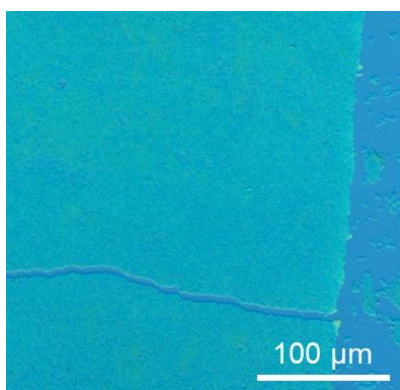


**Figure S3.** OM image of  $\text{Cu}_2[\text{PcCu-O}_8]$  film.

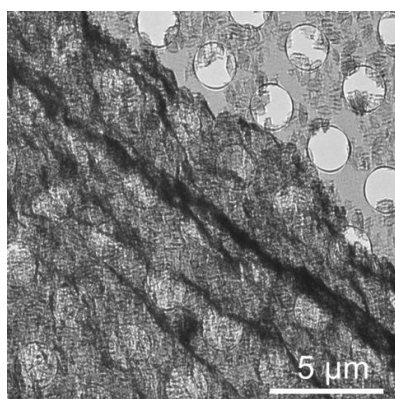


**Figure S4.** TEM image of Cu<sub>2</sub>[PcCu-O<sub>8</sub>] film.

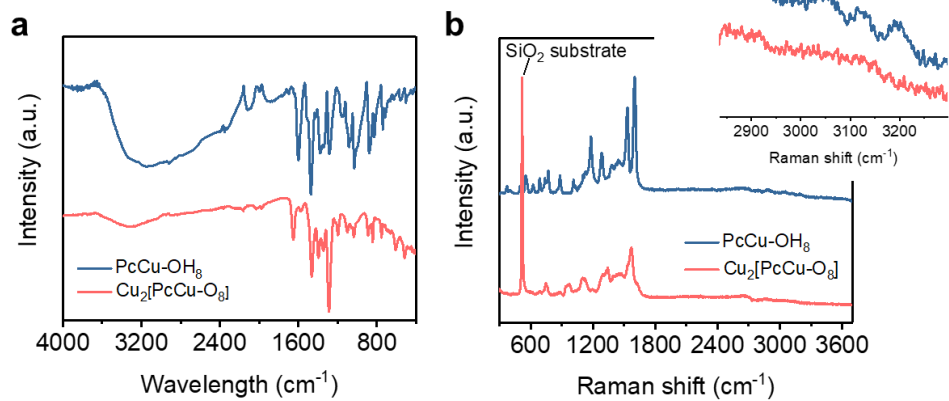


**Figure S5.** ATR-FTIR (a) and Raman (b) spectra of PcCu-OH<sub>8</sub> monomer and Cu<sub>2</sub>[PcCu-O<sub>8</sub>].

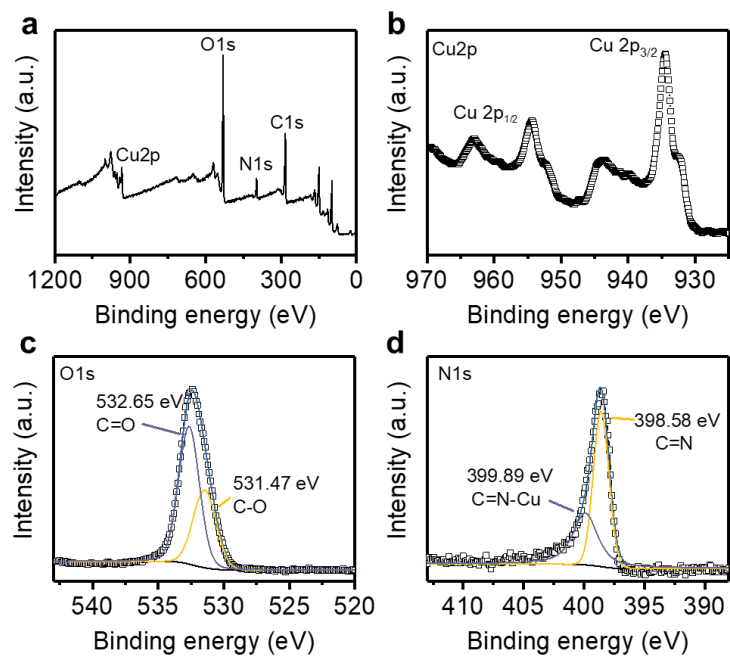


**Figure S6.** Chemical structure analysis. Survey (a) Cu 2p (b), O 1s(c) and N 1s (d) XPS spectra of  $\text{Cu}_2[\text{PCu-O}_8]$ .

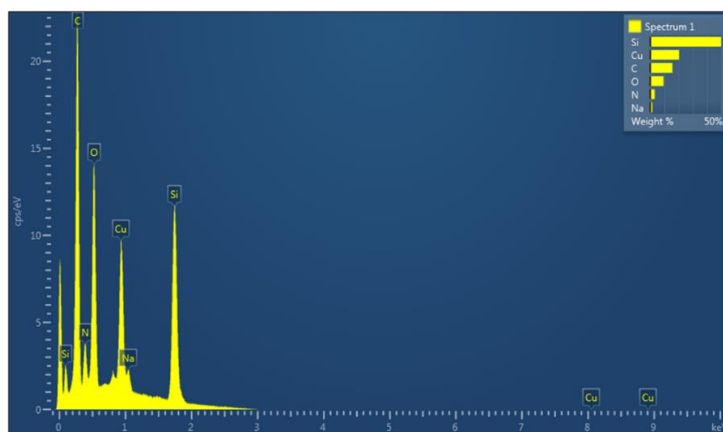


**Figure S7.** EDS spectrum revealing the sheet composition with respect to C, N, O, Cu and Na.

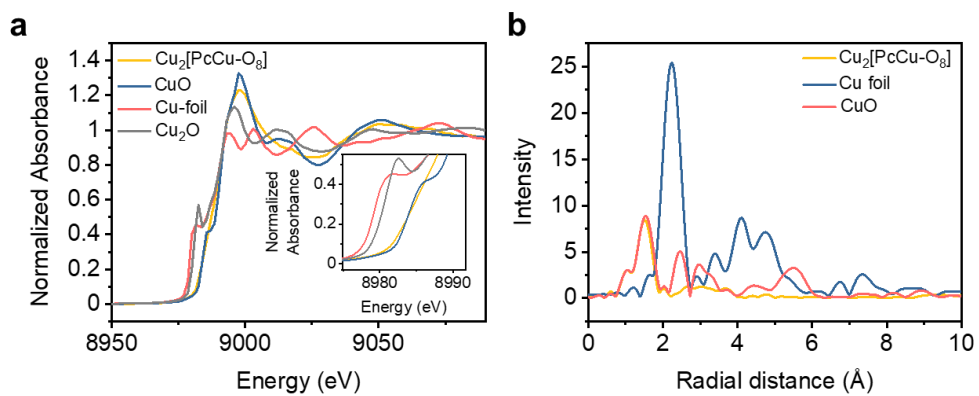


**Figure S8.** (a) Normalized Cu K-edge XANES spectra of  $\text{Cu}_2[\text{PcCu-O}_8]$ , CuO, Cu foil and  $\text{Cu}_2\text{O}$ . (b) Fourier transformation EXAFS spectra at Cu K-edge of  $\text{Cu}_2[\text{PcCu-O}_8]$  with Cu foil and CuO as contrast.

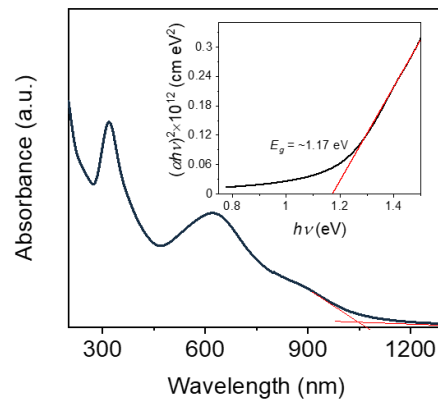


**Figure S9.** The UV-vis spectrum of  $\text{Cu}_2[\text{PcCu-O}_8]$ . Inset: the Tauc plot indicates a direct bandgap of  $\sim 1.17$  eV for  $\text{Cu}_2[\text{PcCu-O}_8]$  film.

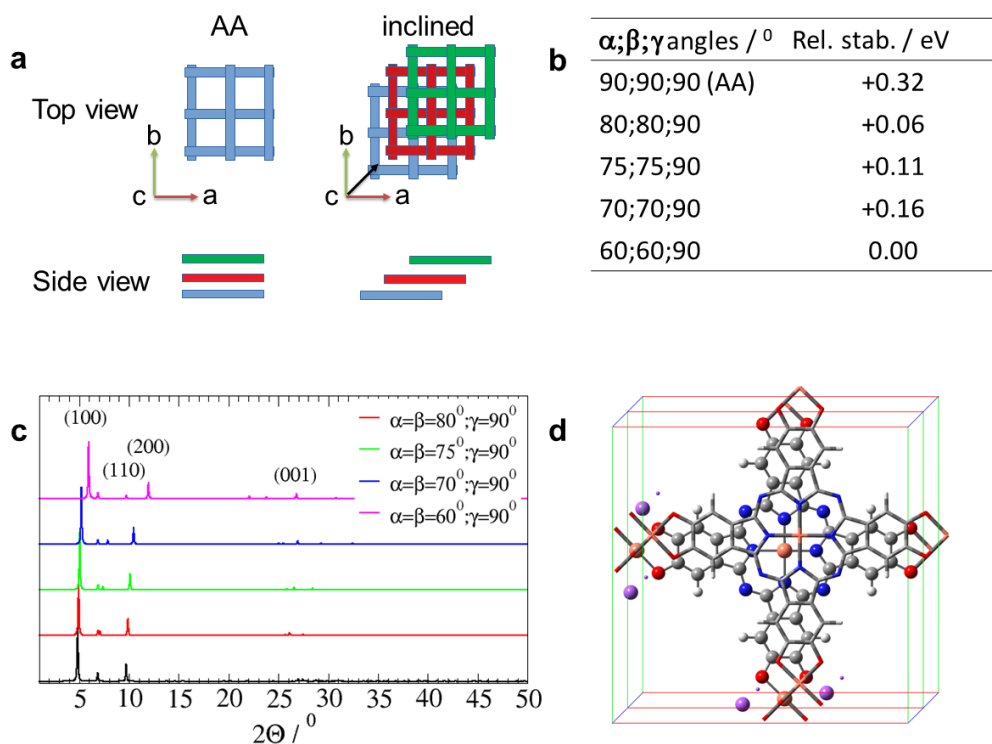


**Figure S10.** (a) Schematic representation of transformation from AA to inclined stacking mode. (b) Relative stability for different stacking orders starting from AA toward inclined stacking. The inclination of the structure was achieved by changing  $\alpha$  and  $\beta$  angles from  $90^\circ$  to  $60^\circ$  of the unit cell, at a constant interlayer distance of 0.33 nm. The relative stability of different stacking orders starting from AA towards inclined stacking was calculated and the corresponding numbers are collected. (c) Simulated PXRD for several different structures of AA  $\rightarrow$  inclined stacking transformation. Note that the stronger (200) peak in the GIWAXS profile might be due to the edge-on orientation of the  $\text{Cu}_2[\text{PcCu-O}_8]$  film, and the presence of an unresolved angle (should be below  $90^\circ$ ) between the basal plane and the substrate. (d) Atomistic model of the inclined structure with  $\alpha = \beta = 75^\circ$ . Orange, grey, red, blue, and purple spheres represent Cu, C, O, N, and Na atoms, respectively.

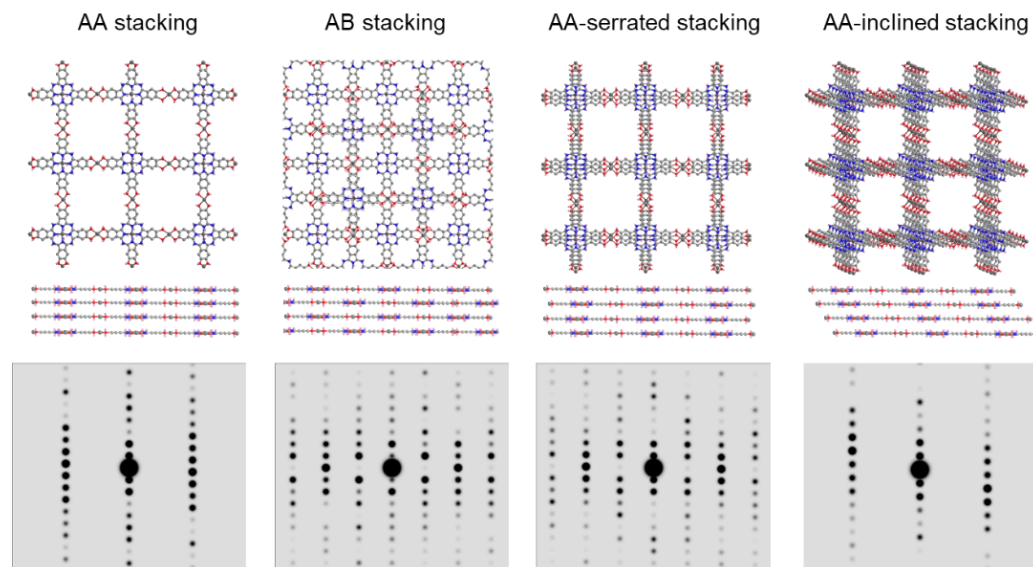


**Figure S11** DFT models of different stacking modes of  $\text{Cu}_2[\text{PcCu-O}_8]$  ([001] projection) and corresponding simulated SAED patterns ([100] projection).

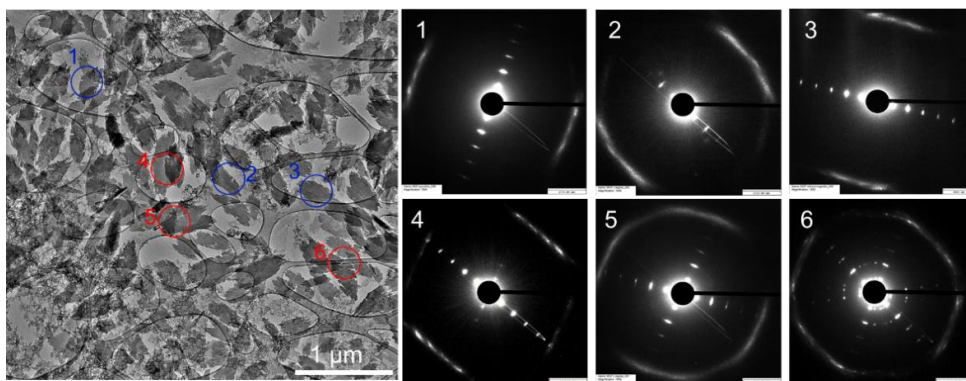


**Figure S12.** The SAED patterns obtained from isolated sheets.

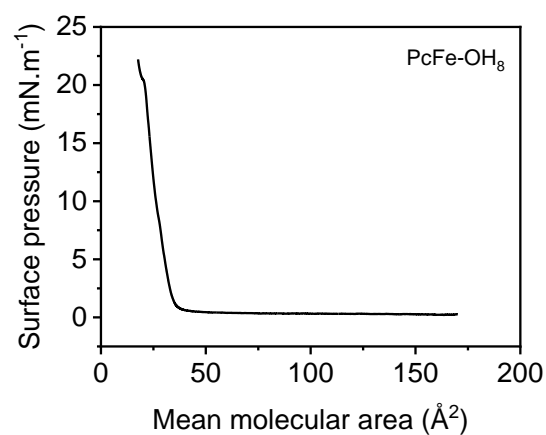


**Figure S13.**  $\pi$ -A isotherm for PcFe-OH<sub>8</sub>. 50  $\mu$ l freshly prepared solution of PcFe-OH<sub>8</sub> (0.45 mM) in chloroform/DMF (2:1 in volume) was spread onto the water surface. After 10 min evaporation of the solvent, the Delrin barriers were driven forward to compress PcFe-OH<sub>8</sub> on the water surface at a rate of 5 mm min<sup>-1</sup> until the surface pressure reached 22 mN m<sup>-1</sup>. The small molecular area implies that the PcFe-OH<sub>8</sub> molecules stand vertically on the water surface.

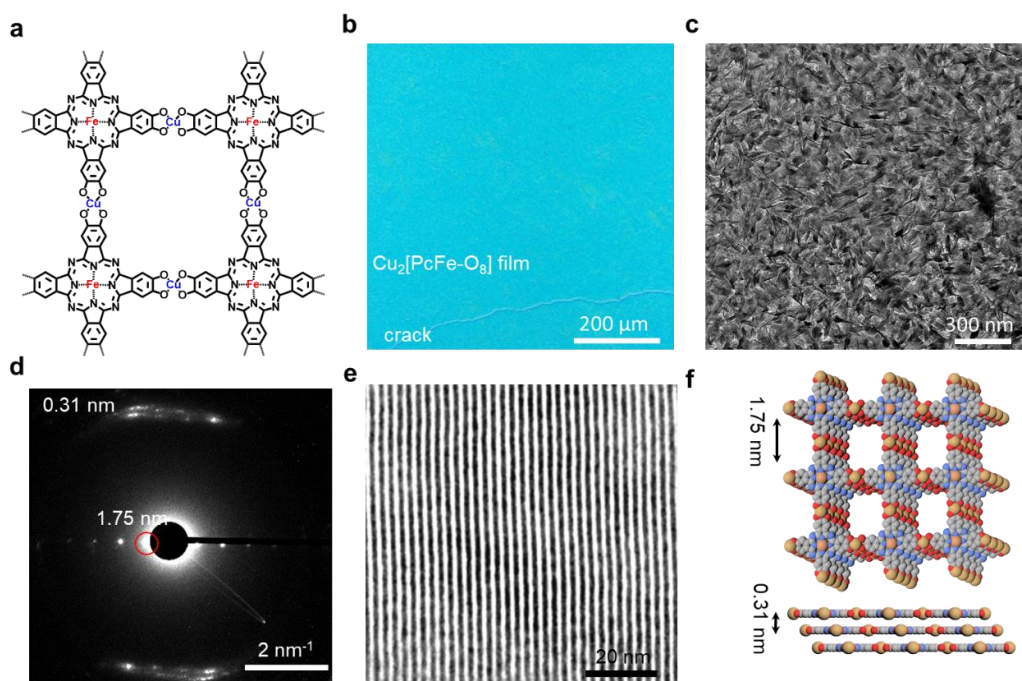


**Figure S14.** Crystal-structural characterization of the  $\text{Cu}_2[\text{PcFe-O}_8]$ . (a) Scheme for  $\text{Cu}_2[\text{PcFe-O}_8]$ . OM (b), and (c) TEM images of  $\text{Cu}_2[\text{PcFe-O}_8]$ . (d) Corresponding SAED pattern. (e) HRTEM image of  $\text{Cu}_2[\text{PcFe-O}_8]$ . (f) Crystal structure of  $\text{Cu}_2[\text{PcFe-O}_8]$ . Grey, brown, red, blue, and white spheres represent Cu, Fe, O, N, and C atoms, respectively.

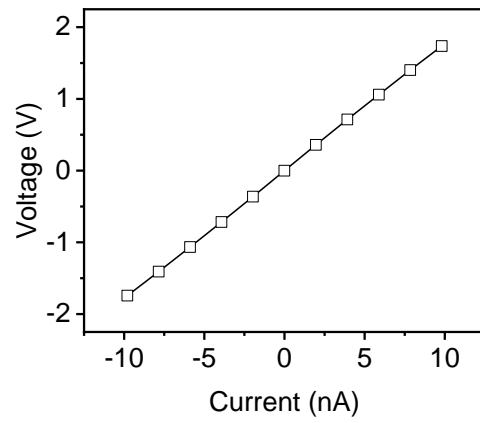


**Figure S15.** *I-V* curve of  $\text{Cu}_2[\text{PcCu-O}_8]$  for van der Pauw measurement.

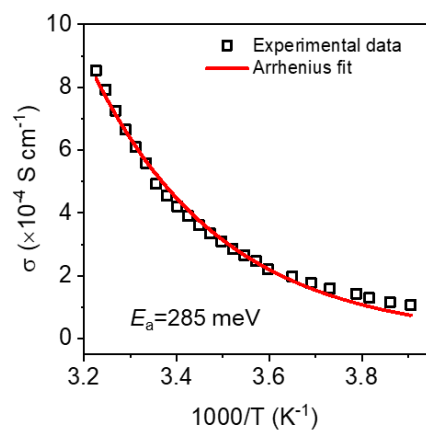


**Figure S16.** The plot of  $\sigma$  versus the reciprocal of the temperature ( $1000/T$ ).

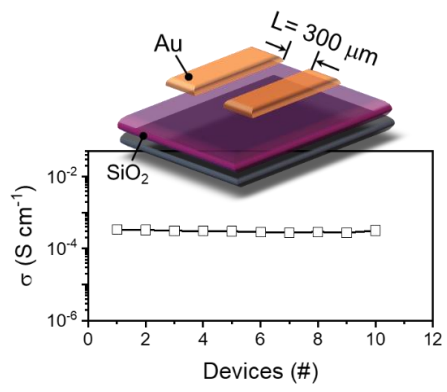


**Figure S17.** The conductivity of 10 two-probe devices with channel length of 300 μm.

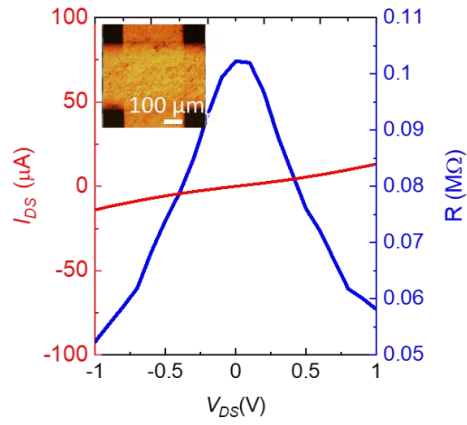


**Figure S18.** Measured  $I$ - $V$  curve for the vertical device with a thickness of 20 nm. Inset: optical microscopy image of the vertical device; the device area is determined as  $\sim 1.3 \times 10^{-3} \text{ cm}^2$ , i.e., the area overlapped between the top and bottom electrodes. Note that the resistance was measured by linear fitting of the  $I$ - $V$  curve in the voltage range from -1 to +1 V.

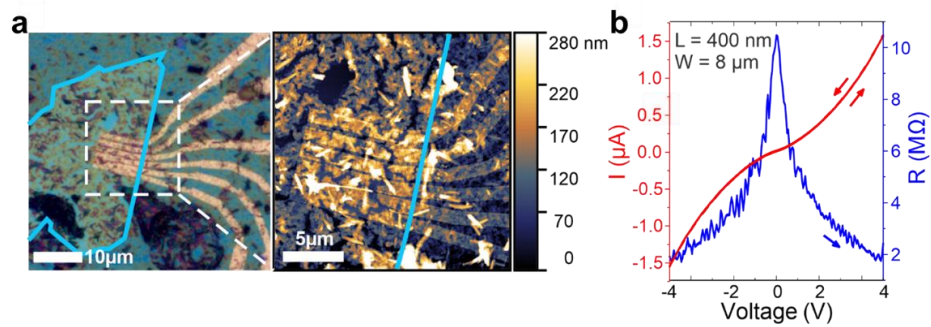


**Figure S19.** (a) Optical microscope image (left) and AFM image (right) of contact structures on one exemplary *h*-BN flake, which is marked in blue. Each flake contains several contacts. *I*-*V* curves were measured for each pair of neighboring contacts. (b) Measured *I*-*V* curve and inverse of derivative (*R*) for lateral contacts with separation of 400 nm.

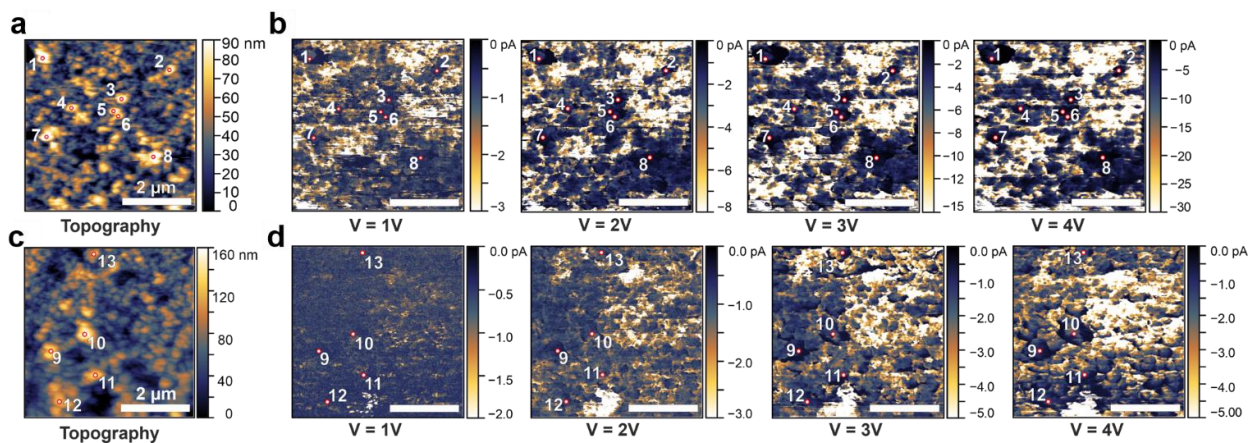


**Figure S20.** Topography of two arbitrarily chosen spots on the  $\text{Cu}_2[\text{PcCu-O}_8]$  film (a, c) and corresponding currents at the given applied voltages (b, d). The 8 and 5 highest points, respectively, from which the conductivity was derived as shown in Scheme 6, are labeled.

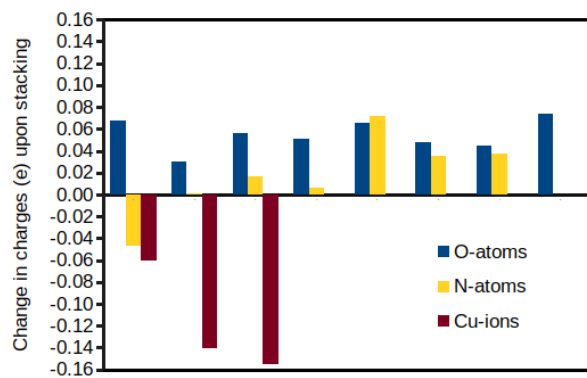


**Figure S21.** Changes in the calculated Bader atomic charges upon stacking.

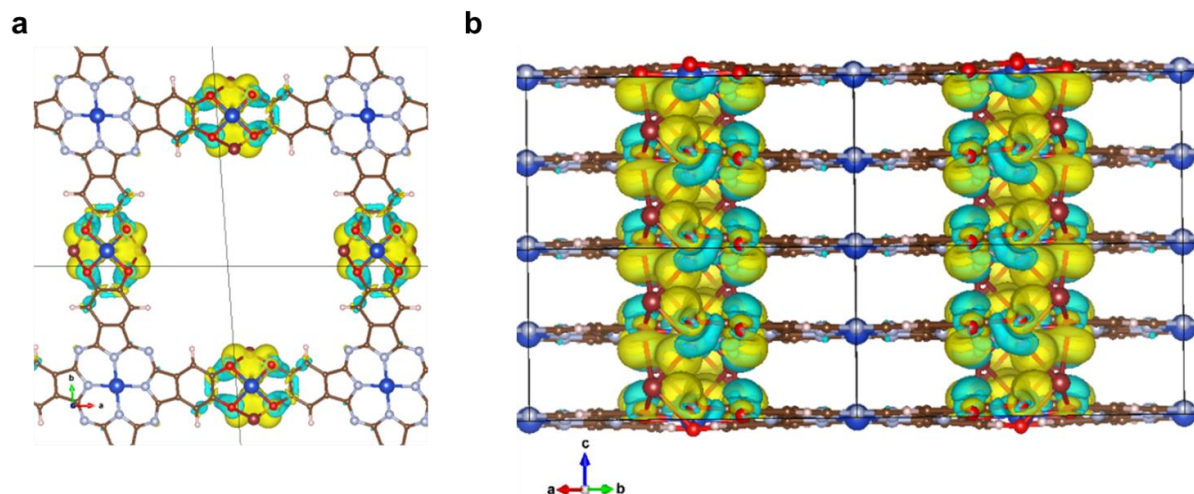


**Figure S22.** The charge density difference map of  $\text{Cu}_2[\text{PcCu-O}_8]$  multilayer with respect to the monolayer. (a) top view, (b) side view. Colour code: positive-yellow, negative-cyan. The charge density difference map shows, that the main charge density redistribution happens at the  $\text{Cu-O}_4$  moiety, as it is demonstrated already by the Bader charge analysis.

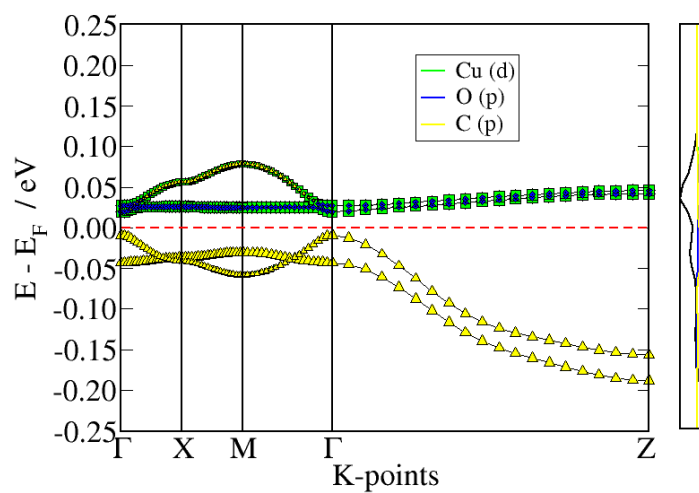


**Figure S23.** The fat bands show main contributions from O, C and Cu at the band edges. Cu(d) levels and O(p) levels overlap and form the conductive bands, while the C(p) levels are below the Fermi level and form the edge of the valence bands.

**Table S1. Interfacial synthetic MOF thin films.**

MOFs	Linker/build units	Configuration	Method	Thickness	Ref
CoTCPP-py-Cu	-COOH/Cu <sup>2+</sup>	face-on	LB <sup>[c]</sup>	monolayer	20
NAFS-1	-COOH/Cu <sup>2+</sup>	face-on	LB	monolayer	21
H <sub>2</sub> TCPP_Cu	-COOH/Cu <sup>2+</sup>	face-on	LB	monolayer	22
THTNi	-SH/Ni <sup>2+</sup>	face-on	LB	0.7-0.9	23
THTA-Co	-SH(NH <sub>2</sub> )/Co <sup>2+</sup>	face-on	LB	0.8 nm	24
[Cu <sub>2</sub> I <sub>2</sub> (TAA)] <sub>n</sub>	-I,S/Cu <sup>2+</sup>	face-on	petri dish	4	25
N1	Pyridine/Zn <sup>2+</sup>	face-on	vial	1.2 nm	26
FeNi-mono	-CN/Ni <sup>2+</sup>	face-on	LB	Monolayer	27
nano-1	-SH/Ni <sup>2+</sup>	face-on	beaker	0.6 nm	28
Cu-BHT	-SH/Cu <sup>2+</sup>	face-on	L/L <sup>[d]</sup>	15-500 nm	29
Ag-BHT	-SH/Ag <sup>+</sup>	face-on	L/L	~ 1 μm	30
PtBHT	-SH/Pt <sup>2+</sup>	face-on	L/L	0.6 nm	31
Co <sub>3</sub> (BHT) <sub>2</sub>	-SH/Co <sup>2+</sup>	random	L/L	360 nm	32
Ag <sub>3</sub> (BHT) <sub>2</sub>	-SH/Ag <sup>+</sup>	random	L/L	~ 276 nm	33
Au <sub>3</sub> (BHT) <sub>2</sub>	-SH/Au <sup>+</sup>	random	L/L	~ 324 nm	33
Ni-HAB	-NH <sub>2</sub> /Ni <sup>2+</sup>	face-on	L/L	10 nm	34
Cu-HAB	-NH <sub>2</sub> /Cu <sup>2+</sup>	face-on	L/L	11 nm	34
Co-HAB	-NH <sub>2</sub> /Co <sup>2+</sup>	face-on	L/L	13 nm	34
Cu-CAT-1	-OH/Cu <sup>2+</sup>	face-on	L/L	40 nm	35
Fe <sub>3</sub> (THT) <sub>2</sub> (NH <sub>4</sub> ) <sub>3</sub>	-SH/Fe <sup>2+</sup>	face-on	L/L	20 nm-2 μm	36
Ni <sub>3</sub> (HITP) <sub>2</sub>	-NH <sub>2</sub> /Ni <sup>2+</sup>	random	vial	100 nm	37
Cu <sub>3</sub> (HHTP) <sub>2</sub>	-OH/Cu <sup>2+</sup>	face-on	on solid surface	50-250 nm	38
<b>Cu<sub>2</sub>[PcCu-O<sub>8</sub>]</b>	<b>-OH/Cu<sup>2+</sup></b>	<b>edge-on</b>	<b>beaker</b>	<b>20 nm</b>	<b>This work</b>
<b>Cu<sub>2</sub>[PcFe-O<sub>8</sub>]</b>	<b>-OH/Cu<sup>2+</sup></b>	<b>edge-on</b>	<b>beaker</b>	<b>30 nm</b>	<b>This work</b>

[a] M<sup>2+</sup>=Co<sup>2+</sup>, Ru<sup>2+</sup>, Zn<sup>2+</sup>, Pb<sup>2+</sup>, Ni<sup>2+</sup>, Fe<sup>2+</sup>. [b] Hexafunctional terpyridine. [c] Langmuir–Blodgett (LB) method. [d] Liquid/liquid (L/L) interface method.

**Table S2.** Cell vectors and the optimized coordinates for the multilayered ( $\text{Cu}_2[\text{PcCu-O}_8]$ ) 2D *c*-MOF in a POSCAR file format:

C Cu H N Na O

```

1.0000000000000000
18.1262239399999991    0.0000000000000000    0.0000000000000000
-0.0012968900000000    18.1257430900000003    0.0000000000000000
 0.9317485599999999    0.9318152300000000    3.3501589500000000

```

```

C    Cu    H    N    Na    O
32    3    8    8    4    8

```

Direct

```

0.5989748529547967    0.3312881956294760    0.4373032762138749
0.5917393856770730    0.7816720580564152    0.5663689575724362
0.6002060585504339    0.2015163963110638    0.4038398729457953
0.5935824364207463    0.9126692436941255    0.5726912153496713
0.6200876050445245    0.4060295644688523    0.4724239624425479
0.6152506589956204    0.7061722947632774    0.5483155219827083
0.6393455662677781    0.2663476203247015    0.4193429651807605
0.6323619307827428    0.8465575951585649    0.5710287561882552
0.7067998340310311    0.4930202522347358    0.5416222122795986
0.7057610297482029    0.6154548638041106    0.5530491712644121
0.7810918941379654    0.5919303136603205    0.5757218589778645
0.7813423640231250    0.5142657550291574    0.5788382585349154
0.8459233055153561    0.4736924765420980    0.6045614364544889
0.8461964918430382    0.6328185968497877    0.5762091898421886
0.9122169661124033    0.5939201038876689    0.5812905061327100
0.9109902747340541    0.5131867776898815    0.6150838680572122
0.2016156597099652    0.6001646908097058    0.3984083239905587
0.2003061962873716    0.5194948716853034    0.4312254426829369
0.2669851133345205    0.6396154063871791    0.4056302779182204
0.2663761251341654    0.4805411089887812    0.4325919799010478
0.3317021324354386    0.5990152566259894    0.4268681463848409
0.3318530591459847    0.5213845195616571    0.4293342425827404
0.4065168137133739    0.6203756087294892    0.4600899370524587
0.4074526001742100    0.4979603768524186    0.4476732264263745

```

0.4811266037665618	0.2669044932092959	0.4279533014340231
0.4740982849335538	0.8471479956248729	0.5803905285818303
0.4982092652323544	0.4073820151436749	0.4499092194817749
0.4933903191003779	0.7075116203905409	0.5264129783756530
0.5198757051770926	0.2007485967718665	0.4276989630147199
0.5132163735338580	0.9119114545975719	0.5969472368017392
0.5217850427038186	0.3318843506167823	0.4315944279592685
0.5145173297315324	0.7822913686544197	0.5610829197809721
0.5567357889931159	0.5567755073750860	0.4988404715588146
0.5567367450101557	0.0566833197638204	0.5010826689413506
0.0561917320544651	0.5567361615313047	0.5086620039285989
0.6995539232579020	0.2658664881242672	0.4190220975601804
0.6928507360250791	0.8458877984600477	0.5649941078914793
0.8458710026822303	0.4130049376875533	0.6146926835191096
0.8458684858634342	0.6936307628963618	0.5629920077667023
0.2671160977716482	0.7002515078036069	0.3965940239446013
0.2665316211826578	0.4197392128715407	0.4457492107126271
0.4206619252916681	0.2676187170238649	0.4338173199271367
0.4138822337747783	0.8476233690144781	0.5806463710272922
0.5549074779615495	0.6628869083946967	0.5258458951991187
0.5585618930862211	0.4506449613358328	0.4725789479132558
0.6624714748012366	0.5548474558859411	0.5332970927388985
0.6882523003223966	0.4245414430772527	0.5091632720079389
0.6851831073702570	0.6855846640723655	0.5551655051926545
0.4281784097145476	0.4279186738412761	0.4442733534673309
0.4251277995269263	0.6889150074811496	0.4916159919465386
0.4509208174695658	0.5586405188075858	0.4657819086508965
0.6795738202140669	0.0567856460348324	0.8726422569996259
0.0573979270814249	0.6794576303211315	0.8756478837263586
0.0550560442624430	0.4340330450832539	0.1409501237316206
0.4338925997281677	0.0565160475468360	0.1287113701760845
0.6359496681250079	0.1357284619685615	0.3797692884065569
0.6306955095749700	0.9810918257576873	0.5367492602928365
0.9766581309567570	0.4773750884023542	0.6422979514769054
0.9808786652345773	0.6311886888362821	0.5397671949315992

0.1357563730494107	0.6359454138569944	0.3755998698716354
0.1314709966749419	0.4822485161043915	0.4755765199678450
0.4827470452676081	0.1322833095870664	0.4646243584668781
0.4774582495570172	0.9776754212633350	0.6216972677000356

## References

- (1) Kresse, G.; Furthmüller, J., Efficiency of ab-initio total energy calculations for metals and semiconductors using a plane-wave basis set. *Comput. Mater. Sci.* **1996**, *6* (1), 15-50.
- (2) Choudhuri, I.; Truhlar, D. G., HLE17: An efficient way to predict band gaps of complex materials. *The Journal of Physical Chemistry C* **2019**, *123* (28), 17416-17424.
- (3) Kresse, G.; Joubert, D., From ultrasoft pseudopotentials to the projector augmented-wave method. *Phys. Rev. B* **1999**, *59* (3), 1758-1775.
- (4) Perdew, J. P.; Chevary, J. A.; Vosko, S. H.; Jackson, K. A.; Pederson, M. R.; Singh, D. J.; Fiolhais, C., Atoms, molecules, solids, and surfaces: applications of the generalized gradient approximation for exchange and correlation. *Phys. Rev. B* **1992**, *46* (11), 6671-6687.
- (5) Perdew, J. P.; Burke, K.; Ernzerhof, M., Generalized gradient approximation made simple. *Phys. Rev. Lett.* **1996**, *77* (18), 3865-3868.
- (6) Anisimov, V. I.; Aryasetiawan, F.; Lichtenstein, A. I., First-principles calculations of the electronic structure and spectra of strongly correlated systems: theLDA+Umethod. *J. Phys.: Condens. Matter* **1997**, *9* (4), 767-808.
- (7) Li, W.; Sun, L.; Qi, J.; Jarillo-Herrero, P.; Dincă, M.; Li, J., High temperature ferromagnetism in  $\pi$ -conjugated two-dimensional metal-organic frameworks. *Chem. Sci.* **2017**, *8* (4), 2859-2867.
- (8) Monkhorst, H. J.; Pack, J. D., Special points for brillouin-zone integrations. *Phys. Rev. B* **1976**, *13* (12), 5188-5192.
- (9) Grimme, S., Semiempirical GGA-type density functional constructed with a long-range dispersion correction. *J. Comput. Chem.* **2006**, *27* (15), 1787-1799.
- (10) Yu, M.; Trinkle, D. R., Accurate and efficient algorithm for Bader charge integration. *The Journal of Chemical Physics* **2011**, *134* (6), 064111.
- (11) Chwang, R.; Smith, B. J.; Crowell, C. R., Contact size effects on the van der Pauw method for resistivity and Hall coefficient measurement. *Solid State Electron.* **1974**, *17* (12), 1217-1227.
- (12) Rietveld, G.; Koijmans, C. V.; Henderson, L. C.; Hall, M. J.; Harmon, S.; Warnecke, P.; Schumacher, B., DC conductivity measurements in the Van der Pauw geometry. *IEEE. Trans. Instrum. Meas.* **2003**, *52* (2), 449-453.
- (13) Van der Pauw, L., Philips Res. Rep., 13 {1958} 1. *Philips Tech. Rev* **1958**, *20*, 320.
- (14) Winkler, M. T.; Recht, D.; Sher, M. J.; Said, A. J.; Mazur, E.; Aziz, M. J., Insulator-to-metal transition in sulfur-doped silicon. *Phys. Rev. Lett.* **2011**, *106* (17), 178701.
- (15) Jiang, L.; Weber, J.; Puglisi, F. M.; Pavan, P.; Larcher, L.; Frammelsberger, W.; Benstetter, G.; Lanza, M., Understanding current instabilities in conductive atomic force microscopy. *Materials* **2019**, *12* (3), 459.
- (16) Nečas, D.; Klapetek, P., Gwyddion: an open-source software for SPM data analysis. *Open Phys.* **2012**, *10* (1), 181-188.
- (17) Ding, X.; Feng, X.; Saeki, A.; Seki, S.; Nagai, A.; Jiang, D., Conducting metallophthalocyanine 2D covalent organic frameworks: the role of central metals in controlling  $\pi$ -electronic functions. *Chem. Commun.* **2012**, *48* (71), 8952-8954.
- (18) Mineo, P.; Alicata, R.; Micali, N.; Villari, V.; Scamporrino, E., Water-soluble star polymers with a phthalocyanine as the core and poly (ethylene glycol) chains as branches. *J. Appl. Polym. Sci.* **2012**, *126* (4), 1359-1368.
- (19) Nagatomi, H.; Yanai, N.; Yamada, T.; Shiraishi, K.; Kimizuka, N., Synthesis and electric properties of a two-dimensional metal-organic framework based on phthalocyanine. *Chem. Eur. J.* **2018**, *24* (8), 1806-1810.
- (20) Makiura, R.; Motoyama, S.; Umemura, Y.; Yamanaka, H.; Sakata, O.; Kitagawa, H., Surface nano-architecture of a metal-organic framework. *Nat. Mater.* **2010**, *9* (7), 565-571.
- (21) Rubio-Giménez, V. c.; Tatay, S.; Volatron, F.; Martínez-Casado, F. J.; Martínez-Gastaldo, C.; Coronado, E., High-quality metal-organic framework ultrathin films for electronically active interfaces. *J. Am. Chem. Soc.* **2016**, *138* (8), 2576-2584.
- (22) Motoyama, S.; Makiura, R.; Sakata, O.; Kitagawa, H., Highly crystalline nanofilm by layering of

- porphyrin metal-organic framework sheets. *J. Am. Chem. Soc.* **2011**, *133* (15), 5640-5643.
- (23) Dong, R.; Pfeiffermann, M.; Liang, H.; Zheng, Z.; Zhu, X.; Zhang, J.; Feng, X., Large-area, free-standing, two-dimensional supramolecular polymer single-layer sheets for highly efficient electrocatalytic hydrogen evolution. *Angew. Chem., Int. Ed.* **2015**, *54* (41), 12058-12063.
- (24) Dong, R.; Zheng, Z.; Tranca, D. C.; Zhang, J.; Chandrasekhar, N.; Liu, S.; Zhuang, X.; Seifert, G.; Feng, X., Immobilizing molecular metal dithiolene-diamine complexes on 2D metal-organic frameworks for electrocatalytic H<sub>2</sub> production. *Chem. Eur. J.* **2017**, *23* (10), 2255-2260.
- (25) Moreno-Moreno, M.; Troyano, J.; Ares, P.; Castillo, O.; Nijhuis, C. A.; Yuan, L.; Amo-Ochoa, P.; Delgado, S.; Gómez-Herrero, J.; Zamora, F., One-pot preparation of mechanically robust, transparent, highly conductive, and memristive metal-organic ultrathin film. *ACS Nano* **2018**, *12* (10), 10171-10177.
- (26) Sakamoto, R.; Hoshiko, K.; Liu, Q.; Yagi, T.; Nagayama, T.; Kusaka, S.; Tsuchiya, M.; Kitagawa, Y.; Wong, W.-Y.; Nishihara, H., A photofunctional bottom-up bis (dipyrrinato) zinc (II) complex nanosheet. *Nat. Commun.* **2015**, *6*, 6713.
- (27) Culp, J. T.; Park, J.-H.; Meisel, M. W.; Talham, D. R., Monolayer, bilayer, multilayers: evolving magnetic behavior in langmuir-blodgett films containing a two-dimensional iron-nickel cyanide square grid network. *Inorg. Chem.* **2003**, *42* (9), 2842-2848.
- (28) Kambe, T.; Sakamoto, R.; Kusamoto, T.; Pal, T.; Fukui, N.; Hoshiko, K.; Shimojima, T.; Wang, Z.; Hirahara, T.; Ishizaka, K.; Hasegawa, S.; Liu, F.; Nishihara, H., Redox control and high conductivity of nickel bis (dithiolene) complex  $\pi$ -nanosheet: a potential organic two-dimensional topological insulator. *J. Am. Chem. Soc.* **2014**, *136* (41), 14357-14360.
- (29) Huang, X.; Sheng, P.; Tu, Z.; Zhang, F.; Wang, J.; Geng, H.; Zou, Y.; Di, C.; Yi, Y.; Sun, Y.; Xu, W.; Zhu, D., A two-dimensional  $\pi$ -d conjugated coordination polymer with extremely high electrical conductivity and ambipolar transport behaviour. *Nat. Commun.* **2015**, *6*, 7408.
- (30) Huang, X.; Li, H.; Tu, Z.; Liu, L.; Wu, X.; Chen, J.; Liang, Y.; Zou, Y.; Yi, Y.; Sun, J.; Xu, W.; Zhu, D., Highly conducting neutral coordination polymer with infinite two-dimensional silver-sulfur networks. *J. Am. Chem. Soc.* **2018**, *140* (45), 15153-15156.
- (31) Pal, T.; Doi, S.; Maeda, H.; Wada, K.; Tan, C. M.; Fukui, N.; Sakamoto, R.; Tsuneyuki, S.; Sasaki, S.; Nishihara, H., Interfacial transmetallation synthesis of a platinadithiolene nanosheet as a potential 2D topological insulator. *Chem. Sci.* **2019**, *10* (20), 5218-5225.
- (32) Clough, A. J.; Yoo, J. W.; Mecklenburg, M. H.; Marinescu, S. C., Two-dimensional metal-organic surfaces for efficient hydrogen evolution from water. *J. Am. Chem. Soc.* **2015**, *137* (1), 118-121.
- (33) Chen, I.-F.; Lu, C.-F.; Su, W.-F., Highly conductive 2D metal-organic framework thin film fabricated by liquid-liquid interfacial reaction using one-pot-synthesized benzenehexathiol. *Langmuir* **2018**, *34* (51), 15754-15762.
- (34) Lahiri, N.; Lotfizadeh, N.; Tsuchikawa, R.; Deshpande, V. V.; Louie, J., Hexaaminobenzene as a building block for a family of 2D coordination polymers. *J. Am. Chem. Soc.* **2017**, *139* (1), 19-22.
- (35) Rubio-Giménez, V.; Galbiati, M.; Castells-Gil, J.; Almora-Barríos, N.; Navarro-Sánchez, J.; Escorcia-Ariza, G.; Mattera, M.; Arnold, T.; Rawle, J.; Tatay, S.; Coronado, E.; Martí-Gastaldo, C., Bottom-up fabrication of semiconductive metal-organic framework ultrathin films. *Adv. Mater.* **2018**, *30* (10), 1704291.
- (36) Dong, R.; Han, P.; Arora, H.; Ballabio, M.; Karakus, M.; Zhang, Z.; Shekhar, C.; Adler, P.; Petkov, P. S.; Erbe, A.; Mannsfeld, S. C. B.; Felser, C.; Heine, T.; Bonn, M.; Feng, X.; Cónovas, E., High-mobility band-like charge transport in a semiconducting two-dimensional metal-organic framework. *Nat. Mater.* **2018**, *17* (11), 1027-1032.
- (37) Wu, G.; Huang, J.; Zang, Y.; He, J.; Xu, G., Porous field-effect transistors based on a semiconductive metal-organic framework. *J. Am. Chem. Soc.* **2016**, *139* (4), 1360-1363.
- (38) Song, X.; Wang, X.; Li, Y.; Zheng, C.; Zhang, B.; Di, C.-a.; Li, F.; Jin, C.; Mi, W.; Chen, L.; Hu, W., 2D semiconducting metal-organic framework thin films for organic spin valves. *Angew. Chem., Int. Ed.* **2020**, *59* (3), 1118-1123.

## H Related Theses

Several bachelor and master theses or internships were related to this thesis and conducted by great colleagues and future researchers. This section gives a small overview over their work in chronological order:

**T1** Philipp Klaus Maier: „**Richtungs-und Temperaturabhängigkeit der Mobilität in organischen Dünnfilm-Transistoren**“, Bachelor thesis, 2019

*Philipp investigated in his thesis directional and temperature-dependent charge transport in thin-film transistors of PDI1MPCN2. He investigated these properties in two different devices, one with macroscopic device geometries across several grain boundaries, and one with nanoscopic device geometries within a single crystalline of PDI1MPCN2.*

*He found that the orientation of grain boundaries with respect to charge transport had no significant impact on the mobilities, presumably due to overall low mobilities. Furthermore, mobilities in single grains of PDI1MPCN2 were one to two orders of magnitude higher than across grain boundaries, but highly anisotropic.*

**T2** Theresa Kammerbauer: „**Lösungsprozessierung und Charakterisierung dünner kristalliner Schichten eines Perylendiimids**“, Bachelor thesis, 2019

*Theresa studied the formation of thin films of a molecule similar to PDI1MPCN2. This molecule, N,N'-di((S)-1-ethylpentyl)-1,7(6)-dicyano-perylene-3,4:9,10-bis(dicarboximide) (PDI1EPCN2), has an ethyl group instead of a methyl group at the imide position of the perylene-diimide core, otherwise it has the same chemical structure as PDI1MPCN2. Theresa tested multiple application methods, starting from the same procedure used for PDI1MPCN2 and tested which variations to this application technique influenced the crystallization process of PDI1EPCN2.*

*The best results were obtained when benzyl benzoate was used instead of DMP as a solvent. Here, grain sizes similar to the ones in thin-films of PDI1MPCN2 could be achieved, with, however, significantly lower mobilities.*

**T3** Jakob Martin Braun: „**Towards Freestanding Thin Films of Organic Semiconductors utilizing Blading and Film Transfer Methods**“, Bachelor thesis, 2019

*Jakob investigated a completely new application technique for free-standing semiconductor materials. He used liquid crystals, a material class that is liquid at relatively small temperatures and crystallizes upon cooling toward room temperature.*

*While blading and dropcasting of liquid crystals failed for the moment, Jakob found a way to transfer thin films of 4-(undecyloxy)benzoic acid using thin, free-standing smectic films. This transfer method is a promising starting point for free suspension of organic semiconductors and semiconducting liquid-crystals.*

**T4** Lukas Renn: „**Charge Transport and Hall Effect Measurements in Organic Field Effect Transistors utilizing nanostructured Two Dimensional Materials**“, Master thesis, 2020

*Lukas fabricated and investigated thin-film transistors of PDI1MPCN2 on substrates containing h-BN flakes. Among others, he found increased device performance when introducing h-BN as insulating material into the transistors, he published his results in Publication **P5**.*

*Since Lukas is a specialist in applying organic semiconductors on inorganic two-dimensional materials, he also helped with the sample fabrication for Publication **P1** presented in Chapter 7.*

**T5** Davide Prosperino: „**Reducing Contact Effects in Bottom-Gate-Top-Contact**

**Devices of a Perylene Diimide Using Gentle Evaporation Techniques**“, Internship, 2020

*Davide investigated the impact of different evaporation techniques of gold contacts on top of solution-processed thin-films of PDI1MPCN2. He compared the mobilities of devices with contacts prepared via thermal and e-beam evaporation, and also tested whether an evaporated thin layer in between the solution-processed films and the contacts can act as a protection layer.*

*Due to the short time-scale of his internship, the results allow no statement on results, but the tendency could be observed that thermally evaporated contacts lead to better device performances than contacts evaporated by e-beam deposition.*

**T6 Daniel Vitroler: „Optimierung des Kristallisationsprozesses eines Perylendiimids aus der Lösung auf selbstorganisierenden Monolagen**“, Bachelor thesis, 2020

*Daniel prepared thin films of PDI1MPCN2 on substrates with SAMs and optimized the preparation conditions for 4-ethoxyphenylphosphonic acid (EPPA), TDPA, and ODTS. He investigated the influence of concentration, temperature, and different annealing steps on the surface free energy and roughness of the SAM-covered substrates.*

*Daniel succeeded to prepare thin films of PDI1MPCN2 from solution on top of ODTS, which had not or only with a low reproducibility possible so far.*

## References

- [1] The Nobel Foundation, *The Nobel Prize in Physics 2021* (05.10.2021), <https://www.nobelprize.org/prizes/physics/2021/summary/>.
- [2] Earth Science Communications Team at NASA's Jet Propulsion Laboratory, *Climate Change: Vital Signs of the Planet: Sustainability and Government Resources | Solutions* (14.09.2022), <https://climate.nasa.gov/solutions/resources/>.
- [3] A. Köhler and H. Bässler, *Electronic processes in organic semiconductors: An introduction*. Wiley-VCH Verlag GmbH & Co, Weinheim (2015), ISBN 978-3-527-33292-2.
- [4] Q. Zhang, W. Hu, H. Sirringhaus, and K. Müllen, *Recent Progress in Emerging Organic Semiconductors*. *Advanced materials* (Deerfield Beach, Fla.), 34(22):e2108701 (2022), <http://dx.doi.org/10.1002/adma.202108701>.
- [5] H. Sirringhaus, *25th anniversary article: organic field-effect transistors: the path beyond amorphous silicon*. *Advanced materials* (Deerfield Beach, Fla.), 26(9):1319–1335 (2014), <http://dx.doi.org/10.1002/adma.201304346>.
- [6] H. Chen, W. Zhang, M. Li, G. He, and X. Guo, *Interface Engineering in Organic Field-Effect Transistors: Principles, Applications, and Perspectives*. *Chemical reviews*, 120(5):2879–2949 (2020), <http://dx.doi.org/10.1021/acs.chemrev.9b00532>.
- [7] Y. Liu, B. Liu, C.-Q. Ma, F. Huang, G. Feng, H. Chen, J. Hou, L. Yan, Q. Wei, Q. Luo, Q. Bao, W. Ma, W. Liu, W. Li, X. Wan, X. Hu, Y. Han, Y. Li, Y. Zhou, Y. Zou, Y. Chen, Y. Li, Y. Chen, Z. Tang, Z. Hu, Z.-G. Zhang, and Z. Bo, *Recent progress in organic solar cells (Part I material science)*. *Science China Chemistry*, 65(2):224–268 (2022), <http://dx.doi.org/10.1007/s11426-021-1180-6>.
- [8] Y. Liu, B. Liu, C.-Q. Ma, F. Huang, G. Feng, H. Chen, J. Hou, L. Yan, Q. Wei, Q. Luo, Q. Bao, W. Ma, W. Liu, W. Li, X. Wan, X. Hu, Y. Han, Y. Li, Y. Zhou, Y. Zou, Y. Chen, Y. Liu, L. Meng, Y. Li, Y. Chen, Z. Tang, Z. Hu, Z.-G. Zhang, and Z. Bo, *Recent progress in organic solar cells (Part II device engineering)*. *Science China Chemistry*, 65(8):1457–1497 (2022), <http://dx.doi.org/10.1007/s11426-022-1256-8>.
- [9] J. Borges-González, C. J. Kousseff, and C. B. Nielsen, *Organic semiconductors for biological sensing*. *Journal of Materials Chemistry C*, 7(5):1111–1130 (2019), <http://dx.doi.org/10.1039/C8TC05900D>.
- [10] S.-J. Zou, Y. Shen, F.-M. Xie, J.-D. Chen, Y.-Q. Li, and J.-X. Tang, *Recent advances in organic light-emitting diodes: toward smart lighting and displays*. *Materials Chemistry Frontiers*, 4(3):788–820 (2020), <http://dx.doi.org/10.1039/C9QM00716D>.

- [11] J. H. Burroughes, D. D. C. Bradley, A. R. Brown, R. N. Marks, K. Mackay, R. H. Friend, P. L. Burns, and A. B. Holmes, *Light-emitting diodes based on conjugated polymers*. *Nature*, 347(6293):539–541 (1990),  
<http://dx.doi.org/10.1038/347539a0>.
- [12] C. W. Tang and S. A. VanSlyke, *Organic electroluminescent diodes*. *Applied Physics Letters*, 51(12):913–915 (1987),  
<http://dx.doi.org/10.1063/1.98799>.
- [13] 2020 BOE Technology Group Co., Ltd., *Flexible AMOLED Display* (16.09.2022),  
<https://www.boe.com/en/innovation/dynamic-316fd4e61b5d4eeab084d65820a12ec5>.
- [14] Heliatek GmbH, *Heliatek - The future is light* (16.09.2022),  
<https://www.heliatek.com/de/>.
- [15] Solar fabric (16.09.2022),  
<https://www.solarfabric.com/>.
- [16] E. G. Jeong, Y. Jeon, S. H. Cho, and K. C. Choi, *Textile-based washable polymer solar cells for optoelectronic modules: toward self-powered smart clothing*. *Energy & Environmental Science*, 12(6):1878–1889 (2019),  
<http://dx.doi.org/10.1039/c8ee03271h>.
- [17] X. Ren, K. Pei, B. Peng, Z. Zhang, Z. Wang, X. Wang, and P. K. L. Chan, *A Low-Operating-Power and Flexible Active-Matrix Organic-Transistor Temperature-Sensor Array*. *Advanced materials* (Deerfield Beach, Fla.), 28(24):4832–4838 (2016),  
<http://dx.doi.org/10.1002/adma.201600040>.
- [18] Welt der Physik, *Solarzellentypen im Überblick* (25.02.2016),  
<https://www.weltderphysik.de/gebiet/technik/energie/solarenergie/photovoltaik/solarzellentypen/>.
- [19] National Renewable Energy Laboratory, *Best Research-Cell Efficiency Chart* (16.09.2022),  
<https://www.nrel.gov/pv/cell-efficiency.html>.
- [20] P. Hu, X. He, and H. Jiang, *Greater than  $10\text{ cm}^2\text{ V}^{-1}\text{ s}^{-1}$  : A breakthrough of organic semiconductors for field-effect transistors*. *InfoMat*, 3(6):613–630 (2021),  
<http://dx.doi.org/10.1002/inf2.12188>.
- [21] F. Schindler, J. Geilker, W. Kwapil, W. Warta, and M. C. Schubert, *Hall mobility in multicrystalline silicon*. *Journal of Applied Physics*, 110(4):043722 (2011),  
<http://dx.doi.org/10.1063/1.3622620>.
- [22] N. B. Kotadiya, H. Lu, A. Mondal, Y. Ie, D. Andrienko, P. W. M. Blom, and G.-J. A. H. Wetzelaer, *Universal strategy for Ohmic hole injection into organic semiconductors with high ionization energies*. *Nature materials*, 17:329–334 (2018),  
<http://dx.doi.org/10.1038/s41563-018-0022-8>.
- [23] A. F. Paterson, S. Singh, K. J. Fallon, T. Hodsdon, Y. Han, B. C. Schroeder, H. Bronstein, M. Heeney, I. McCulloch, and T. D. Anthopoulos, *Recent Progress in High-Mobility Organic Transistors: A Reality Check*. *Advanced materials* (Deerfield Beach, Fla.), p. e1801079 (2018),  
<http://dx.doi.org/10.1002/adma.201801079>.

- [24] R. Rödel, F. Letzkus, T. Zaki, J. N. Burghartz, U. Kraft, U. Zschieschang, K. Kern, and H. Klauk, *Contact properties of high-mobility, air-stable, low-voltage organic n-channel thin-film transistors based on a naphthalene tetracarboxylic diimide*. Applied Physics Letters, 102(23):233303 (2013),  
<http://dx.doi.org/10.1063/1.4811127>.
- [25] M. Waldrip, O. D. Jurchescu, D. J. Gundlach, and E. G. Bittle, *Contact Resistance in Organic Field-Effect Transistors: Conquering the Barrier*. Advanced Functional Materials, 39:1904576 (2019),  
<http://dx.doi.org/10.1002/adfm.201904576>.
- [26] J. W. Borchert, *On the minimization of contact resistance in organic thin-film transistors*.  
<http://dx.doi.org/10.18419/OPUS-11325>.
- [27] R. Ahmed, M. Sams, C. Simbrunner, M. Ullah, K. Rehman, G. Schwabegger, H. Sitter, and T. Ostermann, *Reproducibility and stability of C(60) based organic field effect transistor*. Synthetic Metals, 161(23-24):2562–2565 (2012),  
<http://dx.doi.org/10.1016/j.synthmet.2011.08.008>.
- [28] Q. Burlingame, M. Ball, and Y.-L. Loo, *It's time to focus on organic solar cell stability*. Nature Energy, 5(12):947–949 (2020),  
<http://dx.doi.org/10.1038/s41560-020-00732-2>.
- [29] R. Gui, Y. Liu, Z. Chen, T. Wang, T. Chen, R. Shi, K. Zhang, W. Qin, L. Ye, X. Hao, and H. Yin, *Reproducibility in Time and Space-The Molecular Weight Effects of Polymeric Materials in Organic Photovoltaic Devices*. Small methods, 6(5):e2101548 (2022),  
<http://dx.doi.org/10.1002/smtd.202101548>.
- [30] P. P. Cielecki, T. Leißner, M. Ahmadpour, M. Madsen, H.-G. Rubahn, J. Fiutowski, and J. Kjelstrup-Hansen, *Photo-induced and electrical degradation of organic field-effect transistors*. Organic Electronics, 82:105717 (2020),  
<http://dx.doi.org/10.1016/j.orgel.2020.105717>.
- [31] H. F. Iqbal, Q. Ai, K. J. Thorley, H. Chen, I. McCulloch, C. Risko, J. E. Anthony, and O. D. Jurchescu, *Suppressing bias stress degradation in high performance solution processed organic transistors operating in air*. Nature communications, 12(1):2352 (2021),  
<http://dx.doi.org/10.1038/s41467-021-22683-2>.
- [32] C. Yumusak, N. S. Sariciftci, and M. Irimia-Vladu, *Purity of organic semiconductors as a key factor for the performance of organic electronic devices*. Materials Chemistry Frontiers, 4(12):3678–3689 (2020),  
<http://dx.doi.org/10.1039/D0QM00690D>.
- [33] O. D. Jurchescu, S. Subramanian, R. J. Kline, S. D. Hudson, J. E. Anthony, T. N. Jackson, and D. J. Gundlach, *Organic Single-Crystal Field-Effect Transistors of a Soluble Anthradithiophene*. Chemistry of Materials, 20(21):6733–6737 (2008),  
<http://dx.doi.org/10.1021/cm8021165>.
- [34] X. Zhang, H. Dong, and W. Hu, *Organic Semiconductor Single Crystals for Electronics and Photonics*. Advanced materials (Deerfield Beach, Fla.), 30(44) (2018),  
<http://dx.doi.org/10.1002/adma.201801048>.

- [35] S. H. Jin, K. D. Jung, H. Shin, B.-G. Park, and J. D. Lee, *Grain size effects on contact resistance of top-contact pentacene TFTs*. *Synthetic Metals*, 156(2-4):196–201 (2006), <http://dx.doi.org/10.1016/j.synthmet.2005.11.012>.
- [36] R. R. Lunt, J. B. Benziger, and S. R. Forrest, *Relationship between crystalline order and exciton diffusion length in molecular organic semiconductors*. *Advanced materials (Deerfield Beach, Fla.)*, 22(11):1233–1236 (2010), <http://dx.doi.org/10.1002/adma.200902827>.
- [37] K. Shi, A. T. Healy, I. J. Curtin, T. Zhang, D. A. Blank, and R. J. Holmes, *Impact of Grain Boundaries on Triplet Exciton Diffusion in Organic Singlet-Fission Materials*. *The Journal of Physical Chemistry C*, 126(10):4792–4798 (2022), <http://dx.doi.org/10.1021/acs.jpcc.1c10308>.
- [38] S. Caria, E. Da Como, M. Murgia, R. Zamboni, P. Melpignano, and V. Biondo, *Enhanced light emission efficiency and current stability by morphology control and thermal annealing of organic light emitting diode devices*. *Journal of Physics: Condensed Matter*, 18(33):S2139–S2147 (2006), <http://dx.doi.org/10.1088/0953-8984/18/33/S29>.
- [39] H. F. Haneef, A. M. Zeidell, and O. D. Jurchescu, *Charge carrier traps in organic semiconductors: A review on the underlying physics and impact on electronic devices*. *Journal of Materials Chemistry C*, 8(3):759–787 (2020), <http://dx.doi.org/10.1039/c9tc05695e>.
- [40] S. Müller, R.-P. Baumann, T. Geßner, and R. T. Weitz, *Identification of grain boundaries as degradation site in n-channel organic field-effect transistors determined via conductive atomic force microscopy*. *physica status solidi (RRL) - Rapid Research Letters*, 10(4):339–345 (2016), <http://dx.doi.org/10.1002/pssr.201600008>.
- [41] R. T. Weitz, K. Amsharov, U. Zschieschang, M. Burghard, M. Jansen, M. Kelsch, B. Rhamati, P. A. van Aken, K. Kern, and H. Klauk, *The Importance of Grain Boundaries for the Time-Dependent Mobility Degradation in Organic Thin-Film Transistors*. *Chemistry of Materials*, 21(20):4949–4954 (2009), <http://dx.doi.org/10.1021/cm902145x>.
- [42] S. S. Lee, J. M. Mativetsky, M. A. Loth, J. E. Anthony, and Y.-L. Loo, *Quantifying resistances across nanoscale low- and high-angle interspherulite boundaries in solution-processed organic semiconductor thin films*. *ACS nano*, 6(11):9879–9886 (2012), <http://dx.doi.org/10.1021/mn303446h>.
- [43] D. J. Gundlach, J. E. Royer, S. K. Park, S. Subramanian, O. D. Jurchescu, B. H. Hamadani, A. J. Moad, R. J. Kline, L. C. Teague, O. Kirillov, C. A. Richter, J. G. Kushmerick, L. J. Richter, S. R. Parkin, T. N. Jackson, and J. E. Anthony, *Contact-induced crystallinity for high-performance soluble acene-based transistors and circuits*. *Nature materials*, 7(3):216–221 (2008), <http://dx.doi.org/10.1038/nmat2122>.
- [44] T. Afzal, M. J. Iqbal, M. Z. Iqbal, A. Sajjad, M. A. Raza, S. Riaz, M. A. Kamran, A. Numan, and S. Naseem, *Effect of post-deposition annealing temperature on the charge carrier mobility and morphology of DPPDTT based organic field effect transistors*. *Chemical Physics Letters*, 750:137507 (2020), <http://dx.doi.org/10.1016/j.cplett.2020.137507>.

- [45] G. Horowitz, *Tunneling Current in Polycrystalline Organic Thin-Film Transistors*. *Advanced Functional Materials*, 13(1):53–60 (2003), <http://dx.doi.org/10.1002/adfm.200390006>.
- [46] O. Tal, Y. Rosenwaks, Y. Preezant, N. Tessler, C. K. Chan, and A. Kahn, *Direct determination of the hole density of states in undoped and doped amorphous organic films with high lateral resolution*. *Physical Review Letters*, 95(25):256405 (2005), <http://dx.doi.org/10.1103/PhysRevLett.95.256405>.
- [47] X.-H. Shi, J.-X. Sun, C.-H. Xiong, and Le Sun, *Exponential-type density of states with clearly cutting tail for organic semiconductors*. *Organic Electronics*, 30:60–66 (2016), <http://dx.doi.org/10.1016/j.orgel.2015.11.023>.
- [48] I. Vladimirov, M. Kühn, T. Geßner, F. May, and R. T. Weitz, *Energy barriers at grain boundaries dominate charge carrier transport in an electron-conductive organic semiconductor*. *Scientific reports*, 8 (2018), <http://dx.doi.org/10.1038/s41598-018-33308-y>.
- [49] G. Horowitz and M. Hajlaoui, *Mobility in Polycrystalline Oligothiophene Field-Effect Transistors Dependent on Grain Size*. *Advanced Materials*, 12(14):1046–1050 (2000), [http://dx.doi.org/10.1002/1521-4095\(200007\)12:14%3C1046::AID-ADMA1046%3E3.0.CO;2-W](http://dx.doi.org/10.1002/1521-4095(200007)12:14%3C1046::AID-ADMA1046%3E3.0.CO;2-W).
- [50] S. Verlaak, V. Arkhipov, and P. Heremans, *Modeling of transport in polycrystalline organic semiconductor films*. *Applied Physics Letters*, 82(5):745–747 (2003), <http://dx.doi.org/10.1063/1.1541112>.
- [51] S. Verlaak and P. Heremans, *Molecular microelectrostatic view on electronic states near pentacene grain boundaries*. *Physical Review B*, 75(11) (2007), <http://dx.doi.org/10.1103/PhysRevB.75.115127>.
- [52] T. Meier, H. Bässler, and A. Köhler, *The Impact of Grain Boundaries on Charge Transport in Polycrystalline Organic Field-Effect Transistors*. *Advanced Optical Materials*, 9(14):2100115 (2021), <http://dx.doi.org/10.1002/adom.202100115>.
- [53] I. Vladimirov, M. Kellermeier, T. Geßner, Z. Molla, S. Grigorian, U. Pietsch, L. S. Schaffroth, M. Kühn, F. May, and R. T. Weitz, *High-Mobility, Ultrathin Organic Semiconducting Films Realized by Surface-Mediated Crystallization*. *Nano letters*, 18(1):9–14 (2018), <http://dx.doi.org/10.1021/acs.nanolett.7b03789>.
- [54] M. Schwoerer and H. C. Wolf, *Organische Molekulare Festkörper: Einführung in die Physik von pi-Systemen*. *Lehrbuch Physik*, Wiley-VCH, Weinheim, 1. Auflage edition (2012), ISBN 978-3-527-40539-8.
- [55] H. Haken and H. C. Wolf, *Molekülphysik und Quantenchemie: Einführung in die experimentellen und theoretischen Grundlagen*. Springer, 5 edition (2005), ISBN 3-540-30314-6.
- [56] S. Califano, *Vibrational states*. John Wiley & Sons, London and New York and Sydney and [etc.] (1976), ISBN 978-0471129967.

- [57] L. S. Tischer, *Orientation of Covalently Bound Self-Assembled Monolayers on Indium-Tin-Oxide Investigated by Infrared Spectroscopy*. Master's Thesis, Rheinisch-Westfälische Technische Hochschule, Aachen (2017).
- [58] I. Vladimirov, S. Müller, R.-P. Baumann, T. Geßner, Z. Molla, S. Grigorian, A. Köhler, H. Bäessler, U. Pietsch, and R. T. Weitz, *Dielectric-Semiconductor Interface Limits Charge Carrier Motion at Elevated Temperatures and Large Carrier Densities in a High-Mobility Organic Semiconductor*. *Advanced Functional Materials*, 29(12):1807867 (2019),  
<http://dx.doi.org/10.1002/adfm.201807867>.
- [59] L. S. Schaffroth, J. Lenz, V. Giegold, M. Kögl, A. Hartschuh, and R. T. Weitz, *Freely Suspended, van der Waals Bound Organic Nanometer-Thin Functional Films: Mechanical and Electronic Characterization*. *Advanced materials* (Deerfield Beach, Fla.), 31(16) (2019),  
<http://dx.doi.org/10.1002/adma.201808309>.
- [60] M. Barra, F. Chiarella, F. Chianese, R. Vaglio, and A. Cassinese, *Perylene-Diimide Molecules with Cyano Functionalization for Electron-Transporting Transistors*. *Electronics*, 8(2):249 (2019),  
<http://dx.doi.org/10.3390/electronics8020249>.
- [61] I. Vladimirov, *Crystallization Behavior and Charge Transport of Organic Semiconductors*. Dissertation, Technische Universität Carolo-Wilhelmina zu Braunschweig, Braunschweig (2016).
- [62] C. Ratsch and J. A. Venables, *Nucleation theory and the early stages of thin film growth*. *Journal of Vacuum Science & Technology A: Vacuum, Surfaces, and Films*, 21(5):S96–S109 (2003),  
<http://dx.doi.org/10.1116/1.1600454>.
- [63] A. A. Virkar, S. Mannsfeld, Z. Bao, and N. Stingelin, *Organic semiconductor growth and morphology considerations for organic thin-film transistors*. *Advanced materials* (Deerfield Beach, Fla.), 22(34):3857–3875 (2010),  
<http://dx.doi.org/10.1002/adma.200903193>.
- [64] D. Mokros, *Nucleation and Growth of Organic Thin Films on Polymeric Dielectrics*. Dissertation, Rheinisch-Westfälische Technische Hochschule, Aachen (2016),  
<https://publications.rwth-aachen.de/record/659472/files/659472.pdf>.
- [65] A. K. Hailey, S.-Y. Wang, Y. Chen, M. M. Payne, J. E. Anthony, V. Podzorov, and Y.-L. Loo, *Quantifying the Energy Barriers and Elucidating the Charge Transport Mechanisms across Interspherulite Boundaries in Solution-Processed Organic Semiconductor Thin Films*. *Advanced Functional Materials*, 25(35):5662–5668 (2015),  
<http://dx.doi.org/10.1002/adfm.201501666>.
- [66] L. H. Jimison, M. F. Toney, I. McCulloch, M. Heeney, and A. Salleo, *Charge-Transport Anisotropy Due to Grain Boundaries in Directionally Crystallized Thin Films of Regioregular Poly(3-hexylthiophene)*. *Advanced Materials*, 21(16):1568–1572 (2009),  
<http://dx.doi.org/10.1002/adma.200802722>.
- [67] Z. Pan, N. Rawat, I. Cour, L. Manning, R. L. Headrick, and M. Furis, *Polarization-resolved spectroscopy imaging of grain boundaries and optical excitations in crystalline*

- organic thin films*. Nature communications, 6:8201 (2015),  
<http://dx.doi.org/10.1038/ncomms9201>.
- [68] J. Chen, C. K. Tee, M. Shtein, J. Anthony, and D. C. Martin, *Grain-boundary-limited charge transport in solution-processed 6,13 bis(tri-isopropylsilylethynyl) pentacene thin film transistors*. Journal of Applied Physics, 103(11):114513 (2008),  
<http://dx.doi.org/10.1063/1.2936978>.
- [69] B. B. Patel and Y. Diao, *Multiscale assembly of solution-processed organic electronics: The critical roles of confinement, fluid flow, and interfaces*. Nanotechnology, 29(4):044004 (2018),  
<http://dx.doi.org/10.1088/1361-6528/aa9d7c>.
- [70] S. S. Lee, C. S. Kim, E. D. Gomez, B. Purushothaman, M. F. Toney, C. Wang, A. Hexemer, J. E. Anthony, and Y.-L. Loo, *Organic Thin-Film Transistors: Controlling Nucleation and Crystallization in Solution-Processed Organic Semiconductors for Thin-Film Transistors (Adv. Mater. 35/2009)*. Advanced Materials, 21(35):NA–NA (2009),  
<http://dx.doi.org/10.1002/adma.200990133>.
- [71] A. Yamamura, S. Watanabe, M. Uno, M. Mitani, C. Mitsui, J. Tsurumi, N. Isahaya, Y. Kanaoka, T. Okamoto, and J. Takeya, *Wafer-scale, layer-controlled organic single crystals for high-speed circuit operation*. Science advances, 4(2):eaao5758 (2018),  
<http://dx.doi.org/10.1126/sciadv.aao5758>.
- [72] R. Chen, L. Zhang, D. Zang, and W. Shen, *Wetting and Drying of Colloidal Droplets: Physics and Pattern Formation*. M. M. Rahman and A. M. Asiri, editors, *Advances in Colloid Science*, InTech (2016), ISBN 978-953-51-2773-4,  
<http://dx.doi.org/10.5772/65301>.
- [73] H. Hu and R. G. Larson, *Marangoni effect reverses coffee-ring depositions*. The journal of physical chemistry. B, 110(14):7090–7094 (2006),  
<http://dx.doi.org/10.1021/jp0609232>.
- [74] L. S. Schaffroth, *Charge Transport in Solution-Processed Suspended Organic Semiconducting Thin-Films*. Master’s Thesis, Ludwig-Maximilians-Universität, München (2017).
- [75] V. Kalihari, E. B. Tadmor, G. Haugstad, and C. D. Frisbie, *Grain Orientation Mapping of Polycrystalline Organic Semiconductor Films by Transverse Shear Microscopy*. Advanced Materials, 20(21):4033–4039 (2008),  
<http://dx.doi.org/10.1002/adma.200801834>.
- [76] Y. Hattori and M. Kitamura, *Crystal orientation imaging of organic monolayer islands by polarized light microscopy*. ACS applied materials & interfaces (2020),  
<http://dx.doi.org/10.1021/acsami.0c08672>.
- [77] Y. Zhang, B. de Boer, and P. W. M. Blom, *Trap-free electron transport in poly(*p*-phenylene vinylene) by deactivation of traps with *n*-type doping*. Physical Review B, 81(8) (2010),  
<http://dx.doi.org/10.1103/PhysRevB.81.085201>.
- [78] G. Horowitz, *Validity of the concept of band edge in organic semiconductors*. Journal of Applied Physics, 118(11):115502 (2015),  
<http://dx.doi.org/10.1063/1.4931061>.

- [79] T. Sueyoshi, H. Fukagawa, M. Ono, S. Kera, and N. Ueno, *Low-density band-gap states in pentacene thin films probed with ultrahigh-sensitivity ultraviolet photoelectron spectroscopy*. Applied Physics Letters, 95(18):183303 (2009), <http://dx.doi.org/10.1063/1.3258351>.
- [80] S. M. Sze and K. K. Ng, *Physics of semiconductor devices*. Wiley-Interscience, Hoboken, NJ, 3. ed. edition (2007), ISBN 978-0-471-14323-9, <http://dx.doi.org/10.1002/0470068329>.
- [81] V. Palermo, M. Palma, and P. Samorì, *Electronic Characterization of Organic Thin Films by Kelvin Probe Force Microscopy*. Advanced Materials, 18(2):145–164 (2006), <http://dx.doi.org/10.1002/adma.200501394>.
- [82] W. Demtröder, *Experimentalphysik 3: Atome, Moleküle und Festkörper*. Springer, Berlin Heidelberg New York (2010), ISBN 978-3-642-03910-2.
- [83] V. Gold, *The IUPAC Compendium of Chemical Terminology*. International Union of Pure and Applied Chemistry (IUPAC), Research Triangle Park, NC (2019), <http://dx.doi.org/10.1351/goldbook>.
- [84] H. Klauk, editor, *Organic electronics: More materials and applications*. Wiley-VCH, Weinheim (2012), ISBN 978-3-527-32647-1.
- [85] G. Horowitz, *Organic Field-Effect Transistors*. Advanced Materials, 10(5):365–377 (1998), [http://dx.doi.org/10.1002/\(SICI\)1521-4095\(199803\)10:5%3C365::AID-ADMA365%3E3.0.CO;2-U](http://dx.doi.org/10.1002/(SICI)1521-4095(199803)10:5%3C365::AID-ADMA365%3E3.0.CO;2-U).
- [86] L. G. Kaake, P. F. Barbara, and X.-Y. Zhu, *Intrinsic Charge Trapping in Organic and Polymeric Semiconductors: A Physical Chemistry Perspective*. The journal of physical chemistry letters, 1(3):628–635 (2010), <http://dx.doi.org/10.1021/jz9002857>.
- [87] H. Kobayashi and Y. Tokita, *Modeling of hole transport across grain boundaries in organic semiconductors for mesoscale simulations*. Applied Physics Express, 8(5):051602 (2015), <http://dx.doi.org/10.7567/APEX.8.051602>.
- [88] P. Stallinga, *Electrical characterization of organic electronic materials and devices*. Wiley, Chichester, reprinted. edition (2010), ISBN 978-0-470-75009-4.
- [89] C. R. Newman, C. D. Frisbie, D. A. da Silva Filho, J.-L. Brédas, P. C. Ewbank, and K. R. Mann, *Introduction to Organic Thin Film Transistors and Design of n-Channel Organic Semiconductors*. Chemistry of Materials, 16(23):4436–4451 (2004), <http://dx.doi.org/10.1021/cm049391x>.
- [90] G. Horowitz, R. Hajlaoui, H. Bouchriha, R. Bourguiga, and M. Hajlaoui, *The Concept of “Threshold Voltage” in Organic Field-Effect Transistors*. Advanced Materials, 10(12):923–927 (1998), [http://dx.doi.org/10.1002/\(SICI\)1521-4095\(199808\)10:12%3C923::AID-ADMA923%3E3.0.CO;2-W](http://dx.doi.org/10.1002/(SICI)1521-4095(199808)10:12%3C923::AID-ADMA923%3E3.0.CO;2-W).
- [91] E. G. Bittle, J. I. Basham, T. N. Jackson, O. D. Jurchescu, and D. J. Gundlach, *Mobility overestimation due to gated contacts in organic field-effect transistors*. Nature

- communications, 7:10908 (2016),  
<http://dx.doi.org/10.1038/ncomms10908>.
- [92] H. H. Choi, K. Cho, C. D. Frisbie, H. Sirringhaus, and V. Podzorov, *Critical assessment of charge mobility extraction in FETs*. *Nature materials*, 17(1):2–7 (2017),  
<http://dx.doi.org/10.1038/nmat5035>.
- [93] A. Ortiz-Conde, F. J. Garcia Sánchez, J. J. Liou, A. Cerdeira, M. Estrada, and Y. Yue, *A review of recent MOSFET threshold voltage extraction methods*. *Microelectronics Reliability*, 42(4-5):583–596 (2002),  
[http://dx.doi.org/10.1016/S0026-2714\(02\)00027-6](http://dx.doi.org/10.1016/S0026-2714(02)00027-6).
- [94] M. Rienacker, M. Bossmeyer, A. Merkle, U. Romer, F. Haase, J. Krugener, R. Brendel, and R. Peibst, *Junction Resistivity of Carrier-Selective Polysilicon on Oxide Junctions and Its Impact on Solar Cell Performance*. *IEEE Journal of Photovoltaics*, 7(1):11–18 (2017),  
<http://dx.doi.org/10.1109/JPHOTOV.2016.2614123>.
- [95] K. K. H. Smithe, C. D. English, S. V. Suryavanshi, and E. Pop, *Intrinsic electrical transport and performance projections of synthetic monolayer MoS<sub>2</sub> devices*. *2D Materials*, 4(1):011009 (2017),  
<http://dx.doi.org/10.1088/2053-1583/4/1/011009>.
- [96] J. Lee, S. Cho, and C. Yang, *Highly reproducible organic field-effect transistor from pseudo 3-dimensional triphenylamine-based amorphous conjugated copolymer*. *Journal of Materials Chemistry*, 21(24):8528 (2011),  
<http://dx.doi.org/10.1039/C1JM11515D>.
- [97] P. Blood and J. W. Orton, *The electrical characterization of semiconductors: Majority carriers and electron states*, *Techniques of physics*, volume 14. Acad. Pr, London (1992), ISBN 9780125286275.
- [98] C. Rolin, E. Kang, J.-H. Lee, G. Borghs, P. Heremans, and J. Genoe, *Charge carrier mobility in thin films of organic semiconductors by the gated van der Pauw method*. *Nature communications*, 8:14975 (2017),  
<http://dx.doi.org/10.1038/ncomms14975>.
- [99] U. Zschieschang, R. T. Weitz, K. Kern, and H. Klauk, *Bias stress effect in low-voltage organic thin-film transistors*. *Applied Physics A*, 95(1):139–145 (2009),  
<http://dx.doi.org/10.1007/s00339-008-5019-8>.
- [100] M. Egginger, S. Bauer, R. Schwödauier, H. Neugebauer, and N. S. Sariciftci, *Current versus gate voltage hysteresis in organic field effect transistors*. *Monatshefte für Chemie - Chemical Monthly*, 140(7):735–750 (2009),  
<http://dx.doi.org/10.1007/s00706-009-0149-z>.
- [101] G. Gregori, R. Merkle, and J. Maier, *Ion conduction and redistribution at grain boundaries in oxide systems*. *Progress in Materials Science*, 89:252–305 (2017),  
<http://dx.doi.org/10.1016/j.pmatsci.2017.04.009>.
- [102] J. Levinson, F. R. Shepherd, P. J. Scanlon, W. D. Westwood, G. Este, and M. Rider, *Conductivity behavior in polycrystalline semiconductor thin film transistors*. *Journal of Applied Physics*, 53(2):1193–1202 (1982),  
<http://dx.doi.org/10.1063/1.330583>.

- [103] P. Lupetin, G. Gregori, and J. Maier, *Mesoscopic Charge Carriers Chemistry in Nanocrystalline SrTiO<sub>3</sub>*. *Angewandte Chemie*, 122(52):10321–10324 (2010), <http://dx.doi.org/10.1002/ange.201003917>.
- [104] R. Gegevičius, M. Franckevičius, and V. Gulbinas, *The Role of Grain Boundaries in Charge Carrier Dynamics in Polycrystalline Metal Halide Perovskites*. *European Journal of Inorganic Chemistry*, 2021(35):3519–3527 (2021), <http://dx.doi.org/10.1002/ejic.202100360>.
- [105] M. D. Allendorf, R. Dong, X. Feng, S. Kaskel, D. Matoga, and V. Stavila, *Electronic Devices Using Open Framework Materials*. *Chemical reviews*, 120(16):8581–8640 (2020), <http://dx.doi.org/10.1021/acs.chemrev.0c00033>.
- [106] M. E. Foster, K. Sohlberg, M. D. Allendorf, and A. A. Talin, *Unraveling the Semiconducting/Metallic Discrepancy in Ni<sub>3</sub>(HITP)<sub>2</sub>*. *The journal of physical chemistry letters*, 9(3):481–486 (2018), <http://dx.doi.org/10.1021/acs.jpcllett.7b03140>.
- [107] H. Qi, H. Sahabudeen, B. Liang, M. Položij, M. A. Addicoat, T. E. Gorelik, M. Hamsch, M. Mundsinger, S. Park, B. V. Lotsch, S. C. B. Mannsfeld, Z. Zheng, R. Dong, T. Heine, X. Feng, and U. Kaiser, *Near-atomic-scale observation of grain boundaries in a layer-stacked two-dimensional polymer*. *Science advances*, 6(33):eabb5976 (2020), <http://dx.doi.org/10.1126/sciadv.abb5976>.
- [108] L. S. Xie, G. Skorupskii, and M. Dincă, *Electrically Conductive Metal-Organic Frameworks*. *Chemical reviews*, 120(16):8536–8580 (2020), <http://dx.doi.org/10.1021/acs.chemrev.9b00766>.
- [109] M. Wang, R. Dong, and X. Feng, *Two-dimensional conjugated metal-organic frameworks (2D c-MOFs): chemistry and function for MOFtronics*. *Chemical Society reviews*, 50(4):2764–2793 (2021), <http://dx.doi.org/10.1039/d0cs01160f>.
- [110] M. A. Springer, T.-J. Liu, A. Kuc, and T. Heine, *Topological two-dimensional polymers*. *Chemical Society reviews*, 49(7):2007–2019 (2020), <http://dx.doi.org/10.1039/c9cs00893d>.
- [111] A. Kuc, M. A. Springer, K. Batra, R. Juarez-Mosqueda, C. Wöll, and T. Heine, *Proximity Effect in Crystalline Framework Materials: Stacking-Induced Functionality in MOFs and COFs*. *Advanced Functional Materials*, 30(41) (2020), <http://dx.doi.org/10.1002/adfm.201908004>.
- [112] S. Goswami, D. Ray, K.-I. Otake, C.-W. Kung, S. J. Garibay, T. Islamoglu, A. Atilgan, Y. Cui, C. J. Cramer, O. K. Farha, and J. T. Hupp, *A porous, electrically conductive hexa-zirconium(IV) metal-organic framework*. *Chemical science*, 9(19):4477–4482 (2018), <http://dx.doi.org/10.1039/c8sc00961a>.
- [113] M.-J. Park and J.-S. Lee, *Zeolitic-imidazole framework thin film-based flexible resistive switching memory*. *RSC Advances*, 7(34):21045–21049 (2017), <http://dx.doi.org/10.1039/c6ra28361f>.
- [114] O. Shekhah, H. Wang, S. Kowarik, F. Schreiber, M. Paulus, M. Tolan, C. Sternemann, F. Evers, D. Zacher, R. A. Fischer, and C. Wöll, *Step-by-step route for the synthesis of*

- metal-organic frameworks*. Journal of the American Chemical Society, 129(49):15118–15119 (2007),  
<http://dx.doi.org/10.1021/ja076210u>.
- [115] M. S. Hosseini and S. Zeinali, *Capacitive humidity sensing using a metal-organic framework nanoporous thin film fabricated through electrochemical in situ growth*. Journal of Materials Science: Materials in Electronics, 30(4):3701–3710 (2019),  
<http://dx.doi.org/10.1007/s10854-018-00652-8>.
- [116] I. Stassen, D. de Vos, and R. Ameloot, *Vapor-Phase Deposition and Modification of Metal-Organic Frameworks: State-of-the-Art and Future Directions*. Chemistry (Weinheim an der Bergstrasse, Germany), 22(41):14452–14460 (2016),  
<http://dx.doi.org/10.1002/chem.201601921>.
- [117] S. Casalini, C. A. Bortolotti, F. Leonardi, and F. Biscarini, *Self-assembled monolayers in organic electronics*. Chemical Society reviews, 46(1):40–71 (2017),  
<http://dx.doi.org/10.1039/c6cs00509h>.
- [118] M. Yankowitz, Q. Ma, P. Jarillo-Herrero, and B. J. LeRoy, *van der Waals heterostructures combining graphene and hexagonal boron nitride*. Nature Reviews Physics, 1(2):112–125 (2019),  
<http://dx.doi.org/10.1038/s42254-018-0016-0>.
- [119] L. Wang, I. Meric, P. Y. Huang, Q. Gao, Y. Gao, H. Tran, T. Taniguchi, K. Watanabe, L. M. Campos, D. A. Muller, J. Guo, P. Kim, J. Hone, K. L. Shepard, and C. R. Dean, *One-dimensional electrical contact to a two-dimensional material*. Science (New York, N.Y.), 342(6158):614–617 (2013),  
<http://dx.doi.org/10.1126/science.1244358>.
- [120] Y. Leng, *Materials characterization: Introduction to microscopic and spectroscopic methods*. Wiley-VCH, Weinheim, 2. ed. edition (2013), ISBN 978-3-527-33463-6.
- [121] B. Voigtländer, *Atomic force microscopy*. NanoScience and technology, Springer, Cham, second edition edition (2019), ISBN 9783030136567,  
<https://www.springer.com/de/book/9783030136536>.
- [122] H.-J. Butt, B. Cappella, and M. Kappl, *Force measurements with the atomic force microscope: Technique, interpretation and applications*. Surface Science Reports, 59(1-6):1–152 (2005),  
<http://dx.doi.org/10.1016/j.surfrep.2005.08.003>.
- [123] Asylum Research. Oxford Instruments, editor, *SPM Applications Guide: User Guide 3*, volume Version 17 (31.07.2020).
- [124] L. S. C. Pingree, O. G. Reid, and D. S. Ginger, *Electrical Scanning Probe Microscopy on Active Organic Electronic Devices*. Advanced Materials, 21(1):19–28 (2009),  
<http://dx.doi.org/10.1002/adma.200801466>.
- [125] T. W. Kelley, E. Granstrom, and C. D. Frisbie, *Conducting Probe Atomic Force Microscopy: A Characterization Tool for Molecular Electronics*. Advanced Materials, 11(3):261–264 (1999),  
[http://dx.doi.org/10.1002/\(SICI\)1521-4095\(199903\)11:3%3C261::AID-ADMA261%3E3.O.CO;2-B](http://dx.doi.org/10.1002/(SICI)1521-4095(199903)11:3%3C261::AID-ADMA261%3E3.O.CO;2-B).

- [126] T. W. Kelley and C. D. Frisbie, *Gate Voltage Dependent Resistance of a Single Organic Semiconductor Grain Boundary*. The journal of physical chemistry. B, 105(20):4538–4540 (2001),  
<http://dx.doi.org/10.1021/jp004519t>.
- [127] L. Kelvin, *V. Contact electricity of metals*. The London, Edinburgh, and Dublin Philosophical Magazine and Journal of Science, 46(278):82–120 (1898),  
<http://dx.doi.org/10.1080/14786449808621172>.
- [128] K. Besocke and S. Berger, *Piezoelectric driven Kelvin probe for contact potential difference studies*. The Review of scientific instruments, 47(7):840–842 (1976),  
<http://dx.doi.org/10.1063/1.1134750>.
- [129] M. Nonnenmacher, M. P. O’Boyle, and H. K. Wickramasinghe, *Kelvin probe force microscopy*. Applied Physics Letters, 58(25):2921–2923 (1991),  
<http://dx.doi.org/10.1063/1.105227>.
- [130] B. Moores, F. Hane, L. Eng, and Z. Leonenko, *Kelvin probe force microscopy in application to biomolecular films: Frequency modulation, amplitude modulation, and lift mode*. Ultramicroscopy, 110(6):708–711 (2010),  
<http://dx.doi.org/10.1016/j.ultramicro.2010.02.036>.
- [131] A. Axt, I. M. Hermes, V. W. Bergmann, N. Tausendpfund, and S. A. L. Weber, *Know your full potential: Quantitative Kelvin probe force microscopy on nanoscale electrical devices*. Beilstein journal of nanotechnology, 9:1809–1819 (2018),  
<http://dx.doi.org/10.3762/bjnano.9.172>.
- [132] Y. Sugawara, L. Kou, Z. Ma, T. Kamijo, Y. Naitoh, and Y. Jun Li, *High potential sensitivity in heterodyne amplitude-modulation Kelvin probe force microscopy*. Applied Physics Letters, 100(22):223104 (2012),  
<http://dx.doi.org/10.1063/1.4723697>.
- [133] S. Yogev, R. Matsubara, M. Nakamura, and Y. Rosenwaks, *Local charge accumulation and trapping in grain boundaries of pentacene thin film transistors*. Organic Electronics, 11(11):1729–1735 (2010),  
<http://dx.doi.org/10.1016/j.orgel.2010.07.021>.
- [134] O. Tal and Y. Rosenwaks, *Electronic properties of doped molecular thin films measured by Kelvin probe force microscopy*. The journal of physical chemistry. B, 110(50):25521–25524 (2006),  
<http://dx.doi.org/10.1021/jp065246q>.
- [135] W. S. C. Roelofs, S. G. J. Mathijssen, R. A. J. Janssen, D. M. de Leeuw, and M. Kemerink, *Accurate description of charge transport in organic field effect transistors using an experimentally extracted density of states*. Physical Review B, 85(8) (2012),  
<http://dx.doi.org/10.1103/PhysRevB.85.085202>.
- [136] D. Wrana, K. Cieřlik, W. Belza, C. Rodenbřucher, K. Szot, and F. Krok, *Kelvin probe force microscopy work function characterization of transition metal oxide crystals under ongoing reduction and oxidation*. Beilstein journal of nanotechnology, 10:1596–1607 (2019),  
<http://dx.doi.org/10.3762/bjnano.10.155>.

- [137] P. R. Griffiths and J. A. de Haseth, *Fourier transform infrared spectrometry, Chemical analysis*, volume v. 171. Wiley-Interscience, Hoboken, N.J, 2nd ed. edition (2007), ISBN 978-0-471-19404-0.
- [138] ISO 20473:2007, *Optics and Photonics - Spectral Bands* (09.06.2022), <https://www.iso.org/standard/39482.html>.
- [139] Bruker Optik GmbH, *OPUS - optics user software: Help - FT-IR Introduction* (2005).
- [140] K. Irmer, *personal correspondence (E-Mail)*, 13.06.2022 (Bereichsleiter optische Spektroskopie, Bruker Optics GmbH & Co. KG).
- [141] TYDEX, *TYDEX THz Materials* (10.06.2022), [http://www.tydexoptics.com/products/thz\\_optics/thz\\_materials/](http://www.tydexoptics.com/products/thz_optics/thz_materials/).
- [142] C. C. Lim, *Far-infrared high-density polyethylene windows for low-temperature and moderate-pressure applications*. The Review of scientific instruments, 57(7):1419–1421 (1986), <http://dx.doi.org/10.1063/1.1138613>.
- [143] Bruker Optik GmbH, editor, *IFS 66v/S: User's Manual*, volume 1998.
- [144] M. Hartung, *Photoleitungsspektroskopie an InAs/AlSb-Quantenköpfen*. Dissertation, Ludwig-Maximilians-Universität, München (1997).
- [145] H. Frenzel, H. v. Wenckstern, A. Weber, H. Schmidt, G. Biehne, H. Hochmuth, M. Lorenz, and M. Grundmann, *Photocurrent spectroscopy of deep levels in ZnO thin films*. Physical Review B, 76(3):71 (2007), <http://dx.doi.org/10.1103/PhysRevB.76.035214>.
- [146] J. Yang, G. Chen, T. Han, Q. Zhang, Y.-H. Zhang, L. Jiang, B. Lyu, H. Li, K. Watanabe, T. Taniguchi, Z. Shi, T. Senthil, Y. Zhang, F. Wang, and L. Ju, *Spectroscopy signatures of electron correlations in a trilayer graphene/hBN moiré superlattice*. Science (New York, N.Y.), 375(6586):1295–1299 (2022), <http://dx.doi.org/10.1126/science.abg3036>.
- [147] L. Ju, L. Wang, T. Cao, T. Taniguchi, K. Watanabe, S. G. Louie, F. Rana, J. Park, J. Hone, F. Wang, and P. L. McEuen, *Tunable excitons in bilayer graphene*. Science (New York, N.Y.), 358(6365):907–910 (2017), <http://dx.doi.org/10.1126/science.aam9175>.
- [148] M. Vanecek and A. Poruba, *Fourier-transform photocurrent spectroscopy of microcrystalline silicon for solar cells*. Applied Physics Letters, 80(5):719–721 (2002), <http://dx.doi.org/10.1063/1.1446207>.
- [149] T. Inushima, M. H. Brodsky, J. Kanicki, and R. J. Serino, *Photoconductivity of intrinsic and doped a-Si:H from 0.1 to 1.9 eV*. AIP Conference Proceedings, AIP (1984), pp. 24–31, <http://dx.doi.org/10.1063/1.34748>.
- [150] J. W. Tomm, A. Jaeger, A. Bärwolff, T. Elsaesser, A. Gerhardt, and J. Donecker, *Aging properties of high power laser diode arrays analyzed by Fourier-transform photocurrent measurements*. Applied Physics Letters, 71(16):2233–2235 (1997), <http://dx.doi.org/10.1063/1.120066>.

- [151] Stanford Research Systems, editor, *SR860 Operation Manual: 500 kHz DSP Lock-in Amplifier*, volume Revision 2.09.  
<https://www.thinksrs.com/downloads/pdfs/manuals/SR860m.pdf>.
- [152] F. Winterer, *SuperFunAnalyzer Manual: Version 2.0*.
- [153] Origin Lab Corporation, *Help Online: Algorithms (FFT)* (08.08.2022),  
<https://www.originlab.com/doc/de/Origin-Help/FFT1-Algorithm>.
- [154] V. Podzorov, E. Menard, A. Borissov, V. Kiryukhin, J. A. Rogers, and M. E. Gershenson, *Intrinsic charge transport on the surface of organic semiconductors*. *Physical Review Letters*, 93(8):086602 (2004),  
<http://dx.doi.org/10.1103/PhysRevLett.93.086602>.
- [155] J. A. Merlo and C. D. Frisbie, *Field Effect Transport and Trapping in Regioregular Polythiophene Nanofibers*. *The journal of physical chemistry. B*, 108(50):19169–19179 (2004),  
<http://dx.doi.org/10.1021/jp047023a>.
- [156] A. Di Carlo, F. Piacenza, A. Bolognesi, B. Stadlober, and H. Maresch, *Influence of grain sizes on the mobility of organic thin-film transistors*. *Applied Physics Letters*, 86(26):263501 (2005),  
<http://dx.doi.org/10.1063/1.1954901>.
- [157] M. Geiger, L. Schwarz, U. Zschieschang, D. Manske, J. Pflaum, J. Weis, H. Klauk, and R. T. Weitz, *Quantitative Analysis of the Density of Trap States in Semiconductors by Electrical Transport Measurements on Low-Voltage Field-Effect Transistors*. *Physical Review Applied*, 10(4) (2018),  
<http://dx.doi.org/10.1103/PhysRevApplied.10.044023>.
- [158] L. Bürgi, T. Richards, M. Chiesa, R. H. Friend, and H. Sirringhaus, *A microscopic view of charge transport in polymer transistors*. *Synthetic Metals*, 146(3):297–309 (2004),  
<http://dx.doi.org/10.1016/j.synthmet.2004.08.009>.
- [159] K. P. Puntambekar, P. V. Pesavento, and C. D. Frisbie, *Surface potential profiling and contact resistance measurements on operating pentacene thin-film transistors by Kelvin probe force microscopy*. *Applied Physics Letters*, 83(26):5539–5541 (2003),  
<http://dx.doi.org/10.1063/1.1637443>.
- [160] L. Bürgi, H. Sirringhaus, and R. H. Friend, *Noncontact potentiometry of polymer field-effect transistors*. *Applied Physics Letters*, 80(16):2913–2915 (2002),  
<http://dx.doi.org/10.1063/1.1470702>.
- [161] R. T. Weitz, *Electrical Properties of Functionalized Nanowire Field Effect Transistors*. Dissertation, École polytechnique fédérale de Lausanne, Lausanne (2008).
- [162] A. Rolland, *Electrical Properties of Amorphous Silicon Transistors and MIS-Devices: Comparative Study of Top Nitride and Bottom Nitride Configurations*. *Journal of The Electrochemical Society*, 140(12):3679 (1993),  
<http://dx.doi.org/10.1149/1.2221149>.
- [163] C. D. Dimitrakopoulos and P. Malenfant, *Organic Thin Film Transistors for Large Area Electronics*. *Advanced Materials*, 14(2):99–117 (2002),  
[http://dx.doi.org/https://doi.org/10.1002/1521-4095\(20020116\)14:2%3C99::AID-ADMA99%3E3.O.CO;2-9](http://dx.doi.org/https://doi.org/10.1002/1521-4095(20020116)14:2%3C99::AID-ADMA99%3E3.O.CO;2-9).

- [164] H. Klauk, *Organic thin-film transistors*. Chemical Society reviews, 39(7):2643–2666 (2010),  
<http://dx.doi.org/10.1039/b909902f>.
- [165] A. B. Chwang and C. D. Frisbie, *Temperature and gate voltage dependent transport across a single organic semiconductor grain boundary*. Journal of Applied Physics, 90(3):1342–1349 (2001),  
<http://dx.doi.org/10.1063/1.1376404>.
- [166] N. Vagenas, A. Giannopoulou, and P. Kounavis, *Density and mobility effects of the majority carriers in organic semiconductors under light excitation*. Journal of Applied Physics, 117(3):033105 (2015),  
<http://dx.doi.org/10.1063/1.4906221>.
- [167] S. V. Kalinin and D. A. Bonnell, *Surface potential at surface-interface junctions in SrTiO<sub>3</sub> bicrystals*. Physical Review B, 62(15):10419–10430 (2000),  
<http://dx.doi.org/10.1103/PhysRevB.62.10419>.
- [168] D. Raabe, M. Herbig, S. Sandlöbes, Y. Li, D. Tytko, M. Kuzmina, D. Ponge, and P.-P. Choi, *Grain boundary segregation engineering in metallic alloys: A pathway to the design of interfaces*. Current Opinion in Solid State and Materials Science, 18(4):253–261 (2014),  
<http://dx.doi.org/10.1016/j.cossms.2014.06.002>.
- [169] T. Defferriere, D. Klotz, J. C. Gonzalez-Rosillo, J. L. M. Rupp, and H. L. Tuller, *Photo-enhanced ionic conductivity across grain boundaries in polycrystalline ceramics*. Nature materials, 21(4):438–444 (2022),  
<http://dx.doi.org/10.1038/s41563-021-01181-2>.
- [170] D. W. T. Griffith, N. M. Deutscher, C. G. R. Caldow, G. Kettlewell, M. Riggenbach, and S. Hammer, *A Fourier transform infrared trace gas analyser for atmospheric applications*. Atmos. Meas. Tech. Discuss., 5:3717–3769 (2012),  
<http://dx.doi.org/10.5194/amtd-5-3717-2012>.
- [171] S. Wo, R. L. Headrick, and J. E. Anthony, *Fabrication and characterization of controllable grain boundary arrays in solution-processed small molecule organic semiconductor films*. Journal of Applied Physics, 111(7):073716 (2012),  
<http://dx.doi.org/10.1063/1.3698203>.
- [172] *Number1 AFM Tips Shop Worldwide - NanoAndMore* (14.09.2022),  
<https://www.nanoandmore.com/>.
- [173] *Oxford Instruments - Online Store selling Consumables, Upgrades, Accessories and Spares* (14.09.2022),  
<https://estore.oxinst.com/eu/>.



# Danksagung

(Acknowledgments)

Am Anfang meiner Promotion standen sechs Schreibtische im Sommerfeldkeller der LMU München und ein paar weitere im „Hinterzimmer“. Seitdem wurden Labore ein- und wieder ausgeräumt, eine Holzbank wurde berühmt, mehrere Schwaben zogen von Bayern nach Niedersachsen und ein Baby wurde geboren. Von all diesen Abenteuern durfte ich ein Teil sein. Ich bin sehr, sehr dankbar für diese Zeit und alle Menschen, die mich dabei begleitet haben.

Zunächst möchte ich mich bei Thomas Weitz dafür bedanken, dass er mir die Möglichkeit gegeben hat, Teil seiner sowohl wissenschaftlich als auch zwischenmenschlich wunderbaren Gruppe zu werden. Auch jetzt, nach fünf Jahren, fühle ich mich geehrt durch das Vertrauen, gerade die ersten Jahre seiner Gruppe mitgestalten zu dürfen. Ich habe in dieser Zeit nicht nur sehr viel über Physik gelernt, sondern auch über Durchhaltevermögen, Zeitmanagement und Diplomatie und vor allem eine gewisse Grundeinstellung („Geht nicht gibt's nicht“) vorgelebt bekommen, die ich jetzt nicht mehr missen möchte. Vielen Dank dafür!

Vielen Dank auch an Bert Nickel dafür, dass er sich als Zweitgutachter für diese Arbeit zur Verfügung gestellt hat, aber auch für hilfreiche Diskussionen in der Vergangenheit, ohne die wir zu dem Zeitpunkt sicher nicht mehr voran gekommen wären.

Herzlich bedanken möchte ich mich auch bei Ilia Vladimirov und Michael Kühn für ihre Arbeiten zu „meinem“ organischen Molekül als Ausgangspunkt für weitere super interessante Projekte.

Die AG Weitz wäre nicht die AG Weitz gewesen ohne Fabian, Jakob und Felix, Lili, Stefan Wakolbinger, Stefan Seebauer, Rayner, Daniela und Florin. Danke, dass ihr mich so herzlich aufgenommen habt und mir von Tag eins das Gefühl gegeben habt, dass ich dazu gehöre. Ein besonderer Dank geht an Lili, Stefan und Daniela fürs Puzzlen und Pfeifen, für Nagellack und Schokoküsse und an meine drei Mit-Doktoranden: Jakob, von dir habe ich die besten Streiche gelernt, aber auch Sachen einfach anzupacken und zu MACHEN. Du hast mir geholfen meine Angst vor großen, alten, kaputten Geräten zu überwinden. Auch wenn ich vermutlich nie dein handwerkliches Geschick erreichen werde, werde ich bei allen zukünftigen Handwerksarbeiten immer daran denken, wie schnell und einfach du Dinge repariert oder umgebaut hast und dich als Vorbild nehmen! Felix, wir waren uns zwar nicht immer einig darüber, welche die besten Maultaschen sind und wie man das Wort „Berg“ richtig ausspricht, aber trotzdem konnte ich auch von dir sehr viel lernen. Deine Organisation von Experimenten und deine permanente Bereitschaft über Physik zu diskutieren, selbst wenn die Themen rein gar nichts mit deiner Arbeit zu tun hatten, habe ich immer sehr geschätzt und bewundert. Fabian, danke dass du immer darum besorgt warst, mich vor einer Lebensmittelvergiftung zu bewahren und regelmäßig für Kinderriegel-Nachschub gesorgt hast. Neben deinen kulinarischen Ansprüchen warst du aber auch Ansprechpartner Nummer eins in Sachen Gestaltung und Auftreten: Wie sollen die Folien für meinen Vortrag aussehen? Welche Farbskala nehme ich für ein AFM-Bild? Sollte ich bei einem Vortrag stehen oder lieber sitzen? Und wie kurz darf ein Minirock sein?

Nachdem diese ersten wichtigen Fragen geklärt waren und ein Anfang geschafft war, hat die AG Weitz viele neue Gesichter gesehen, aber die Atmosphäre und das Team-Gefühl blieben immer gleich toll. Dafür herzlichen Dank an alle ehemaligen und aktuellen Mitglieder der AG

Weitz, aber auch an Martina Edenhofer für das Handling unser wachsenden Meute und dass sie mein Rettungsanker in allen Lebenslagen war, an Reinhold Rath und Stephan Manus für Unterstützung in allen technischen Belangen. Danke auch an Bert Lorenz, dass er mich in allen sicherheitstechnischen Fragen unterstützt hat und an Philipp Altpeter und Christian Obermayer für die tolle Organisation des Reinraums. Danke euch allen, dass ich egal mit welcher Frage immer zu euch kommen konnte!

Durch den Zuwachs durfte ich Hiwis, Bachelor- und Masterarbeiten betreuen und Projekte vergeben, für die ich selbst keine Zeit mehr hatte. Lukas, Daniel, Davide, Jakob, Theresa, Philipp und Patrick möchte ich für die Arbeit danken, die sie zu ihrer eigenen gemacht haben. Ein besonderes Dankeschön möchte ich an Theresa richten für ihre unfassbare Freude im Labor und den Satz „Jaaaa da hab ich voll Lust drauf!“ - egal, welche Aufgabe man für sie hatte.

Dankeschön auch an meine lieben Kooperationspartner in Mainz, das für mich durch die vielen Reisen dorthin ein bisschen wie ein zweites Zuhause wurde. Von Amelie und Stefan habe ich alles über AFM und KPFM gelernt und konnte damit auch Neues in unsere Gruppe einbringen.

Auch die nächste Generation an Doktoranden hat ein großes Dankeschön verdient: Lucca, vielen, vielen Dank dafür, dass du immer noch ein bisschen schwäbischer und neuer warst als ich und mich irgendwann mit dem Aufgaben-Overload abgelöst hast. Trotz der vielen Aufgaben hast du jeden Morgen gute Laune mit ins Büro gebracht und die Stimmung gelockert. Außerdem warst du immer mein Ansprechpartner für FTIR-Spektroskopie und hast mir, auch nachdem du nicht mehr bei uns warst, noch mit allen dummen Fragen weiter geholfen. Noelia, leider haben wir es nicht geschafft, meine Spanisch-Kenntnisse auszubauen, aber ich konnte von dir lernen, was es heißt nie aufzugeben, jeden Rückschlag einzustecken und weiterzumachen. Anna, die Energie, die du in deine Arbeit und in die Gruppe steckst, sind unfassbar, und auch wenn du vielleicht nicht immer ganz glücklich damit warst, bin ich sehr, sehr froh, dass du den Umzug nach Göttingen mitgemacht und mitgeschmissen hast. Ohne dich wären die Gruppe und unsere Labore vermutlich irgendwo auf der Strecke geblieben. Am wichtigsten waren für mich aber der Zusammenhalt und die persönlichen Gespräche mit dir: über vergangene Zeiten, kommende Abenteuer, Kuchen und was sonst so wichtig ist!

Unser Umzug nach Göttingen war für uns alle sehr spannend, aber viel Aufregung wurde durch die Techniker des I. Physikalischen Instituts genommen, allen voran Uta: deine Energie, Motivation und Erfahrung sind wirklich unbezahlbar und haben (neben dem Umzug) auch das Experimentieren in Göttingen sehr erleichtert. Darüber hinaus bin ich sehr dankbar für Hartmut und Basti, dass sie alles, einfach alles basteln und bauen können und zwar in Rekordzeit, Simon, dem keiner meiner Wünsche zu viel war, Carsten für seine Unterstützung in allen IT- und Elektronik-Fragen und Kai für simple Lösungen bei (für mich) komplizierten Problemen.

Darüber hinaus haben auch alle Mitglieder der AG Mathias, AG Moshnyaga und AG Ulrichs unsere Ankunft in Göttingen sehr leicht gemacht, uns unterstützt und herzlich empfangen. Vielen lieben Dank dafür! Ganz speziell möchte ich mich bei Daniel Steil und Wiebke bedanken, dass ich mit allen Fragen in Sachen Optik zu ihnen kommen durfte.

Ich bin sehr froh, dass auch nach so einem großen Einschnitt die AG Weitz doch irgendwie dieselbe geblieben ist. Einen wichtigen Beitrag dazu haben sicher Monica, Jonas Schröder, Jonas Pöhls, Jim, Martin, David, Isabell und alle weiteren Mitglieder geleistet, die die Gruppe in Göttingen wieder neu aufgebaut haben. Ein besonderes Dankeschön möchte ich an Monica und Jonas Schröder, unsere „ersten“ Masteranden sowie Martin und Jim für ihren Einsatz als Postdocs richten. *A special thanks goes to Jim for letting me ask you EVERY question,*

*for ALWAYS taking time for me, even when you had none, and for teaching me as much about organic semiconductors as nobody else did.*

Zuletzt auch ein Dankeschön an die aktuelle Doktorandengeneration: Jonas, am Anfang war ich einfach nur dankbar, dass da jemand kam, der mir meine MOF-Projekte abnehmen würde. Aber schon in unserer gemeinsamen Woche in München habe ich gemerkt, dass deine wohlüberlegte und herzliche Art nicht nur das Experimentieren bereichert, sondern auch das „außerdienstliche“ Beisammensein. Darüber hinaus hast auch du in den Aufbau unserer Gruppe und Labore hier in Göttingen viel Zeit und Mühe gesteckt und mir persönlich geholfen, indem du den größten Teil meiner Arbeit Korrektur gelesen hast. Jetzt wirst du eines meiner Lieblingsprojekte weiter führen und ich bin dir schon allein dankbar dafür, dass ich weiß, dass es bei dir in den besten Händen ist! Lukas, du bist jetzt der dienstälteste Organiker und ich weiß, dass du die Aufgaben dieser Position sehr gut meistern wirst, schon allein wegen deiner sehr hilfreichen und kritischen Kommentare zu meiner Arbeit. Abgesehen davon muss ich mich aber auch für deinen guten Süßigkeiten- und Getränkegeschmack bedanken. *Francesca, even if our experiments allowed not so much working together, it was always super nice with you at lunch, after work, sharing an office with you or when we met in the labs. Thanks for your great mood, the perfect Tiramisu and your good jokes!* Und zuletzt noch ein ganz, ganz dickes Danke an Christian, dafür, dass man sich einfach nicht mit dir streiten kann, selbst wenn man es aktiv versucht. Ich werde deine positive Art, das Experimentieren und Achtung-die-Kurve-Spielen mit dir sehr vermissen. Danke, dass ich immer zu dir kommen konnte, egal ob es ums Korrekturlesen ging, technische Fragen, oder persönliche Tiefen und Glücksmomente!

Für Hilfe und Unterstützung in persönlichen Belangen möchte ich mich außerdem explizit bei Finn bedanken. Ohne deine Hilfe wäre ich manches mal komplett aufgeschmissen gewesen. Es ist wirklich toll, dass man mit jeder noch so komplizierten Anfrage zu dir kommen kann, und du nur wenige Tage später alles geregelt hast. Außerdem haben mich Christina, Sabine, Jim, Christian und Thomas in einer ganz besonderen Phase meines Lebens unterstützt und immer wieder ermutigt, sodass ich auch das Arbeiten mit Baby im Bauch und zu Hause genießen konnte.

Zu guter Letzt möchte ich mich bei meiner Familie bedanken. Mama und Papa, danke dass ihr immer für mich da wart und mich unterstützt habt, dass ich mit meinem Essen spielen durfte, beim Kuchenbacken und Fliesenlegen helfen durfte, und von euch mit Musik, Büchern und Liebe überschüttet wurde!

Ich möchte mich auch ganz besonders für das letzte Jahr bedanken: bei meinen Eltern, Lea und Jonas, Basti und Hanna, Esther und Steffen, Hannah, Jonas, David und Daniel fürs Nerven-bewahren, Aufheitern, Zuhören, Umsorgen, Kochen, Babysitten, Da-Sein. Ohne euch alle hätte ich diese Arbeit sicher nicht so schnell und entspannt beenden können.

Der größte Dank geht an Elias, ohne den ich heute nicht wäre, wo ich bin und sein möchte. Du warst bisher in allen Lebenslagen meine Überlebenshilfe, ich durfte mich bei dir ausheulen und die größten Glücksmomente mit dir teilen. Danke, dass du der beste Übungsblattpartner, Freund, Mann und Papa warst und bist, den man sich nur vorstellen kann. Und, last but not least, danke an mein kleines, acht Monate altes, Spielzeug fallenlassendes, zahnloses Monster dafür, dass ich das Schreiben meiner Doktorarbeit als die schönste Zeit meines Lebens bezeichnen kann.